Ultrafast thermo-optical dynamics of single plasmonic nanoparticles

Romain Rouxel

N° d'ordre NNT : 2020LYSE1306

THÈSE DE DOCTORAT DE L'UNIVERSITÉ DE LYON
opérée au sein de
l'Université Claude Bernard Lyon 1

École Doctorale ED52
Physique et Astrophysique

Spécialité de doctorat : Physique

Soutenue publiquement le 11/12/2020, par :
Romain Rouxel

Ultrafast thermo-optical dynamics of single plasmonic nanoparticles

---

Devant le jury composé de :

Arnaud Devos, Directeur de Recherche, IEMN	Rapporteur
Angela Vella, Professeure des Universités, Université de Rouen	Rapporteur
Jean-Jacques Greffet, Professeur des Universités, Université Paris-Saclay	Examinateur
Joël Bellessa, Professeur des Universités, UCBL	Examinateur
Aurélien Crut, Maître de Conférences, UCBL	Directeur de thèse
Natalia Del Fatti, Professeure des Universités, UCBL	Co-directrice de thèse

Université Claude Bernard – LYON 1

Administrateur provisoire de l'Université	M. Frédéric FLEURY
Président du Conseil Académique	M. Hamda BEN HADID
Vice-Président du Conseil d'Administration	M. Didier REVEL
Vice-Président du Conseil des Etudes et de la Vie Universitaire	M. Philippe CHEVALLIER
Vice-Président de la Commission de Recherche	M. Jean-François MORNEX
Directeur Général des Services	M. Pierre ROLLAND

COMPOSANTES SANTE

Département de Formation et Centre de Recherche en Biologie Humaine	Directrice : Mme Anne-Marie SCHOTT
Faculté d'Odontologie	Doyenne : Mme Dominique SEUX
Faculté de Médecine et Maïeutique Lyon Sud - Charles Mérieux	Doyenne : Mme Carole BURILLON
Faculté de Médecine Lyon-Est	Doyen : M. Gilles RODE
Institut des Sciences et Techniques de la Réadaptation (ISTR)	Directeur : M. Xavier PERROT
Institut des Sciences Pharmaceutiques et Biologiques (ISBP)	Directrice : Mme Christine VINCIGUERRA

COMPOSANTES & DEPARTEMENTS DE SCIENCES & TECHNOLOGIE

Département Génie Electrique et des Procédés (GEP)	Directrice : Mme Rosaria FERRIGNO
Département Informatique	Directeur : M. Behzad SHARIAT
Département Mécanique	Directeur M. Marc BUFFAT
Ecole Supérieure de Chimie, Physique, Electronique (CPE Lyon)	Directeur : Gérard PIGNAULT
Institut de Science Financière et d'Assurances (ISFA)	Directeur : M. Nicolas LEBOISNE
Institut National du Professorat et de l'Education	Administrateur Provisoire : M. Pierre CHAREYRON
Institut Universitaire de Technologie de Lyon 1	Directeur : M. Christophe VITON
Observatoire de Lyon	Directrice : Mme Isabelle DANIEL
Polytechnique Lyon	Directeur : Emmanuel PERRIN
UFR Biosciences	Administratrice provisoire : Mme Kathrin GIESELER
UFR des Sciences et Techniques des Activités Physiques et Sportives (STAPS)	Directeur : M. Yannick VANPOULLE
UFR Faculté des Sciences	Directeur : M. Bruno ANDRIOLETTI

Contents

Introduction

Nanoparticles have been during the last decades the subject of an intense research activity, performed by various scientific communities with both fundamental and applicative goals. These efforts are largely motivated by the unique physical and chemical properties of nano-objects, which often strongly differ from those of the bulk form of the same elements. In the case of metal nanoparticles, a striking effect of size reduction is seen in their optical response [1], which is dominated by one or several resonances in their absorption and scattering spectra, called localized surface plasmon resonances (LSPRs). These resonances emerge from the classical laws of electromagnetism as a consequence of dielectric confinement, and are at the origin of the variety of colors of nanoparticle samples in contrast with bulk metals, which are highly dependent on nanoparticle shapes, sizes and local environments. LSPRs have fostered a wide range of applications. Gold nanoparticles have for instance been used for biological imaging and sensing applications and, in the field of medicine, for photothermal cancer therapy (using the high absorption of light by nanoparticles near their LSPR to turn them into nanometric heat sources, allowing the destruction of cancer cells in their vicinity [2]). The high local enhancement of the electromagnetic field around metal nanoparticles is also at the basis of surface-enhanced Raman spectroscopy (SERS), where it is used to dramatically enhance the inelastic scattering signals produced by nearby molecules [3, 4]. Other physical properties of metals are also affected by size reduction, such as their electronic [5, 6], vibrational [7] and thermal [8] properties. Many of these effects are related to the increased importance of surface effects at the nanoscale, as the surface to volume ratio becomes larger. Understanding and precisely modeling these properties is a crucial technological challenge, as the ongoing reduction of devices to the nanoscale is hindered by limits linked to the novel properties emerging at this scale. For instance, the problematic of heat dissipation from nanometer-sized components in electronic and photonic devices represents the major limitation to the improvement of their processing rates [9–11].

The rapid progress made in the recent years in the understanding of these phenomena has been permitted by technological advances in the fields of nanostructure imaging (*e.g.* regarding high-resolution transmission and scanning electron microscopies, atomic force microscopy and superresolution optical microscopies) and synthesis (including colloidal synthesis, evaporation techniques, electron beam lithography), allowing the controlled fabrication of nano-objects within a wide range of sizes and shapes and in various environments. Additionally, the development of femtosecond lasers and optical pump-probe techniques has allowed precise, contactless and nondestructive investigations of the ultrafast dynamics (on femtosecond to nanosecond timescales) of the electrons and of the

ionic lattice in out-of-equilibrium metal nanoparticles. These techniques are based on the photoexcitation of nanoparticles by a femtosecond light pulse, called pump, and on the optical monitoring of their subsequent relaxation, achieved by measuring the transient changes induced on the transmission or reflection of a second, time-delayed pulse (the probe). This approach has notably permitted to determine the size-dependent timescales associated to the internal energy redistribution mechanisms (electron–electron and electron–phonon energy exchanges) occuring in the nano-objects, to their acoustic vibrations (periods and quality factors) and to their cooling.

However, most of the aforementioned studies were based of measurements performed on assemblies of nanoparticles, which present several drawbacks. Firstly, the measured dynamics necessarily represent an average over those of multiple nano-objects, whose morphologies and local environments present an unavoidable dispersion. Secondly, the quantitative analysis of the measured signals is made difficult by the fact that all nano-objects are differently excited and probed, depending on their respective positions in the pump and probe beams. The recent development of single-particle time-resolved optical spectroscopy has allowed a finer correlation between the measured dynamics and the precise morphology of the nano-object (*e.g.* in the case of acoustic vibrations [12]), as well as a more quantitative interpretation of time-resolved signals [13]. However, even in single-particle measurements, disentangling the contributions of the different physical processes involved in the transient optical signals remains difficult.

In this thesis, conducted in the FemtoNanoOptics group of the Light and Matter Institute (LMI), single-particle time-resolved optical spectroscopy was used to investigate the dynamics of internal thermalization and of cooling of individual metal nanoparticles. Throughout this work, the emphasis was put on a quantitative analysis of the transient optical response of the investigated nano-objects induced by these ultrafast processes. In particular, the wavelength dependence of the transient optical changes is experimentally and theoretically explored, allowing to characterize the sensitivity of time-resolved optical measurements to the different physical processes affecting the optical response.

This work is organized in four chapters. In the first one, the physical properties of bulk and nanoscale noble metals are described from a theoretical point of view. The electronic and thermal properties of bulk metals are first reviewed, as well as their optical response. The effect of dielectric confinement is then explained in the cases of a sphere or an ellipsoid small with respect to the wavelength of light (dipolar approximation), and generalized to the case of larger nano-objects. A numerical approach based on the finite element method, allowing to calculate the optical response of nano-objects of any shape, size and environment, is also presented. Finally, the ultrafast relaxation mechanisms triggered by the impulsive excitation of a metal nanoparticle are briefly introduced.

Chapter 2 describes the experimental techniques used during this work, whose configura-

tions have been optimized to enable highly quantitative measurements. We first present the spatial modulation spectroscopy technique (SMS), allowing the detection of a single isolated nano-object and the measurement of its absolute extinction cross-section as a function of the light wavelength and polarization. The principle of time-resolved pump–probe spectroscopy, a technique permitting the measurement of the transient changes of the extinction cross-section of a photoexcited nano-object, is presented in a second part.

The third chapter presents an experimental and theoretical study of the cooling dynamics of single gold nanodisks supported on a sapphire substrate. The aim of this study is twofold. The first aspect of this work is dedicated to determining the wavelength-dependent sensitivity of the extinction cross-section of nanodisks to transient temperature changes. Quantitative analysis of time-resolved measurements made on single nanodisks as a function of the probe wavelength yielded excellent agreement with the results of a numerical opto-thermal model, providing experimental confirmation for purely theoretical results published in the past [14]. The second aspect of this chapter deals with the cooling dynamics of gold nanodisks and their dependence on the nano-object morphology. They are found to be quasi-exponential, with a time constant mainly depending of the nanodisk thickness and weakly on its diameter, showing that these dynamics are limited by heat transfer at the interface with the substrate. This makes the studied system ideal for accurate measurements of the gold–sapphire interface conductance, whose average value is extracted from measurements on many individual nanodisks by comparison between the experimental data and a numerical thermal model. The approach followed in this work was recently used by other groups for interface conductance measurements [15–19], but this work is the first to present thermal measurements at the scale of a single nano-object, allowing notably to estimate the object-to-object dispersion of the interface conductance.

The last chapter of this work focuses on the ultrafast phenomena immediately following the nano-object photo-excitation, leading to its internal thermalization through electron-electron and electron-phonon energy exchanges. In particular, the sensitivity of the optical extinction of individual nanodisks to these phenomena is experimentally investigated as a function of the probe wavelength. These measurements are in quantitative agreement with the results of a complete numerical model based notably on the resolution of the Boltzmann equation, and also including several effects generally omitted in previous works of this kind [13, 20], which are here proved necessary for a satisfying reproduction of the measured data. A simplified version of this model also allowed to highlight the respective roles of the temperature evolutions of the electrons and of the ionic lattice, greatly clarifying the temporal and spectral dependences of the measured time-resolved signals.

Chapter 1

Optical response of metallic nanoparticles

Contents

In the studies described in this thesis, various physical properties (electronic, optical and thermal) of single noble metal nano-objects are quantitatively investigated through measurements of their optical response, both in the stationary and transient regimes (*i.e.* after ultrafast excitation by a light pulse). The connection between the optical properties of the studied nanosystems and their composition, morphology and environment thus plays an essential role in these studies. The optical response of a metal (*i.e.* absorption and scattering) reflects the interaction of light with its electrons, and is therefore closely linked to its electronic band structure. The optical response of a metal nano-object in a dielectric environment strongly differs from that of the bulk. This modification mainly originates from a purely classical dielectric confinement effect emerging from the laws of electromagnetism, although quantum confinement effects may also arise for small nanoparticles, leading to the discretization of energy levels. Dielectric confinement induces resonances in the absorption and scattering spectra of metal nano-objects, called Localized Surface Plasmon Resonances (LSPR). These resonances, which have been extensively investigated in the past, play an important role in this work, as they allow the sensitive probing of the relaxation phenomena determining the ultrafast dynamics of a nano-object after its sudden excitation.

The first section of this chapter will briefly review the electronic, thermal and optical properties of bulk noble metals. The next section will be dedicated to the effects of size reduction and confinement in a dielectric environment. We will then describe in section 1.3 the ultrafast mechanisms following the absorption of a femtosecond laser pulse by a nano-object, inducing time-dependent modifications of its optical response.

1.1 Physical properties of bulk noble metals

1.1.1 Electronic and thermal properties of noble metals

Copper, silver and gold constitute the family of *noble metals*. These three elements are characterized by similar electronic configurations ending with one completely filled $(n-1)d$ subshell and one ns subshell containing one electron (they are thus monovalent). In crystalline form, they present a face-centered cubic structure (fcc), whose main parameters are summarized in table 1.1.

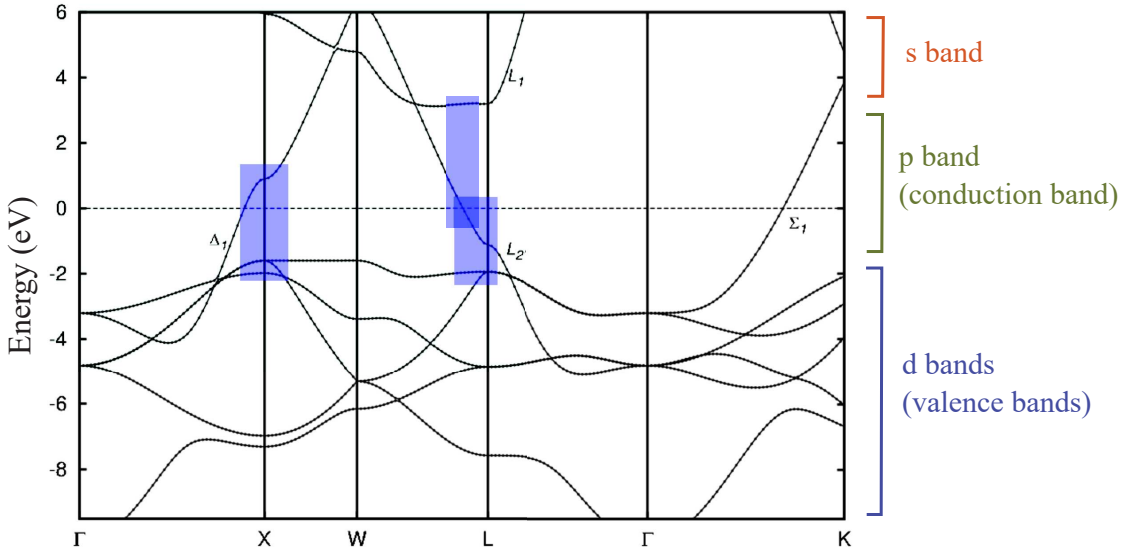

Figure 1.1 – Electronic band structure of gold. The Fermi energy E_F is taken as origin of the energy. The high-symmetry points of the first Brillouin zone are defined in figure 1.2b. The approximate positions of the d, p and s bands are indicated, while the blue rectangles specify the zones where vertical electronic transitions excited by photon absorption (between bands $d \rightarrow p$ or $p \rightarrow s$) are most probable. Reproduced from ref. [21].

metal	electronic structure	$\tilde{a}$ (Å)	n_e (10^{22} cm^{-3})
Cu	[Ar]$3d^{10}4s^1$	3.61	8.47
Ag	[Kr]$4d^{10}5s^1$	4.09	5.86
Au	[Xe]$4f^{14}5d^{10}6s^1$	4.08	5.90

Table 1.1 – Electronic structure, lattice parameter $\tilde{a}$, and density of conduction electrons n_e of noble metals Cu, Ag and Au.

In solids, the discrete energy levels of atoms give rise to continuous energy bands through the interaction of atomic orbitals. The $(n-1)d$ states thus result in five completely-filled, weakly dispersed d bands—also called *valence bands*—, while hybridization of the ns and np orbitals leads to the formation of a half-filled p band—the *conduction band*—and of an empty s band of higher energy. The band structure of bulk gold is shown in figure 1.1.

1.1.1.a Conduction electrons

The nearly-parabolic dispersion of the conduction band enables the description of conduction electrons as quasi-free electrons, with a dispersion relation (linking the energy E and wavevector $\mathbf{k}$ of the states) written as:

$$E(\mathbf{k}) = \frac{\hbar^2 k^2}{2m^*} \ , \tag{1.1}$$

where the electron rest mass m_e has been replaced by an effective mass m^* which includes the effects of the interactions of the electron with the ionic lattice. For a quasi-free electron gas, the density of energy states per unit volume around energy E is given by:

$$\rho(E) = \frac{1}{2\pi^2}\left(\frac{2m^*}{\hbar^2}\right)^{3/2}\sqrt{E}\ . \tag{1.2}$$

The Fermi energy E_F is defined as the energy of the highest occupied level of the electron distribution at temperature 0 K. It is related to the effective mass m^* and the density n_e of conduction electrons via:

$$E_F = \frac{\hbar^2}{2m^*}\left(3\pi n_e\right)^{2/3}\ . \tag{1.3}$$

One can also define several quantities linked to the Fermi energy, such as the Fermi wave vector $k_F = \sqrt{2m^*E_F}/\hbar$, and the Fermi temperature $T_F = E_F/k_B$ (with k_B the Boltzmann constant). Values of these parameters for copper, silver and gold are presented in table 1.2.

metal	m^*/m_e	E_F (eV)	k_F (10^8 cm^{-1})	T_F (10^4 K)
Cu	1.3	4.67	1.36	5.44
Ag	1.1	5.49	1.20	6.38
Au	1.1	5.53	1.21	6.42

Table 1.2 – Effective electron mass m^* divided by the electron rest mass m_e, Fermi energy E_F, Fermi wave vector k_F, and Fermi temperature T_F in Cu, Ag and Au [22].

The Fermi surface is the surface of the reciprocal space which separates occupied from unoccupied states at zero temperature. For a free-electron gas, the Fermi surface is a sphere of radius k_F, the energy only depending on $\|\mathbf{k}\|$ (equation 1.1). In noble metals, deviations from the ideal free-electron model lead to slight deformations of this surface around points L and X of the first Brillouin zone (figure 1.2).

The equilibrium occupation probability of an electronic state of energy E at electronic temperature T_e is given by the Fermi–Dirac distribution:

$$f(E) = \frac{1}{e^{(E-E_F)/(k_BT_e)}+1}\ , \tag{1.4}$$

where the chemical potential $\mu(T_e)$ was identified to E_F. This assumption is valid when

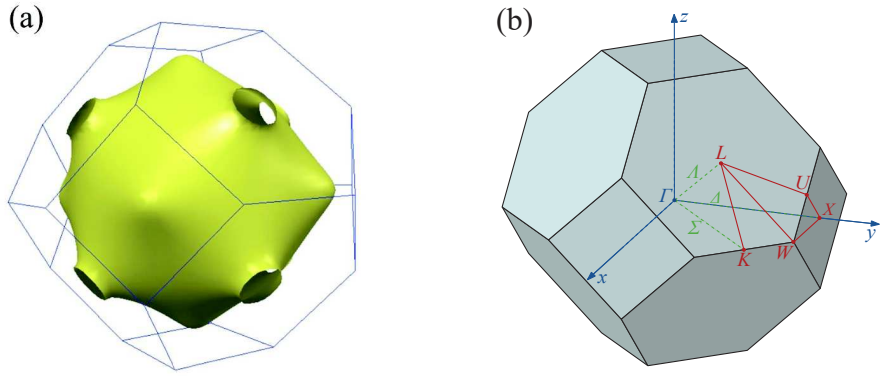

Figure 1.2 – Fermi surface in Au (a) and illustration of the first Brillouin zone of a fcc lattice (b), showing its symmetry lines and characteristic points [23].

$T_e \ll T_F$, which is verified at room temperature in the case of noble metals (see table 1.2). This implies that the electronic distributions at room temperature and at 0 K differ significantly only around the Fermi energy, *i.e.* for **k**-states close to the Fermi surface.

The volumetric specific heat of the electron gas $c_e(T_e)$ is computed as the temperature derivative of the electron volumetric internal energy u_e:

$$c_e(T_e) = \frac{\partial u_e}{\partial T_e} = \int_0^\infty E\rho(E)\frac{\partial f(E)}{\partial T_e}dE \ , \tag{1.5}$$

where $\rho(E)$ is given by equation 1.2. In the free electron gas approximation, assuming $T_e \ll T_F$ (which allows using expression 1.4), one finds after integration that the electronic specific heat is linear with the electron temperature:

$$c_e(T_e) = \frac{\pi^2 n_e k_B}{2T_F} T_e = aT_e \ , \tag{1.6}$$

with $a = \dfrac{\pi^2 n_e k_B}{2T_F} \sim 65 \ \mathrm{J\,K^{-2}\,m^{-3}}$ in gold [22]. The temperature dependence of c_e plays an important role in the dynamics of relaxation of a photoexcited metal, as will be described in chapter 4.

1.1.1.b Ionic lattice

The primitive cell of noble metal crystals containing a single atom, only *acoustic* vibrational modes of the ionic lattice are permitted, whose energy vanishes when their wave vector **q** is zero. The phonon band structure of noble metals contains three acoustic

branches, two of them corresponding to transverse vibrations and one to longitudinal vibrations. Each branch contains N_i modes, with N_i the number of ions in the lattice.

To evaluate the dispersion relations $\omega_s(\mathbf{q})$ associated to the these three branches, hypotheses must be made about the interatomic potential. In the model initially developed by P. Debye in 1912, linear dispersion relations are assumed. By also assuming isotropy (*i.e.*, identical dispersion relations in the three branches, which is not the case in real materials), one obtains:

$$\omega_s(\mathbf{q}) = v_s\, q \ . \tag{1.7}$$

v_s represents the average sound velocity of the three branches. The N_i vibrational modes of each branch are contained within a sphere, whose radius k_D is called the Debye wave vector. The volume of a primitive cell in the reciprocal space being $(2\pi)^3/V$ (with V the metal volume), one obtains:

$$q_D = (6\pi^2 n_i)^{1/3} = \left(\frac{2}{Z}\right)^{1/3} k_F \ , \tag{1.8}$$

with $n_i = N_i/V$ the volumetric density of modes and Z the metal valence, equal to 1 for noble metals. Similarly, one defines the Debye frequency $\omega_D = v_s\, q_D$, and the Debye temperature T_D, defined through $k_B T_D = \hbar\omega_D$. T_D may be interpreted as the temperature above which all vibrational modes are excited. For gold, this temperature is 170 K [22], *i.e.* well below the temperature at which our experiments are performed (~ 300 K).

The equilibrium phonon occupation number at temperature T_L is given by a Bose–Einstein distribution:

$$n_{BE}(\mathbf{q}, T_L) = \frac{1}{e^{\hbar\omega_s(\mathbf{q})/(k_B T_L)} - 1} \ . \tag{1.9}$$

The volumetric lattice heat capacity may be calculated similarily to equation 1.5, using the occupation number given in equation 1.9. This calculation leads to:

$$c_L = \frac{1}{V}\frac{\partial}{\partial T_L} \sum \hbar\omega_s(\mathbf{q}) \left[n_{BE}(\mathbf{q}, T_L) + \frac{1}{2} \right], \tag{1.10}$$

where the summation is over all wave vectors $\mathbf{q}$ in the three branches. For high enough temperatures ($\hbar\omega_s(\mathbf{q})/(k_B T_L) \ll 1$, which is valid for gold at room temperature), no assumption about the dispersion relation is required to calculate the heat capacity. Indeed, a first-order development of equation 1.9 ($(e^x - 1)^{-1} \approx x^{-1}$ with $x = \hbar\omega_s/(k_B T_L)$) permits the simplification of the $\hbar\omega_s$ terms, leading to a constant lattice volumetric specific

heat:

$$c_L \approx 3 n_i k_B \ , \tag{1.11}$$

corresponding to the classical Dulong–Petit law. For gold, this expression leads to $c_L \approx 2.5 \times 10^6 \ \mathrm{J\,m^{-3}\,K^{-1}}$. Combining this result with the expression of $c_e(T_e)$ given by equation 1.6, one obtains $c_L/c_e \approx 100$ at $T = 300$ K, meaning that the heat capacity of metals at room temperature is only given by c_L, and thus weakly dependent on temperature.

1.1.2 Optical response of bulk metals

1.1.2.a Definitions

A monochromatic electromagnetic field with wave vector $\mathbf{k}$ and angular frequency ω:

$$\mathbf{E}(\mathbf{r}, t) = \mathrm{Re}[\mathbf{E_0} e^{i(\mathbf{k}\cdot\mathbf{r} - \omega t)}] \ , \tag{1.12}$$

interacting with a material, induces a polarization density $\mathbf{P}$ resulting from an opposite displacement of the bound positive and negative charges. In the case of a homogeneous, linear and isotropic material, the polarization is expressed simply as $\mathbf{P} = \varepsilon_0 \chi \mathbf{E}$, where the electric susceptibility $\chi(\omega)$ is a scalar function of ω. The electric displacement field then writes:

$$\mathbf{D} = \varepsilon_0 \mathbf{E} + \mathbf{P} = \varepsilon_0 \varepsilon \mathbf{E} \tag{1.13}$$

with ε_0 the vacuum permittivity, and where $\varepsilon = 1 + \chi$ represents the dielectric function (or relative permittivity) of the material. ε may be written as $\varepsilon(\omega) = \varepsilon_1(\omega) + \mathrm{i}\varepsilon_2(\omega)$, with ε_1 and ε_2 real. Alternatively, the optical properties may be described using the complex optical index $\tilde{n} = n + i\kappa$, related to ε via $\tilde{n}^2 = \varepsilon$. Its real part n is the refraction index, related to the phase velocity of light in the material v by $v = c/n$, while κ, the extinction coefficient, specifies the absorption of electromagnetic energy by the solid. Indeed, propagation of an electromagnetic wave over a distance L in the material results in an intensity reduction given by:

$$I_t = I_0 e^{-\alpha L} \quad \text{with} \quad \alpha(\omega) = 2\frac{\omega}{c}\kappa(\omega) \tag{1.14}$$

The explicit relation between $(\varepsilon_1, \varepsilon_2)$ and (n, κ) writes:

$$\begin{cases} \varepsilon_1 &= n^2 - \kappa^2 \\ \varepsilon_2 &= 2n\kappa \end{cases} \tag{1.15}$$

Thus, for $\kappa = 0$ (transparent medium), $\varepsilon_1 = n^2$ and $\varepsilon_2 = 0$.

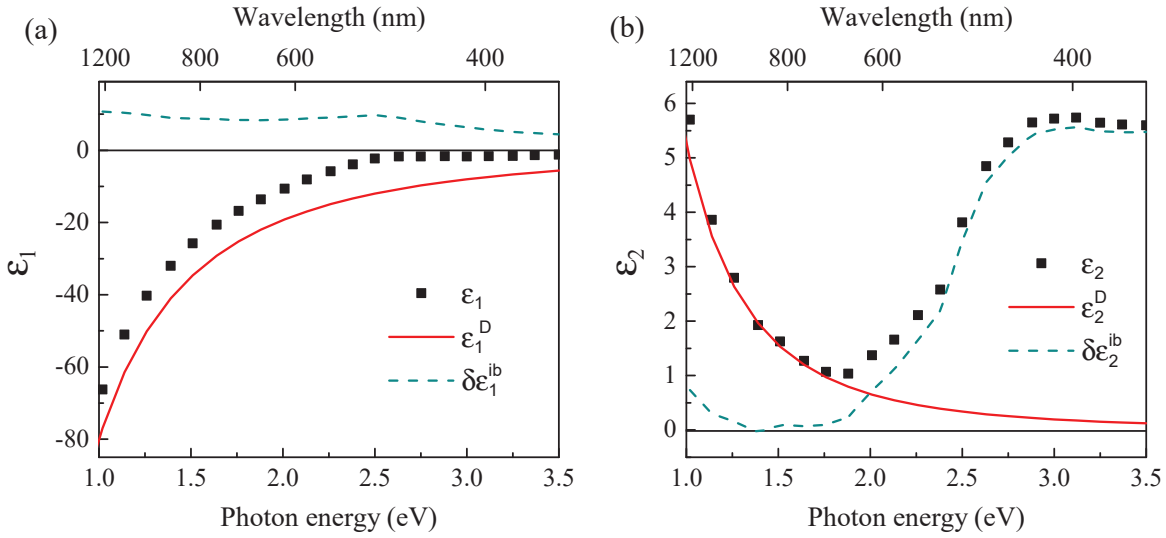

Figure 1.3 – Spectral dependence of the real part ε_1 (a) and imaginary part ε_2 (b) of gold dielectric function. Experimental values of $\varepsilon_{1,2}$ (black squares) are taken from data tabulated by Johnson and Christy [24]. Contributions $\varepsilon^D_{1,2}$ resulting from intraband electronic transitions, computed using the Drude model, are shown as red plain lines. The dashed green lines are estimations of the contributions of interband transitions $\delta\varepsilon^{ib}_{1,2}$ to the dielectric function, obtained from the experimental data through $\delta\varepsilon^{ib} = \varepsilon - \varepsilon^D$. ε^{ib} is then retrieved through $\varepsilon^{ib} = \delta\varepsilon^{ib} + 1$.

The spectral dependence of the dielectric function of bulk gold is shown in figure 1.3. Two distinct light absorption mechanisms, schematized in figure 1.4, contribute to ε:

- photon-excited transitions between quasi-free electronic states within the conduction band (*intraband* transitions). Because of the dispersion relation of quasi-free electrons (equation 1.1), a transition to a higher-energy state of this band implies a momentum increase. The momentum of the absorbed photon being negligible, interaction with a third body (another electron, a phonon, or a lattice defect) is necessary to respect momentum conservation (figure 1.4). Intraband transitions are thus three-body processes. They are well-described by the classical Drude model of conduction electrons [22].

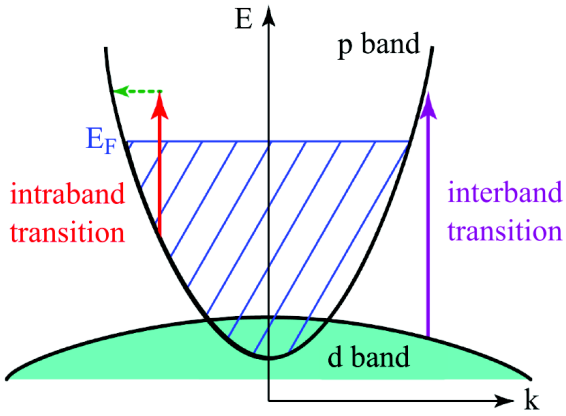

Figure 1.4 – Simplified representation of the band structure of noble metals. The weakly-dispersed valence bands (d bands) are completely filled, while the nearly-parabolic conduction band (s-p band) is half-filled. Absorption of a photon by the metal can occur through the transition of a conduction electron to a higher state of the same band (*intraband transition*), which must involve a third particle (electron or phonon) to respect the momentum conservation. A photon may also be absorbed through the direct transition of a d-band electron to an empty state of the conduction band (*interband transition*), which requires a high enough photon energy.

- photon-excited transitions of valence electrons to the conduction band (*interband* transitions). These transitions may occur only for high enough photon energies, in order to allow for the direct (vertical) transition of electron from the valence band to a free state of the conduction band (figure 1.4). The associated threshold, corresponding to the energy difference between the top of the valence band and the Fermi energy E_F, is about 2.4 eV for gold. As opposed to intraband transitions, description of interband transitions requires a fully quantum theory.

The total electric susceptibility is given by the sum of these two effects and writes $\chi = \chi^D + \chi^{ib}$. We also define symmetrically $\varepsilon^{D,ib} = 1 + \chi^{D,ib}$, which implies that $\varepsilon = 1 + \chi = \varepsilon^D + \varepsilon^{ib} - 1$. We will now detail these two contributions to the dielectric function.

1.1.2.b Intraband contribution to the dielectric function: Drude model

Shortly after the discovery of the electron by J.J. Thomson, P. Drude applied the classical theory of gas kinetics to metals, by modeling them as an electron gas. The assumptions made by Drude partly reflect the lack of knowledge of the structure of solids at the time. The Drude model treats the electrons as being completely free, independent from one another, and only subject to collisions of unspecified nature with rate $\gamma_0 = 1/\tau_0$ (where τ_0 is the average time between two collisions), after which their movement is arbitrarily directed with a random velocity following Maxwell's distribution. On average, these

assumptions are equivalent to considering that each electron is submitted to a friction force $\mathbf{F} = -m_e\gamma_0\mathbf{v}$. To account for the fact that the electrons are weakly bound instead of free (as discussed in paragraph 1.1.1), the electron mass m_e appearing in the original Drude model must be replaced by the effective mass m^*. In the presence of an oscillating electric field $\mathbf{E}(t) = \mathbf{E}_0\cos(\omega t)$, position $\mathbf{r}$ of an electron follows the equation of motion:

$$m^*\frac{d^2\mathbf{r}}{dt^2} = -m^*\gamma_0\frac{d\mathbf{r}}{dt} - e\mathbf{E} \tag{1.16}$$

From the solution $\mathbf{r}$ of equation 1.16 in the stationary regime, the polarization of the metal is obtained through $\mathbf{P} = -n_e e\mathbf{r}$. Since $\mathbf{P}$ is also defined as $\mathbf{P} = \varepsilon_0\chi^D\mathbf{E}$, the Drude permittivity writes:

$$\varepsilon^D(\omega) = 1 + \chi^D = 1 - \frac{\omega_p^2}{\omega(\omega + i\gamma_0)} \tag{1.17}$$

where $\omega_p = \sqrt{\frac{n_e e^2}{m^*\varepsilon_0}}$ represents the plasma frequency. By expressing the real and imaginary parts of ε, one finds:

$$\begin{cases} \varepsilon_1^D &= 1 - \dfrac{\omega_p^2}{\omega^2+\gamma_0^2} \simeq 1 - \dfrac{\omega_p^2}{\omega^2} \quad \text{for } \gamma_0 \ll \omega \\ \varepsilon_2^D &= \dfrac{\gamma_0\omega_p^2}{\omega(\omega^2+\gamma_0^2)} \simeq \gamma_0\dfrac{\omega_p^2}{\omega^3} \quad \text{for } \gamma_0 \ll \omega \end{cases} \tag{1.18}$$

Fits of experimental measurements of gold dielectric function by the Drude formula above (figure 1.3) provides estimations for the plasma frequency ω_p and the optical scattering rate γ_0, yielding $\hbar\omega_p \approx 9.01$ eV and $\hbar\gamma_0 \approx 70$ eV [24]. The condition $\gamma_0 \ll \omega$, necessary to obtain the approximations made in equation 1.18, is thus valid for gold in the visible and near-infrared ranges (corresponding to $\hbar\omega \approx$ 1-3 eV).

The optical scattering rate γ_0 reflects photon absorption by electrons in the conduction band, which must be assisted by a third particle (electron, phonon, or lattice defect), as discussed above. It may be written as:

$$\gamma_0(\omega, T_e, T_L) = \gamma_{e-e}(\omega, T_e) + \gamma_{e-ph}(\omega, T_e, T_L) + \gamma_{e-d}(\omega, T_e) \tag{1.19}$$

with γ_{e-e}, γ_{e-ph} and γ_{e-d} the electron–electron, electron–phonon and electron–defect scattering rates. T_e and T_L are the temperatures of the electron gas and of the lattice, respectively.

Calculation of the electron–phonon term γ_{e-ph} has been performed in the hypothesis of a parabolic conduction band and for a photon energy $\hbar\omega$ lower than the Fermi energy, where electron–phonon interactions are modeled via a deformation potential [25, 26]. Starting from Fermi's golden rule at second order, this calculation yields:

$$\gamma_{e-ph}(\omega, T_e, T_L) = \frac{G_{e-ph}(T_L)}{\hbar\omega} \int_0^\infty \sqrt{E(E+\hbar\omega)} f(E)[1 - f(E+\hbar\omega)]\mathrm{d}E \ , \tag{1.20}$$

where G_{e-ph} is an electron–phonon interaction parameter. If the lattice temperature is larger than the Debye temperature ($T_L > T_D$), G_{e-ph} is approximately proportional to T_L, while the T_e dependence of γ_{e-ph} is included in the occupation numbers $f(E)$ [27].

The term γ_{e-e} corresponds to the rate of photon absorption assisted by electron–electron scattering processes. A calculation made by R. Gurzhi in the case of a thermalized electron gas leads to [28]:

$$\gamma_{e-e}(\omega, T_e) = \frac{\omega^2}{4\pi^2\omega_p} \left[1 + \left(\frac{2\pi k_B T_e}{\hbar\omega}\right)^2\right] \ . \tag{1.21}$$

The electron–defect scattering rate γ_{e-d} appearing in equation 1.19 is more difficult to model, but this term may cause a significant increase of γ_0 for polycrystalline metal samples such as those used in this work (synthesized using electron beam lithography) [29, 30], as will be discussed in chapter 3.

For small nanoparticles (typically < 30 nm), an additional damping rate γ_{e-S} must be included in equation 1.19. Classically interpreted as an electron–surface scattering term, its precise description requires a quantum-mechanical treatment, where it emerges as an effect of the discretization of electronic energy levels induced by confinement [31]. For spherical nanoparticles with diameter D, it may be expressed as [13, 32]:

$$\gamma_{e-S}(\omega, T_e) = 2g(\omega, T_e)\frac{v_F}{D} \ , \tag{1.22}$$

with v_F the Fermi velocity ($\approx 1.4 \times 10^6$ m s^{-1} for gold [22]), and $g \approx 0.7$ in gold at room temperature in the optical domain [27].

As shown in figure 1.3, the Drude model (solid red line) is in correct agreement with

experimental measurements of the dielectric function of gold for low photon energies. For energies higher than ~ 2 eV, the imaginary part ε_2 largely deviates from the Drude model, due to photon-induced interband transitions, leading to an additional contribution ε^{ib}. Assuming that the intraband transitions are perfectly described by the Drude model, ε^{ib} can be empirically deduced from experimental measurements of ε through $\varepsilon^{ib} = 1+\varepsilon-\varepsilon^D = 1+\delta\varepsilon^{ib}$. The differences $\delta\varepsilon^{ib}_{1,2}$ are plotted in figure 1.3 as green dashed lines.

However, to enable the description of the time-dependent modifications of ε^{ib} resulting from an out-of-equilibrium excitation of the electrons (a necessary element in the theoretical reproduction of time-resolved experiments), an explicit modeling of the interband contribution is required. This can only be done from a quantum description of the band structure, which we now present.

1.1.2.c Interband contribution to the dielectric function

To describe the contribution of interband transitions to the imaginary dielectric function ε_2 of noble metals, which is directly related to photon absorption, we present the model developed by Rosei and collaborators based on a simplified description of the band structure of gold [33]. For a photoexcitation in the visible range, resonant transitions mainly involve electronic states located around the L and X points of the first Brillouin zone, either between the valence and conduction bands d and p ($L_{d\to p}$ and $X_{d\to p}$) or between the p band and the empty s band around the L point ($L_{p\to s}$) (see figure 1.1). The energy-dependent joint density of states $D_{i\to j}(E,\hbar\omega)$, which describes the probability of a transition from a state in band i with energy E to a state in band j with energy $E+\hbar\omega$, is expressed as:

$$D_{i\to j}(E,\hbar\omega) = \frac{1}{(2\pi)^3}\int \delta\Big[E_f(\mathbf{k}) - E_i(\mathbf{k}) - \hbar\omega\Big]\,\delta\Big[E - E_i(\mathbf{k})\Big]\,\mathrm{d}^3k\ . \tag{1.23}$$

The first delta function in equation 1.23 imposes that the energies of the initial and final states E_i and E_f are separated by $\hbar\omega$, while the second delta function selects initial states of energy E. In the Rosei model, calculation of $D_{i\to j}(E,\hbar\omega)$ is achieved by approximating the d, p and s bands around the L and X points by anisotropic parabolas, associated to effective electron masses $m_\parallel$ and $m_\perp$ along perpendicular directions in the reciprocal space [33].

The total probability for a transition between bands i and j is given by the joint density of states $J_{i\to j}(\hbar\omega)$, which is obtained by integrating $D_{i\to j}(E,\hbar\omega)$ over the energy E, taking into account the occupation probability of the initial and final states:

$$J_{i\to j}(\hbar\omega) = \int_{E_{min}^{i,j}}^{E_{max}^{i,j}} D_{i\to j}(E,\hbar\omega) f(E)[1-f(E+\hbar\omega)]\,\mathrm{d}E\ , \tag{1.24}$$

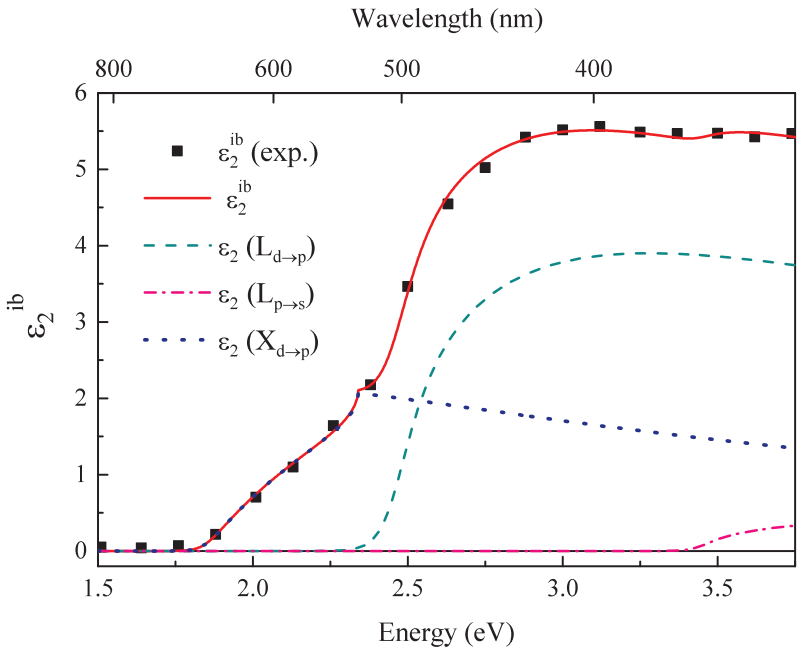

Figure 1.5 – Experimental and calculated interband component to the imaginary part of Au dielectric function, ε_2^{ib}. The contributions of the three interband transitions appearing in equation 1.25 are shown as indicated in the legend.

where the integration limits $E_{min}^{i,j}$ and $E_{max}^{i,j}$ are chosen so as to include all possible transitions from band i to band j. ε_2^{ib} may then be evaluated by summing the three types of transitions discussed above:

$$\varepsilon_2^{ib}(\hbar\omega) = \frac{4\pi^2 e^2\hbar^2}{\varepsilon_0 m_e^2(\hbar\omega)^2}\left[A_{d\to p}^X J_{d\to p}^X(\hbar\omega) + A_{d\to p}^L J_{d\to p}^L(\hbar\omega) + A_{p\to s}^L J_{p\to s}^L(\hbar\omega)\right]\ . \tag{1.25}$$

In equation 1.25, coefficients $A_{i\to j}$ are the squared matrix elements of the momentum operator $\mathbf{p}$ describing the transition strengths:

$$A_{i\to j} = |\langle i|\mathbf{p}|j\rangle|^2\ . \tag{1.26}$$

In the work of Stoll *et al.* [34], amplitudes $A_{i\to j}$ were empirically determined by fitting experimental room-temperature measurements of $\varepsilon_2(\hbar\omega)$ by the sum of the Drude and

interband contributions (equations 1.18 and 1.25). Determination of ε_2^{ib} was based on the Au band structure calculated by Rangel *et al.* [35], with the energy gaps at the L and X points being left as free parameters. The results are shown in figure 1.5, where the black squares represent the measurements of Au dielectric function reported by Johnson and Christy [24] after subtraction of the Drude part ε_2^D, and the red line the computed ε_2^{ib} function. The contributions of the three considered transitions are plotted. The main contribution is that of the $L_{d\to p}$ transitions. Its energy dependence presents an onset at $\hbar\omega \approx 2.4$ eV (515 nm), which is often taken as reference for the interband transition threshold, although the onset for the weaker $X_{d\to p}$ contribution is only $\hbar\omega \approx 1.8$ eV (690 nm). Finally, the $L_{p\to s}$ transitions do not contribute to ε_2^{ib} in the visible range, as their threshold is $\hbar\omega \approx 3.4$ eV (360 nm).

In the context of time-resolved experiments on metal films or nano-objects, the dielectric function undergoes transient variations following the ultrafast absorption of a light pulse. As will be discussed in chapter 4, this excitation leads to a transient modification $\Delta f(E,t)$ of the electronic distribution around the Fermi energy. Using the calculation method presented above, it is possible to calculate the induced variations $\Delta\epsilon_2^{ib}(t)$ of the imaginary part of the interband contribution to the dielectric function, by replacing in equation 1.24 the equilibrium distribution at room temperature f by its transient modification $\Delta f(t)$. In this calculation, the amplitudes $A_{i\to j}$ deduced from the fit of room-temperature measurements of ε_2 (figure 1.5) must be used.

1.2 Linear optical response of metal nano-objects

The optical response of noble metal nano-objects is characterized by one or several resonances in their absorption and scattering spectra, called localized surface plasmon resonances (LSPRs), which are a consequence of dielectric confinement. These resonances, associated to a collective electron motion induced by light, result in a strong enhancement of the electromagnetic field in and around the nano-objects. Their amplitudes, spectral positions and widths are strongly dependent on the geometry, size and composition of the nano-objects, as well as on their local environment. In this section, we start by general energetic considerations enabling a precise definition of the extinction cross-section of a nano-object, which is the physical quantity investigated in linear and time-resolved spectroscopy. We then present analytical descriptions of the optical response of small nano-objects and a numerical calculation method adapted in the case of a particle of arbitrary size, shape and environment.

1.2.1 Energetic considerations

We consider a metal nano-object embedded in a non-absorbing dielectric medium, submitted to an oscillating electromagnetic field $(\mathbf{E}_0, \mathbf{H}_0)$ with total power P_0. This incident field causes an oscillation of the metal electrons at the frequency and in the direction of $\mathbf{E}_0$, generating a scattered electromagnetic field at the same frequency $(\mathbf{E}_{scat}, \mathbf{H}_{scat})$ in the surrounding medium. The time-averaged Poynting vector of the total electromagnetic field outside the particle (corresponding to $\mathbf{E}_{tot} = \mathbf{E}_0 + \mathbf{E}_{scat}$ and $\mathbf{H}_{tot} = \mathbf{H}_0 + \mathbf{H}_{scat}$) can be separated into three contributions [36]:

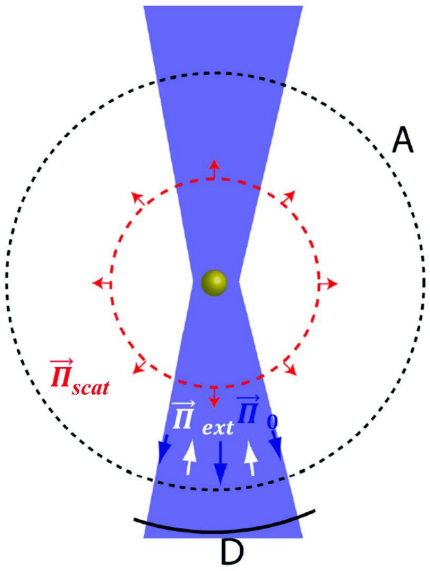

Figure 1.6 – Electromagnetic energy flows in the context of single-particle optical experiments. See equations 1.27 and 1.28.

$$\mathbf{\Pi}_{tot} = \frac{1}{2} Re(\mathbf{E}_{tot} \wedge \mathbf{H}^*_{tot}) = \mathbf{\Pi}_0 + \mathbf{\Pi}_{scat} + \mathbf{\Pi}_{ext} \tag{1.27}$$

with

$$\begin{cases} \mathbf{\Pi}_0 &= \frac{1}{2}\mathrm{Re}(\mathbf{E}_0 \wedge \mathbf{H}^*_0) \\ \mathbf{\Pi}_{scat} &= \frac{1}{2}\mathrm{Re}(\mathbf{E}_{scat} \wedge \mathbf{H}^*_{scat}) \\ \mathbf{\Pi}_{ext} &= \frac{1}{2}\mathrm{Re}(\mathbf{E}_0 \wedge \mathbf{H}^*_{scat} + \mathbf{E}_{scat} \wedge \mathbf{H}^*_0) \end{cases} \tag{1.28}$$

The Poynting vectors defined in equation 1.28 are represented in figure 1.6. When

the dielectric environment is transparent, as assumed here, the electromagnetic power absorbed by Joule effect by the nano-object, P_{abs}, may be expressed as the opposite of the flux of the Poynting vector of the total field $\mathbf{\Pi}_{tot}$ through an arbitrary closed surface A enclosing the nano-object (figure 1.6). Scattering and extinction powers are similarly defined as:

$$\begin{cases} P_{abs} &= -\oiint_A \mathbf{\Pi}_{tot} \cdot \mathbf{n}\,\mathrm{d}S \\ P_{scat} &= \oiint_A \mathbf{\Pi}_{scat} \cdot \mathbf{n}\,\mathrm{d}S \\ P_{ext} &= -\oiint_A \mathbf{\Pi}_{ext} \cdot \mathbf{n}\,\mathrm{d}S\ , \end{cases} \tag{1.29}$$

with $\oiint_A \mathbf{\Pi}_0 \cdot \mathbf{n}\,\mathrm{d}S = 0$ for a transparent environment. Combining equations 1.27, 1.28 and 1.29 leads to the following power balance:

$$P_{ext} = P_{abs} + P_{scat}\ . \tag{1.30}$$

P_{scat} represents the power scattered by the nano-object, while P_{ext} characterizes the power attenuation of the incident field, resulting both from the absorption and the scattering by the nano-object.

The extinction, absorption and scattering cross-sections of a nano-object (usually expressed in nm^2) are defined as the ratios between the corresponding powers and I_0, the intensity of the incident field at the position of particle:

$$\sigma_{ext} = \frac{P_{ext}}{I_0}, \quad \sigma_{abs} = \frac{P_{abs}}{I_0}, \quad \sigma_{scat} = \frac{P_{scat}}{I_0}\ . \tag{1.31}$$

It follows from equation 1.30:

$$\sigma_{ext} = \sigma_{abs} + \sigma_{scat}\ . \tag{1.32}$$

In extinction-based single-particle measurement techniques, such as the ones used in this work (spatial modulation spectroscopy and single-particle time-resolved spectroscopy), which will be presented in chapter 2, the photodector is placed on the path of the incident light beam. Indicating with D the surface of the detector (figure 1.6), the power

measured by the detector $P^D = \iint_D \mathbf{\Pi}_{tot} \cdot \mathbf{n}\, dS$ may be expressed as:

$$P^D = P_0^D - P_{ext}^D + P_{scat}^D \tag{1.33}$$

with

$$\begin{cases} P_0^D &= \iint_D \mathbf{\Pi}_0 \cdot \mathbf{n}\, \mathrm{d}S \\ P_{scat}^D &= \iint_D \mathbf{\Pi}_{scat} \cdot \mathbf{n}\, \mathrm{d}S \\ P_{ext}^D &= -\iint_D \mathbf{\Pi}_{ext} \cdot \mathbf{n}\, \mathrm{d}S\ . \end{cases} \tag{1.34}$$

P_0^D and P_{ext}^D are equal to P_0 and P_{ext}, the incident and extinction powers, if the detector area D is large enough to fully collect the incident light. In this case, it comes from equation 1.33 that the power attenuation $\Delta P = P_0 - P^D$ induced by the nanoparticle is equal to $P_{ext} - P_{scat}^D = \sigma_{ext} I_0 - P_{scat}^D$. Thus, partial collection of the scattered light by the detector reduces the measurement contrast. To reduce this effect, area D must not be chosen too large, the ideal configuration being that the detector surface coincides with that of the incident beam. Additionally, if the nanoparticle is small enough, the scattered power is negligible compared to the extinction (as discussed below). In this case:

$$\Delta P = P_0 - P^D \approx P_{ext} = \sigma_{ext} I_0\ . \tag{1.35}$$

In this work, $\Delta P \approx P_{ext}$ was generally assumed, despite the fact that the studied nano-objects present non-negligible scattering cross-sections as compared to their absorption ones. An evaluation of the impact of the recollected scattered light (P_{scat}^D term in equation 1.34) is presented at the end of chapter 3.

1.2.2 Nanosphere and nanoellipsoid in the dipolar approximation

We consider here a metal nano-object with dielectric function $\varepsilon(\omega) = \varepsilon_1(\omega) + i\varepsilon_2(\omega)$ surrounded by a homogeneous dielectric medium with permittivity ε_m, assumed real and weakly dispersed (figure 1.7). For a nanoparticle much smaller than the wavelength of light, the spatial variations of the oscillating electric field $\mathbf{E}_0$ may be neglected at the

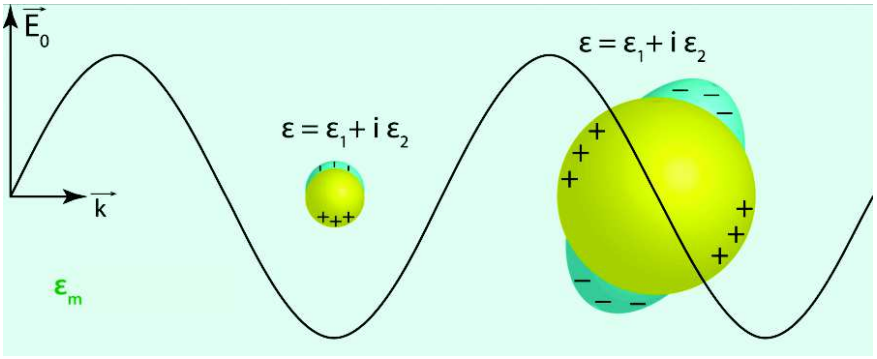

Figure 1.7 – Gold nanoparticle in a transparent medium under illumination by an oscillating electric field. The external field creates an internal polarization in the particle corresponding to a collective motion of the electrons (blue zones), leading to charge accumulation at the surface. The electromagnetic response of an object much smaller than the wavelength of light (left) may be assimilated to that of a dipole, whereas the response of larger objects (right) implies higher-order multipolar electromagnetic modes, as the electric field is not uniform in the particle.

scale of the particle (quasistatic approximation), as illustrated in figure 1.7 (left). This homogeneous field generates a collective oscillation of the electrons in the metal. In this case, the electromagnetic response of the nano-object may be assimilated to that of an induced dipole $\mathbf{p}(\omega)$ aligned with $\mathbf{E}$ (dipolar approximation), which writes [34]:

$$\mathbf{p}(\omega) = \varepsilon_0\, \varepsilon_m\, \tilde{\alpha}(\omega)\, \mathbf{E}_0(\omega)\ , \tag{1.36}$$

where $\tilde{\alpha}$ is the linear polarizability of the nano-object. Analytical expressions of this quantity exist for small nano-objects with simple shapes, such as a sphere. For more generality, we consider a small ellipsoid with arbitrary semi-axes a, b, c (figure 1.8), a case treated by R. Gans in 1912 [37]. The polarizability of such a nano-object writes [38]:

$$\tilde{\alpha}(\omega) = \frac{V}{L_i}\frac{\varepsilon(\omega) - \varepsilon_m}{\varepsilon(\omega) + [(1-L_i)/L_i]\varepsilon_m}\ , \tag{1.37}$$

with $V = \frac{4}{3}\pi abc$ the ellipsoid volume, and L_i a factor depending on the object geometry (through parameters a, b and c) and on the (linear) polarization of the incident light. In the case of a sphere ($a = b = c$), $L_i = 1/3$ and $\tilde{\alpha}$ is independent on the polarization. For an oblate spheroid ($a = b > c$) and a polarization along x or y (see figure 1.8), $L_x = L_y$ are given, as a function of the ellipsoid eccentricity e, by [38]:

$$\begin{aligned} L_x = L_y &= \frac{g(e)}{2e^2}\left[\frac{\pi}{2} - \arctan g(e)\right] - \frac{g^2(e)}{2}\ , \\ g(e) &= \left(\frac{1-e^2}{e^2}\right)^{1/2}\ , \quad e = \left(1 - \frac{c^2}{a^2}\right)^{1/2}\ . \end{aligned} \tag{1.38}$$

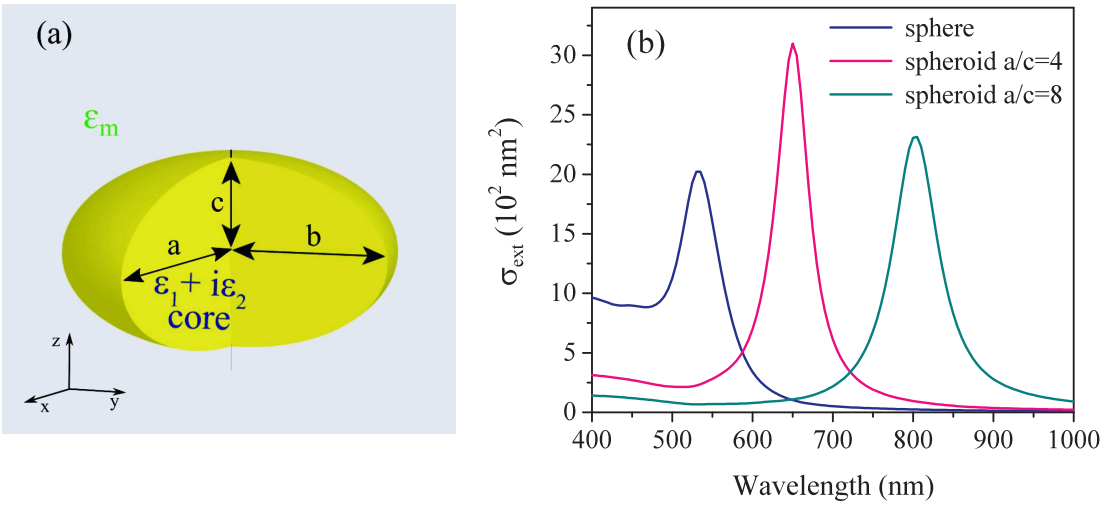

Figure 1.8 – Optical response of a small nanoellipsoid. (a) Definition of semi-axes a,b,c of the ellipsoid. The represented object is an oblate spheroid with $a = b > c$. (b) Extinction cross-section spectra of a gold nanosphere of radius 15 nm and of two gold oblate spheroids with semi-axes $a = b = 15$ nm and aspect ratios $a/c = 4$ or 8, computed in the dipolar approximation for a linear light polarization along one of the major axes, using an environment refractive index $n = \sqrt{\varepsilon_m} = 1.5$ and the Johnson and Christy tables of gold dielectric function $\varepsilon_{1,2}$ [24].

This case is relatively close to the nanosystem studied in the experiments described in the next two chapters, namely, gold nanodisks with diameter larger than their thickness, with an illumination polarized along their diameter. For an electric field polarized along the z direction, L_z is obtained from equation 1.8 by $L_z = 1 - 2L_x$. If we note $H_i = (1 - L_i)/L_i$, the absorption and scattering cross-sections may be expressed from polarizability $\tilde{\alpha}$ as:

$$\sigma_{abs}(\omega) = k\,\mathrm{Im}(\tilde{\alpha}) = \frac{\omega V}{cL_i^2}\,\frac{\varepsilon_m^{3/2}\,\varepsilon_2(\omega)}{|\varepsilon(\omega) + H_i\varepsilon_m|}\ , \tag{1.39}$$

$$\sigma_{scat}(\omega) = \frac{k^4}{6\pi}|\tilde{\alpha}|^2 = \frac{\omega^4 V^2}{6\pi c^4 L_i^2}\varepsilon_m^2\,\frac{|\varepsilon(\omega) - \varepsilon_m|^2}{|\varepsilon(\omega) + H_i\varepsilon_m|^2}\ . \tag{1.40}$$

Here, $k = \omega\varepsilon_m^{1/2}/c$ represents the modulus of the wave vector of the incident field. The absorption cross-section is proportional to the volume V, while the scattering cross-section varies as V^2. For a small enough particle, scattering is therefore negligible compared to absorption. For instance, equations 1.39 and 1.40 show that for a spheroid with $a = b = 15$ nm and $a/c = 4$, the maximal value of σ_{scat} represents only 3% of the maximal value of σ_{abs}. In this case, we obtain:

$$\sigma_{ext}(\omega) \approx \sigma_{abs}(\omega) = \frac{\omega V}{cL_i^2} \frac{\varepsilon_m^{3/2}\,\varepsilon_2(\omega)}{(\varepsilon_1(\omega) + H_i\varepsilon_m)^2 + \varepsilon_2^2(\omega)} \tag{1.41}$$

If ε_2 is either weak or weakly dispersed, vanishing of the first term in the denominator leads to a strong enhancement of σ_{ext}, corresponding to the (dipolar) localized surface plasmon resonance (LSPR). The resonance condition writes in this case:

$$\varepsilon_1(\omega) + H_i\varepsilon_m = 0 \tag{1.42}$$

By replacing $\varepsilon_1 = \varepsilon_1^D + \varepsilon_1^{ib} - 1 = -\frac{\omega_p^2}{\omega^2} + \varepsilon_1^{ib}$ (equation 1.18), the resonance frequency ω_R may be expressed as:

$$\omega_R = \frac{\omega_p}{\sqrt{\varepsilon_1^{ib}(\omega_R) + H_i\varepsilon_m}} \ . \tag{1.43}$$

In the dipolar approximation, the resonance position ω_R thus depends on the ellipsoid shape and on light polarization (through H_i), as well as on the compositions of the nano-object and its environment (through ω_p, ε_1 and ε_m). In contrast, it is independent of the nanoparticule volume.

Still in the approximation of a weak or weakly-dispersed ε_2, and further assuming a weakly-dispered ε_1 (both conditions being valid in gold if $\hbar\omega_R$ is well below the inter-band transition threshold ≈ 2.4 eV), it may be shown that the extinction cross-section expressed as a function of photon frequency has a quasi-Lorentzian profile [39], centered at ω_R, whose full width at half-maximum (FWHM) Γ is expressed as:

$$\Gamma = \frac{\Omega_R^3}{\omega_p^2}\,\varepsilon_2(\omega_R) = \gamma_0(\omega_R) + \frac{\omega_R^3}{\omega_p^2}\,\varepsilon_2^{ib}(\omega_R) \ . \tag{1.44}$$

The first term $\gamma_0(\omega_R)$ includes the different electron scattering processes implied in intra-band photon absorption (see equation 1.19), while the last term $\frac{\omega_R^3}{\omega_p^2}\,\varepsilon_2^{ib}(\omega_R)$ corresponds to damping of the resonance through interband transitions.

In the case of a small gold nanosphere in an environment of refractive index $n = \sqrt{\varepsilon_m} = 1.5$, the resonance wavelength is found near 530 nm, in a zone where ε_2 is dominated by the contribution of interband transitions (figure 1.3). ε_1^{ib} and ε_2^{ib} being neither small nor constant, the extinction spectrum is not Lorentzian and presents a strongly asymmetric

profile, as may be seen in figure 1.8b (blue curve). For an oblate spheroid ($a = b > c$), ω_R is a decreasing function of the geometrical parameter H_i (equation 1.43). Assuming a polarization along one of the major axes (x or y), the resonance red-shifts as the aspect ratio a/c becomes larger, *i.e.* as the spheroid becomes flatter. As shown in figure 1.8b, the resonances of small spheroids with $a/c = 4$ and $a/c = 8$ (assuming $\sqrt{\varepsilon_m} = 1.5$) are centered around $\lambda_R = 650$ nm and $\lambda_R = 800$ nm, respectively. Their shapes are approximately Lorentzian functions of the photon energy, the contribution of interband transitions to ε_2 being small in this range.

1.2.3 Models for nano-objects of arbitrary size

When the particle is not small enough compared to the wavelength, several additional effects appear as compared to the previous paragraph: retardation effects, radiative damping, and multipolar mode excitation. Additionally, the part of the scattering cross-section in the total extinction cross-section increases with the nano-object volume. These effects lead to a red-shift and a broadening of the LSPR as compared to the dipolar case, and to the appearance of additional resonances corresponding to non-dipolar electromagnetic modes [36, 40]. The LSPR broadening is described by an additional radiative damping term Γ_{rad} in equation 1.44, reflecting the relaxation of the collective electron oscillation by the emission of light [41].

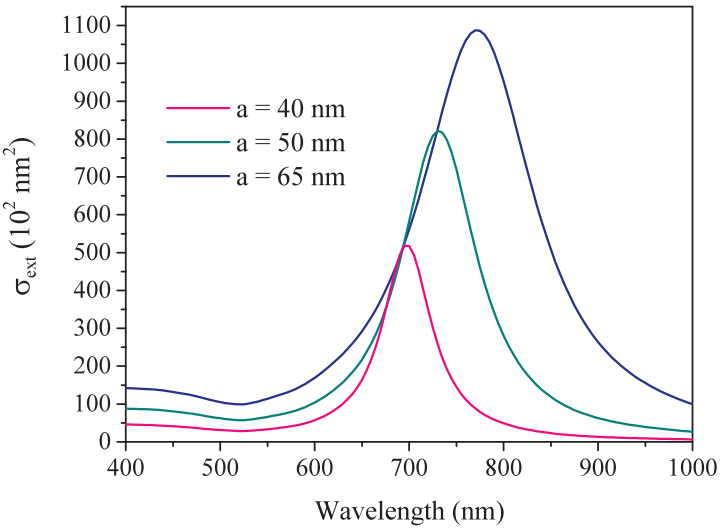

Figure 1.9 – Extinction spectra of nanoellispsoids computed using the extended Mie theory. The spectra shown correspond to ellipsoids with aspect ratios $a/c = 4$ and various values of major axis a, indicated in the legend. The light is polarized along one of the major axes (a or b). The environment refractive index is $n = \sqrt{\varepsilon_m} = 1.5$, while gold dielectric function $\epsilon_{1,2}$ is taken from the Johnson and Christy tables [24].

In the case of a sphere, an exact analytical development into multipolar modes was performed by Gustav Mie in 1908 ([38, 42]). This approach has since been extended to ellipsoids of any shape [43, 44]. For example, figure 1.9 shows the extinction spectra of oblate spheroids with same aspect ratio $a/c = 4$ and of different volumes, calculated using the extended Mie theory. A red-shift and broading of the LSPR with the nano-object volume is observed, as a consequence of the effects described above.

For more complex nano-object shapes or non homogeneous environments (*e.g.* particle at an interface), calculation of the absorption and scattering spectra can hardly be performed analytically. Numerical methods, including discrete dipole approximation (DDA) and finite-element method (FEM), are then prescribed to calculate the optical response [40, 45].

1.2.4 Numerical modeling of the optical response of nano-objects

In this work, the optical response of the investigated nano-objects, namely isolated gold nanodisks (ND) supported on a sapphire substrate, was computed by finite-element method (FEM), using the radiofrequency (RF) module of the COMSOL commercial software. To introduce this method, we now describe the process that we used to simulate the optical response of gold NDs in the experimental configuration. Numerical results obtained *via* this technique will be commented in section 3.2.2.b of chapter 3.

FEM is a numerical method for solving partial differential equations relying on a particular discretization of space, with the simulation volume being decomposed into a large number of small domains called *finite elements*. This discretization, called meshing, allows an approximate solution to be found by the resolution of a finite system of linear equations, the unknowns being the values of the sought quantity at the vertices of the mesh. In the context of optical simulations, calculation of the electromagnetic field around a nano-object requires several steps:

- first, modeling the geometry of the system,
- defining the optical properties (*i.e.*, the dielectric function) in the different space domains,
- defining the incident electromagnetic wave and the boundary conditions.

After constructing a mesh of the domain, the program solves Maxwell's equations in space with the indicated boundary conditions. One must take care that the mesh grid size is small enough compared to the the wavelength and that it allows to correctly capture the rapid changes of the electromagnetic fields around all sharp features of the geometry.

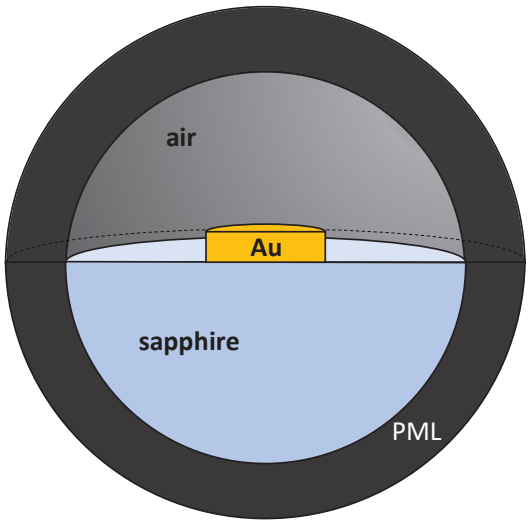

Figure 1.10 – Geometry used for optical FEM simulations (vertical plane section). The system is modeled as a gold cylinder at the interface between air and sapphire half-spheres. Perfect contact at the gold–sapphire interface is assumed. Bulk optical constants are used for all three materials, corrected in the case of gold to account for the observed additional damping (see main text). A spherical perfectly-matched layer (PML) is introduced at the border of the simulation domain in order to suppress spurious boundary effects.

The geometry used in our simulations is shown in figure 1.10. Gold NDs were described as circular cylinders characterized by their height h and diameter D. Their environment including air and sapphire half-spaces was explicitly included, refractive indexes of 1 and 1.76 being respectively used for those two media. To avoid spurious effects linked to the finite size of the simulation domain, we introduced a spherical perfectly matched layer (PML), whose role is to prevent any reflection of the incident and scattered electromagnetic waves at the border of the volume.

Gold dielectric function ε was adapted from Johnson and Christy's tables of bulk gold dielectric function ε_{JC} [24] by writing:

$$\varepsilon(\omega) = \varepsilon_{JC}(\omega) + \frac{\omega_p^2}{\omega(\omega + i\gamma_0)} - \frac{\omega_p^2}{\omega(\omega + i\gamma)} \ , \tag{1.45}$$

which corresponds to describing the dielectric response of gold conduction electrons by a Drude term [36] involving the bulk gold plasma frequency ω_P ($\hbar\omega_P = 9.01$ eV) but leaving the optical scattering rate γ of the conduction electrons (equation 1.19) as a free parameter, possibly larger than its value for bulk gold ($\hbar\gamma_0 \sim 70$ meV) to account for possible defect scattering (equation 1.19) and quantum confinement (equation 1.22) effects [32, 46]. Such modification of ε is essential to correctly reproduce the measured LSPR widths.

The total electric field in the simulation domain is written as $\mathbf{E} = \mathbf{E_0} + \mathbf{E_{scat}}$ (*scattered field formulation*), with $\mathbf{E_0}$ the user-defined incident electric field, solution of Maxwell's equations in the absence of the nano-object, and $\mathbf{E_{scat}}$ the field scattered by the ND. $\mathbf{E_0}$ is defined as a linearly polarized plane wave arriving from air with normal incidence, taking into account its partial reflection at the air–sapphire interface. Calculation of the internal field in the nano-object and of the field $\mathbf{E_{scat}}$ scattered in the environment is then performed by the program, from which the absorption and scattering cross-sections are deduced. If we note I_0 the intensity of the incident plane wave transmitted in the substrate, the absorption component is calculated by integrating the differential expression of Joule heating over the ND volume V:

$$\sigma_{abs} = \frac{1}{I_0} \iiint_V \mathrm{Re}\{\mathbf{j} \cdot \mathbf{E}^*\} \mathrm{d}V \ . \tag{1.46}$$

where $\mathbf{j}$ is the current density.

The scattering cross-section is obtained by calculating the flux of the Poynting vector of the scattered field through a surface A enclosing the ND (see paragraph 1.2.1):

$$\sigma_{scat} = \frac{1}{I_0} \oiint_A \frac{1}{2} \mathrm{Re}\{\mathbf{E_{scat}} \times \mathbf{H^*_{scat}}\} \cdot \mathbf{dS} \ . \tag{1.47}$$

The extinction cross-section is then evaluated by summing the absorption and scattering cross-sections (equation 1.32). To generate the complete extinction spectrum of a ND, the solving process must be repeated for multiple wavelengths of the incident electric field. Extinction spectra of gold nanodisks on a sapphire substrate computed using this method will be shown in chapter 3.

1.3 Time-dependent optical response of metal nano-objects after impulsive excitation

In this work, the transient properties of gold nano-objects are studied by time-resolved optical spectroscopy (or *pump–probe* spectroscopy). In this technique, which will be described in detail in the next chapter, a nano–object is impulsively excited by a light pulse (*pump* pulse), which triggers a series of ultrafast processes ultimately leading to its return to equilibrium. These processes are described in figure 1.11, along with their typical timescales. Starting from a thermalized nano-object at temperature T_0, femtosecond excitation by a pump pulse leads to a strongly athermal distribution of the electron gas, which then internally thermalizes over a time τ_{e-e}^{th} (of several hundreds of fs in gold)

through electron–electron scattering processes[1], leading to an electronic temperature T_0 higher than that of the ionic lattice (initially unaffected by the pump pulse). Through electron–phonon scattering, the electron and lattice temperatures T_e and T_L equilibrate over a time τ_{e-L} of the order of 1 ps in gold[2], leading to a thermalized nano-object at temperature $T_{eq} > T_0$ a few ps after photoexcitation. This fast heating causes the rapid dilation of the metal, which may trigger acoustic vibrations of the nano-object. These vibrational modes have size-dependent periods of typically $\sim$ 1–10 ps, and are damped in a few hundred ps. Simultaneously, the nano-object, described by temperature $T_p(t)$, cools down through heat transfer towards its environment, permitting its return to equilibrium at temperature T_0 after several hundred ps to several ns, depending on its dimensions.

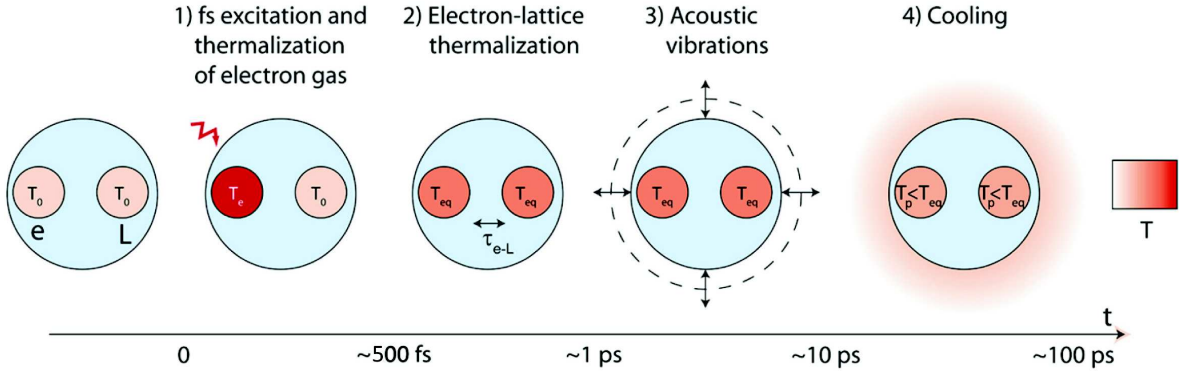

Figure 1.11 – Ultrafast phenomena triggered by impulsive photoexcitation of a metal nano-object. Indices e and L indicate the electron gas and the ionic lattice of the nano-object, respectively, while the other notations are defined in the main text. The color code represents the temperature, red being the highest.

The transient changes of the metal dielectric function, $\Delta\varepsilon_{1,2}(\lambda, t)$, contain the signatures of these different phenomena. In time-resolved spectroscopy, they are indirectly accessed through the measurement of the nano-object transient extinction cross-section change, $\Delta\sigma_{ext}(\lambda, t)$, which is related to $\Delta\varepsilon_{1,2}(\lambda, t)$, at first order, through:

$$\Delta\sigma_{ext}(\lambda, t) = \frac{\partial\sigma_{ext}}{\partial\varepsilon_1}(\lambda)\,\Delta\varepsilon_1(\lambda, t) + \frac{\partial\sigma_{ext}}{\partial\varepsilon_2}(\lambda)\,\Delta\varepsilon_2(\lambda, t)\ . \tag{1.48}$$

The $\frac{\partial\sigma_{ext}}{\partial\varepsilon_{1,2}}(\lambda)$ derivatives are strongly enhanced in the vicinity of a LSPR, and will thus

[1] This time τ_{e-e}^{th} must not be confused with $\tau_{e-e}(\omega = 0)$, the inverse of the electron–electron scattering rate $\gamma_{e-e}(\omega = 0)$ in the absence of photon (equation 1.19), which corresponds to the average time between two electronic collisions. Indeed, many collisions are necessary to achieve the internal thermalization of the electron gas [34]).

[2] Similarly, τ_{e-L} must not be confused with $\tau_{e-ph}(\omega = 0) = 1/\gamma_{e-ph}(\omega = 0)$ (equation 1.19), the average duration between electron–phonon scattering events.

be referred to as *plasmonic derivatives* in the following.

Equation 1.48 neglects the possible effect of a transient modification of the environment dielectric function ε_m (which greatly affects the LSPR of plasmonic nano-objects, as discussed above) due to heat transfer from the nanoparticle. This approximation is always valid in the first $\sim$ 10 ps following the excitation, as environment heating is negligible at this timescale (figure 1.11). Therefore, equation 1.48 will be used in chapter 4 of this work, where we study the different phenomena leading to the nano-object internal thermalization. Conversely, during the subsequent cooling, the effect of the environment must generally been taken into account. Assuming for simplicity a homogeneous environment undergoing uniform variations of its dielectric constant ε_m, one obtains:

$$\Delta\sigma_{ext}(\lambda,t) = \frac{\partial\sigma_{ext}}{\partial\varepsilon_1}(\lambda)\,\Delta\varepsilon_1(\lambda,t) + \frac{\partial\sigma_{ext}}{\partial\varepsilon_2}(\lambda)\,\Delta\varepsilon_2(\lambda,t) + \frac{\partial\sigma_{ext}}{\partial\varepsilon_m}(\lambda)\,\Delta\varepsilon_m(\lambda,t)\ . \qquad (1.49)$$

In chapter 3, which focuses on the cooling dynamics of nano-objects, we will discuss the conditions enabling to neglect the added term related to environment heating. We will find these conditions to be met in our experiments, making equation 1.48 also valid in this case.

A much more thorough description of the different ultrafast phenomena mentioned above and summarized in figure 1.11 will be given over the course of chapters 3 and 4, the former focusing on the long-timescale dynamics (with a complete study of a nano-object's cooling dynamics and a mention of its vibrations), and the latter providing a detailed theoretical modeling of the electron and lattice dynamics previous to the nano-object internal thermalization.

Chapter 2

Linear and ultrafast single-particle optical spectroscopy techniques

Contents

Optical techniques have been widely used in the study of nano-objects and nanomaterials. In the case of metal particles, in particular, the high sensitivity of plasmonic effects to the intrinsic properties (morphology, structure, composition) and local evironments (surface-bound molecules, substrate, other nanoparticles) of the nano-objects may be used to access these parameters. Similarly, optical time-resolved experiments take advantage of the enhanced transient variations of the optical response of nanoparticles near their LSPRs to investigate the mechanisms underlying these optical changes (electron and lattice dynamics, nano-object vibrations, thermal relaxation).

Until recently, however, optical measurements could only be performed on nano-object assemblies. In such experiments, the measured quantities are averaged over the individual responses of all probed nano-object, whose properties present an unavoidable dispersion. Thus, the development of single-particle spectroscopy techniques has led to many advances in the fundamental understanding of the properties of nanosystems, as they enable a more precise (and often quantitative) comparison with theoretical models.

In this chapter, the methods used for the characterization of the stationary and transient optical responses of a single nano-object are presented. In the first section, we introduce spatial modulation spectroscopy (SMS), a microscopy/spectroscopy approach originally developed in our laboratory [47]. This technique enables us to detect single nano-objects, to measure their quantitative extinction spectra, as well as to characterize their morphologies. The second section is dedicated to the presentation of the time-resolved spectroscopy technique in its version adapted for single-particle measurements, which provides access to the transient modifications of the extinction cross-section of a nano-object.

2.1 Spatial modulation spectroscopy

Spatial Modulation Spectroscopy (SMS) is a sensitive far-field optical spectroscopy technique able to probe nano-objects at the individual scale [36, 47]. It is used in our experiments to locate individual nano-objects dispersed on a solid substrate and measure their absolute extinction cross-sections as a function of the wavelength and polarization of the incident light.

2.1.1 Principle

A nano-object placed in the path of a laser beam absorbs and scatters a portion of the incident power. As discussed in section 1.2.1 of the last chapter, the power attenuation measured by a photodetector placed in the direction of propagation of light—assuming complete collection of the incident light in the absence of a nano-object—writes, in the

case of a small nanoparticule (equation 1.35):

$$\Delta P = P_0 - P^D \approx P_{ext} = \sigma_{ext} I(x_0, y_0), \tag{2.1}$$

where P_0 and P^D are the incident and detected light powers, respectively, and $I(x_0, y_0)$ the intensity of the incident light beam at position (x_0, y_0) of the nano-object, assumed punctiform.

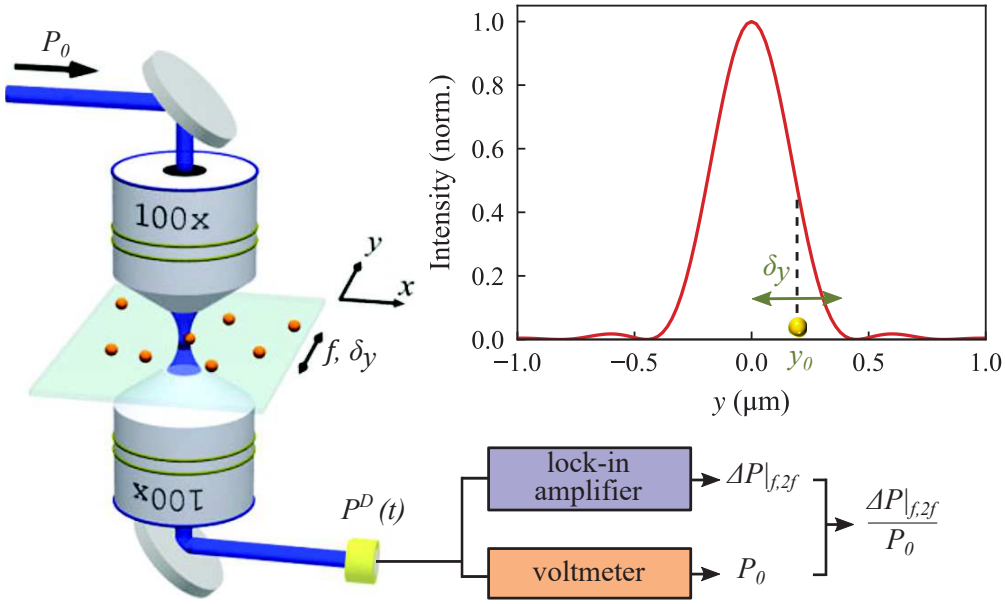

Figure 2.1 – SMS principle. A laser beam of power P_0 is focused on a single nanoparticle supported on a transparent substrate. A piezoelectric actuator drives a periodic displacement of the sample along direction y with frequency f and amplitude δ_y. This vibration modulates the intensity illuminating the nano-object (here represented as an Airy profile) and thus the transmitted power $P^D(t) = P_0 - \Delta P(t)$, collected by a photodiode. The measured signal is filtered by a lock-in amplifier to extract the oscillating component at frequency f or $2f$, while the signal average $\langle P^D \rangle$ ($\approx P_0$ for a small nanoparticle) is measured by a voltmeter.

Generally, however, the extinction cross-section σ_{ext} may not be retrieved from a direct measurement of ΔP as its value is of the order of or lower than the laser's power fluctuations for a small nano-object. For instance, $\Delta P/P_0 \sim 10^{-3}$ for a 20 nm diameter gold nanosphere placed at the waist of a Gaussian beam with a size limited by diffraction (∼300–800 nm full-width at half maximum (FWHM) in our experimental conditions). In order to increase the signal-to-noise ratio, a general technique consists in making ΔP oscillate in time, for instance by modulating the light wavelength[1] [48] or polarization [49], or the position of the nano-object in the beam [50, 51]. Synchronous detection of $\Delta P(t)$ at the modulation frequency (or one of its harmonics) then enables to drastically enhance

[1] As done in the first study having reported single molecule detection, published in 1989 by Moerner ans Kador [48].

the signal-to-noise ratio of the detection, by eliminating noise components at frequencies other than that chosen for the synchronous detection.

SMS is based on the periodic displacement of a single nano-object in the focal plane of a tightly focused light beam. Its general principle is schematized in figure 2.1. Vibration of the sample is generated by a piezoelectric actuator, while a XY piezoelectric stage is used to position the nano-object under the beam. For an oscillation of amplitude δ_y with frequency f along the y direction, the nano-object position relative to the beam is noted $(x_0, y(t))$, with $y(t) = y_0 + \delta_y \sin(2\pi f t)$. Following equation 2.1, the time-dependent power attenuation writes:

$$\Delta P(t) = \sigma_{ext}\, I(x_0, y_0 + \delta_y \sin(2\pi f t)) \tag{2.2}$$

Experimentally, the transmitted power $P^D(t) = P_0 - \Delta P(t)$ is measured using a photodiode. The non-constant part of the signal $\Delta P(t)$ is demodulated using a lock-in amplifier, allowing to extract the Fourier components of the signal at frequencies nf (with n integer), given by[2]:

$$\begin{aligned} \Delta P|_{nf}(x_0, y_0) &= \frac{2n}{T}\,\sigma_{ext} \int_{-\frac{T}{2n}}^{\frac{T}{2n}} I(x_0, y(t)) \sin(2\pi n f t)\,\mathrm{d}t \qquad && n \text{ odd} \\ \Delta P|_{nf}(x_0, y_0) &= \frac{2n}{T}\,\sigma_{ext} \int_{-\frac{T}{2n}}^{\frac{T}{2n}} I(x_0, y(t)) \cos(2\pi n f t)\,\mathrm{d}t \qquad && n \text{ even} \end{aligned} \tag{2.3}$$

with $T = 1/f$. One can note that all components are proportional to the nano-object extinction cross-section σ_{ext}. In practice, either the f or $2f$ components are used, the higher harmonics presenting much lower amplitudes.

More insight of the $\Delta P|_{nf}$ coefficients is gained by considering the simple situation where the oscillation amplitude δ_y is small as compared to the beam FWHM d_0. In this case, a second-order development of equation 2.2 around y_0 permits a direct evaluation of the f and $2f$ components:

$$\Delta P(t) = \Delta P_0 + \Delta P|_f \sin(2\pi f t) + \Delta P|_{2f} \cos(4\pi f t) + o(\delta_y^2)\ , \tag{2.4}$$

[2]These expressions correspond to the components in phase with the modulation function $\sin(2\pi f t)$. The out-of-phase components are obtained by reversing the parity condition on n in equation 2.3.

with

$$\begin{cases} \Delta P_0(x_0, y_0) = \sigma_{ext} \left[I(x_0, y_0) + \dfrac{\delta_y^2}{4} \dfrac{\partial^2 I}{\partial y^2}(x_0, y_0) \right] \\ \Delta P|_f(x_0, y_0) = \sigma_{ext}\, \delta_y \dfrac{\partial I}{\partial y}(x_0, y_0) \\ \Delta P|_{2f}(x_0, y_0) = -\dfrac{1}{4}\, \sigma_{ext}\, \delta_y^2 \dfrac{\partial^2 I}{\partial y^2}(x_0, y_0)\ . \end{cases} \tag{2.5}$$

Under the $\delta_y \ll d_0$ approximation, the $\Delta P|_f$ and $\Delta P|_{2f}$ components are thus proportional to the first and second derivatives of the beam intensity profile along the direction of modulation y, evaluated at the average position of the particle (x_0, y_0) in the beam.

The signal from the lock-in amplifier $\Delta P|_{nf}$ must be normalized in order to obtain a quantity independent from the laser power P_0. For small nanoparticles, this may be done by dividing at all times $\Delta P|_{nf}$ by the average value $\langle P^D \rangle$ of the detected power, measured using a voltmeter. Indeed, if the nano-object is small, $\Delta P \ll P_0$ and therefore $\langle P^D \rangle \approx P_0$. This method allows reducing the noise component associated to fluctuations of the laser power, since the measured quantities $\Delta P|_{nf}(t)$ and $\langle P^D \rangle(t)$ vary conjointly. For larger nano-objects, this technique cannot be used, and P_0 is determined by a direct measurement performed in the absence of nano-objects on the path of the beam. The latter method was used in our experiments, where the investigated nano-objects (gold nanodisks) induce non-negligible $\Delta P(t)$ power attenuations.

Additionally, the frequency response of the photodiode must be taken into account in order to achieve a quantitative interpretation of the measured signals. If we note $S(t)$ the (voltage) signal generated by the photodiode detector, the $\Delta P|_{f,2f}/P_0$ ratio is obtained through:

$$\frac{\Delta P|_{f,2f}}{P_0} = \frac{1}{A_{f,2f}} \frac{S|_{f,2f}}{\langle S_0 \rangle}\ , \tag{2.6}$$

where $A_{f,2f}$ represents the gain of the photodiode at frequency f or $2f$ (depending on the used SMS configuration), corresponding to that of a low-frequency filter. Practically, this attenuation coefficient is evaluated before the experiments. To obtain it, the signal $\langle S_0 \rangle$ generated by the photodiode for a stationary laser illumination, measured with the voltmeter, is compared to the signal $S_{ch}(f, 2f)$ of the same beam modulated at frequency f or $2f$ using a mechanical chopper, demodulated by the lock-in amplifier.

$A_{f,2f}$ is expressed as:

$$A_{f,2f} = \frac{\pi}{2}\frac{S_{ch}(f,2f)}{\langle S_0 \rangle} \ , \tag{2.7}$$

where factor $\pi/2$ accounts for the fact that the chopper generates a square wave instead of a sinusoid.

Equations 2.3, 2.6 and 2.7 connect the measured signal to the extinction cross-section σ_{ext} of the nano-object. Provided the modulation amplitude δ_y and the intensity profile $I(x,y)$ are known, the Fourier coefficients appearing in equation 2.3 may be computed numerically as a function of the particle average position (x_0, y_0). Experimentally, the $I(x,y)$ profile is close to an Airy distribution, being the result of the diffraction of a quasi plane wave by the entrance pupil of the objective [52]. For a beam centered at $(0,0)$, the associated intensity may be written as:

$$I(r) = I_0 \left[\frac{2J_1\left(1.62 \cdot \frac{2r}{d_0}\right)}{1.62 \cdot \frac{2r}{d_0}} \right]^2 \ , \tag{2.8}$$

with J_1 the Bessel function of the first kind of order one, $r = \sqrt{x^2+y^2}$ the distance to the center, and d_0 the FWHM of the Airy function. $I(x,y)$ is related to the incident power P_0 through:

$$P_0 = \iint I(x,y)\, dxdy \ , \tag{2.9}$$

from which one obtains $I_0 \approx 0.831\, P_0/d_0^2$. An example of Airy profile is given in figure 2.1, normalized to its maximum value I_0. In some cases, it may be more convenient to describe the intensity profile as a Gaussian distribution, written in the form:

$$I(x,y) = \frac{2P_0}{\pi w^2} \exp\left(-2\frac{x^2+y^2}{w^2}\right) \ , \tag{2.10}$$

where the waist w is related to the FWHM d_0 by $d_0 = \sqrt{2\ln 2}\, w$. This function is very close to the Airy profile around the center of the distribution, but presents a smooth decay on the sides while the Airy function shows a cancellation and several small rebounds (figure 2.1). In this thesis, we use the more accurate Airy formula in the description of SMS experiments.

Simulations of signals $\Delta P|_f/P_0$ and $\Delta P|_{2f}/P_0$ based on their general definitions (equation 2.3) are shown in figure 2.2 as a function of the particle average position (x_0, y_0)

for an Airy intensity profile centered at $(0, 0)$. They correspond to the images generated using SMS for a small isolated nanoparticle by scanning the surface of a sample (which is achieved by displacing the sample relative to the fixed laser beam using the XY translation stage). Parameters close to the experimental values were used for these calculations ($\delta_y = 300$ nm and $d_0 = 380$ nm). For comparison, the first and second derivatives of $I(x, y)$ with respect to y are also shown. As discussed above, in the $\delta_y \ll d_0$ limit, their spatial dependences are the same as the f and $2f$ signals, respectively (equation 2.5). The calculated SMS signals and the corresponding intensity derivatives also present similar shapes here, the formers being only more extended in the y direction. For a demodulation at frequency f, the signal $\Delta P|_f/P_0$ presents two identical lobes of opposite sign, and a cancellation at the position of the nano-object. In contrast, the signal at $2f$ exhibits one central positive peak and two negative satellites of lower amplitude on each side. For particle detection, using the demodulation at $2f$ is generally the most practical choice, since in this case the position of the nano-object corresponds to a signal maximum. This configuration is therefore the one used in our experiments.

2.1.2 Experimental setup and calibration

2.1.2.a Setup and experimental method

In the SMS setup used in this work, the nano-objects lay on a substrate whose position in the horizontal (x, y) plane is controlled by a manual XY stage (for coarse motion), complemented by a XY piezoelectric stage able to scan a 100×100 µm^2 window with a 0.3 nm spatial resolution, achieved thanks to a retroaction loop. A $\geqslant 1$ µm separation between neighboring nanoparticles is necessary to allow selective illumination of a single nano-object by a focused laser beam. Spatial modulation of the sample is obtained through a second piezoelectric actuator oscillating in the y direction with tunable frequency and amplitude, of typically $f = 1.5$ kHz and $\delta_y \approx 300$ nm in our experiments.

A light beam with wavelength in the 380–1000 nm range, produced by one of three possible sources—described in the following—, is focused on the surface of the sample by a 100X apochromatic infinity-corrected objective with numerical aperture $N.A. = 0.95$. Before the objective, the incident beam section is enlarged using a telescope in order to obtain a quasi plane wave on the entrance pupil of the objective. In such conditions, the intensity profile in the focal plane is an Airy distribution, whose FWHM d_0 is close to the theoretical diffraction limit:

$$d_0 = 0.515\frac{\lambda}{N.A.} \approx 0.55\lambda \ , \tag{2.11}$$

with λ the wavelength of the incident light. The objective is mounted on a piezoelectric

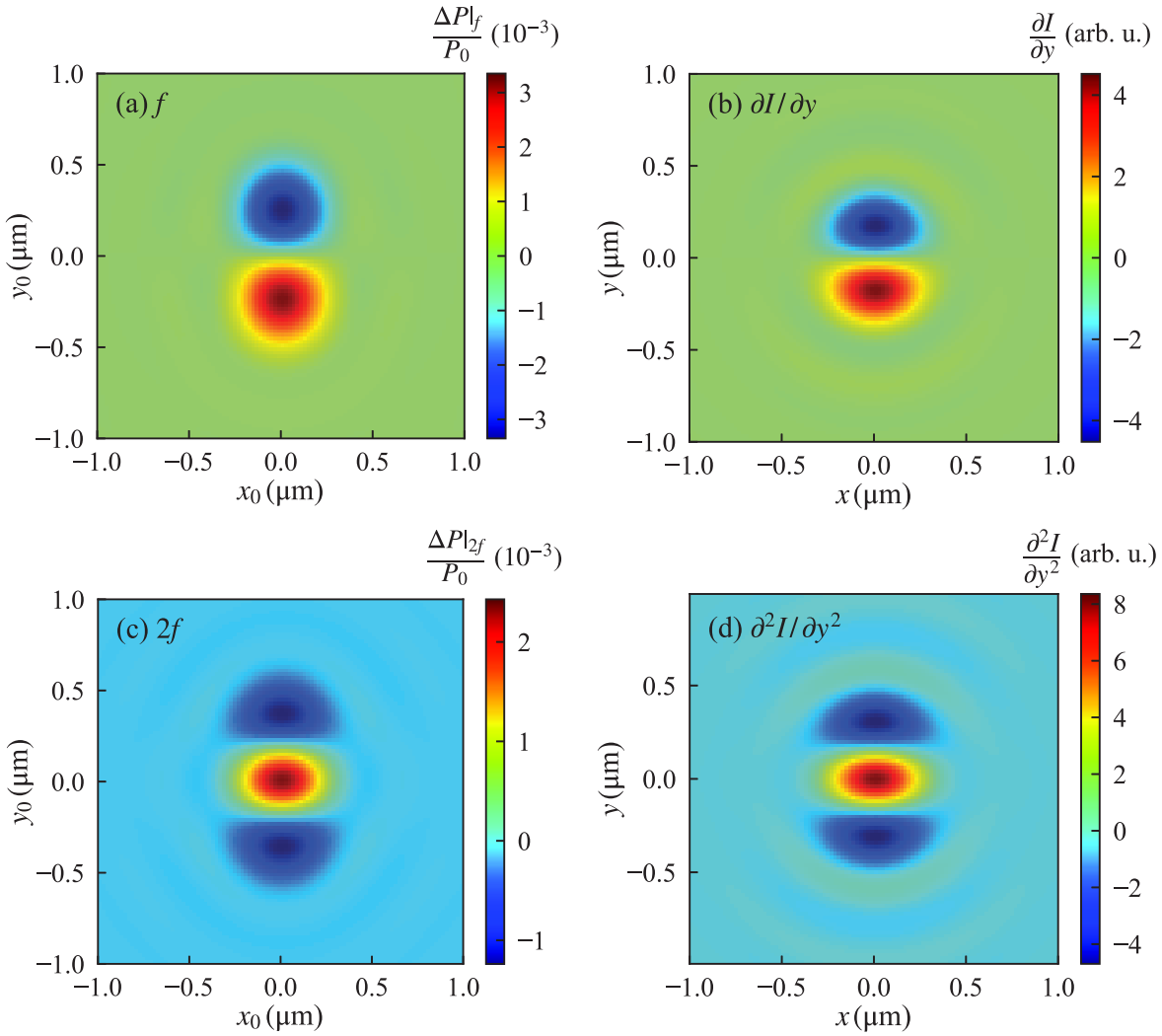

Figure 2.2 – Theoretical SMS images of a small nanoparticle generated by a scan of a sample. (a,c) Calculated SMS signal for a demodulation at f (a) or $2f$ (c), as a function of the particle position (x_0, y_0). The illumination spot is centered in (0,0). (b,d) First (b) and second (d) derivatives of the intensity profile $I(x, y)$ with respect to y, the coordinate corresponding to the direction of modulation.

controller allowing to precisely focus the incident beam. The light transmitted through the sample is collected by a second objective with 100X magnification and numerical aperture $N.A.' = 0.75$, and sent to an avalanche photodiode[3]. The measured signal is demodulated by a lock-in amplifier at frequency $2f$, while its time-averaged value is measured by a voltmeter, as described above. A data acquisition system allows the processing of these signals by a computer, providing the instantaneous value of $|\Delta P|_{2f}/P_0(t)|$ (the absolute value being used for convenience).

Nano-objects are detected by scanning the sample surface using the XY piezoelectric stage, each small isolated particle giving rise to a figure similar to that shown in figure 2.2c. The extinction cross-section of a nano-object at a given wavelength is obtained by measuring the value of the SMS signal with the particle at the center of the beam, and converting this signal into σ_{ext} using the method described in the next section. The extinction spectrum $\sigma_{ext}(\lambda)$ is obtained by repeating this procedure at several wavelengths of the illumination beam delivered by tunable lasers.

SMS measurements as a function of the polarization direction of light provide useful informations about a nano-object's morphology and orientation. In the dipolar approximation (see section 1.2.2), the extinction spectrum of a small nano-object with a non-circular section in the plane of illumination displays two distinct LSPRs corresponding to two orthogonal dipolar modes, whose associated extinction cross-sections are noted $\sigma_{\parallel}$ and $\sigma_{\perp}$ (for the long and short axes, respectively). Each mode may be selectively excited by tuning the direction of linear polarization of the illumination with the corresponding axis of the nano-object, which is achieved using a wire-grid polarizer. For an arbitrarily-directed polarization indexed by angle θ, the extinction cross-section may generally be written as:

$$\sigma_{ext}(\theta,\omega) = \sigma_{\parallel}(\omega)\cos^2(\theta-\theta_{max}) + \sigma_{\perp}(\omega)\sin^2(\theta-\theta_{max}) \ , \tag{2.12}$$

where θ_{max} is the direction of the nano-object long axis. In the case of elongated nano-objects, the longitudinal and orthogonal LSPRs are spectrally well-separated. Therefore, close to one of these resonances, the nano-object extinction presents large periodic variations as a function of the polarization angle. This is illustrated in figure 2.3 presenting the polarization-dependent extinction cross-section of a gold nanobipyramid measured at $\lambda = 820$ nm, close to the central position of the longitudinal LSPR. The signal is maximal at $\theta = \theta_{max}$ (indicating the direction of the long axis) and nearly cancels at $\theta_{max}+90°$. Figure 2.3 shows the extinction spectrum of the same bipyramid measured in SMS with a polarization along θ_{max}. This spectrum, plotted as a function of the photon energy $\hbar\omega$, is dominated by the longitudinal LSPR of the bipyramid which presents a

[3] A collection objective with a 0.95 numerical aperture similar to the focusing objective could not be used, as the latter has a working distance of 0.35 mm, inferior to the substrate thickness.

nearly Lorentzian profile, as shown by its correct fitting by a Lorentz function (solid line).

For a spherical or cylindrical nano-object, such as the gold nanodisks studied in this work, polarization-dependent SMS measurements may be used to detect a possible deviation from perfect circularity resulting from fabrication/synthesis imperfections. This point will be described in detail in chapter 3.

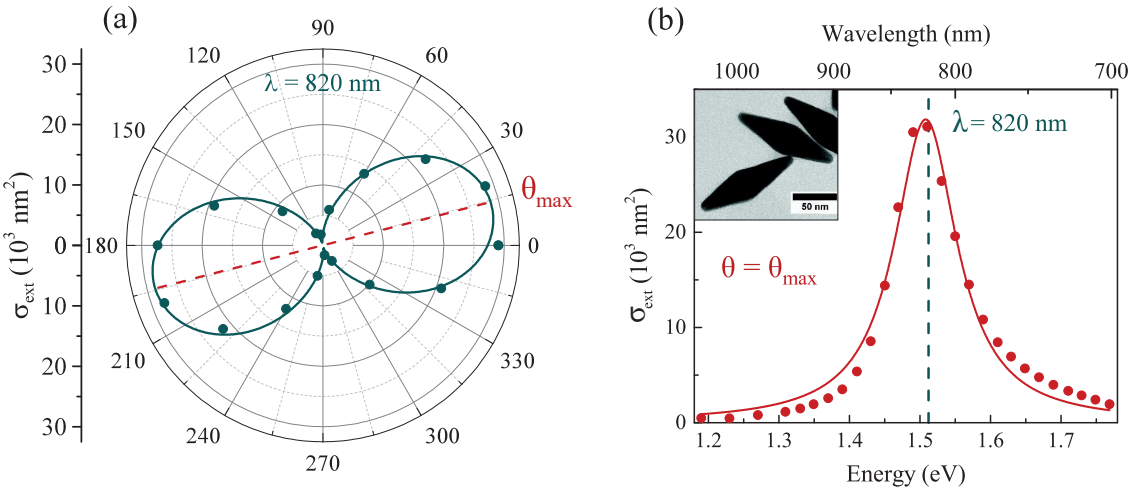

Figure 2.3 – Extinction cross-section of an elongated single nano-object as a function of the linear polarization (a) or the incident beam photon energy (b). The investigated object is a single gold nanobipyramid similar to those shown in the inset of (b) (TEM image). (a) SMS measurements of σ_{ext} as a function of the polarization angle (dots) and fit using equation 2.12 (solid line). The red dashed line indicates the angle maximizing the SMS signal, corresponding to the nano-object long axis. (b) SMS-measured extinction spectrum for a linear light polarization along the longitudinal direction of the object (dots) and fit by a Lorentz function (solid line).

2.1.2.b Conversion of SMS signal to σ_{ext}

To obtain the extinction cross-section of a nano-object from a measurement of the SMS signal with the nanoparticle centered in the beam, $[\Delta P|_{2f}/P_0](0,0)$, one first needs to evaluate the proportionality factor between the two, *i.e.* the $R_{2f}(d_0, \delta_y)$ function defined by:

$$\frac{\Delta P|_{2f}}{P_0}(0,0) = R_{2f}(d_0, \delta_y)\, \sigma_{ext} \ . \tag{2.13}$$

A general integral expression of $R_{2f}(d_0, \delta_y)$ is given by equation 2.3, with $n = 2$ and $(x_0, y_0) = (0,0)$, introducing the intensity profile $I(x,y)$ given by expression 2.8 (Airy

profile). Using a formal calculation software (Mathematica), the following analytical expression for R_{2f} was obtained:

$$R_{2f}(d_0, \delta_y) = \frac{0.8316\,\pi}{d_0^2} \left[{}_2F_3\left(\frac{3}{2}, \frac{3}{2}; 2, 2, 3; -10.45\frac{\delta_y^2}{d_0^2}\right) - {}_2F_3\left(\frac{1}{2}, \frac{3}{2}; 1, 2, 3; -10.45\frac{\delta_y^2}{d_0^2}\right)\right], \tag{2.14}$$

where ${}_pF_q(a_1, ..., a_p; b_1, ..., b_q; z)$ are the generalized hypergeometric functions [53]. The R_{2f} coefficient thus depends on two parameters, which must be experimentally determined: the FWHM of the light beam in the plane of the nanoparticles d_0, and the vibration amplitude δ_y, dependent on the voltage applied to the piezoelectric actuator generating the spatial modulation.

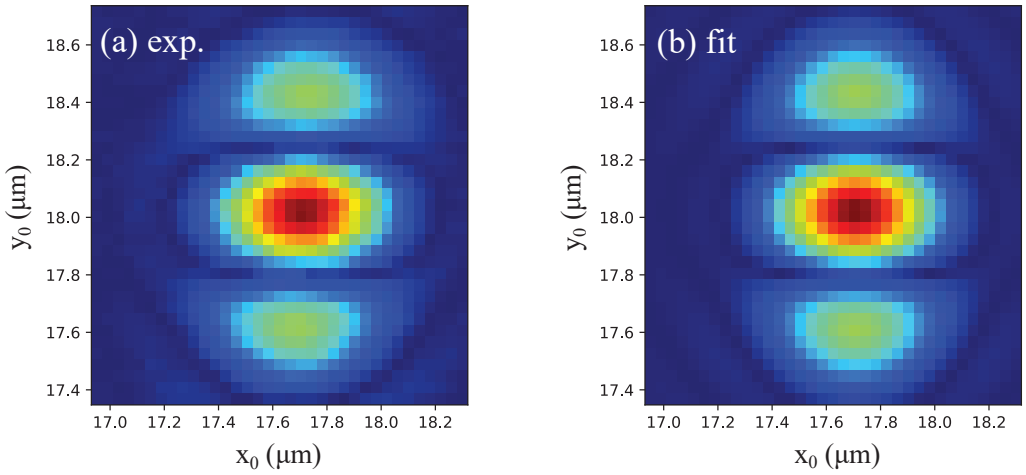

Figure 2.4 – Two-dimensional fit of the SMS scan of a small nano-object. (a) Experimental SMS scan of a small gold nanodisk for an $\lambda = 740$ nm illumination wavelength. The signal is shown in absolute value. (b) Fit of image (a) by the numerical evaluation of $|\Delta P|_{2f}|(x_0, y_0)$ from equation 2.3, with d_0 and δ_y left as free parameters. Images (a) and (b) share the same color code.

For this purpose, SMS images of a small nano-object were acquired at several wavelengths. These images were then fitted by the theoretical $|\Delta P|_{2f}/P_0|$ spatial distributions calculated numerically from equation 2.3 at each position (x_0, y_0) of the maps (figure 2.2c), with d_0 and δ_y as fitting parameters. While d_0 depends on the wavelength of light (through a relation close to equation 2.11), δ_y is a constant and was therefore defined as a shared parameter for all fits. The fits are generally excellent, except in the 380–450 nm range where a few divergences are observed, possibly due to optical aberrations caused by the objective in this spectral range. An example of experimental scan

made on a small gold nanodisk (60 nm diameter, 20 nm thickness) at $\lambda = 740$ nm is shown in figure 2.4, along with its two-dimensional fit. In the configuration used in our experiments, the complete calibration yielded $\delta_y = 300$ nm and $d_0(\lambda) \approx 0.65\lambda$, which is close to the theoretical diffraction limit (0.55λ, equation 2.11).

Figure 2.5a shows function $R_{2f}(d_0, \delta_y)$ plotted as a function of the vibration amplitude δ_y at several wavelengths (with $d_0(\lambda) = 0.65\lambda$). This function presents a maximum whose position is approximately given by $\delta_y \approx d_0$, thus depending on the wavelength, the $\delta_y = 300$ nm value used in our experiments being optimal for $\lambda \approx 500\ nm$. R_{2f} is also plotted as a function of λ (figure 2.5b) for $\delta_y = 300$ nm, the value used in our experiments. This function (by which the raw SMS signal must be divided to obtain σ_{ext}) presents a rapid decrease for increasing wavelengths, showing that SMS is more sensitive to the extinction cross-section at shorter wavelengths (for which the diffraction limit enables smaller spot sizes).

An estimation of the uncertainty affecting the determination of the calibration function $R_{2f}(\lambda)$ led to $\sim 10\%$. Therefore, a 10% uncertainty must be assumed on the absolute amplitudes of the measured extinction spectra. However, the uncertainty on $R_{2f}(\lambda)$ affects only weakly the positions and widths of the LSPRs of nano-objects.

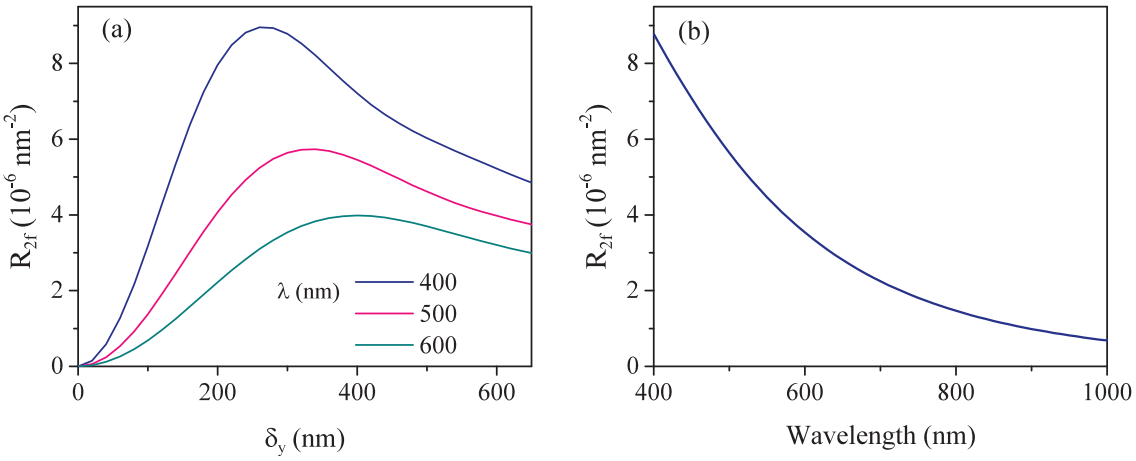

Figure 2.5 – Conversion from raw SMS signal to σ_{ext}. (a) Function $R_{2f}(d_0, \delta_y)$ (equation 2.5) plotted as a function of vibration amplitude δ_y for several wavelengths (with $d_0 = 0.65\lambda$). (b) $R_{2f}(d_0, \delta_y)$ as a function of the wavelength in the experimental conditions ($\delta_y = 300\ nm$, $d_0 = 0.65\lambda$).

2.1.2.c Extension of SMS: optical response of single nano-objects under high pressure

This paragraph briefly presents SMS measurements on single nanoparticles under high pressure, on which I have worked during this Ph.D. thesis and which are still ongoing in the FemtoNanoOptics group. These experiments are based on an original setup combining the SMS one with a diamond anvil cell (DAC), an apparatus allowing the generation of tunable hydrostatic pressures up to hundreds of GPa in a submillimetric volume. The main interest motivating the study of plasmonic nano-objects in such extreme conditions lies in the possibility of continuously tuning their optical response as a function of the applied pressure.

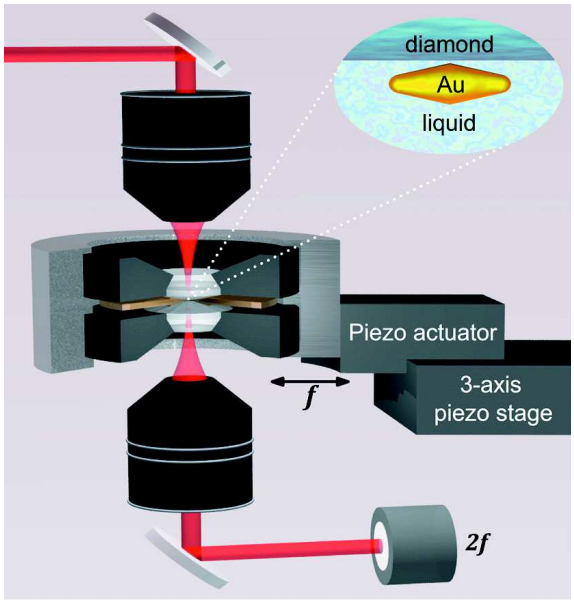

Figure 2.6 – High-pressure SMS setup. The nano-objects (here represented, a gold bipyramid) are placed in the chamber formed by two diamond anvils and the walls of a Cu–Be metal gasket. This space is filled with a mixture of ethanol and methanol, playing the role of pressure-transmitting medium. Pressure is generated in the chamber by applying a vertical force on the upper anvil using a pneumatic system. Its measurement is realized through the detection of the pressure-induced shift of the fluorescence lines of a small ($\sim$ 5 µm) ruby crystal placed in the cell. For SMS measurements, a laser beam passes through the upper objective (magnification $\times$100, numerical aperture 0.75) and the upper diamond and is focused close to the diffraction limit in the nanoparticle plane. The transmitted beam passes through the lower diamond before being collected by an objective with similar characteristics, and sent to a silicon photodiode. Spatial modulation is achieved through vibration of the whole cell by a piezoelectric actuator, while a second piezoelectric stage permits the 3-dimensional positioning of the cell.

Demonstrations of a pressure-induced spectral shift of the LSPRs of metal nano-objects have been performed in the past on ensemble measurements [54, 55], but a precise characterization and modeling of this effect was precluded by the size and shape dispersion

of the investigated nanoparticles. To solve this issue, our group developed an original system, made by the combination of a DAC with the SMS setup (in collaboration with the group of A. San Miguel at ILM), allowing the measurement of the absolute extinction cross-section of a single nano-object under high pressure. The development and proof-of-principle of this setup, whose main elements and principle are described in figure 2.6, was realized during the Ph.D. thesis of F. Medeghini [39, 56], with whom I collaborated for this work. It allowed to demonstrate a large reversible red-shift of the LSPR of a metal nano-object (gold bipyramid) induced by pressure in the 0-10 GPa range. This effect was correctly reproduced by a numerical model, which allowed to interpret the observed red-shift as a consequence of the pressure-induced modification of the refractive index of the transparent liquid surrounding the nano-object. Additionnally, the metal particle compression, which increases its electronic density, was predicted to have an opposite effect (*i.e.*, a blue-shift) of smaller amplitude.

These studies of pressure-induced LSPR shifts [56] were pursued during my thesis, with the goal to focus now on the modification of the LSPR linewidth (or FWHM) induced by high pressure. This work, still in progress, is motivated by the current incomplete understanding of plasmonic linewidths, in particular regarding the surface-related contributions affecting the LSPR linewidths of small NPs. As discussed in section 1.2.2, in the case of an elongated gold nano-object, the LSPR is an approximately Lorentzian function of the photon energy, whose linewidth is given by equation 1.19, with the addition of a quantum confinement term for small nanoparticles (equation 1.22), and of a radiative damping term Γ_{rad} for large ones (see section 1.2.3). High-pressure experiments are promising to achieve a much better understanding of the former effect, as they enable in particular a continuous modification of the environment refractive index, which has been theoretically predicted to affect the g factor governing the amplitude of quantum confinement effects [53].

Figure 2.7 presents preliminary results on the modification of the LSPR linewidth of a single nano-object with pressure, whose analysis and interpretation are still incomplete. The nano-object studied was a gold bipyramid with approximate length 100 nm and width 30 nm, coated with a $\sim$ 5 nm silica shell. As compared to the nanobipyramids used in the previous study [56], which were coated with surfactant molecules (whose role is to prevent particle agglomeration in colloidal solution), the silica coating allows avoiding any chemical damping effect, causing a large broadening of the LSPR of surfactant-coated NPs. Extinction spectra measured from 0 to 8.2 GPa on this nano-object are reported in figure 2.7a. They show an important red-shift with increasing pressure, from 1.5 eV at atmospheric pressure in the pressure-transmitting medium (figure 2.6, red dots) to $\sim$ 1.4 eV at 8.2 GPa. This shift was reversible during the pressure decrease (not shown), as in the previously published study [56]. In figure 2.7b, the LSPR linewidths, extracted from Lorentzian fits of the experimental extinction spectra, are shown. An

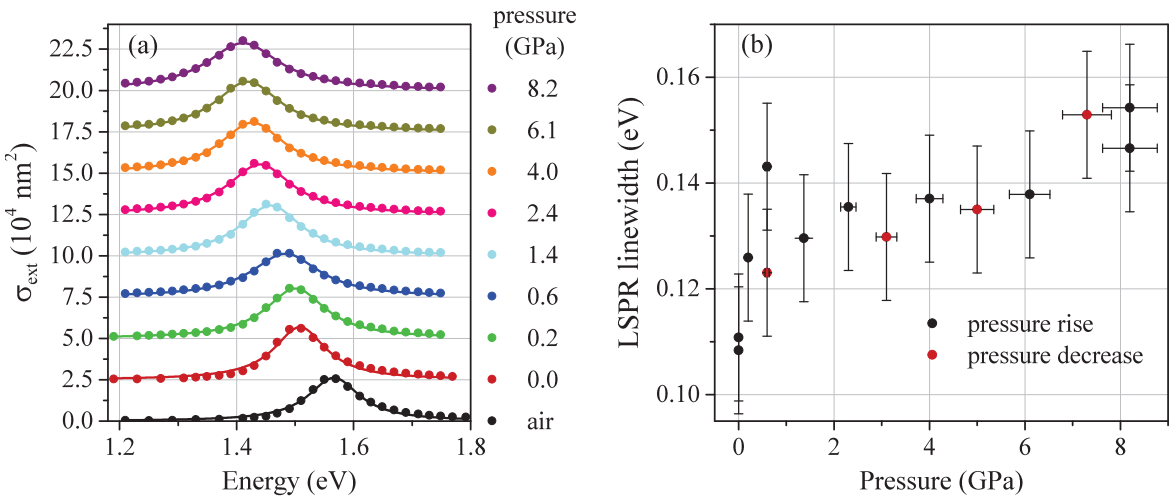

Figure 2.7 – Pressure dependence of the LSPR linewidth (FWHM) of a single silica-coated gold nanobipyramid. (a) Extinction spectra measured using SMS at different pressures ranging from 0 to 8.2 GPa (dots). The lines represent Lorentzian fits of the spectra in the energy domain. The curves are vertically shifted by 2.5 $\times 10^4$ nm^2. Only the spectra measured during the pressure rise of this experiment are shown. (b) Linewidths (FWHMs) of the Lorentzian fits of the extinction spectra shown in (a) (with the addition of the measurements made during the pressure decrease), plotted as a function of the applied pressure.

increase of the linewidth is observed with pressure, whose amplitude is larger than the estimated uncertainty for the linewidth determination from the spectra (resulting from the uncertainties related to the conversion of SMS signal into extinction cross-section, see section 2.1.2.b). In the future, reproduction of these measurements will be necessary to ascertain this effect, while a theoretical model still has to be constructed.

2.1.3 Laser sources

Measurement of the plasmonic responses of the nano-objects studied in this work requires light sources covering a broad spectral range, from the near ultraviolet to the near infrared (375–1040 nm). To this purpose, we used a combination of several light sources, whose spectral ranges are indicated in figure 2.8, and which we now describe. The same sources were used in time-resolved spectroscopy measurements, whose principle will be presented in the next section.

The first source, generating wavelengths in the 690–1000 nm range, is a commercial mode-locked oscillator using as an amplifying medium a sapphire (Al_2O_3) crystal doped with trivalent titanium ions Ti^{3+} (Ti:Sapphire). Population inversion within the titanium ions is achieved through the use of a continuous wave Nd:YVO_4 laser, generating a wavelength of 1064 nm which is then frequency-doubled by a non-linear lithium triborate

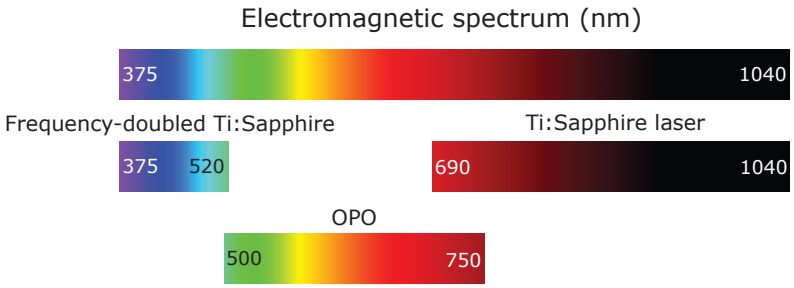

Figure 2.8 – Light sources used in SMS and time-resolved experiments, with the associated wavelength ranges.

crystal (LBO), thus generating a 532 nm wavelength close to the absorption peak of the Ti:Sapphire rod. The longitudinal modes of the cavity allow the generation of short pulses of the order of 150 fs with a repetition frequency of 80 MHz and an average output power of the order of 2 W.

To produce wavelengths in the UV–blue part of the spectrum (375–520 nm), the output of the Ti:Sapphire oscillator is frequency-doubled using the second-harmonic generation (SHG) of a 100 nm-thick barium beta-borate (βBaB_2O_4) crystal (BBO). The use of wavelengths shorter that 375 nm is precluded by the low reflectivity of the mirrors in this spectral domain, as well as by the poor transmission of the objectives.

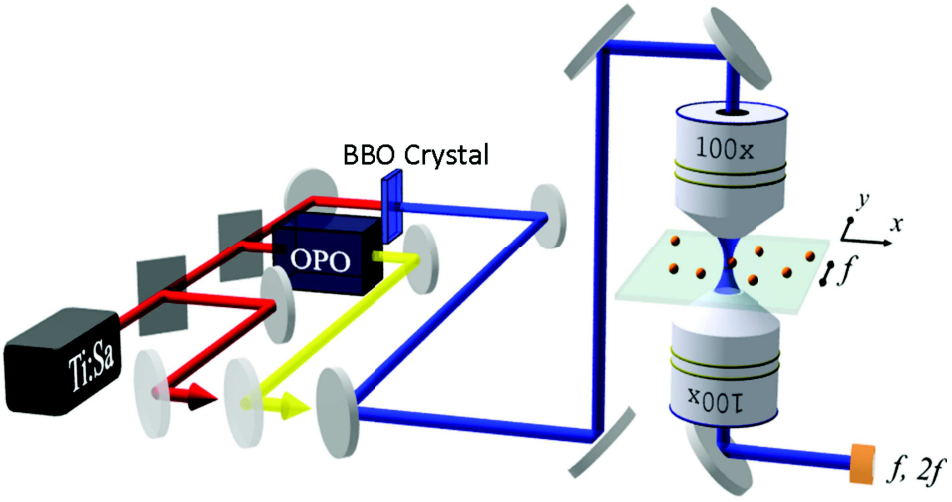

Figure 2.9 – Configuration of the light sources used in SMS experiments. Moveable mirrors are used to switch between the different laser sources.

The intermediate spectrum range (500–750 nm) is covered with an automated optical parametric oscillator (OPO). This coherent light source is based on the parametric amplification of an incident pump beam (here, the frequency-doubled pulsed beam of the Ti:Sapphire oscillator) in a birefringent crystal (BBO). This non-linear optical process

allows the conversion, in the birefringent medium, of a photon of frequency and wavevector $(\omega_p, \mathbf{k}_p)$ into two photons $(\omega_s, \mathbf{k}_s)$ and $(\omega_i, \mathbf{k}_i)$ (*signal* and *idler* waves) respecting the energy and momentum conservation ($\omega_p = \omega_s + \omega_i$, $\mathbf{k}_p = \mathbf{k}_s + \mathbf{k}_i$). The signal wave, whose frequency ω_s can be tuned through the rotation of the BBO crystal, is then amplified in a resonant cavity, thus leading to the generation of coherent ultrashort light pulses of durations comparable to those of the pump pulses.

Figure 2.9 schematizes the experimental SMS configuration and the different light sources used to produce wavelengths in the 375–1040 nm range.

2.2 Single-object ultrafast time-resolved spectroscopy

In the studies described in this thesis, the transient modifications of the properties of a nano-object were studied by means of single-particle time-resolved spectroscopy (or pump–probe spectroscopy), used in combination with SMS. In this section, we briefly present the principle of this technique and the configuration of the experimental setup. Further details about the experimental methods used in this thesis will be given in chapters 3 and 4.

2.2.1 Principle

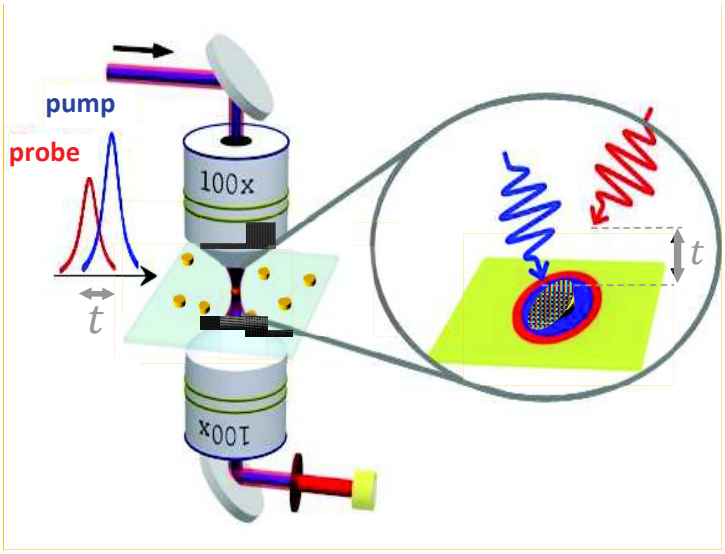

Figure 2.10 – Principle of single-particle time-resolved spectroscopy. A pump light pulse (shown in blue) focused onto a nano-object, impulsively excites this particle out of equilibrium. The subsequent relaxation of the nano-object is monitored by measuring the transmission variation of a probe pulse (red) following the pump pulse with a controllable delay t.

The general principle of time-resolved spectroscopy is presented in figure 2.10 in the

configuration of single-particle measurements [13, 50]. In a transmission optical pump-probe experiment, a femtosecond light pulse (the *pump* pulse) excites a nano-object, inducing a time-dependent modification of its extinction cross-section caused by different relaxation mechanisms (see section 1.3). A second pulse (*probe* pulse), delayed with respect to the pump by a controllable time t, probes the state of the system at instant t after excitation. The pump-induced variations of probe pulse transmission are directly connected to the extinction cross-section change, $\Delta\sigma_{ext}(t)$, thus yielding information on the electronic, vibrational and thermal relaxation dynamics within the system.

2.2.2 Experimental configuration

In the configuration used in our experiments, referred to as two-color pump-probe spectroscopy (figure 2.11), the pump and probe beams are quasi-monochromatic pulsed beams of different wavelengths λ_{pp} and λ_{pr}, with the same repetition rate. To generate these beams, the output pulse train from the Ti:Sapphire oscillator is split in two parts. One of these parts is frequency-doubled using second harmonic generation to produce the pump beam (yielding λ_{pp} in the 375–510 nm range), whereas the probe beam is either the signal from the Ti:Sapphire oscillator (with λ_{pr} = 750–1040 nm) or the output of the OPO (λ_{pr} = 500–730 nm). The pump and probe beams are sent into the objective used in SMS experiments, and tightly focused onto a single nano-object, SMS being used to superimpose the beams and to position the particle in the center of the focal spots. The transmitted beams, collected by a second objective, are discriminated using an edgepass filter, only the probe beam reaching the avalanche photodiode.

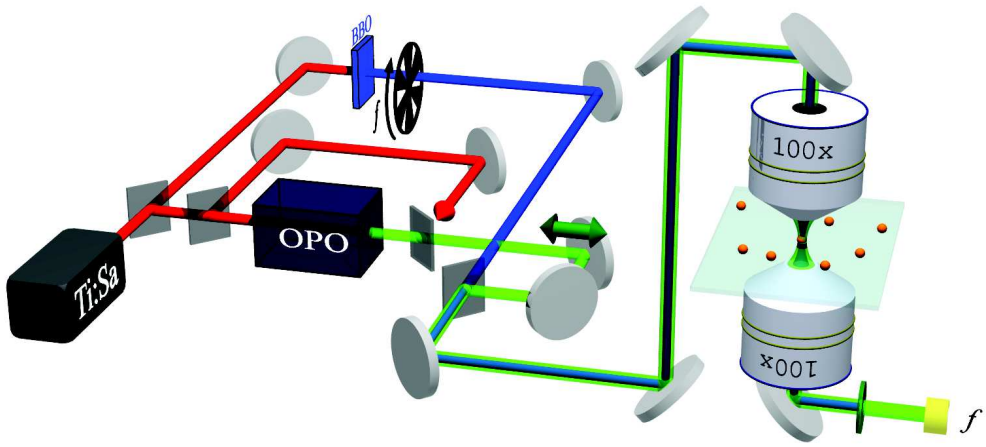

Figure 2.11 – Schematics of the pump-probe setup, showcasing the differnt light sources used. The pump beam is the frequency-doubled output of the Ti:Sapphire oscillator (thus lying in the 375–520 nm range), while the probe beam is either generated by the OPO (500–750 nm) or directly taken as the output of the Ti:Sapphire laser (750–1040 nm).

To control the delay between the pump and probe pulses, a motorized linear translation

stage is used, enabling to modify the optical path length of the probe beam. Measurement of the probe transmission change $\Delta Tr/Tr(t)$, as a function of the delay t following the nano-object excitation, enables a quantitative determination of the time-dependent extinction changes of the nano-object, $\Delta\sigma_{ext}(t)$, through:

$$\frac{\Delta Tr}{Tr} = -\frac{\Delta\sigma_{ext}(\lambda_{pr})}{S_{pr}} \ , \tag{2.15}$$

where S_{pr} is the area of the probe beam ($S_{pr} = d_{pr}^2/(4\ln 2)$ for a Gaussian beam with FWHM d_{pr} [13]). To detect and measure these variations with high sensitivity, the pump power is modulated at frequency $f = 30$ kHz using a mechanical chopper placed in the beam path (see figure 2.11). The transmission variations of the probe beam induced by the modulated pump beam, detected by the avalanche photodiode, are then demodulated by a lock-in amplifier operating at frequency f.

Chapter 3

Cooling dynamics of a single supported nano-object

Contents

A detailed understanding of nanoscale heat transfer is required in many technologies. It is for instance essential to manage the crucial problem of heat dissipation from nanoscale components in nanoelectronics, to create nanostructured materials with good thermoelectric properties and to maximize the efficiency of nanoparticle-based photothermal therapies [9, 10, 57, 58]. Nanoscale heat transfer fundamentally differs from that at macroscopic scale for two major reasons. First, the thermal resistances limiting heat transfer at interfaces (*Kapitza resistances* [59, 60]) play a much greater role in the former case, and rule the cooling rate of small nanostructures [15, 61–63]. Second, Fourier's law of heat conduction, which assumes a diffusive motion of heat carriers, ceases to be applicable to describe heat propagation over distances smaller than their characteristic mean free paths (ballistic regime [64, 65]) and in situations where the causality relation between the temperature gradient and heat flux becomes manifest (hydrodynamic regime [66, 67]).

A lot of the current understanding of nanoscale heat transfer has been obtained using non-contact optical pump–probe techniques. The main idea of this approach consists in investigating the dissipation of the energy injected by a pump light beam in a sample by monitoring the induced modifications of the sample optical properties, *e.g.* by measuring the transmission or reflection of a probe beam. This general strategy can be implemented in various ways, differing by the types of light sources, spectroscopy methods and samples used. For instance, pump–probe techniques can work either in the frequency domain [68, 69] (modulating pump power, the use of continuous beams being possible in this case) or time domain [70] (using time-delayed pump and probe pulses, which can be spatially overlapped or separated), and can be applied to both bulk and nanostructured materials, provided that they are partly absorbing [71, 72].

Time-resolved experiments involving absorbing nanostructures (playing the role of both heaters and thermometers) dispersed in a dielectric environment are particularly interesting to study nanoscale heat transfer. Indeed, as illustrated in figure 3.1, the sizes of the heated volumes correspond in this case to those of the absorbing nano–objects (which can be of the order of a few or a few tens of nm), rather than that of the pump beam, whose lateral size is limited by diffraction to about half of its wavelength, *i.e.* a few hundreds of nm (and which constitutes the relevant length scale for heating of bulk materials and thin films). This approach has for instance been used to measure the thermal conductances at the interface between metal nanoparticles and their environment, and to investigate the dependence of these conductances on composition of nanoparticles, environment and interfaces (*e.g.*, nature and length of surfactant molecules) [15–19]. It has also allowed the study of transient phase transitions either in the nanoparticle (melting of the metal [73, 74]) or its environment (formation of bubbles in the surrounding liquid [75]).

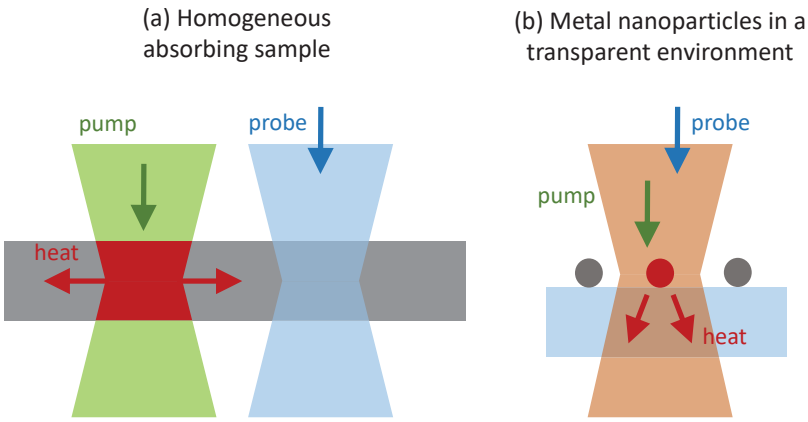

Figure 3.1 – Several approaches for studying nanoscale heat transfer using pump-probe spectroscopy. (a) Homogeneous absorbing samples: pump and probe can be spatially shifted, but the size of the heated area necessarily exceeds a few hundred nm as it is defined by the diffraction-limited spot of the pump beam. (b) NPs dispersed in a dielectric medium: the locally heated volume corresponds to that of a NP, whose cooling is monitored by the probe beam.

The relation between the measured time-resolved optical signals and the thermal kinetics in the nanoparticles and their local environment has also been recently modeled [14, 17, 76], allowing more precise estimations of interface conductances in cases where environment heating significantly influences time-resolved signals. Additionally, some time-resolved experiments performed on arrays of metal nanowires patterned on crystalline substrates with high phonon mean free paths (*e.g.* sapphire and silicon) have demonstrated the failure of Fourier's law at the nanoscale [65, 77–80].

All the studies mentioned above were performed on ensembles of nanostructures. The signals measured in these investigations thus represent an average over nanostructures affected by an unavoidable dispersion of their morphology and thermal contact with the environment. This approach makes analysis of the amplitude of time-resolved signals extremely challenging, as it would require to precisely know the density of the nanoparticles and their size dispersion, and to take into account the different efficiencies with which their heating is generated and probed (due to their different locations in the non-uniform pump and probe beams, and to the dispersion of their optical responses resulting from their morphological differences). Single-particle methods, which have already been applied to study the linear optical response [36, 81], internal thermalization [13] and acoustic vibrations [7, 12, 82, 83] of metal nano-objects, constitute an ideal way to overcome these limitations.

In the work presented in this chapter, we applied for the first time the single-particle time-resolved spectroscopy technique to the study of the cooling dynamics of individual metal nanoparticles, namely gold nanodisks (NDs) supported on sapphire. This allowed us to

perform quantitative investigations of the sensitivity of the measured signals to ND heating, by measuring the proportionality factor between optical cross-section changes and nanoparticle temperature rise. This sensitivity is shown to strongly depend on the probe wavelength used, in agreement with the results of previous thermo-optical models [14, 17]. By performing experiments on a large number of individual NDs with different diameters and thicknesses, we also characterized the size-dependence of ND cooling dynamics. Finite-element method (FEM) was used to demonstrate that ND cooling dynamics are essentially determined by the thermal resistance at the gold–sapphire interface, whose value can be determined by comparison between the measured and simulated signals.

3.1 Cooling dynamics of nano-objects and impact on their optical response

3.1.1 Cooling dynamics of a metal nano-object

We focus on the cooling process of a metal nano-object in a transparent environment following impulsive heating by a laser pulse, in the context of pump-probe experiments. After the absorption of a pump pulse and the establishment of a uniform nano-object temperature $T_p > T_0$, where T_0 is the equilibrium (room) temperature (a process achieved after about 5 ps in gold, see section 1.3), heat is evacuated into the environment. The cooling dynamics are essentially ruled by two mechanisms: heat transfer through the interface, and diffusion into the surrounding medium. These two processes, which are discussed in the following paragraphs, are represented in figure 3.2 in the experimentally investigated nanosystem of a gold nanodisk supported on a sapphire substrate and surrounded by air.

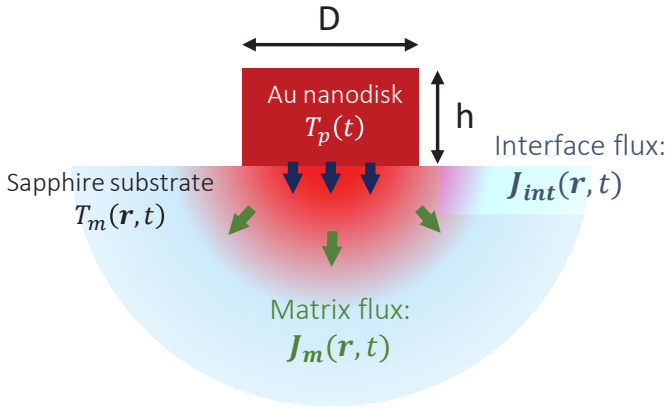

Figure 3.2 – Schematics of heat transfer in the experimental conditions. The system geometry is shown as well as the two cooling processes considered (heat transfer at the interface and in the substrate, with associated heat current densities $\mathbf{J_{int}}$ and $\mathbf{J_m}$).

3.1.1.a Interfacial heat transfer

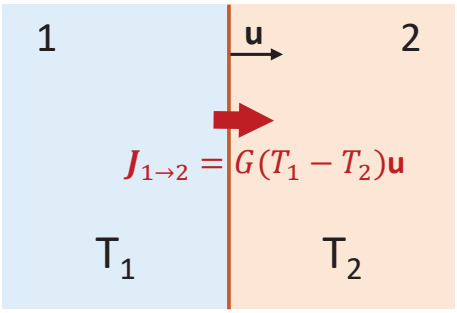

Figure 3.3 – Schematics of heat transfer through an infinite plane interface between two materials 1 and 2 with temperatures T_1 and T_2. **u** is a unit vector perpendicular to the interface.

The thermal boundary resistance (or Kapitza resistance), and its inverse, the thermal boundary conductance G (in $\mathrm{W\,m^{-2}\,K^{-1}}$) were introduced in 1941 by P. Kapitza to describe heat transfer between a copper heater and liquid helium, whose flux was found to be linearly related to the temperature difference between both media [59, 84]. In the case of an infinite plane interface between two materials with temperatures T_1 and T_2 (figure 3.3), G represents the proportionality constant between the heat flow at the interface, $\mathbf{J_{1\to2}}$, and the difference between the temperatures of the two media in contact:

$$\mathbf{J_{1\to2}} = G\,(T_1 - T_2)\,\mathbf{u}\ . \tag{3.1}$$

In the more complex system represented in figure 3.2, for which the interface has a finite size, the heat flow remains perpendicular to the interface plane, but depends on local temperatures in both materials at position $\mathbf{r}$ on the interface. If the ND temperature T_p is assumed to remain uniform throughout the cooling process[1] (an *a priori* relevant assumption due to the high thermal conductivity of gold, $\Lambda_{Au} = 315\ \mathrm{W\,m^{-1}\,K^{-1}}$), the heat flow writes:

$$\mathbf{J_{int}(r,t)} = G\,(T_p(t) - T_m(\mathbf{r},t))\,\mathbf{u}\ , \tag{3.2}$$

with $\mathbf{u}$ a unit vector directed towards the sapphire. Heat transfer between the ND and air is neglected in our model, as the corresponding boundary resistance is expected to

[1] This assumption will be justified in more detail in the following of this section.

be very high due to the low density of air as compared to that of gold[2].

Giving a theoretical expression of G requires a detailed description of the thermal properties of the two materials in contact and of their interface, which is rarely achieved for actual systems. For two solid materials of which at least one is not a metal, heat transfer is governed by the phonons. Historically, two simple models have been proposed to describe phonon transport through an interface: the acoustic mismatch model (AMM) and the diffuse mismatch model (DMM).

In the AMM, developed by by Khalatnikov [85] and independently by Mazo [86], a continuum mechanical model is employed to describe the propagation of acoustic waves, with the assumption of a perfect interface inducing no scattering. Wavevectors propagating across the interface are determined by conservation of momentum. The transmission coefficient t, defined as the ratio between the transmitted and incident energy fluxes, is then analogous to the Fresnel transmission coefficient in wave optics (replacing refractive indexes by acoustic impedances), and is independent of the phonon frequency ω. For a normal incidence on a plane interface, it is given by [59]:

$$t = \frac{4Z_1Z_2}{(Z_1 + Z_2)^2} \ , \tag{3.3}$$

where Z_1 and Z_2 are the acoustic impedances of the two media ($Z = \rho v_l$, with ρ the density and v_l the longitudinal sound velocity). The corresponding interface conductance may then be calculated from t and from the bulk properties of the two materials in contact [60].

The DMM conversely assumes a perfectly scattering interface. Proposed by E.T. Swartz in 1987 [87], it represents an upper limit of the effect that diffuse scattering can have on the interface resistance, which is neglected in the AMM. In this model, phonons that propagate across the interface lose memory of the incident wave and thus exit with a random wave vector. The transmission coefficient is then only dependent on the phonon density of states of the two media [59, 60].

These two models describe interface thermal transfer only with the bulk properties of the two materials. Despite their opposite assumptions on the role of the interface, they predict similar thermal resistance values at low temperatures for solid–solid interfaces [59], in good agreement with experiments. However, they both fail at higher temperatures, in many cases underpredicting or overpredicting the resistance by up to an order of magnitude [88]. To go beyond these simple models, explicit modeling of the interface region at the atomic level is generally required. For example, Young and Maris [89] studied the case of two face-centered cubic lattices with an interface along adjacent

[2]See equation 3.3.

(001) atomic planes, by modeling atomic interactions as springs connecting each atom to its nearest neighbors. Solving the equations of motion allowed them to determine the frequency-dependent transmission coefficient $t(\omega)$ and thus the interface conductance at temperature T, $G(T)$, in this particular case. In more complex systems, for instance when one of the materials is amorphous, or polycrystalline (as is most probably the case for gold in the sample studied in this work, synthesized using electron beam lithography), an accurate theoretical prediction of thermal boundary conductances at room temperature remains extremely challenging. However, these conductances can be determined experimentally using time-resolved optical methods, as discussed in the introduction of this chapter. This approach was used in this Ph.D. thesis to measure the thermal conductance of gold–sapphire interfaces, as will be discussed in section 3.4.

3.1.1.b Heat dispersion into the environment

At the macroscopic scale, heat transport by conduction in a homogeneous medium is ruled by Fourier's law of diffusion:

$$\mathbf{J_m}(\mathbf{r},t) = -\Lambda_m \, \mathbf{grad}(T_m(\mathbf{r},t)) \ , \tag{3.4}$$

where $\mathbf{J_m}(\mathbf{r},t)$ is the heat current density and Λ_m the thermal conductivity of the considered material.

Equation 3.4 assumes a diffusive propagation of heat, and is therefore relevant to describe heat propagation over distances longer than the phonon mean free path (MFP), which is typically of the order of 1 and 100 nm, respectively, for amorphous and crystalline materials such as silica and sapphire at room temperature. Its validity becomes however questionable to describe heat propagation in the vicinity of nanostructures with characteristic sizes of the order of these MFPs, in which case ballistic effects are expected to play an important role. Deviations from Fourier's law have been experimentally observed, notably in the context of time-resolved experiments on metal nanostripes supported on sapphire or silicon substrates [65, 70, 77, 78].

3.1.1.c Calculations of the cooling dynamics

From the equations of thermal transfer at the interface (equation 3.2) and of the diffusion in the matrix (equation 3.4), associated to the conservation of the heat flux at the interface ($\mathbf{J_{int}} = \mathbf{J_m}(\mathbf{r})|_{\mathbf{r}\in int}$), the temperatures of the ND $T_p(t)$ and of the sapphire $T_m(\mathbf{r},t)$ may be retrieved. While simpler systems, such as metal nanospheres in a homogeneous matrix, permit a semi-analytical resolution of the equations of thermal transfer [17],

numerical methods must be used in the case of a substrate-supported nanodisk. In this work, we used a finite-element method (FEM) model, which will be detailed along with our results in section 3.4 of this chapter dedicated to the study of the ND cooling dynamics.

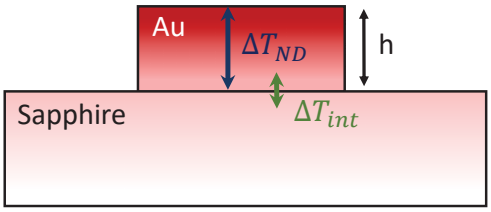

Figure 3.4 – Definition of temperature differences ΔT_{ND} and ΔT_{int} used in the calculation of the Biot number in the experimental configuration.

Although it is not required for running FEM simulations, the temperature of the gold ND may be considered uniform at all times, as assumed in figure 3.2. To verify this, one needs to compare the efficiency of thermal diffusion within the nano-object to that of thermal transfer at the interface. This comparison is given by the dimensionless Biot number, which may be defined in our case as the ratio of the maximal temperature variation within the nano-object, ΔT_{ND}, to the temperature difference at its boundary, ΔT_{int}, as represented in figure 3.4. To express these two quantities, we write the conservation of the heat flux at the interface:

$$\begin{aligned} J_{int} &= G\,\Delta T_{int} \\ &= J_{ND}|_{int} = -\Lambda_{Au}\,\|\mathbf{grad}(T_p)|_{int}\| \approx -\Lambda_{Au}\,\frac{|\Delta T_{ND}|}{h}\ , \end{aligned} \tag{3.5}$$

with J_{ND} the modulus of the heat flux in the ND, and where a constant temperature gradient was assumed in the last step. The Biot number is then:

$$Bi = \frac{\Delta T_{ND}}{\Delta T_{int}} = \frac{hG}{\Lambda_{Au}}\ . \tag{3.6}$$

Performing a preliminary estimation of Bi in our experimental conditions, using a $G = 50\ \mathrm{MW\,m^{-2}\,K^{-1}}$ value consistent with measurements for gold–sapphire interfaces reported in the literature [60, 90–93], $\Lambda_{Au} = 25\ \mathrm{W\,m^{-1}\,K^{-1}}$, and $h = 40$ nm (one of the two values of h used in the experiments), leads to $Bi = 8 \times 10^{-2} \ll 1$. This guarantees that temperature variations within the ND remain much smaller than those at the interface during the thermal relaxation process.

3.1.2 Heating-induced transient changes of the optical response

A successful interpretation of time-resolved signals requires to understand the link between the thermal dynamics in the nano-object and its environment, $\Delta T_p(t)$ and $\Delta T_m(\mathbf{r}, t)$, and the measured optical signals, related to the transient changes of the nano-object's extinction cross-section $\Delta\sigma_{ext}(t)$ (chapter 2).

3.1.2.a Simplified case: uniform temperatures

For illustrative purposes, we first consider the simplified situation of uniform temperatures in both the nanoparticle and its local surrounding medium (here also assumed homogeneous for simplicity), noted T_p and T_m [14, 17]. In this case, time- and probe wavelength-dependent transient extinction changes are related, to first order, to the temporal evolutions of T_p and T_m via

$$\Delta\sigma_{ext}(\lambda_{pr}, t) = A_p(\lambda_{pr})\Delta T_p(t) + A_m(\lambda_{pr})\Delta T_m(t) \tag{3.7}$$

with

$$A_p(\lambda) = \frac{\partial\sigma_{ext}}{\partial\varepsilon_1}(\lambda)\frac{\mathrm{d}\varepsilon_1}{\mathrm{d}T_p}(\lambda) + \frac{\partial\sigma_{ext}}{\partial\varepsilon_2}(\lambda)\frac{\mathrm{d}\varepsilon_2}{\mathrm{d}T_p}(\lambda) \tag{3.8}$$

$$A_m(\lambda) = \frac{\partial\sigma_{ext}}{\partial\varepsilon_m}(\lambda)\frac{\mathrm{d}\varepsilon_m}{\mathrm{d}T_m}(\lambda) \tag{3.9}$$

where $\varepsilon = \varepsilon_1 + i\ \varepsilon_2$ is the complex dielectric function of the metal nanoparticle, and $\varepsilon_m \in \mathbb{R}$ that of its environment, assumed transparent.

3.1.2.b Impact of environment heating on time-resolved signals

A common assumption made in the analysis of pump-probe experiments is that transient extinction changes only reflect the nano-object temperature changes. Equation 3.7 however shows that they generally reflect a combination of the thermal dynamics in the nanoparticle and its environment, with λ_{pr}-dependent weights. This may lead to a complex dependence on probe wavelength of the temporal evolution of pump-probe signals, due to the different dynamics of the temperatures in the nanoparticle and its local environment. Indeed, the former is suddenly increased by pump pulse absorption and monotonously decays towards its equilibrium value, while the latter reaches its maximum with a position-dependent delay, because of the time needed for the heat generated in

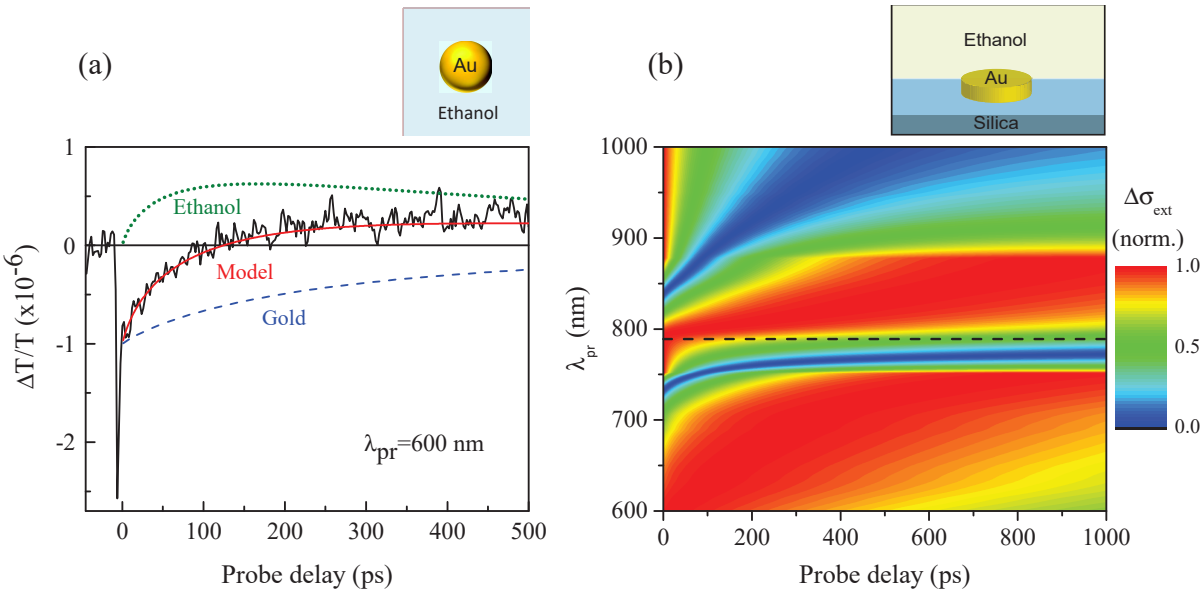

Figure 3.5 – Influence of the environment temperature changes on time-resolved signals (previous works performed in the FemtoNanoOptics group). (a) Experimental time-resolved signal for an ensemble of gold nanospheres in ethanol measured with $\lambda_{pr} = 600$ nm (black), and simulated signal from a semi-analytical opto-thermal model (red). The simulated signal is the sum of two components presenting different dynamics, associated to the effects of the heating of the gold nanoparticle (blue dashed line) and ethanol (green dotted line), respectively. (adapted from ref. [17]) (b) FEM-computed time- and probe wavelength-dependence of the transient extinction cross-section changes of a gold nanodisk in ethanol supported on a silica substrate. The dashed black line indicates the position of the nanodisk localized surface plasmon resonance (LSPR). Figure adapted from ref. [14].

the nanoparticle to be transferred and to propagate into its environment. This effect was experimentally demonstrated in a precedent study performed in our group [17, 27], in the case of gold nanospheres in ethanol (figure 3.5a), a liquid known for the large dependence of its refractive index on temperature. A semi-analytical opto-thermal model based on calculations of the temperature evolutions of a nanosphere and its environment (decomposed into multiple concentric shells in order to avoid the assumption of a homogeneous environment temperature) was used to reproduce the experimental signals, the contribution of the environment being non-negligible over a wide range of probe wavelengths. Similarly, Gandolfi et al. [14] numerically computed the complete time- and probe wavelength-dependences of time-resolved signals in the more complex case of a gold nanodisk on a silica substrate and surrounded by ethanol. A thermal FEM model similar to the one used in this study (see section 3.4) was used to calculate the temperature evolution at all points of the modeled space, after which optical FEM simulations allowed to retrieve the induced extinction changes. Figure 3.5b presents the normalized $\Delta\sigma_{ext}$ as a function of time and probe wavelength, demonstrating important variations of the dynamics over the whole zone of the plasmon resonance.

The importance of these effects in a given system is mainly determined by the sensitivity of the materials' dielectric functions to temperature changes. In the two studies mentioned above, the high amplitude of the temperature-induced optical changes of the environment are ascribed to the particularly large temperature-dependence of the dielectric function of ethanol, which is comparable to that of gold ($\mathrm{d}\varepsilon_{ethanol}/\mathrm{d}T \sim \mathrm{d}\varepsilon_{Au}/\mathrm{d}T \sim 10^{-3}$). In the studies discussed in this work, environment heating has conversely a negligible influence on the measured transient extinction changes of the studied nano-objects, as will be discussed in section 3.3.1.a.

3.2 Experimental approach

3.2.1 Samples

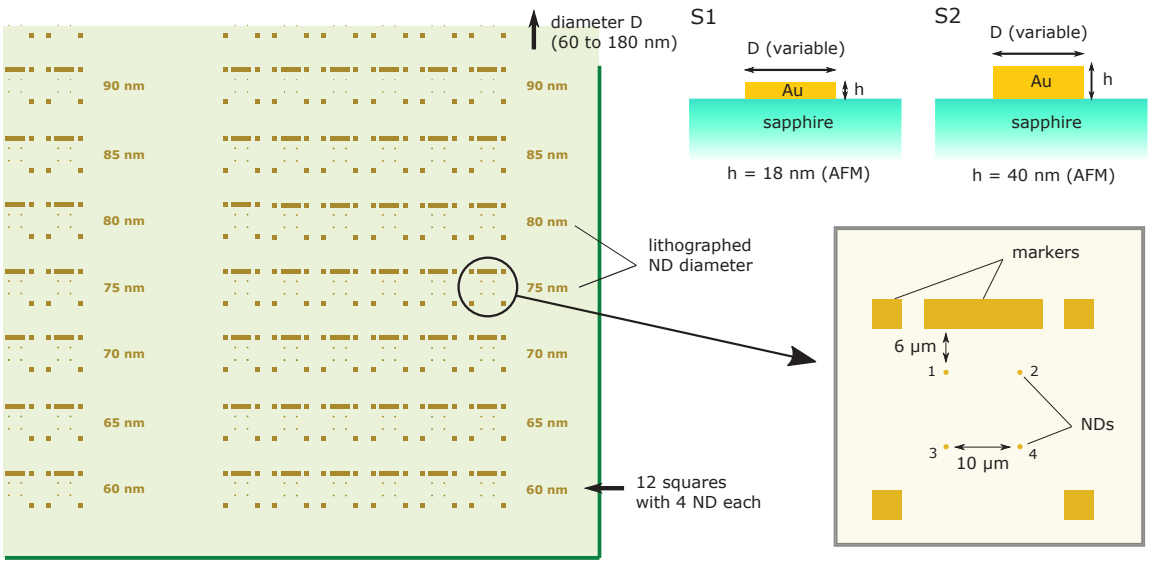

Figure 3.6 – Common layout for the two ND samples S1 and S2. Lithographed markers indicate the positions of the gold NDs on the sapphire substrate. The NDs are isolated from any other metal structure by at least 6 µm. Their diameters range from 60 to 180 nm, each series containing 48 identical NDs. Samples S1 and S2 differ only by the ND thicknesses (top right).

The investigated samples were designed for a systematic study of the morphology-dependence of the cooling dynamics of gold nanodisks (as well as that of their vibrational properties, which were the object of former studies [12, 30]). For this purpose, they contain NDs in a wide range of dimensions and shapes.

Two samples of gold NDs, referred to as S1 and S2, were produced via electron beam lithography (EBL), gold thermal evaporation and lift-off techniques [12, 30] within the

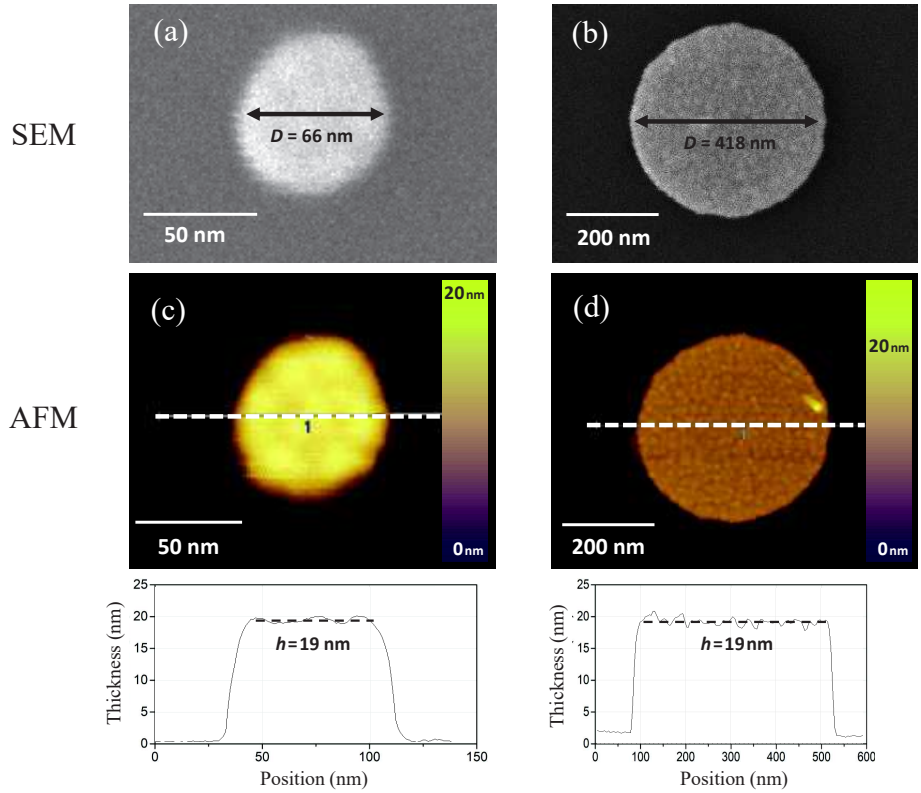

Figure 3.7 – SEM and AFM images of two NDs with nominal thicknesses $h = 15$ nm and diameters $D = 60$ nm (a,c) and $D = 400$ nm (b,d). These NDs are from a sample similar to S1 in its fabrication. (a,b) SEM images of the two NDs. (c,d) AFM images of the same NDs and profiles along the indicated lines, from which the average ND thicknesses are deduced. For the measurements on S1 and S2 in our study, where a coarser AFM probe was used, convolution with the tip precluded the precise determination of the diameters by AFM. SEM images were used instead, although their resolution is affected by substrate charging issues.

framework of a collaboration with F. Banfi (Cattolica university, Brescia) and F. Rossella (Scuola Normale Superiore, Pisa). NDs with targeted thicknesses of $h = 15$ nm (sample S1) and $h = 30$ nm (sample S2) and nominal diameters D ranging from 60 to 180 nm were nanopatterned on the optically polished surface of the sapphire substrate, which is a 0.48 mm thick single-crystal $\alpha-Al_2O_3$ slab cut along the (0001) plane. The layout of these samples is shown in figure 3.6. For each value of diameter D, each sample contains 48 nominally identical NDs separated from other metallic structures by at least 6 µm to prevent coupling effects that may affect their optical and thermal responses.

To characterize the actual dimensions of the fabricated NDs, which may differ from those targeted during the fabrication process, scanning electron microscopy (SEM) and atomic force microscopy (AFM) were performed. NDs from various locations of the samples were investigated using both techniques, which allowed to confirm the homogeneity of

the samples. While AFM is useful for determining the ND thicknesses, information it provides about the diameter is less reliable because of the convolution of the profile by the tip lateral size. For this reason, diameters were rather estimated from SEM images, although the resolution of this technique was also limited due to charge accumulation at the surface of the insulating sapphire substrate. Examples of SEM and AFM images of gold NDs are presented in figure 3.7. The examples shown correspond to a sample synthesized with the same approach as S1 and S2, but containing larger NDs and for which AFM characterization was made with a sharper tip by our Pisa collaborators, resulting in higher-quality images.

Because SEM was seen to modify the nano-objects' properties (in particular their optical response), NDs that had been investigated in SEM were not used in our experiments. Therefore, the ND dimensions were determined by using average values deduced from a large number of AFM and SEM measurements.

Thicknesses estimated from AFM measurements were higher than their targeted values, with $h = 18 \pm 2$ nm for S1 and $h = 40 \pm 5$ nm for S2. Diameters derived from SEM images were also larger than the nominal values (by about 5% for S1 and 15% for S2), with a dispersion corresponding to about 10% of the nominal diameter.

3.2.2 Nanodisk optical characterization

The extinction spectra of the investigated single NDs were determined using spatial modulation spectroscopy (SMS), described in section 2.1. These measurements enable the precise characterization of the optical response of each investigated ND, from which information on ND morphology complementary to that obtained from AFM and SEM images can be deduced. More precisely, measuring the polarization-dependence of the ND extinction permits the rapid selection of quasi-circular NDs, while reproduction of the extinction spectra by FEM simulations yields an estimation of the geometrical parameters D and h of each optically investigated ND.

3.2.2.a Selection of circular NDs

The synthesized gold NDs may differ from perfect cylinders. This is notably due to the standard ∼5–10 nm resolution limit achievable in practice with the EBL technique [94]. Systematic errors may also affect the positioning, size, and intensity of the electron beam scanned across the sample surface during the lithography [95]. SMS is a useful tool to obtain information about the ellipticity of NDs, which may be precisely quantified by comparison to FEM calculations. As was shown in a recent study to which I took part [30], performed in the context of the Ph.D. thesis of F. Medeghini, polarization-

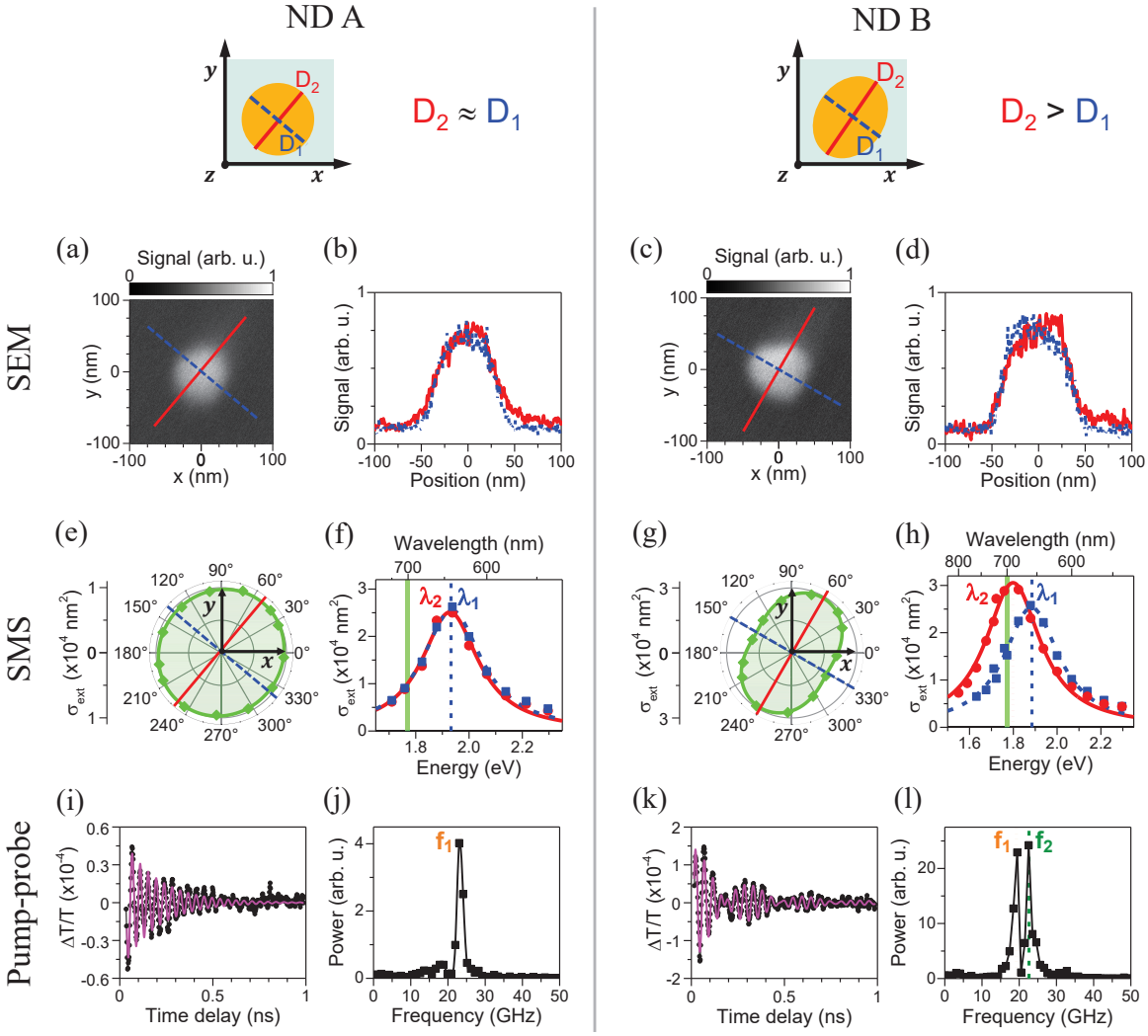

Figure 3.8 – Effects of the morphological anisotropy of NDs on their optical and vibrational responses. Two NDs with same approximate dimensions $h \approx 18$ nm and $D \approx 70$ nm (respectively deduced from AFM and SEM measurements), with quasi-circular (ND A, left column) and noncircular (ND B, right column) sections, are investigated. (a) SEM image of ND A. (b) Intensity profile along two orthogonal directions. (c,d) Same for ND B, where the two directions correspond to the major (red) and minor (blue) axes of the ND. (e) Polarization-dependent extinction cross-section of ND A at wavelength 700 nm, measured using a $\sim 10^{-3}$ J m^{-2} incident beam fluence. (f) Extinction spectra of ND A measured with a linear polarization along the two directions defined in (a) and (b) (same color code). Lines correspond to Lorentzian fits in the energy domain. (g,h) Same for ND B, where the polarization directions are defined in (c) and (d). (i) Oscillating part of a time-resolved spectroscopy signal measured on ND A, with pump wavelength $\lambda_{pp} = 610$ nm, incident pump fluence $F_{pp} \approx 1$ J m^{-2}, and probe wavelength $\lambda_{pr} = 610$ nm. (j) Fourier transform. (k,l) Same for ND B (same λ_{pp}, λ_{pr}, and F_{pp} values). Figure adapted from ref. [30].

dependent extinction measurements allow the detection of minute deviations of actual ND shapes from the targeted cylindrical ones, as they induce polarization-dependent extinction cross-sections and lift the degeneracy of ND in-plane dipolar LSPRs. As shown in figure 3.8, which summarizes these studies, a spectral shift between the spectra measured along the two privileged orthogonal directions may easily be detected, with a resolution as low as a few nanometers. For instance, FEM reproduction of the cross-polarized spectra of nanodisk ND B (figure 3.8), assuming an elliptical shape with semi-axes $D_1/2$ and $D_2/2$, indicates that they correspond to a 14% difference between D_1 and D_2 (although detection of differences of only a few percent have been reported in the same article). Such small geometrical imperfection may hardly be detected in SEM (due to the issues caused by the insulator character of the substrate, see figure 3.8a–d) or in AFM (due to its poor lateral resolution).

This feature of SMS is important for the present study, since it provides an easy means of selecting NDs with quasi-circular morphologies for time-resolved measurements of their cooling dynamics. As was shown in our study [30], deviation from the cylindrical shape may cause a degeneracy lift not only of the LSPR, but also of the vibrational modes. While for a perfect cylinder with $D/h \approx 3.5$, a single vibrational mode is detected (figure 3.8i–j), introduction of a small ellipticity leads to the detection of two modes with close frequencies instead of a single one, causing beatings in the vibrational part of ultrafast signals (figure 3.8k–l). This added complexity is detrimental to the accurate measurements of the cooling dynamics (especially at timescales < 500 ps), since these vibrational signals need to be fitted and subtracted to access the thermal dynamics, as will be discussed in section 3.2.3.

3.2.2.b ND morphological characterization by FEM analysis of SMS spectra

For this study, two NDs from sample S1 were selected, referred to as ND1 and ND2. Their experimental extinction spectra are shown in figure 3.9a–b. They display marked resonances near 710 nm and 870 nm wavelength, respectively, associated to their in-plane LSPRs. Both spectra were found to be quasi-independent of polarization, thus suggesting quasi-circular shapes. Spectra were taken before and after the complete series of time-resolved measurements, in order to ensure that no important changes were induced by pump-probe measurements. In both cases the spectra underwent only minute changes, with the appearance of a small polarization dependence for ND1 (indicating the introduction of a $\sim 4\%$ ellipticity) and a < 10 nm red-shift for ND2. Such differences were seen to have a minor impact on the following analysis.

Combination of SMS measurements with numerical modeling of ND optical response constitutes a powerful tool for determining the ND dimensions, considering the difficulties

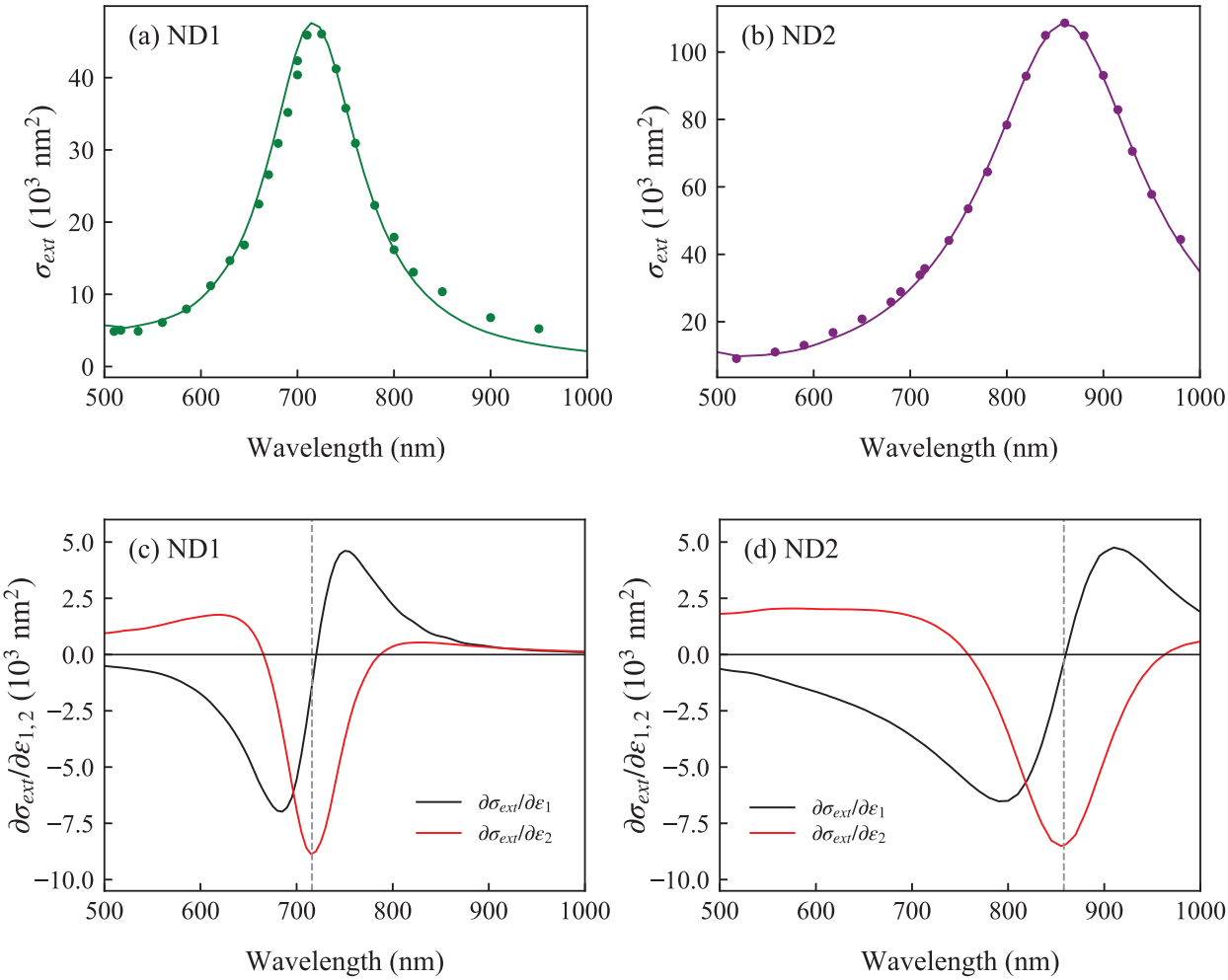

Figure 3.9 – ND1 and ND2 extinction spectra and their derivatives with respect to $\varepsilon_{1,2}$. (a,b) Absolute extinction spectra of individual gold nanodisks ND1 and ND2, respectively. Dots represent the SMS measurements, while lines are FEM calculations with parameters adjusted to best reproduce the experimental spectra, corresponding to D = 101 nm and h = 21 nm for ND1, D = 153 nm and h = 22 nm for ND2. (c,d) $\partial\sigma_{ext}/\partial\varepsilon_1$ (black) and $\partial\sigma_{ext}/\partial\varepsilon_2$ (red) derivatives deduced from FEM calculations for the ND1 and ND2, using the same geometrical parameters as in panels (a) and (b). The dashed lines indicate the central position of the ND LSPRs.

posed by electron microscopy imaging in this context. Three parameters are varied to achieve correct reproduction of the experimental data: diameter D, thickness h and the optical scattering rate γ (see chapter 1). For a perfect cylinder, the spectral position of the LSPR is mostly determined by the aspect ratio D/h, while the spectrum area (when plotted in the energy domain) mainly depends on the volume V. As for the LSPR linewidth, which is correlated to the plasmonic damping factor γ, its modeling is out of reach, as it would require precise knowledge of the gold–air and gold–sapphire interface properties and of the level of crystalline defects in the metal. It is therefore left as a free parameter. By adjusting D, h and γ to achieve the best reproduction of the experimental spectrum, one then obtains an estimate of theses parameters. Values of D, h and D/h deduced by this method for ND1 and ND2 are presented in table 3.1, and compared with the values extracted from SEM and AFM measurements.

parameter method	$\langle h \rangle$ (nm) AFM	h (nm) SMS/FEM	$\langle D \rangle$ (nm) SEM	D (nm) SMS/FEM	$\langle D \rangle / \langle h \rangle$ SEM/AFM	D/h SMS/FEM
ND1	18	21	84	101	4.67	4.81 (+3%)
ND2	18	22	137	153	7.61	6.95 (-9%)

Table 3.1 – Estimated geometrical parameters for ND1 and ND2, extracted either from AFM and SEM measurements of NDs of same nominal dimensions, or from reproduction of ND1 and ND2 experimental extinction spectra by a FEM analysis.

For the two investigated NDs, the deduced D and h values are in reasonable agreement (about 10–20% larger) with the mean values measured with atomic force and scanning electron microscopies, respectively, on NDs of same nominal dimensions. Note that determination of these parameters by the former numerical method is allowed by the quantitative character of SMS measurements (yielding absolute extinction cross-section values). One must however bear in mind the ∼10% uncertainty attached to the amplitudes of experimental extinction spectra (see section 2.1.2.b), which induces uncertainties on estimations of the ND volume $h\pi D^2/4$ and hence on h and D. Conversely, the aspect ratio D/h is estimated with a greater confidence, since it is mainly determined from the LSPR position (table 3.1). This explains why the difference between SEM/AFM and SEM/FEM estimations are smaller for D/h ($< 10\%$) than for D and h individually.

To reproduce the measured LSPR widths, the optical scattering rate γ of conduction electrons had to be increased as compared to that of bulk gold γ_0 ($\hbar\gamma_0 \sim 50$ meV), with $\hbar\gamma = \hbar\gamma_0 + 100$ meV for ND1, and $\hbar\gamma = \hbar\gamma_0 + 45$ meV for ND2. This effect has already been noted in previous analyses on NDs of similar sizes [29, 30]. Quantum confinement effects being negligible for metal structures in this size range ($\hbar\gamma_{e-S} < 10^{-2}$ meV, see equation 1.22), the large damping factors may rather be ascribed to the presence of defects in the metal (usually important for lithographed nano-objects), responsible for a scattering term γ_{e-d} in equation 1.19 (chapter 1).

From FEM simulations, we also determined the sensitivity of the extinction spectra of NDs to changes in the gold dielectric function $\varepsilon = \varepsilon_1 + i\varepsilon_2$, which is an essential ingredient to analyze the effect of ND heating on its optical response, as will be discussed later on. This sensitivity is quantified by $\partial\sigma_{ext}/\partial\varepsilon_1$ and $\partial\sigma_{ext}/\partial\varepsilon_2$ partial derivatives. To do so, new spectra are computed after numerically applying a small uniform variation (typically 10^{-3}) on the $\varepsilon_1(\lambda)$ and $\varepsilon_2(\lambda)$ tables. Comparison of these modified spectra to the original one then allows to compute the quantities $\partial\sigma_{ext}/\partial\varepsilon_1$ and $\partial\sigma_{ext}/\partial\varepsilon_2$ by discrete derivation. These derivatives both present enhanced amplitudes in the LSPR domain but display different spectral shapes (figure 3.9 (c) and (d)), reflecting the fact that ε_1 and ε_2 mostly affect LSPR position and width, respectively.

Finally, FEM simulations enable to separate the contributions of absorption and scattering to the extinction cross-sections. As may be seen in figure 3.10, the importance of scattering is far from negligible in the experimental conditions, being equivalent to absorption in the spectrum of ND1 in the LSPR range, and even largely dominant for ND2. As discussed in section 1.2.1 (equation 1.35), the light power attenuation induced by the nano-object, and thus the SMS signal, is proportional to the nano-object extinction cross-section only if absorption largely dominates over scattering, which is not the case here. This makes an evaluation of the fraction of scattered light that is recollected by the objective necessary. This evaluation using refined FEM calculations will be discussed in the last paragraph of this section.

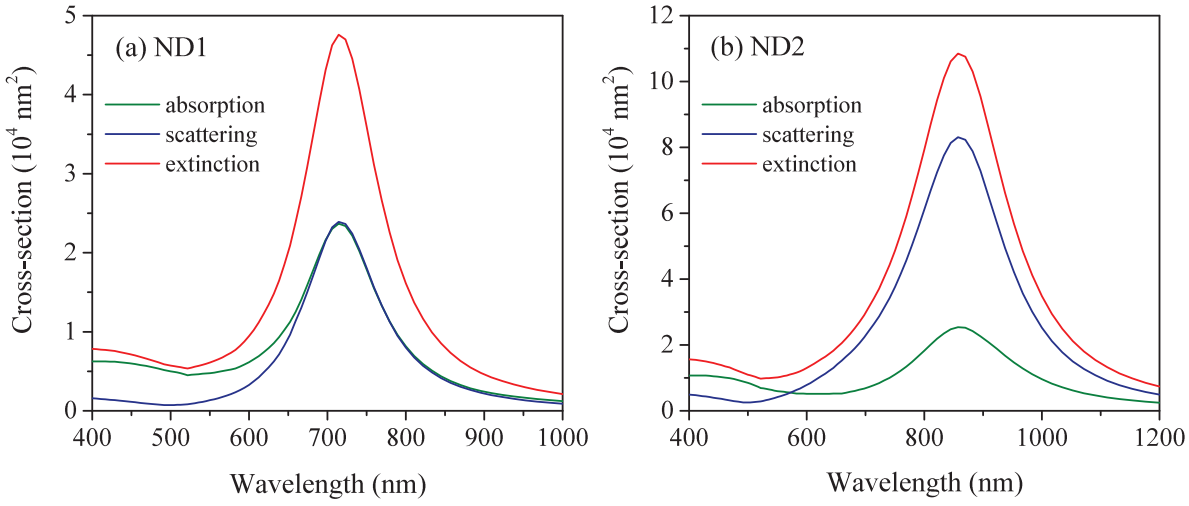

Figure 3.10 – FEM-calculated absorption, scattering and extinction cross-section spectra for ND1 and ND2.

3.2.3 Time-resolved measurements of ND cooling dynamics

3.2.3.a Signal acquisition procedures

Time-resolved measurements on individual NDs were performed by combining the SMS microscope with a two-color pump–probe setup based on the femtosecond laser source described in section 2.2. The oscillator pulse train was split in two parts to generate the pump and probe beams. The pump beam was produced using second harmonic generation (yielding λ_{pp} in the 375–520 nm range), while the probe beam was either the signal from the Ti:Sapphire oscillator (with λ_{pr} = 690–1040 nm in this case) or the output of the optical parametric oscillator (λ_{pr} = 500–750 nm). A mechanical chopper operating at 30 kHz was used to modulate the pump power. The relative changes of probe beam transmission, $\Delta Tr/Tr$, were measured using synchronous detection as a function of the time interval separating pump and probe pulses, controlled by a mechanical delay line.

SMS was used before pump-probe measurements to align the two laser beams together on the chosen ND. First, the ND is placed at the center of the pump beam (the probe beam being blocked) by maximizing the pump SMS signal with the XY piezo stage. The pump beam is then blocked and replaced by the probe beam, which is aligned using the micrometric adjustment screws of two injection mirrors controlling the beam angle and position. These mirrors are simultaneously adjusted so as to optimize the probe SMS signal, while verifying the beam correct injection using its back-reflection on the sample, detected by the CCD camera. Following this operation, the two beams are axially superimposed and centered on the ND. However, because of chromatic aberrations induced by the objective, their focal planes do not necessarily coincide. The objective's vertical position z is set by maximizing pump-probe signal, which usually corresponds to an intermediate position of the ND between the focal planes of the pump and probe beams. During the measurements, instability of the XY piezo stage typically caused a gradual shift of the sample. Frequent realignments were thus performed so as to maintain the pump and probe beams centered on the investigated ND.

Pump-probe signals were acquired with a 4 ps time step and a 100 ms lock-in time constant. The length of the translation stage (15 cm), associated with the multiple passes of the probe beam into the stage (3 round trips), corresponds to a 3 ns time window[3]. The optical paths of pump and probe beams were set so that superposition of their pulses occurs at $\sim$ 300 ps after the beginning of the time window. This allows us to verify that the signal is always zero when the probe pulse precedes the pump pulse. Indeed, the contrary would indicate that heat dissipation is not completely achieved within the 12.5 ns separating pump pulses, resulting in cumulative heating of the nano-

[3]Investigations at shorter timescales will be discussed in chapter 4.

object. Such effect was however not observed in the investigated NDs at the low pump fluences used in the measurements, in agreement with the cooling dynamics measured in our NDs.

As the experiment required measuring signals with very low amplitudes, work was made to reduce the noise level. An important source of noise was found to be related to random movements of the pump and probe spots on the sample, caused by fluctuations of air density along the laser paths. Tubes and boxes were then added to protect the beams and mirrors from air movements (notably originating from the air conditioning system). A factor of ∼10 was gained on the noise level, yielding a value of about 5×10^{-6} standard deviation for all $\Delta Tr/Tr$ signals.

To increase the signal-to-noise (S/N) ratio, signals were averaged over multiple measurements, this ratio scaling as $\sqrt{n}$ with the number n of averaged traces. In our experiment, n was varied from 3 to 40 depending on the signal amplitude.

Pump and probe beam powers impact differently on the signal level. The relative probe beam transmission $\Delta Tr/Tr$ being independent of the probe power, the latter was simply tuned in a range corresponding to the linear response of the the avalanche photodiode. In contrast, the signal amplitude is proportional to the pump power[4]. However, permanent modifications of the signals were noted for excessive pump fluences, as will be discussed in paragraph 3.2.3.d. For this reason, we typically used pump fluences leading to a moderate ($\lesssim$ 15 K) increase of the ND temperature following internal thermalization.

3.2.3.b Determination of pump and probe beam characteristics

The time-averaged pump power P_{pp} was determined in several steps. A powermeter equipped with a thin sensor head that may be placed directly after the focusing objective was used to assess directly the power on the sample. However, because the used pump powers were weak (a few microwatt), the power was first measured before the objective, and then converted using the transmission coefficient determined systematically from measurements on both sides of the objective at a higher power. Because of the large section of the beam shining the entrance pupil of the objective (see section 2.1.2.a), this coefficient showed important variations depending on the beam wavelength and alignment, with values ranging from 10 to 60%.

As was noted in section 2, SMS enables the accurate determination of the laser beam section in the plane of the studied nano-object, provided the latter is small enough with respect to the wavelength. This feature was exploited in pump-probe measurements to determine the probe and pump beam equivalent areas S_{pr} and S_{pp} on the surface of the

[4]Strict proportionality was verified over a wide range of pump fluences for the signal after ∼20 ps, *i.e.* after the internal thermalization of the ND. Directly after pump pulse absorption, the signal is nonlinear with the absorbed power, as will be discussed in chapter 4.

sample, defined as $S_{pp,pr} = \pi\, d_{pp,pr}^2/(4\ln 2)$, where $d_{pp,pr}$ is the FWHM of the pump or probe beam intensity profile. SMS maps of NDs illuminated with pump and probe beams were acquired systematically following each time-resolved measurement. This procedure allowed to determine the beam sections in the plane where pump-probe measurements were performed, which is especially important in cases where the two beam waists cannot be made to coincide (despite acting on the beams' divergence/convergence)[5].

Such systematic measurements of parameters P_{pp}, S_{pp} and S_{pr} are required, as they are needed in the quantitative analysis of the experiments. As explained in section 2.2, S_{pr} is necessary to convert raw time-resolved signals into extinction cross-section changes, via $\Delta Tr/Tr = -\Delta\sigma_{ext}(\lambda_{pr})/S_{pr}$. The other two parameters, S_{pp} and P_{pp}, appear in the expressions of the deposited pump energy and of the nano-object temperature increase, which are determined as follows. We first calculate the pump fluence F_{pp}, defined as the surface density of energy of a single pulse:

$$F_{pp} = \frac{T_{rep}\ P_{pp}}{S_{pp}} \tag{3.10}$$

where $T_{rep} = 1/(80\ \text{MHz}) = 12.5$ ns is the laser repetition time. We then estimate the volumetric density of energy absorbed by a ND for each pump pulse, which writes:

$$u_{abs} = \frac{\sigma_{abs}(\lambda_{pp})F_{pp}}{V} \tag{3.11}$$

with $\sigma_{abs}(\lambda_{pp})$ the ND absorption cross-section at the pump wavelength, and V the ND volume. Finally, the ND initial temperature increase (after thermalization) is evaluated through $u_{abs} = c_{Au}\ (T_{eq} - T_0) = c_{Au}\ \Delta T_{eq}$, with c_{Au} the volumetric heat capacity of bulk gold ($c_{Au} = 2.5\ \text{J}\,\text{cm}^{-3}\,\text{K}^{-1}$), yielding:

$$\Delta T_{eq} = \frac{\sigma_{abs}(\lambda_{pp})T_{rep}P_{pp}}{c_{Au}V\,S_{pp}} \tag{3.12}$$

V and $\sigma_{abs}(\lambda_{pp})$ are obtained from optical FEM calculations. Specifically, V corresponds to the values of D and h used in the simulation to achieve an optimal reproduction of the experimental extinction spectrum. FEM simulations also allow to separate the contributions of absorption and scattering to extinction (see paragraph 1.2.4), and thus to estimate $\sigma_{abs}(\lambda_{pp})$. For pump powers in the microwatt range, the determined energy

[5] In such cases, the measured beam sections can extend up to twice the section at the focal plane, which results in both decreased heating and decreased sensitivity to extinction changes (see following).

densities u_{abs} were of the order of a few J cm^{-3} and the temperature increases of a few K.

3.2.3.c Signal processing

Figure 3.11 shows a typical time-resolved signal along with the steps of processing permitting to extract the thermal part. The different structures discussed in section 2.2 of chapter 2 are clearly visible: a high peak directly following pump absorption corresponding to the non-equilibrium electron excitation, followed by a slow decay of the signal with a nanosecond timescale (linked to ND cooling) accompanied by damped oscillations related to vibrational modes. The initial peak is taken as origin for the time axis, as it roughly corresponds to the instant of pulse superposition, given the large 4 ps time step. Only the signal at pump-probe delays exceeding 10–20 ps (*i.e.* after complete internal thermalization) is considered in the following. This signal is fitted by the sum of a biexponential decay reflecting the ND cooling dynamics and of damped sinusoids, each corresponding to the contribution of a different detected vibrational mode, with period T_n, phase ϕ_n and damping time τ_n^{osc}:

$$f_{fit}(t) = A_1\ e^{-t/\tau_1} + A_2\ e^{-t/\tau_2} + \sum_{n=1}^{N} B_n\ e^{-t/\tau_n^{osc}} \sin\left(\frac{2\pi}{T_n}t + \phi_n\right)\ . \tag{3.13}$$

In this expression, time constants τ_1 and τ_2 from the exponential decays are defined so that $\tau_1 > \tau_2$. Depending on the considered signal, the number N of damped sinusoids included in the fit was chosen between 0 and 3, the amplitudes of the detected vibrational modes being very dependent on the probe wavelength and on ND morphology. The periods T_n are found between 30–200 ps (frequencies in the GHz range), while the damping time constants τ_n^{osc} are in the nanosecond range. In a previous work by Medeghini et al. [12], the vibrational parts of the time-resolved signals of many NDs from sample S2 and another sample similar to S1 have been studied. The measured oscillation frequencies were found in excellent agreement with the predictions from an acoustic FEM model, while the quality factors showed a strong enhancement around a particular D/h aspect ratio (≈ 2.5), which was also predicted by the model.

In the context of thermal measurements, oscillations are an undesirable feature of time-resolved signals as they complicate the extraction of the component associated to the cooling dynamics. In the experiment that will be described in section 3.3, where the probe wavelength was varied over the whole LSPR range, NDs were carefully chosen so that no beating pattern linked to vibrational modes with close frequencies was visible in the signals, in order to ease the fitting process. In the experiment of section 3.4, where

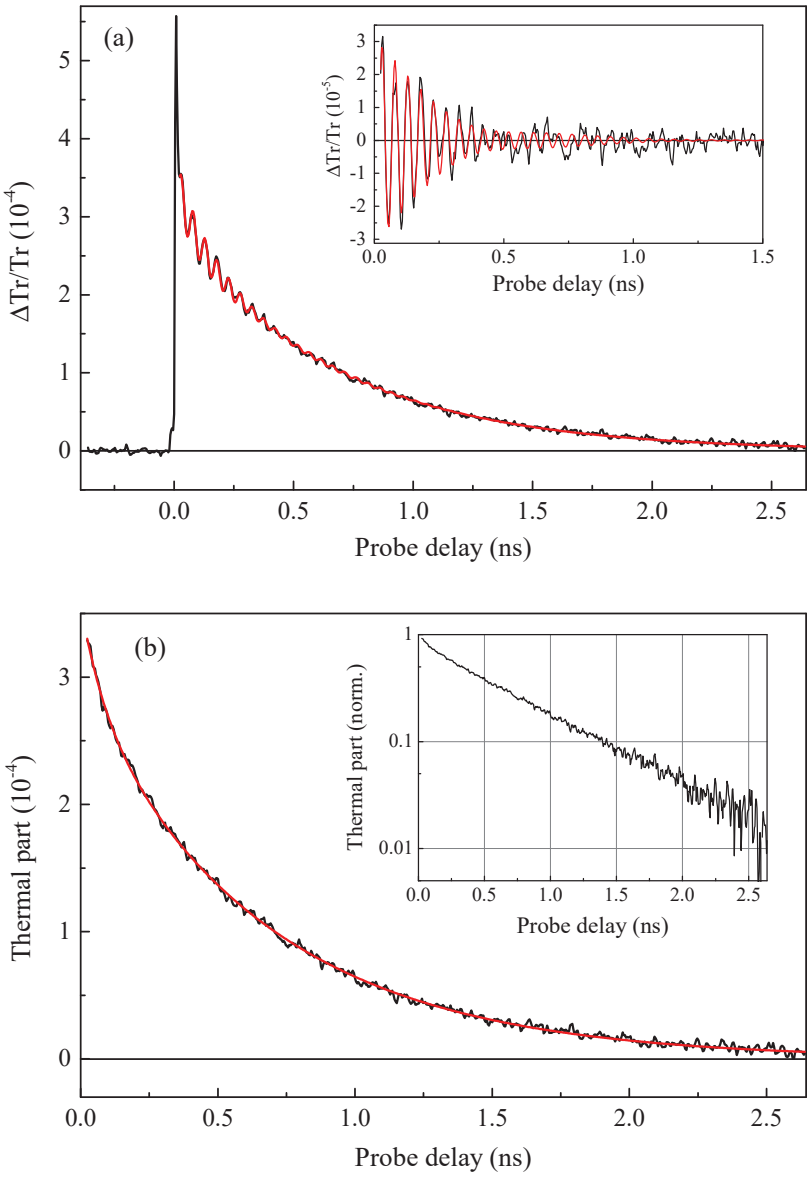

Figure 3.11 – Fitting method of experimental pump-probe signals. (a) Transient variations of the transmission change, $\Delta Tr/Tr(t)$, measured using $\lambda_{pp} = 410$ nm and $\lambda_{pr} = 690$ nm pump and probe wavelengths for a ND with $h = 18$ nm, $D \approx 100$ nm (black line). The red line is a fit of the signal after $t = 20$ ps (*i.e.* after the ND internal thermalization) with the function defined in equation 3.13. Inset: the same signal to which the two decaying exponentials from the complete fit were substracted (thus isolating the contribution of acoustic vibrations) (black) and its fit by a sum of two damped sinusoids with periods ~ 49 and 52 ps. (b) Same signals as in (a) to which the oscillatory part of the fit was substracted (thus isolating the contribution of the ND cooling to the signal) (black) and its biexponential fit (red). The normalized thermal signal is shown in the inset in semi-log scale.

the cooling dynamics of multiple NDs were studied, the probe wavelength was chosen away from the LSPR to minimize the oscillation amplitudes.

The so-called thermal part is obtained by subtracting to the signal the sum of the damped sinusoidal functions defined from the complete fit $f_{fit}(t)$. It is naturally well reproduced by the remaining sum of two damped exponentials, whose amplitudes $A_{1,2}$ and decay times $\tau_{1,2}$ may be used to characterize the signal dynamics. However, because of the uncertainties attached to these fitting parameters, it is useful to visualize the experimental signals normalized to their initial values (in linear or semi-log scale), especially when comparing the dynamics of two different signals.

3.2.3.d Irreversible changes of the cooling dynamics at high pump fluence

In the transient signal shown in figure 3.11, the thermal component (inset of (b)) presents a quasi mono-exponential decay over the whole investigated range of pump–probe delays (up to 2.5 ns). More generally, mono-exponential decays were observed at long timescales (> 500 ps) for all signals, but deviations from a mono-exponential behavior were observed at shorter timescales for some of the investigated NDs (in particular in the case of excitation with high pump fluence, as discussed below). All thermal components could however be accurately reproduced using a biexponential decay function $A_1 \exp(-t/\tau_1) + A_2 \exp(-t/\tau_2)$, with $A_1 > A_2$ amplitudes and characteristic times of the order of $\tau_1 \sim 700$ ps and $\tau_2 \sim 100$ ps in the case of $h = 18$ nm NDs, and $\tau_1 \sim 1800$ ps and $\tau_2 \sim 200$ ps for $h = 40$ nm NDs. Interpretation of the morphological dependence of τ_1 and τ_2 will be the object of section 3.4 of this chapter.

The experiments demonstrated a correlation between the biexponential character of the cooling dynamics (which can be quantified by the $A_2/(A_1 + A_2)$ ratio involving the parameters of the biexponential fit) and the history of exposition of the ND to high pump fluences. Figure 3.12 presents a series of signals measured on a large ($h = 40$ nm, $D = 150$ nm) ND, referred to as ND3, at successive pump fluences. Parameters from the biexponential fits of these measurements are reported in table 3.2. The first measurement, performed at low fluence ($F_{pp} = 0.4$ J m^{-2}), resulted in nearly exponential dynamics with $A_2/(A_1 + A_2) \sim 19\%$. After the fluence was increased to 2.3 Jm^{-2}, the signal underwent a rapid change until it stabilized after a few minutes. The signal then recorded showed an increased value of $A_2/(A_1 + A_2)$ (reaching 38%) as well as a 15% increase of the longer time constant τ_1 (measurement 2 in figure 3.12). Those changes were preserved when returning to low fluence (measurement 3), thus evidencing the irreversibility of the process. Finally, a low-power measurement was made on a similar ND ('ND4') immediately after the latter one, in order to exclude the possibility that the change resulted from a modification of the conditions (in particular, alignments and

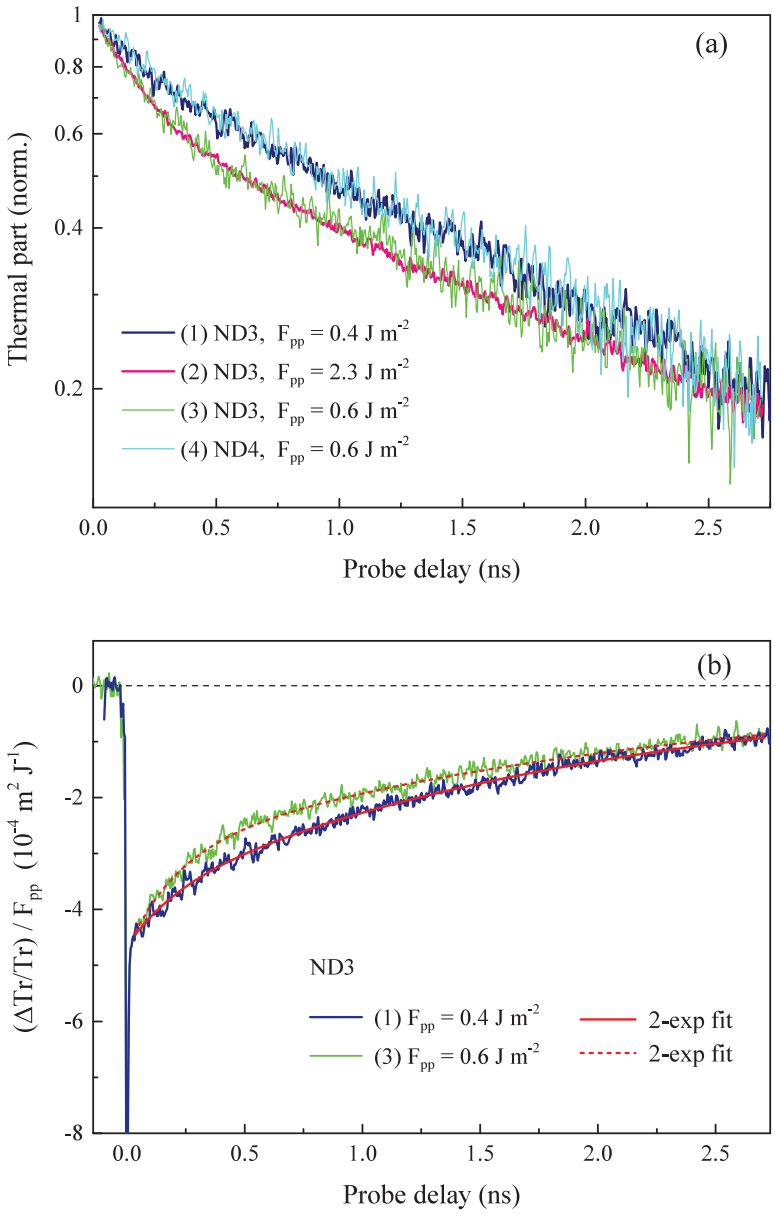

Figure 3.12 – Pump fluence-induced modifications of the thermal dynamics of gold NDs. a) Normalized thermal components of the transient optical responses of two NDs with same thicknesses and diameters $h \approx 40$ nm and $D \approx 150$ nm, called ND3 and ND4, successively measured at different pump fluences in the order indicated in the legend (with $\lambda_{pp} = 410$ nm and $\lambda_{pr} = 510$ nm). Measurement 1, performed at low fluence on ND3, results in a quasi-exponential cooling dynamics. Excessive pump fluence induces a clear change in the dynamics of thermal decay of ND3 (measurement 2), which is irreversible (measurement 3, at low power). Measurement 4 was performed on ND4 in the exact same conditions of beam alignments and powers as measurement 3, resulting in a quasi-exponential thermal signal similar to measurement 1. b) Complete raw signals for ND3 at low power before and after exposition to high pump fluence (corresponding to measurements 1 and 3 in graph (a)) divided by their respective pump fluences to facilitate their comparison. Oscillations were weak for those signals and were not subtracted. Results from fitting by a sum of two damped exponentials are also shown.

powers of the two beams). The resulting signal (measurement 4 in figure 3.12) superposes perfectly–after normalization–to the first measurement of ND3, confirming that the change of dynamics observed in the optical signals reflects an actual change in the nano-object's cooling dynamics rather than a measurement artefact. This result also suggests that similar NDs from our samples share the same quasi-exponential dynamics as long as they are not exposed to excessive light intensities.

#	ND	F_{pp} ($\mathrm{Jm^{-2}}$)	$A_2/(A_1+A_2)$ (%)	τ_1 (ns)	τ_2 (ns)
1	ND3	0.4	18.7	1.92	0.19
2	ND3	2.3	38.5	2.21	0.23
3	ND3	0.6	36.2	2.18	0.21
4	ND4	0.6	17.9	1.91	0.22

Table 3.2 – Parameters from the biexponential fits of the measurements performed on ND3 and ND4. The parameters are defined in equation 3.13.

A similar test was also performed on a ND of much smaller dimensions ($h = 18$ nm, $D \approx 100$ nm), referred to as ND5[6]. Results are presented in figure 3.13. A first measurement was performed with a pump fluence $F_{pp} = 1\ \mathrm{J\,m^{-2}}$, followed by a second one with $F_{pp} = 2.7\ \mathrm{J\,m^{-2}}$, and then by a return to the initial fluence. As was seen with the larger ND, irreversible changes of the dynamics were observed after exposure to high fluence, though the lower amplitude of the signal as well as the much faster cooling dynamics prevented precise comparison of the signals on a long timescale. Indeed, for the measurement performed at low power, the low signal to noise ratio resulting from the small amplitude could not be compensated by a larger number of acquisitions, since the exposition time proved to be another factor causing modifications of the signal.

Additionally, extinction spectra of ND5 were taken before and after the pump-probe measurements (figure 3.13b), demonstrating permanent modifications after exposure to the $2.7\ \mathrm{J\,m^2}$ fluence, with the LSPR of the second spectrum being red-shifted and presenting a larger maximal amplitude. As we discussed in section 1.2 of the first chapter, these modifications may *a priori* result from changes either in the ND or its local environment.

In the two former experiments, the temperature increases corresponding to the highest values of the fluence were estimated to 27 K for ND3 and 40 K for ND5. Therefore, the observed changes may not be explained by melting of the metal. For example, Plech *et al.* [73] found the first changes attributed to pre-melting—monitored by X-ray diffraction—to occur only beyond 500 K lattice heating for gold nanoparticles of similar dimensions, while complete melting occured near the melting point of bulk gold (1337 K). Furthermore, no chemical reaction modifying the properties of the ND or its

[6] ND5 was made with the same nanofabrication parameters as ND1, whose dimensions are reported in table 3.1.

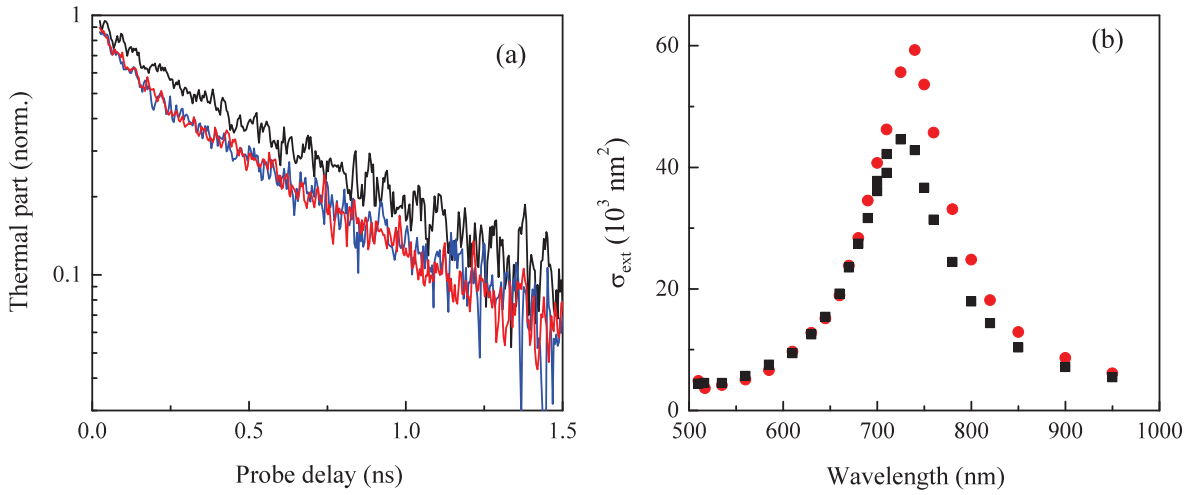

Figure 3.13 – Pump fluence effect on the cooling dynamics and extinction spectrum of a ND with $D \approx 100$ nm and $h = 18$ nm (ND5). a) Thermal component of the transient optical responses successively measured on ND5 using $\lambda_{pp} = 410$ nm, $\lambda_{pr} = 515$ nm and pump fluences of $F_{pp} = 1\ \mathrm{J\,m^{-2}}$ (black line), $2.7\ \mathrm{J\,m^{-2}}$ (red line) and $1\ \mathrm{J\,m^{-2}}$ again (blue line). After exposure to the higher fluence, the ratio $A_2/(A_1 + A_2)$ from the biexponential fit of the signal decay changed permanently from 18% to 36%. b) SMS-measured extinction spectra of ND5 before (black squares) and after (red circles) the pump–probe measurement at high pump fluence.

local environment is *a priori* expected, as both gold and sapphire are chemically stable. An attempt to clarify the mechanisms underlying this effect will be discussed at the end of this chapter. In the following studies, only ΔT_{eq} values below ∼15 K were considered, so as to avoid modification of ND linear and ultrafast optical responses during the course of the experiments.

3.3 Probe-wavelength dependence of ultrafast thermal signals

3.3.1 Experimental results

3.3.1.a Effect of probe wavelength on time-resolved signals

The effect of probe wavelength on the time-resolved signals measured on ND1 and ND2 is illustrated in figures 3.14 and 3.15. In our experimental setup based on a Ti:sapphire oscillator, either frequency-doubled or driving an optical parametric oscillator (see section 2.2), the wavelengths of the pump and probe beams cannot be chosen fully independently; therefore the parameters of these beams, and in particular the pump fluence on the sample, could not be kept constant throughout this series of experiments. In order

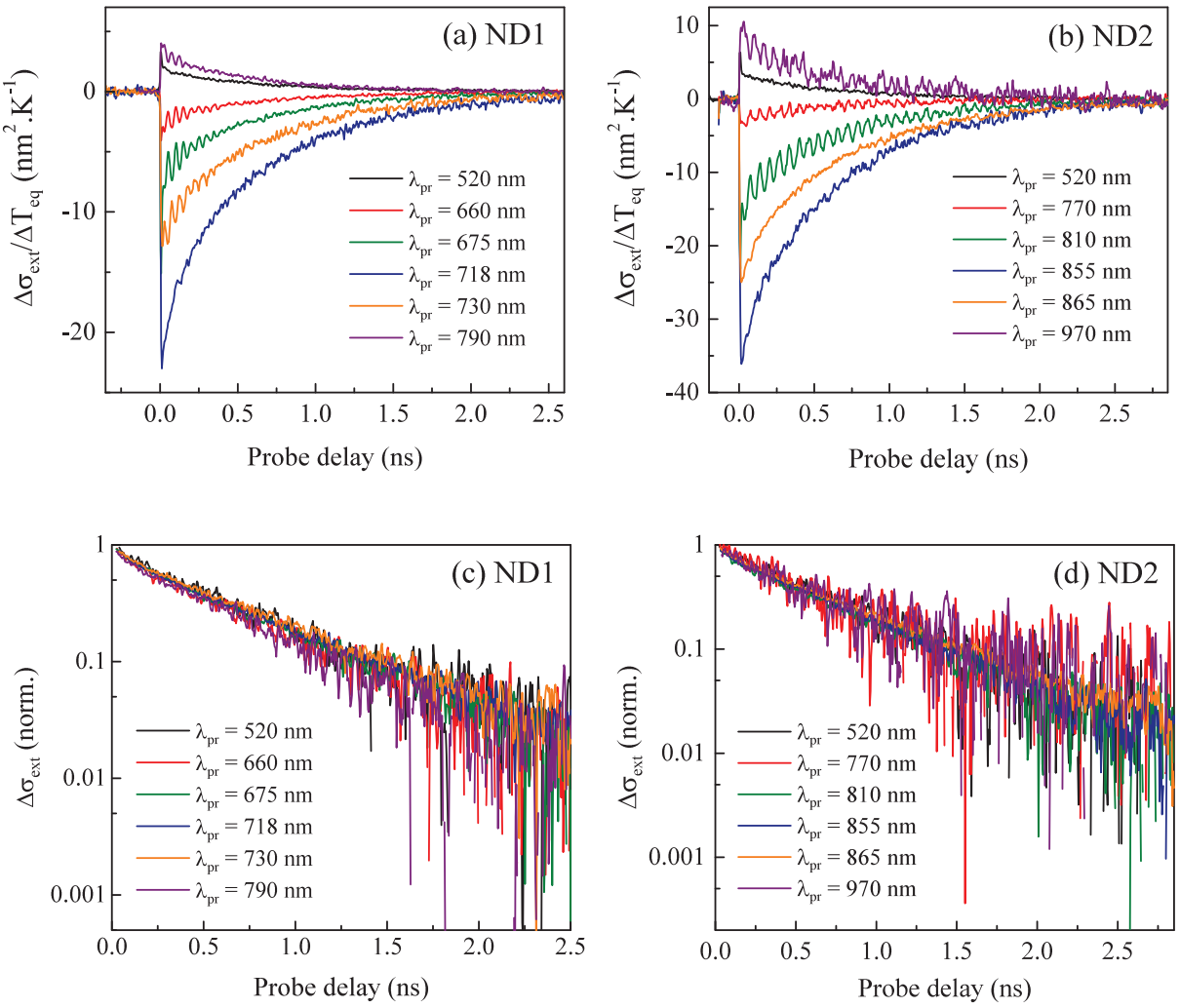

Figure 3.14 – Influence of probe wavelength on the measured time-resolved signals of two gold NDs. (a,b) Raw time-resolved signals measured on ND1 and ND2 with the indicated probe wavelengths (with $\lambda_{pp} = 410$ nm for all signals with $\lambda_{pr} < 750$ nm, and $\lambda_{pp} = \lambda_{pr}/2$ when $\lambda_{pr} > 750$ nm), divided by the estimated initial ND temperature rise ΔT_{eq}. (c,d) Normalized thermal components of the same signals (in semi-logarithmic scale).

to isolate the effect of probe wavelength from that of pump excitation, the measured transient extinction cross-section changes $\Delta\sigma_{ext}$ were divided by the estimated initial temperature rise ΔT_{eq}, with $\Delta T_{eq} \sim 10$ K for the $F_{pp} \sim 0.7$ J/m^2 typical pump beam fluence used in these experiments. Figure 3.14 shows that the probe wavelength considerably affects the amplitude of time-resolved signals, but weakly their temporal dynamics. Figures 3.14a–b allow one to appreciate their variations of sign and amplitude in the spectral range of the ND LSPRs, while figures 3.14c–d demonstrate that the thermal components of all signals (obtained by subtraction of the vibrational part of the fits) overlap once normalized by their initial values.

In paragraph 3.1.2.b, we mentioned the possibility for time-resolved signals to be affected by the temperature changes in the vicinity of the nano-object, strongly impacting for instance the signals associated to NPs immersed in ethanol [14, 17]. In the present study, the similarities of the signal shapes measured using a large number of probe wavelengths and the monotonous decay of $|\Delta\sigma_{ext}|$ as a function of time demonstrated by figures 3.14c–d imply that sapphire substrate heating has a negligible influence on the measured signals. This can be ascribed to the weak sensitivity of the dielectric function of sapphire to temperature changes, with $\mathrm{d}\varepsilon_m/\mathrm{d}T \sim 4.10^{-5}$ K^{-1} in the visible range [96], to be compared to the 10^{-3} K^{-1} typical values of $|\mathrm{d}\varepsilon_1/\mathrm{d}T|$ and $|\mathrm{d}\varepsilon_2/\mathrm{d}T|$ for gold in the same spectral range [34, 97]. Additionally, the high thermal conductivity of sapphire (25 W m^{-1} K^{-1}) favors heat dissipation in the substrate away from the ND vicinity, and thus limits the temperature rise in this region.

3.3.1.b Signal amplitude dependence on probe wavelength

Since environment heating plays a negligible role in our time-resolved signals, expression of the heating-induced extinction cross-section changes (equation 3.7) reduces to the product of a probe wavelength-dependent amplitude $A_p(\lambda_{pr})$ and of the time-dependent ND temperature increase $\Delta T_p(t)$:

$$\Delta\sigma_{ext}(\lambda_{pr}, t) = A_p(\lambda_{pr})\Delta T_p(t) \tag{3.14}$$

The decay dynamics of $\Delta T_p(t)$ will be the object of section 3.4 of this chapter. In the following of this section, we discuss the wavelength-dependence of amplitude A_p. From an experimental pump-probe signal, the A_p coefficient can be extracted as the ratio between the initial heating-induced extinction change and the estimated initial ND temperature rise $\Delta T_p(t = 0) = \Delta T_{eq}$. Practically, we used the sum $A_1 + A_2$ of the amplitudes of the two exponentials appearing in the fit of $\Delta Tr/Tr(t)$ (equation 3.13), as it corresponds to an extrapolation at $t = 0$ of the thermal signal $\Delta\sigma_{ext}^{th}$ (which is well-defined only for

pump-probe delays $t > 10$–20 ps, after the ND internal thermalization), and gives a more reliable result than averaging the signal in this zone.

A_p thus writes, as a function of the experimental parameters (see equations 2.15 and 3.12):

$$\begin{aligned} A_p &= \frac{\Delta\sigma_{ext}^{th}(t=0)}{\Delta T_{eq}} \\ &= [-S_{pr}(A_1+A_2)] \cdot \left[\frac{\sigma_{abs}(\lambda_{pp})\ F_{pp}}{c_{Au}\ V}\right]^{-1} \\ &= -\frac{c_{Au}\ V\ S_{pr}\ S_{pp}}{T_{rep}\ P_{pp}\ \sigma_{abs}(\lambda_{pp})}(A_1+A_2)\ . \end{aligned} \tag{3.15}$$

The A_p spectra of ND1 and ND2 retrieved from time-resolved measurements are shown in figure 3.15. Their spectral shapes resemble that of the $\partial\sigma_{ext}/\partial\varepsilon_2$ derivatives shown in figure 3.9 c and d, respectively: they display large and negative values near the central position of the LSPR (dashed green lines in figure 3.15 a and b) and smaller, positive values on the LSPR sides.

Calculation of the error bars represented on the two graphs of figure 3.15 was based on equation 3.15. The relative error of A_p is the quadratic sum of the relative errors of all the terms in the product (only the non-systematic sources of error were considered, see discussion below):

$$\frac{\Delta A_p}{A_p} = \left(\left(2\frac{\Delta d_{pr}}{d_{pr}}\right)^2 + \left(2\frac{\Delta d_{pp}}{d_{pp}}\right)^2 + \left(\frac{\Delta P_{pp}}{P_{pp}}\right)^2 + \left(\frac{\Delta(A_1+A_2)}{A_1+A_2}\right)^2\right)^{\frac{1}{2}}\ , \tag{3.16}$$

the notation ΔX for any quantity X here representing the 95% confidence level.

In expression 3.16, uncertainties on the pump and probe beams FWHM were evaluated from the dispersion of values derived from SMS cartographic measurements, and that on P_{pp} from the error associated to the used powermeter. The uncertainty on $(A_1 + A_2)$, originating both from the signal noise and the presence of oscillations, was empirically evaluated. Error due to the possibility of accidental misalignment of pump and probe beams was not taken into account. In most cases, the main contributions to A_p error bars originate from evaluations of d_{pp} and d_{pr}, except near cancellations of A_p, where the error linked to the retrieval of the $(A_1 + A_2)$ amplitude becomes predominant because of the decreased S/N ratio.

The former calculation only takes into account the non-systematic sources of error, evaluated from the quantities' experimental dispersion around a central value. However, the method used for retrieving laser spot sizes from SMS maps, which is based on the

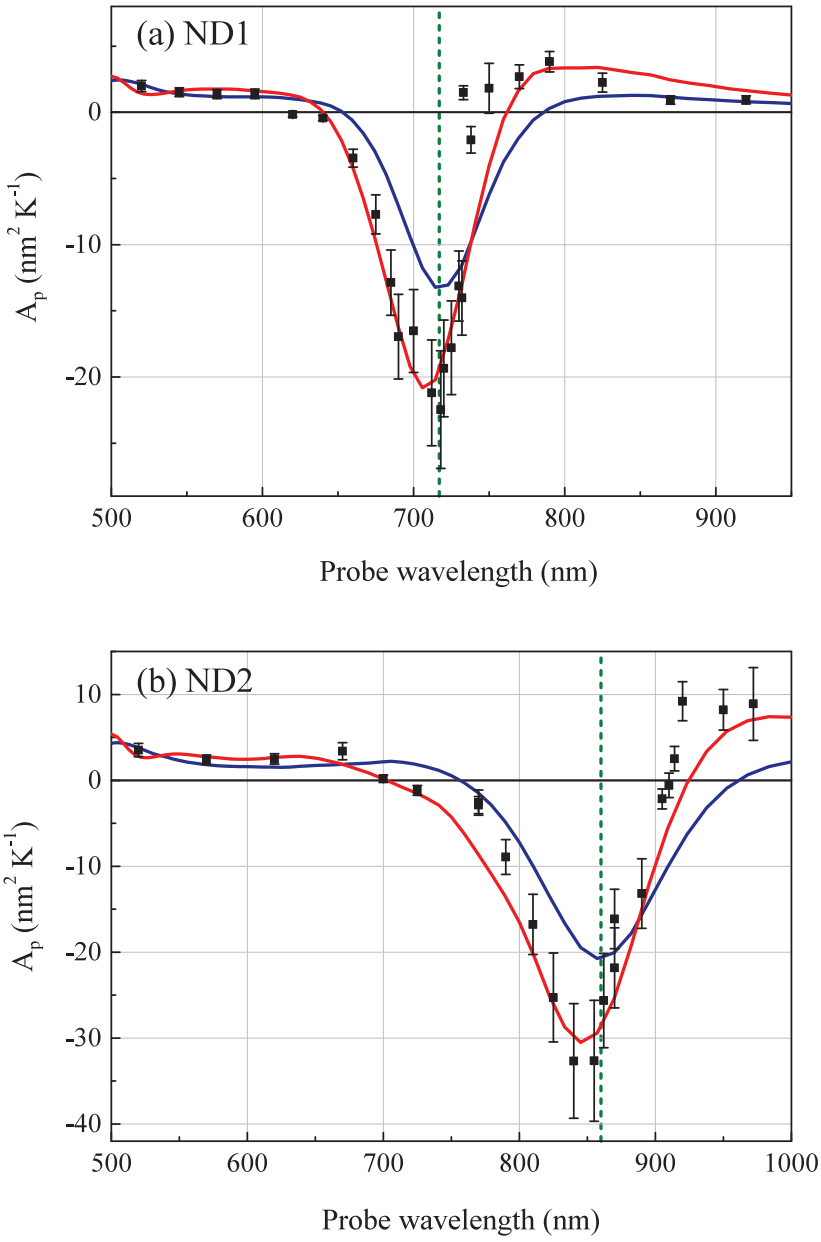

Figure 3.15 – Sensitivity of time-resolved spectroscopy to ND temperature changes as a function of probe wavelength, measured on ND1 (a) and ND2 (b). Black dots represent the A_p coefficients deduced from the amplitude of the thermal components of experimental time-resolved signals (equation 3.15). Error bars only include the non-systematic sources of error, as discussed in the main text. The blue and red lines are calculations of A_p based on equation 3.8 using the $\partial\sigma_{ext}/\partial\varepsilon_{1,2}$ spectra deduced from FEM calculations (figure 3.9) and $\mathrm{d}\varepsilon_{1,2}/\mathrm{d}T$ values taken either from ref. [97] (solid blue lines) or [34] (dashed red lines). The dashed green lines indicate the respective central positions of the ND LSPRs.

assumption of illumination by an Airy-distributed spot, may potentially represent an important source of systematic error, as it not only influences the values of S_{pp} and S_{pr} (appearing explicitely in the expression of A_p), but also—through the conversion of SMS signal—the amplitudes of the measured extinction spectra, and thus the FEM-determined V and σ_{abs}. Note however that the latter two quantities must not be treated as independent parameters, as they show correlated variations. One must instead consider the error for the σ_{abs}/V ratio (appearing in expression 3.15), which is much smaller than the quadratic sum of σ_{abs} and V relative errors. From these considerations, we estimate that an additional $\sim 10\%$ uncertainty must be assumed for the overall amplitude of A_p, which does however not affect its spectral shape.

3.3.2 Comparison to a numerical model

3.3.2.a Calculation of A_p and A_m

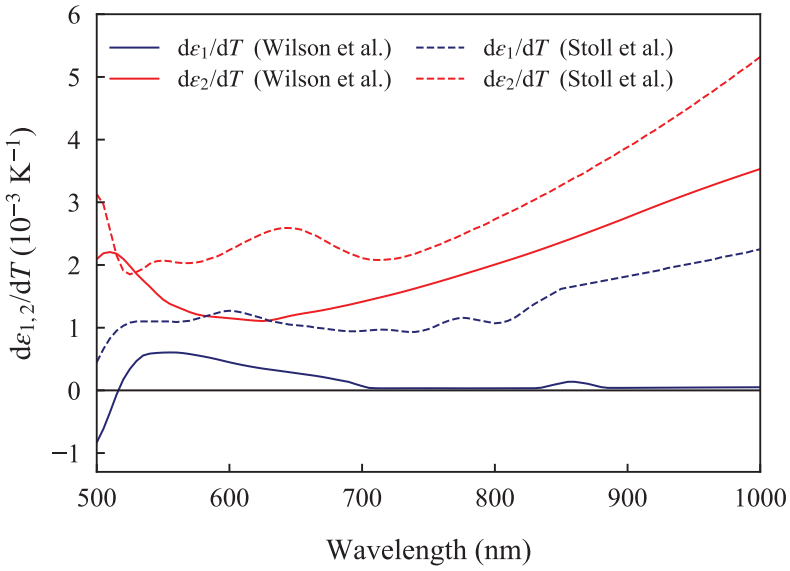

Figure 3.16 – $\mathrm{d}\varepsilon_{1,2}/\mathrm{d}T$ **derivatives from refs. [97] (continuous lines) and [34] (dashed lines).**

A_p can also be theoretically estimated from equation 3.8, which requires knowledge of $\partial\sigma_{ext}/\partial\varepsilon_{1,2}$ and $\mathrm{d}\varepsilon_{1,2}/\mathrm{d}T$ derivatives for the investigated gold ND. The determination of $\partial\sigma_{ext}/\partial\varepsilon_{1,2}$ (figure 3.9 c and d) from optical FEM computations has been presented above. The temperature dependence of gold dielectric function has been the object of multiple recent measurements and models [34, 97–102]. The thermal derivatives $\mathrm{d}\varepsilon_{1,2}/\mathrm{d}T$ extracted from these measurements strongly depend on the type of gold sample used (continuous or granular, annealed or not, deposited thickness) and on temperature. As a result, the values of the $\mathrm{d}\varepsilon_{1,2}/\mathrm{d}T$ coefficients of gold reported in the

literature are dispersed, in particular for the $d\varepsilon_1/dT$ derivative, as ε_1 presents large values but weak relative changes with temperature in the visible range. To evaluate the impact of these uncertainties on A_p spectra, two different $d\varepsilon_{1,2}/dT$ tables were used for computing A_p (figure 3.15): one experimentally determined by Wilson and Cahill [97], and one theoretically estimated from the expected temperature dependences of Drude and interband components of gold dielectric function, as discussed in ref. [34] (see figure 6 of this reference)[7]. Values of $d\varepsilon_{1,2}/dT$ from these two sources, which are plotted in figure 3.16, present significant differences in the red/near infrared range relevant to the present experiments. For instance, at 800 nm wavelength, the former table yield $d\varepsilon_1/dT \sim 3.10^{-5}$ K^{-1} and $d\varepsilon_2/dT \sim 2.10^{-3}$ K^{-1}, while the latter one corresponds to $d\varepsilon_1/dT \sim 1.10^{-3}$ K^{-1} and $d\varepsilon_2/dT \sim 3.10^{-3}$ K^{-1} (figure 3.16). As a result, the computed A_p spectra differ depending on the chosen table. However, for both NDs, the two versions present spectral variations in good agreement with the experimental results, close to those of the $\partial\sigma_{ext}/\partial\varepsilon_2$ derivative (figure 3.9 c and d) which results from the fact that $|d\varepsilon_2/dT| > |d\varepsilon_1/dT|$ in the investigated spectral range for both considered $d\varepsilon_{1,2}/dT$ tables (see equation 3.8 and figure 3.16). The measured and computed A_p amplitudes, which have maximal values of a few tens of nm^2 K^{-1}, also show a good quantitative agreement, considering the high number of parameters involved in the analysis and the large uncertainties affecting $d\varepsilon_{1,2}/dT$ coefficients[8].

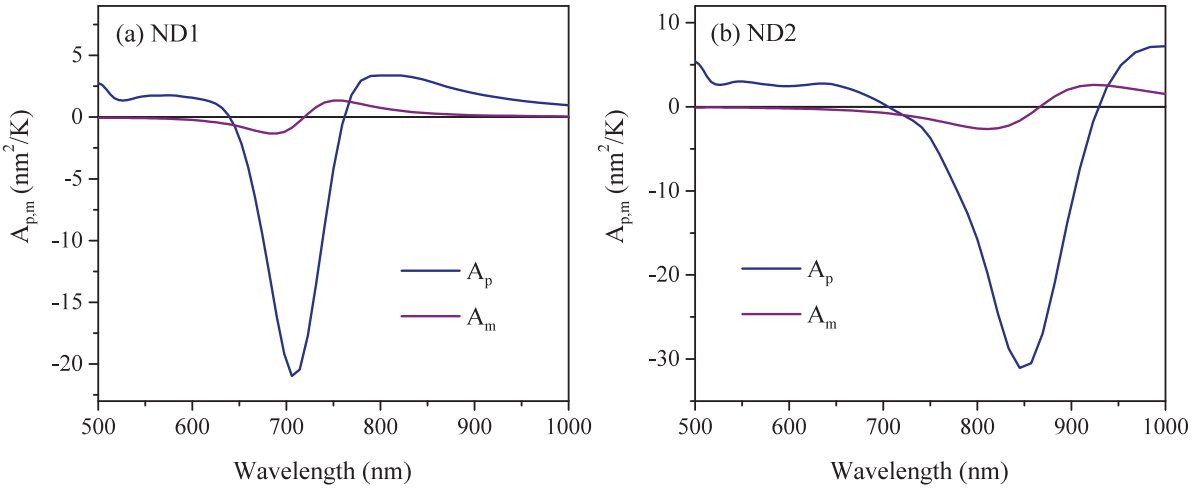

Figure 3.17 – Sensitivities of time-resolved measurements to temperature changes in the ND (A_p) and its environment (A_m) for ND1 and ND2. A_m is computed by assuming a homogeneous temperature change in the sapphire substrate.

[7] The construction method for these tables will also be shortly described in chapter 4, section 4.1.2.b of this work.

[8] Although the agreement is correct for both $d\varepsilon_{1,2}/dT$ tables, a closer match is found with the tables from ref. [34], either in the amplitudes and the positions of A_p cancellations. These tables will therefore be taken as reference in chapter 4.

Finally, the same FEM model was also used to evaluate the A_m amplitude appearing in equation 3.9, which describes the sensitivity of time-resolved signals to changes in the environment temperature T_m, which must be assumed homogeneous at all times. A_m was calculated from equation 3.9, where the plasmonic derivative $\partial\sigma_{ext}/\partial\varepsilon_m$ was computed by FEM (by applying a small variation on the dielectric function of sapphire), and where we took a 4×10^{-5} K^{-1} value for the $\mathrm{d}\varepsilon_m/\mathrm{d}T_m$ derivative, independent of the wavelength [96]. The computed A_m spectra for ND1 and ND2 are shown in figure 3.17, and compared to their A_p counterparts. Except in restricted zones located around cancellations of A_p, one verifies that $|A_m| \ll |A_p|$ for most probe wavelengths. This observation, added to the fact that the temperature elevation in the substrate is small as compared to that of the ND (as confirmed by thermal FEM calculations described in the next section), *a posteriori* validates the approximation made when writing the transient ND extinction change $\Delta\sigma_{ext}$ as the product of A_p and ΔT_p (equation 3.14). While this approximation had already found an experimental confirmation in the similar dynamics of the thermal parts of all signals (paragraph 3.3.1.a), the above considerations provide a complementary demonstration of its validity.

3.3.2.b Analysis refinement: effects of the partial collection of scattered light in optical measurements

Up to now, we have implicitely assumed that the physical quantity measured in the context of SMS and time-resolved experiments is the nano-object extinction cross-section in the former case, or its transient changes in the latter case. This corresponds to neglecting the partial recollection of the light scattered by the nano-object in these measurements (see section 2.1). While this assumption is fully valid for small metal nano-objects, for which absorption largely predominates over scattering, it is *a priori* questionable for the gold NDs used in our study, as was shown precedently in figure 3.10 (section 3.2.2). Indeed, for ND1, the absorption and scattering spectra display equivalent amplitudes in the LSPR range, while scattering is even dominant over absorption for ND2. Therefore, complementary FEM analyses were performed to evaluate the fraction of the scattered light recollected in our experiments.

We used a simple approach combining considerations from geometrical optics and complete optical FEM calculations based on the model described in section 3.2.2. First, we determined the solid angle around the ND corresponding to the fraction of the light scattered by a ND able to enter the collection objective. The geometry of the extreme light rays collected the objective is sketched in figure 3.18a. In the present study, the collection objective has a numerical aperture NA = 0.75. In air, this corresponds to a half-angle of collection $\alpha = \arcsin(\mathrm{NA}) = 48.6°$, but in sapphire this corresponds to the light emitted within a cone of angle $\alpha' = \arcsin(\mathrm{NA}/n_{Al2O3}) = 25.2°$, according to

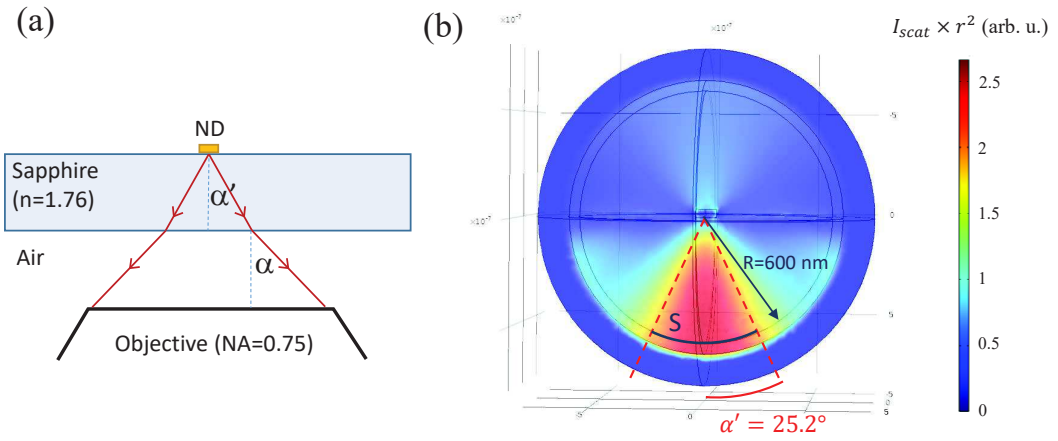

Figure 3.18 – Calculation of the ND scattering pattern and evaluation of the fraction of scattered light that is recollected in the experiments. (a) Schematics of the extreme light rays able to enter the collection objective, in an approach based on geometrical optics. Angles $\alpha = 48.6°$ and $\alpha' = 25.2°$ are found from the definition of the objective's numerical aperture and the Snell-Descartes law, respectively. (b) FEM calculation of the scattered light intensity of a ND illuminated by a $\lambda = 670$ nm plane wave propagating from the top, multiplied by the squared distance to the ND, r^2. One then obtains a function independent from r in the far-field region, thus providing access to the ND scattering pattern. The cone with angle α', corresponding to the light collected by the objective, is represented along with its section S by a sphere of radius 600 nm, over which the scattered intensity is integrated.

Snell-Descartes' law of refraction.

We then deduced the fraction of recollected scattered light from FEM calculations of the optical response of the ND by computing the ratio of the powers scattered within the previous cone and in all directions. Both values were obtained by integration of the scattered intensity over the surface of a sphere centered on the ND, with a radius ($R = 600$ nm) large enough to ensure that the spatial profile of the scattered field corresponds to its far-field behavior (with a typical $1/r^2$-dependence of its power). The value of this radius was chosen based on the spatial variations of $I_{scat} \times r^2$, which are shown in figure 3.18b along with the collection cone in the configuration of the FEM simulation. *In fine*, these calculations led to a collected scattered power of only 13-14% of the total scattered power for both NDs in the investigated wavelength range.

This analysis shows that the cross-section actually measured in SMS, which corresponds to the extinction cross-section minored by the effects of partial scattered light recollection (referred to as the *corrected extinction* and noted σ_{corr} in the following), is much closer from the extinction cross-section than from the absorption one. Figure 3.19 compares these three cross-sections for ND1 and ND2 (using the same ND dimensions as in the previous analyses). The non-corrected and corrected extinction cross-sections differ only

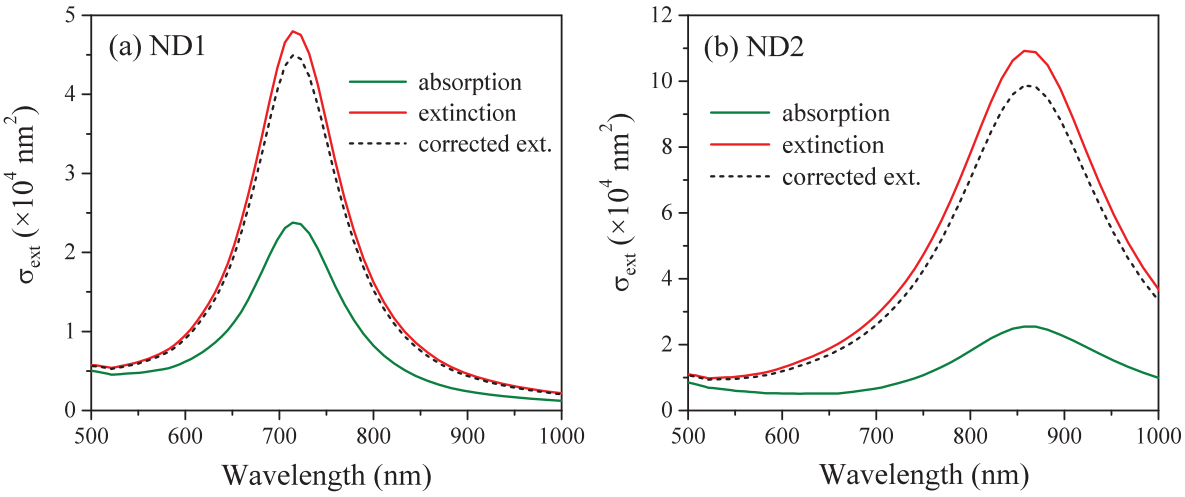

Figure 3.19 – Corrected extinction spectra taking into account the partial recollection of scattered light, computed using FEM for ND1 and ND2. The corrected extinction corresponds to the optical cross-section actually measured in our SMS experiments. The computed extinction and scattering spectra, shown previously (figure 3.10), are reminded for comparison.

by about 7% for ND1 and 10% for ND2. The A_p coefficients obtained by using the $\varepsilon_{1,2}$ derivatives of these three extinction cross-sections in equation 3.8 are compared in figure 3.20. Here too, the spectra obtained using the corrected (dashed black lines) and uncorrected (red lines) extinction cross-sections are similar, with maximal variations of the A_p coefficient of 13 and 20% for ND1 and ND2, respectively. Conversely, the A_p spectra derived using the absorption cross-sections (green lines in figure 3.20) strongly differ from the two former ones. In particular, they remain positive over the whole considered spectral range, only vanishing near the LSPR central position for ND1, where $|A_p|$ displays its maximal absolute value for the two former spectra. As shown by the insets of figure 3.20, these differences mostly result from the different spectral shapes of the $\partial\sigma_{ext}/\partial\varepsilon_2$ and $\partial\sigma_{abs}/\partial\varepsilon_2$ derivatives.

The fact that the experimentally determined A_p profiles agree well with those computed using uncorrected or corrected extinction cross-sections (figure 3.14), but not with those computed using the absorption cross-sections is fully consistent with the results of the FEM optical calculations described above, indicating that light scattering by the NDs significantly contributes to their extinction and that only a fraction of the scattered light is recollected in our optical experiments. Indeed, if one of these conclusions was incorrect, the measured A_p profile should follow that computed using absorption, which is not the case.

In conclusion, the additional FEM investigations presented above largely support the *a priori* questionable validity of the assumption made in the analysis leading to figure 3.15

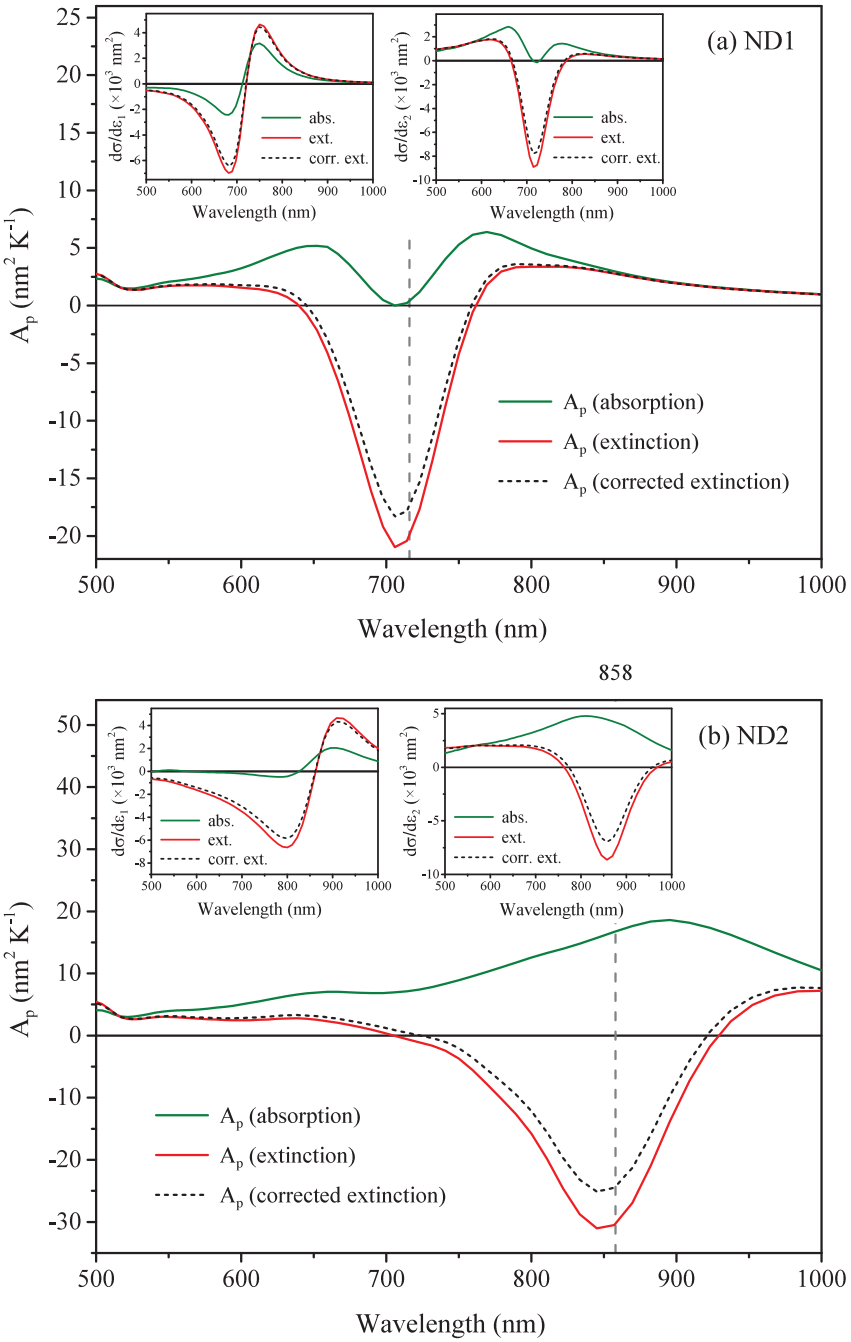

Figure 3.20 – A_p **spectra of ND1 and ND2 computed using either** $\partial\sigma_{ext}/\partial\varepsilon_{1,2}$ **derivatives in equation 3.8 or replacing them by** $\partial\sigma_{abs}/\partial\varepsilon_{1,2}$ **or** $\partial\sigma_{corr}/\partial\varepsilon_{1,2}$ **in this equation.** All these derivatives are shown in the insets. $\mathrm{d}\varepsilon_{1,2}/\mathrm{d}T$ derivatives are taken from ref. [34]. The grey dashed lines indicate the central position of the LSPRs.

(*i.e.* that the cross-sections measured in SMS and time-resolved spectroscopy corresponds to the extinction ones), showing that it leads to errors smaller than uncertainties on $\mathrm{d}\varepsilon_{1,2}/\mathrm{d}T$ derivatives (figure 3.15). Therefore, we did not perform a complete new analysis of our experiments, which would have also required to compare the SMS-measured spectra (figure 3.9a-b) with the FEM-computed corrected extinction ones (figure 3.19), leading to small variations of the deduced ND dimensions.

3.4 Cooling dynamics of supported nanodisks: morphology effects and thermal boundary conductance determination

The proportionality between the measured time-resolved signals and ND transient temperature rise was exploited for systematic investigations of the size-dependence of ND cooling dynamics by performing experiments on a large number of NDs with different thicknesses and diameters.

3.4.1 Experimental approach

Time-resolved signals were collected for 60 NDs of different sizes from samples S1 and S2. In all the experiments, sample illumination with a $\lambda_{pp} = 410$ nm, low fluence ($< 1\ \mathrm{J\,m^{-2}}$) pump beam was used in order to achieve moderate (~ 10 K) initial temperature rises and avoid ND modification throughout the measurements. Since the choice of λ_{pr} is not critical to achieve $\Delta\sigma_{ext} \propto \Delta T_p$ (as shown by figure 3.14), the probe wavelength was fixed at 510 nm for all measurements, *i.e.* away from the LSPR domains of all NDs. Although systematically tuning λ_{pr} near the ND LSPRs (whose positions range from 620 to 950 nm depending on D and h) would have achieved higher signal amplitudes, as demonstrated in section 3.3 of this chapter (see figure 3.15), the used method offered several advantages. Indeed, because of chromatic aberrations induced by the focusing objective, changing the probe wavelength often requires moving the objective's focus in order to get sufficient pump-probe signal, thus modifying the pump fluence. Depending on λ_{pr}, it may also imply a modification of the pump wavelength. Conversely, keeping the probe wavelength fixed allowed measuring several NDs with little or no realignment of the pump and probe beams between acquisitions, thus dramatically improving the measurement throughput while reducing the dispersion of the acquired data. Finally, signal oscillations induced by ND vibrations were generally weak or inexistent at this wavelength, facilitating the extraction of the cooling dynamics.

All bare time-resolved signals were processed as described in subsection 3.2.3 by fitting with function $f_{fit}(t)$ (equation 3.13) and subtraction of their vibrational signatures.

3.4.2 Results and interpretation

3.4.2.a Results

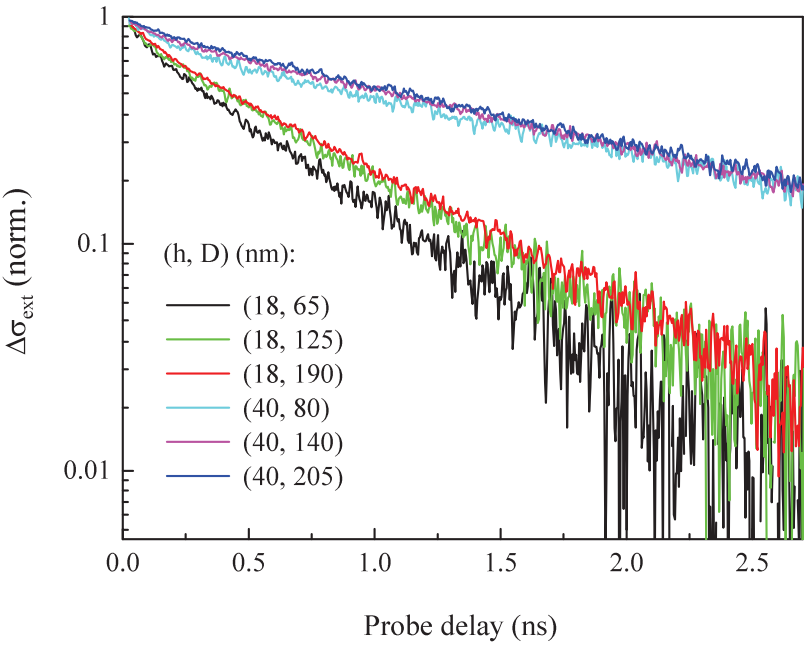

Figure 3.21 – Morphological dependence of the cooling dynamics of individual gold NDs. Normalized thermal components of experimental time-resolved signals measured on individual gold NDs from samples S1 and S2, with the thicknesses h and diameters D indicated in the legend.

Figure 3.21 presents representative normalized thermal signals obtained for NDs with different thicknesses ($h = 18$ and $h = 40$ nm) and diameters (from 65 to 205 nm), estimated as the average values from AFM and SEM measurements on NDs with same nominal dimensions (see section 3.2.1; note that SMS spectroscopy, which provides additional estimates of D and h, was not performed systematically as it would have cost too much time). This figure demonstrates that the ND cooling kinetics is strongly dependent on h and weakly dependent on D in this size range. All measured thermal components present a monoexponential decay at long timescales (> 500 ps delays), with an associated decay time τ_1 of about 0.7 and 1.7 ns for $h = 18$ and $h = 40$ nm NDs, respectively[9]. Such exponential behaviour suggests interface-limited cooling dynamics [15, 61]. Indeed, as discussed in section 3.1.1, if the ND is assumed to remain isothermal throughout the thermal relaxation process (which is relevant for a Biot number $Bi = hG/\Lambda_{Au} \ll 1$) and that the substrate temperature undergoes little modification in the vicinity of the ND (a relevant assumption considering the high heat conductivity of sapphire), then the heat

[9] As discussed above, biexponential dynamics were found when measurements were performed at too high pump fluences. Their description requires a second characteristic time $\tau_2 \ll \tau_1$.

transfer is entirely described by equation 3.2, with $T_m(\mathbf{r}, t) = T_0$:

$$\mathbf{J_{int}(t)} = \frac{c_{Au} V}{S} \frac{\mathrm{d}T_p}{\mathrm{d}t} = G\,(T_p(t) - T_0)\ , \tag{3.17}$$

with V the nanodisk volume, S the area in contact with the substrate, c_{Au} the volumetric heat capacity of gold, and G the Kapitza thermal conductance of the nanostructure/substrate interface. The solution of this equation is an exponential decay of $\Delta T_p(t) = (T_p(t) - T_0)$ with characteristic time $\tau = c_{Au}\, h/G$.

Such an exponential decay, with a characteristic time linearly scaling with ND height, has been experimentally reported for permalloy NDs nanopatterned on a Si substrate [63] and the transient thermal dynamics theoretically investigated for the case of Cu NDs deposited on Si [103]. Within the context of the present study, the $\tau_1 \propto h$ scaling is in approximate agreement with the 2.4× larger τ_1 values determined experimentally for $h = 40$ nm NDs as compared those for $h = 18$ nm, and their weak dependence on the ND diameter. Furthermore, preliminary G estimation via $G = c_{Au}\, h/\tau$ leads to G values in the order of 60 MW m^{-2} K^{-1} for the gold–sapphire interface, which is consistent with the 20–70 MW m^{-2} K^{-1} range reported in the literature for thin gold films [60, 90–93].

A more thorough modeling of ND cooling dynamics requires to include the effect of the finite heat conductivity Λ_m of the sapphire substrate, associated to a heat current density $\mathbf{J_m}(t) = -\Lambda_m\, \mathbf{grad}(T_m(\mathbf{r}, t))$ according to Fourier's law. This was achieved using FEM numerical simulations, which will now be described.

3.4.2.b FEM calculations of the cooling dynamics

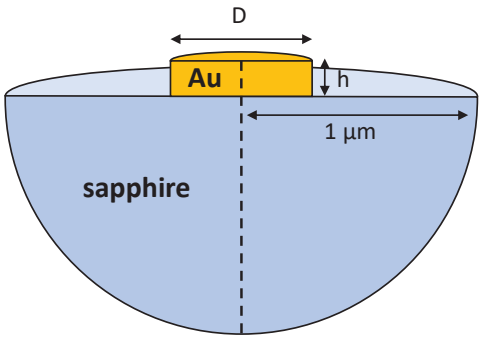

Figure 3.22 – Geometry of thermal FEM simulations. The axial symmetry of the system was exploited to reduce computational time.

The cooling dynamics of gold NDs were modeled using the Heat Transfer module of COMSOL. Gold NDs were described as perfect cylinders. The sapphire substrate was included as a half-sphere of 1 µm radius, large enough to ensure that the choice of

boundary conditions at its external border (here, open boundary) does not influence the computed dynamics. Gold and sapphire were described using their bulk thermal parameters, i.e. $c_{Au} = 2.5\ \mathrm{J\,cm^{-3}\,K^{-1}}$ and $c_{Al2O3} = 3.1\ \mathrm{J\,cm^{-3}\,K^{-1}}$ volumetric heat capacities, and $\Lambda_{Au} = 317\ \mathrm{W\,m^{-1}\,K^{-1}}$ and $\Lambda_{Al2O3} = 25\ \mathrm{W\,m^{-1}\,K^{-1}}$ thermal conductivities, heat diffusion in both materials being described by Fourier's law. The temperature-dependence of these quantities was neglected, considering the small temperature excursions involved in our experiments. Perfect contact and finite thermal conductance G were assumed at their interface. Simulations were performed in the time domain with a 10 ps time step, the axial symmetry of the system being exploited to reduce computational costs. A ΔT_{eq} initial temperature rise was defined in the ND. ND temperature was seen to remain quasi-uniform throughout the cooling process, as expected from $Bi = hG/\Lambda_{Au} \ll 1$ (see section 3.1.1.c).

The dynamics computed using the complete FEM model for NDs with 18 or 40 nm thicknesses and 80 or 160 nm diameters (solid lines in figure 3.23) are slightly slower than the purely exponential ones with $\tau_1 = c_{Au}\, h/G$ decay time obtained by assuming infinitely fast heat diffusion in the substrate for the same $G = 70\ \mathrm{MW\,m^{-2}\,K^{-1}}$ considered value of interface conductance (dashed lines), the difference increasing with ND diameter. They also deviate from a purely exponential decay, as also observed in a previous theoretical work addressing the cooling of a metal ND in contact with a dielectric substrate, in the case where the latter does not remain isothermal during the cooling process [103]. However, their non-exponential character is noticeable only at timescales exceeding those considered in the experiments. The fact that ND cooling dynamics are primarily limited by heat transfer at the ND–substrate interface is confirmed by comparing the cooling dynamics computed by assuming a purely interface-limited process (corresponding to infinite Λ_{Al2O3} sapphire thermal conductivity, dashed lines in figure 3.23) and a purely diffusion-limited process (corresponding to infinite G, dotted lines in figure 3.23). This comparison shows that the latter dynamics are strongly non-exponential, dependent on ND diameter and considerably faster than the former ones for the whole range of ND sizes explored in the experiments.

3.4.2.c Estimation of gold–sapphire interface conductance

The difference between the dynamics computed using the complete FEM model and in the simple interface-limited case implies that extracting a precise G value from time-resolved experimental data requires their comparison with results of the complete FEM model, especially for the NDs with the largest diameter values, i.e. approaching the continuum film case, for which the difference is the largest. To do so, the measured cooling times τ_1 were compared to those extracted from exponential fits of the FEM-

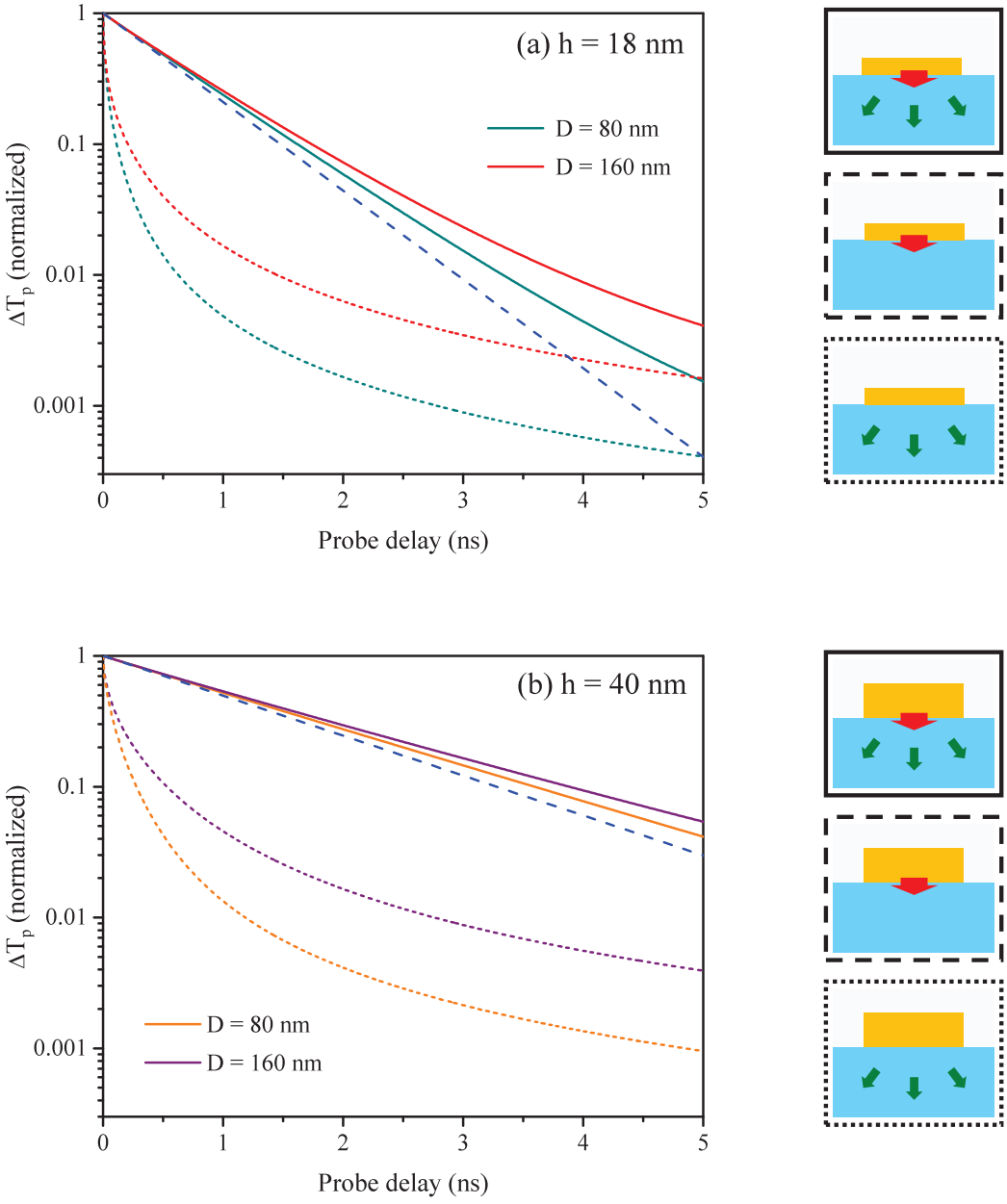

Figure 3.23 – FEM-computed ND cooling dynamics. Temperature dynamics for NDs with thicknesses $h = 18$ nm (a) and $h = 40$ nm (b) and diameters $D = 80$ nm or $D = 160$ nm (plain lines, see legend), assuming a $G = 70$ MW m^{-2} K^{-1} conductance at the gold–sapphire interface. The cooling dynamics computed for these NDs in the $\Lambda_{Al2O3} \to \infty$ (dashed lines) and $G \to \infty$ (dotted lines) limits are also shown, corresponding to the extreme cases of interface- and diffusion-limited heat transfers, respectively.

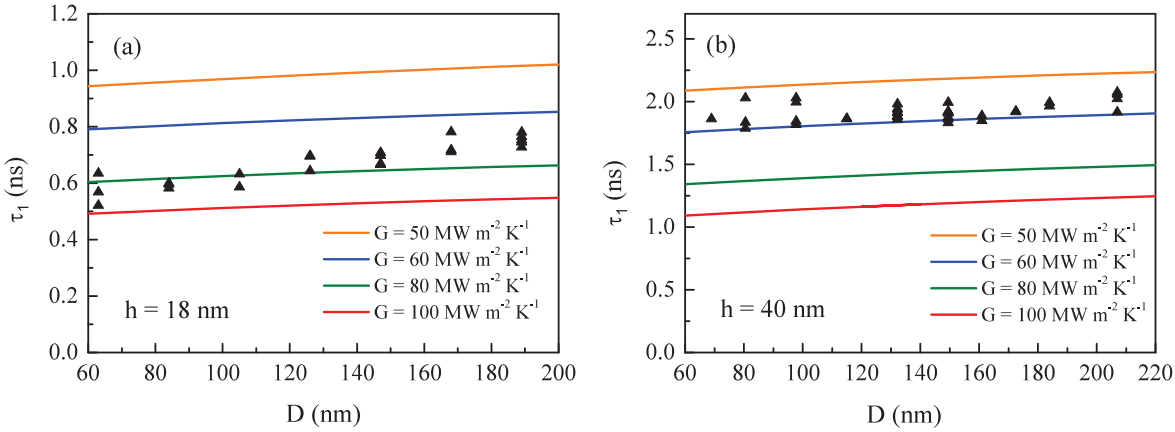

Figure 3.24 – Experimental and simulated τ_1 time constants as a function of ND diameter for $h = 18$ nm (a) and $h = 40$ nm (b). The black triangles are the τ_1 cooling times measured on NDs of different diameters, each triangle corresponding to a different ND. The lines represent the FEM-computed cooling times for several values of interface conductance G.

simulated cooling dynamics using different G values (figure 3.24). The cooling times determined for $h = 40$ nm NDs are well reproduced by calculations assuming $G = (60 \pm 10)$ MW m^{-2} K^{-1}. Those of $h = 18$ nm NDs correspond to a slightly larger $G = (75 \pm 10)$ MW m^{-2} K^{-1} average value. The difference between the G values extracted from the two ND thicknesses, corresponding to two distinct samples fabricated during two different processing sessions, could be due to either small differences in the gold–sapphire interface in these two samples or to uncertainties associated to the determination of their average thicknesses by AFM.

3.4.2.d Role of nano-object composition and dimensionality in the cooling process

The large difference demonstrated in this study between the timescales associated to interfacial heat transfer and heat diffusion in the sapphire substrate, resulting in almost interface-limited cooling dynamics (weakly sensitive to the precise modalities of heat diffusion in the substrate), is not general, but rather the consequence of both the composition and the geometry of our system.

First, the thermal boundary conductance for a gold–sapphire interface is lower than for most other metals with sapphire, according to the measurements reported in the literature. For instance, interfacial heat transfer would be about 5 times faster for a nickel ND than for a gold one, as $G \sim 300$ MW m^{-2} K^{-1} for a nickel–sapphire interface [93]. Other examples of measured metal–sapphire interface conductances are given in table 3.3, reproduced from Blank and Weber [93].

metal	Au	Ag	Pt	Pd	W	Al	Cu	Mo	Ni	Cr
G(MW m^{-2} K^{-1})	43–68	77	106–113	151–165	131	160–178	175–195	216	283	349

Table 3.3 – Thermal boundary conductances measured for the interfaces of various metals with sapphire. Reproduced from ref. [93].

Second, the small size of the investigated NDs accelerates heat diffusion in the substrate as compared to interfacial heat transfer. This is demonstrated in figure 3.25, presenting the simulated cooling dynamics of NDs with thicknesses $h = 20$ and 40 nm and diameters $D = 60$, 180 and 400 nm. For $D = 60$ nm, the dynamics are quasi-exponential for both values of h and close to those computed in the hypothesis of an interface-limited cooling (namely, an exponential decay with constant $\tau = c_{Au}\ h/G$). As the diameter increases, the cooling process is slowed at long timescales because of the increased difficulty for heat evacuation in the substrate, and rapidly tends towards the limit of an infite film. This dependence on the diameter may be interpreted as a dimensionality effect. Indeed, in the case of a small nanoparticle, heat can spread in three dimensions in the substrate, versus only one dimension for an infinite film.

In the intermediary case of a supported nanowire (*i.e.*, a nanostructure with one non-nanometric dimension), heat can radiate in two dimensions in the substrate. This structure has proved to be particularly interesting for studies of the breakdown of Fourier's law at the nanoscale. Indeed, it combines a lateral dimension smaller than the phonon mean free path (possibly inducing the emergence of quasi-ballistic phonon transport) and an increased sensitivity to the modalities of heat transport in the matrix compared to a nanoparticle. For instance, several studies were performed on nickel nanolines supported on various substrates, all suggesting the presence of ballistic effects [65, 77, 78].

3.4.2.e Comparison between the vibrational and thermal responses of single NDs

Time-resolved experiments on single gold NDs enable the investigation of either the cooling dynamics (as described in this work) or the vibrational dynamics, which were the object of a recent study of our group [12]. Although they yield distinct signatures in time-resolved signals, these two physical processes are related as the vibrational damping and the cooling process of supported nanostructures are both governed by phonon propagation from the nanoparticles into their underlying substrate, making a comparison of their morphology dependence particularly interesting.

In a previous study performed in our group, vibrational modes of single NDs were investigated using measurements made on sample S2 of the present study (NDs with $h = 40$ nm) and another sample similar to S1 ($h = 18$ nm) [12]. The quality factors of the detected

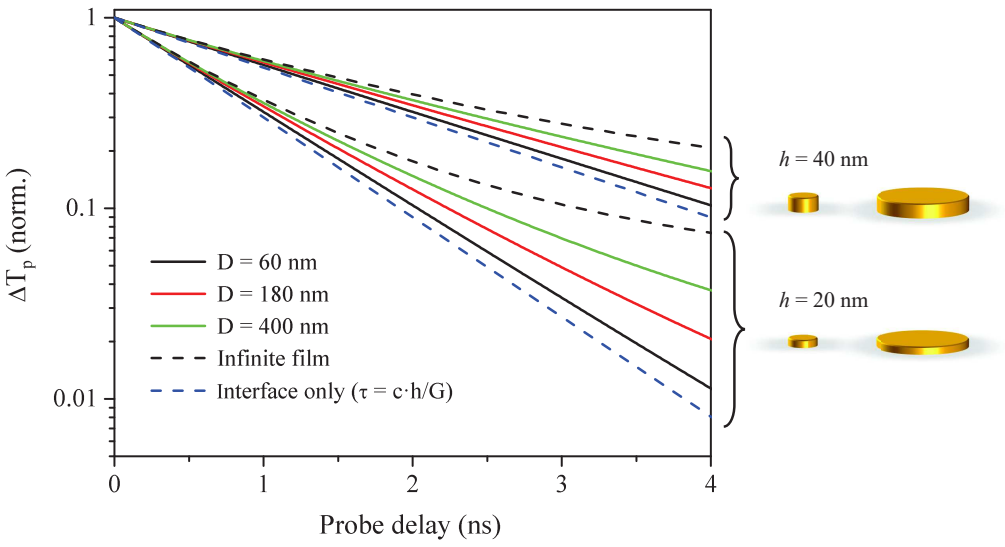

Figure 3.25 – Cooling dynamics computed by FEM for gold NDs of various thicknesses and diameters. For each thickness value, computations for an infinite film and assuming an interface-limited heat transfer (resulting in an exponential cooling) are also shown.

vibrations, defined as $Q = \pi f/\Gamma$ (with f the oscillation frequency and Γ its damping rate), were determined from time-resolved measurements on NDs of various dimensions h and D. The results are plotted in figure 3.26a as a function of the ND aspect ratio $\eta = D/h$, displaying large variations with η, and in particular a dramatic enhancement of Q around aspect ratio $\eta \approx 2.5$. This enhancement may be appreciated by comparing the oscillating parts of time-resolved signals measured on a ND with aspect ratio $\eta = 3.5$ (figure 3.26b) and on a ND with $\eta = 2.5$ (figure 3.26d): the number of visible oscillations is indeed much larger in the latter case. A FEM model of the sapphire-supported NDs was used to identify the detected modes and numerically estimate their frequencies and quality factors, for NDs of different aspect ratios. The found quality factors, shown in figure 3.26c, correctly reproduce the enhancement found around $\eta = 2.5$, the higher simulated Q values with respect to the experimental ones resulting from the omission of intrinsic damping mechanisms. In the numerical model, the only damping source considered is the radiation of acoustic energy in the substrate, triggered by the displacement and strain profile created at the interface. Thus, the quality factor enhancement near a given aspect ratio observed both in the experiments and the simulations corresponds to ND vibrations which remain "confined" within the ND on a long timescale, as if the ND were separated from its substrate.

Such large effect of ND morphology on the quality factor of specific, low-frequency vibrational modes is in contrast with the smooth variations of the ND cooling times τ_1 observed when varying D and h close to the $\tau_1 \propto h$ limit associated to a purely interface-

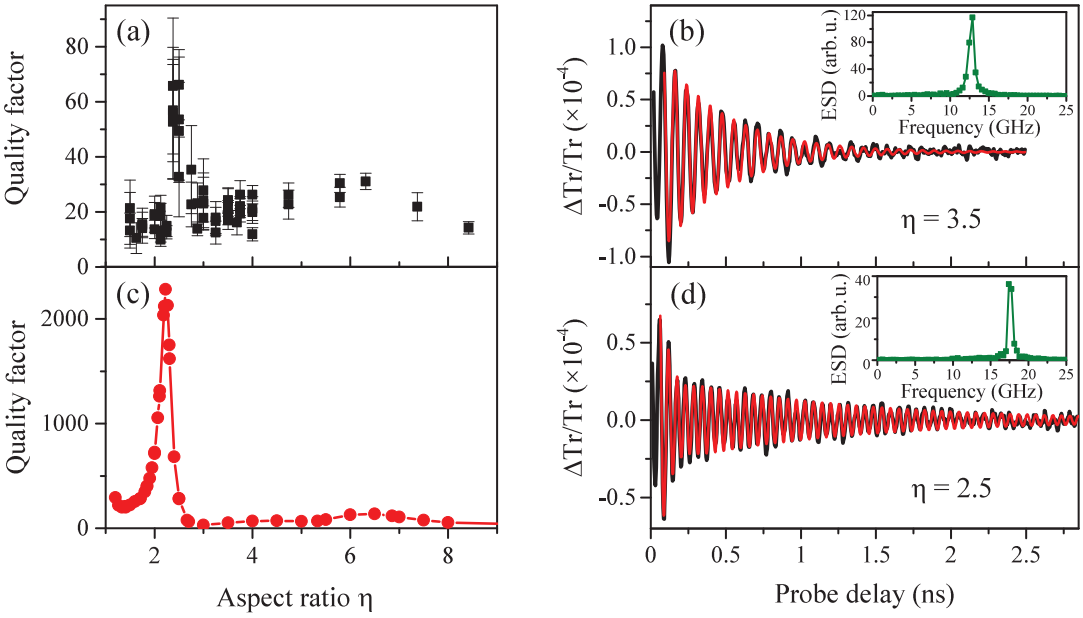

Figure 3.26 – Morphology-dependence of the quality factor of vibrational modes of gold NDs. Experiments performed by Medeghini *et al.* on one of the samples (S2) used in this work [12, 39]. (a,c) Quality factor (a) of the experimentally detected vibrational modes (each dot corresponds to a single ND measurement) and (c) of the FEM-computed modes as a function of ND aspect ratio $\eta = D/h$. (b,d) Oscillating components of time-resolved signals measured for two gold NDs with thickness $h = 40$ nm and aspect ratios $\eta = 3.5$ (b) and 2.5 (d). The red lines correspond to fits with a damped sinusoid. The energy spectral densities (ESD) of the measured oscillating components are shown in the insets as a function of frequency . Figures adapted from ref. [12].

limited cooling process (figure 3.24). Therefore, this means that while morphology has a strong and complex impact on the quality factor of the vibrational modes of a supported nano-object, which may reach high values in specific cases, it has a simpler and weaker impact on thermal interface resistances, which involves the entirety of its vibrational modes. As a result (and unsurprisingly), it is not possible to keep heat localized in a supported nano-object by tuning its morphology.

In addition, the qualitative agreement between the morphological dependences of experimental and simulated quality factors suggest that the samples have an excellent ND–substrate contact for most NDs (as a perfect contact was assumed in the modeling). This is further supported in our investigation of thermal properties by the similarity of the measured cooling dynamics for NDs with same nominal dimensions, leading to a weak dispersion of their deduced interface conductances (figure 3.24). Moreover, the fact that their deduced G values lie at the upper end of the range observed in previous measurements (see table 3.3) is consistent with a good contact between gold and sapphire in our samples.

3.4.3 Investigation on the possible causes for non-exponential dynamics

We now propose a simple model to account for the gradual and irreversible modifications of the cooling dynamics of gold NDs observed under laser illumination as a function of the fluence and of the exposure time, described in paragraph 3.2.3.d.

3.4.3.a Hypothesis: presence of an impurity

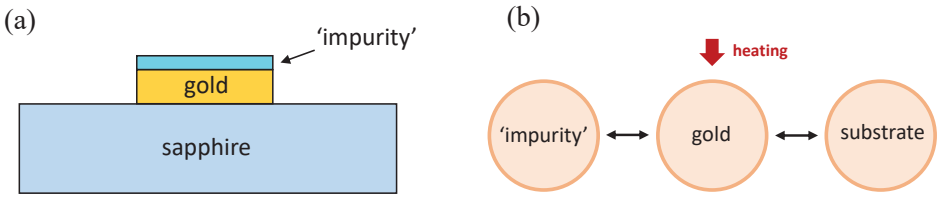

Figure 3.27 – Hypothesis of an impurity on the ND and its effect on the cooling dynamics. (a) Considered configuration including an additional transparent layer on top of the ND. The primary role of the layer is to provide a second pathway for ND heat dissipation (b), which may account for the faster cooling dynamics observed in the first few hundred ps in some of our measurements.

The observed changes, featuring the acceleration of the cooling kinetics at short timescales and its subsequent slowdown, may be accounted for by the introduction of an additional "impurity" layer in contact with the ND, in the configuration sketched in figure 3.27a. This impurity must be transparent, so as not to be heated directly by the pump pulses. Its possible nature and origin will be discussed in the next paragraph. The effect of this layer in our model is twofold. First, immediately after ND heating, the impurity represents a secondary pathway for heat evacuation from the ND (figure 3.27b), therefore accounting for the measured initial cooling acceleration. This process quickly stops as the temperature of the impurity reaches equilibrium with the ND. To describe the subsequent dynamics, ruled by transfer at the interface with the substrate, one must consider the enlarged system {ND+impurity} in place of the ND. This system having a larger specific heat compared to the ND, its cooling is slower than without impurity, explaining the change observed in the long timescale dynamics.

To verify and illustrate this analysis, thermal FEM calculations were performed in the configuration shown in figure 3.27a, where the impurity was assumed to be composed of water with specific heat $c_{H_2O} = 4.18\ \mathrm{kJ\,K^{-1}\,kg^{-1}}$. The computed cooling dynamics for a $D = 60$ nm and $h = 40$ nm ND, a layer thickness $h_i = 5$ nm and an interface conductance with gold fixed arbitrarily to $G_i = 100\ \mathrm{MW\,m^{-2}\,K^{-1}}$ are shown in figure 3.28, as well as the same calculation without an impurity. As expected, the cooling dynamics of the ND with an impurity resemble those observed experimentally following ND exposure to

high fluences (figures 3.12 and 3.13). Indeed, they display a non-exponential character, and are respectively faster and slower at short and long timescales than those computed without impurity. Although a closer match with the experimental data could be achieved by tuning the parameters of the model (layer thickness, specific heat and boundary conductance with gold), this approach was not deemed pertinent, as the results of this analysis are related to the various arbitrary assumptions made. Indeed, we insist on the illustrative nature of this simple model, whose aim is only to propose a plausible scenario to explain the observed non-exponential dynamics.

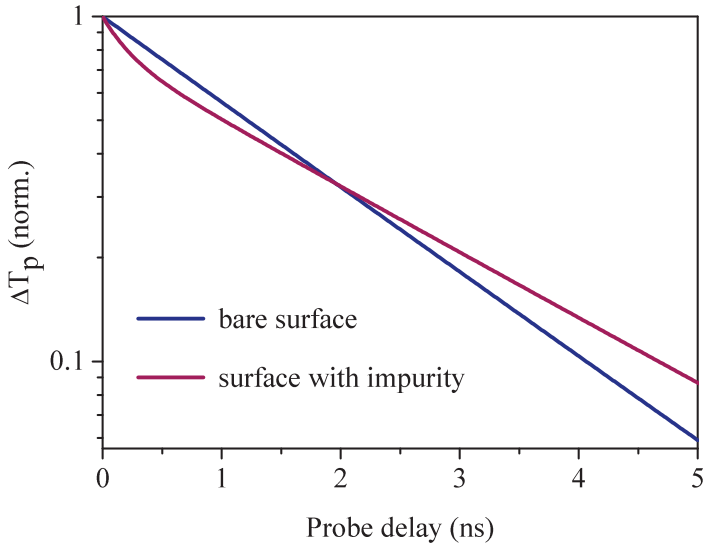

Figure 3.28 – FEM-computed cooling dynamics for a $D = 60$ nm, $h = 40$ nm gold ND with or without an impurity layer.

3.4.3.b Effect of plasma cleaning of the samples

The results from the FEM simulations described in the previous paragraph support the idea that the changes in the cooling dynamics may be linked to the presence of an impurity around the ND. This raises the question of the nature and conformation of this impurity, and the reason for the gradual modification of its physical properties and/or contact with the ND under high-fluence illumination. The possible presence around the NDs of residues of the resist used during the fabrication process or other organic contaminants appeared to us as a possible source of such impurities. This hypothesis was tested by cleaning one of the samples using acetone (the solvant usually used to eliminate the resist), and then by submitting it to a plasma cleaning treatment, which is supposed to destroy most organic contaminants. Preliminary to this operation, the cooling dynamics of a ND were measured at low pump fluence (0.5 $\mathrm{J\,m^{-2}}$) and at higher fluence (2.7 $\mathrm{J\,m^{-2}}$) to induce a modification of the cooling dynamics. Time-resolved

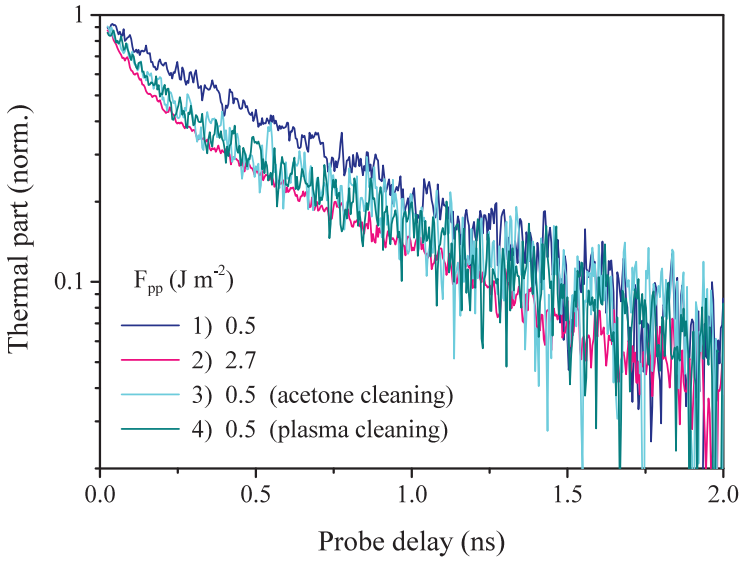

Figure 3.29 – Effects of acetone and plasma cleaning of the sample on ND thermal dynamics after modification by exposition to high fluence.

signals were then measured on this ND at low fluence after each step of the cleaning process. The normalized thermal parts of these signals are shown in figure 3.29. After the initial change of the dynamics caused by the high-fluence measurement, no significant modifications are induced by acetone and plasma cleaning, ruling out a possible effect of organic contaminants on the non mono-exponential dynamics induced by high-fluence pump beams.

A relevant subsequent test would be to compare the ND morphologies using AFM and SEM before and after exposure to high fluence. This test has not been carried out yet. However, only drastic morphological changes in the NDs could be detected using this approach, due to the limited resolution of these techniques for these particular samples (see section 3.2.1).

3.5 Conclusion and perspectives

In the work presented in this chapter, which has also been described in a recent paper [104], the cooling dynamics of individual supported gold NDs were quantitatively investigated using an approach based on the combination of optical pump–probe spectroscopy with a spatial modulation microscope.

In the first part of this study (section 3.3), the sensitivity $A_p(\lambda_{pr})$ of time-resolved signals to the nano-object transient temperature changes at probe wavelength λ_{pr} was measured for the first time for two gold NDs with diameters 101 and 153 nm and thicknesses ∼20 nm. This study was made possible by the highly quantitative character of

single-object pump-probe spectroscopy in the context of thermal measurements, a quality which confers to this technique a marked advantage over the now common pump-probe measurements on ensembles of nano-objects, as it permits the accurate retrieving of the absolute temperature changes. In our work, the ND initial temperature elevation was evaluated from the characteristics of the pump beam (power and spatial profile) and of the ND (volume and absorption cross-section, deduced from the analysis of its extinction spectrum). The excellent agreement between the measured and modeled amplitudes of the thermal components of time-resolved signals implies that the analysis of these amplitudes constitutes an alternative way to access the ND temperature, based this time on its interaction with the probe beam and yielding similar results.

Understanding the sensitivity of time-resolved measurements to the various physical processes occuring in the ultrafast response of a nano-object is crucial for making an optimal use of these techniques. Calculation of the optical sensitivity of a nano-object to its temperature changes, described by its A_p spectrum, is a useful preliminary step to time-resolved thermal studies, either on single nano-objects or in ensembles, as it allows optimizing the choice of the probe wavelength to maximize the amplitude of the thermal component of time-resolved signals. The sensitivity of the transient extinction changes to the nano-object heating, computed using a FEM-based method which has been used up to now only in a purely theoretical work [14], has found experimental confirmation for the first time in our study. Although in the case of nano-objects featuring a single LSPR (such as the ones used), it is easy to predict an enhancement of A_p around the LSPR, the behavior of A_p may be less straightforward for nano-objects with more complex spectra. FEM calculations may therefore be of great use in these cases. Furthermore, while environment heating played no part in the optical signals in this experiment, this is generally incorrect for other systems. Calculating the contributions of the temperature changes of the nano-object and its environment to time-resolved signals, even in a simplified form (obtained by assuming a homegeneous temperature environment, which allows to define A_p and A_m coefficients), is thus crucial to correctly interprete the signals. It also provides the conditions on the probe wavelength for selectively addressing the temperature changes of the nano-object or its environment.

The second part of this study (section 3.4) focused on the dependence of the cooling dynamics on the morphology of gold NDs. Time-resolved signals were acquired for NDs with 60–205 nm diameters and 18–40 nm thicknesses. The use of moderate pump fluences limiting lattice heating to < 15 K values was essential to avoid permanent modification of the measured signals during the experiments. We showed that all experimental signals could be theoretically reproduced using Fourier's law with bulk sapphire thermal properties, and a gold–sapphire thermal interface conductance of about 70 $\mathrm{MW\,m^{-2}\,K^{-1}}$ showing weak size dependence in the investigated size range and consistent with previous measurements on thin films. As demonstrated by FEM investigations, the cooling

dynamics measured here are mostly limited by the gold–sapphire interface, the characteristic times associated with interfacial heat transfer from the ND to the substrate being considerably longer than those associated with substrate heat diffusion (the dynamics are therefore weakly sensitive to the precise modalities of heat conduction in sapphire, *e.g.* the possible presence of quasi-ballistic effects). These experiments may be extended to other compositions and geometries of the nano-objects and their supporting substrate, opening the way to direct investigations of the different nanoscale thermal transport regimes at the single-particle level.

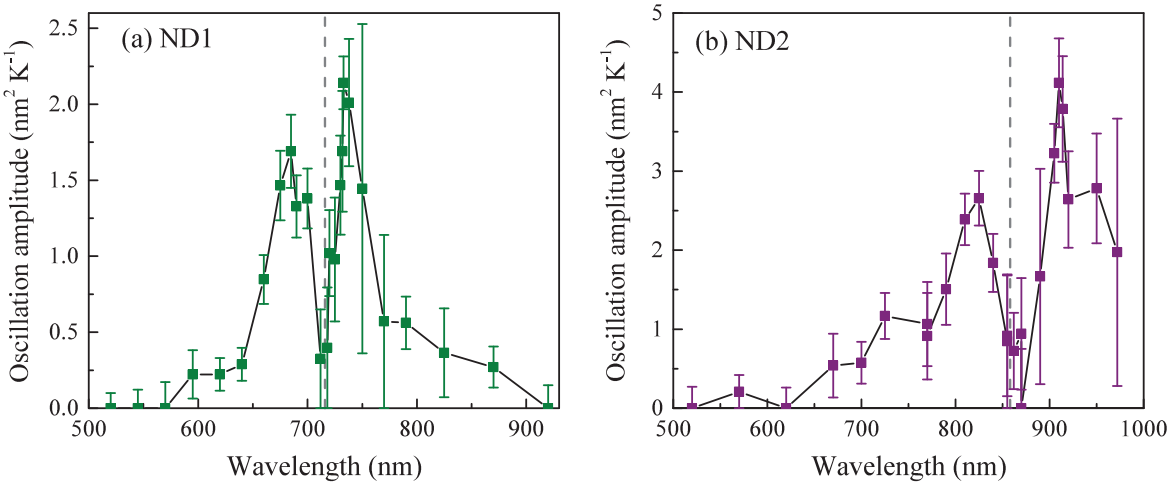

Figure 3.30 – Amplitudes of the oscillation signals in time-resolved measurements of ND1 (a) and ND2 (b). The amplitudes are given in $\mathrm{nm^2\,K^{-1}}$, corresponding to extinction cross-section changes divided by the ND initial temperature increase. The grey dashed lines indicate the LSPR central position.

As an extension of this work, the approach followed here to investigate the probe wavelength-dependence of the sensitivity of transient extinction changes was applied to the vibrational component of time-resolved signals. Figure 3.30 presents preliminary results on this theme, showing the amplitude of the oscillations measured in time-resolved signals, still recorded on ND1 and ND2 (expressed as extinction cross-section changes divided by the initial temperature rise, in $\mathrm{nm^2\,K^{-1}}$). These oscillation amplitudes were estimated as the average of the amplitudes (in absolute value) of the first two measured half-oscillations. The error bars plotted in figure 3.30 correspond to estimations of the noise level of each signal after the complete damping of the oscillations. For both NDs, the oscillation amplitudes feature a cancellation near the LSPR center (associated with a change of the initial phase of the oscillations in the time-resolved signals) and vanishes on the sides of the LSPR. This general shape resembles that of $|\partial\sigma_{ext}/\partial\varepsilon_1|$ (figure 3.9c,d), indicating that the vibrational signal originates mainly from periodical variations of ε_1, which mostly translate into oscillations of the LSPR energy. Beyond this simple observation, performing a complete analysis of these signals would require a FEM model

of greater complexity as compared to the one used in our thermal analysis. Following the approach developed by Ahmed *et.al.* for suspended nanoparticles of various geometries [105], such analysis should include the explicit calculation of the deformations in the ND and in the substrate related to the different excited vibrational modes, and of the associated spatial and temporal variations of the dielectric functions of the two media.

While such detailed analysis is beyond the scope of this dissertation, the results of figure 3.30 show that the sensitivity of time-resolved measurements to the vibrational modes of a nano-object has a very different spectral dependence as compared to the sensitivity to temperature changes. This illustrates the more general idea that different physical phenomena usually lead to different transient spectra, which will also be investigated in the next chapter. Knowledge—even partial—of these dependences helps to guide the choice of the best optical detection (*e.g.* probe wavelength), depending on the aim of the study. For instance, in order to reduce the relative contribution of ND vibrations as compared to that of nano-object heating, one should use a probe wavelength at the LSPR central position or out of resonance; if one conversely wishes to maximize the oscillation signal, one must rather use a wavelength located at the flanks of the LSPR. Because of the changes of sign observed in A_p spectra (figure 3.15), it is also possible to cancel completely the amplitude of the thermal signal (provided environment heating has no influence on the optical changes, as is the case here), and hence obtain a purely oscillating signal.

Chapter 4

Optical probing of ultrafast electron and lattice dynamics in a single gold nanodisk

Contents

The ultrafast phenomena occurring in metal nano-objects on a femtosecond to picosecond timescale after impulsive excitation have received much attention over the last 25 years. In the 1980s, the development of femtosecond lasers and pump–probe techniques has launched many studies of the electron dynamics in thin metal films. The use of fs light pulses to selectively excite the electrons of a metal allowed precise studies of the dynamics of electron internal thermalization [106, 107] and of electron–phonon energy exchanges [108–110], which presents a dependence on excitation power [111, 112]. These studies were later extended to ensembles of metal nanoparticles [113–116], which present the advantage of suppressing the effects of electronic transport away from the photoexcited region. Modifications of the electron–electron and electron–phonon interaction dynamics have been reported as a function of the nanoparticle size [5, 117]. Finally, single-particle measurements [50, 118] allowed to perform a direct connection between the measured transient extinction changes and the stationary extinction spectrum of the studied nanoparticle (free from spurious inhomogeneous effects), permitting a more precise characterization of the relationship between the probed electron and lattice dynamics and the optical changes that they induce [13, 20].

In this chapter, we present a study of the ultrafast dynamics of individual gold nanodisks following impulsive excitation and previous to the establishment of a uniform particle temperature, T_p, by electron–lattice energy exchanges. This work is an extension to shorter timescales of the analysis presented in chapter 3 (section 3.3) of the temporal dynamics and probe wavelength-dependence of time-resolved signals. In chapter 3, we saw that the heating-induced extinction cross-section changes could be written as $\Delta\sigma_{ext}(\lambda_{pr}, t) = A_p(\lambda_{pr})\Delta T_p(t)$, allowing independent investigations of their spectral and temporal dependences. Conversely, during the first ~ 10 ps following pump absorption, the temporal shapes of pump-probe signals are strongly probe wavelength-dependent and their description requires a more sophisticated modeling.

In the first section of this chapter, we present a complete model enabling the analysis of time-resolved signals in this time range, based on numerical time-domain calculations of the electronic distribution modification following a sudden excitation and of the induced changes on the interband component of the dielectric function ε^{ib}, and also taking into account the transient modification of the scattering rate of conduction electrons (effecting the intraband component ε^{D}) and the effects of lattice heating. Inclusion of the latter two effects, which were omitted in a previous study performed in our group on different plasmonic nanoparticles (gold nanorods) [13], provides us with a more complete description of the transient optical changes. We also introduce a greatly simplified version of this model, valid after the internal thermalization of the electron gas, where the extinction changes $\Delta\sigma_{ext}$ are described as the sum of two components respectively proportional to the electron and the lattice temperature rises, $\Delta T_e(t)$ and $\Delta T_L(t)$, contributing with weights depending on the probe wavelength. In the second section, we

present experimental measurements of the transient response of two gold NDs using time-resolved spectroscopy at numerous probe wavelengths. In the last section, these measurements are then compared to the complete model formulated in the first section, yielding a good qualitative and quantitative agreement for both NDs. Using our simplified model, we propose simple interpretations of the variety of temporal shapes observed in the experimental signals and of the transient modifications of the spectral response of NDs.

4.1 Ultrafast electron and lattice dynamics in metals and induced transient optical changes

To understand the transient changes of the extinction cross-section of a single metal nanoparticle at short pump–probe delays, we first describe the initial modification of the electron energy distribution following the absorption of a pump pulse and its subsequent relaxation through electronic interactions. The modifications induced by these processes on the metal dielectric function are then described through a complete model, based notably on Rosei's description of the band structure of gold and taking into account the effect of lattice heating. In the last part of this section, we will show that the transient extinction changes occuring once the electron temperature is well-defined (*i.e.* for pump–probe delays exceeding the characteristic times of excitation and electron–electron energy transfers) can also be described using a simplified modeling approach.

4.1.1 Transient electron distribution changes following impulsive excitation

To describe the electron dynamics in a metal nano-object, the most relevant physical quantity is the energy- and time-dependent electronic distribution function $f(E,t)$, where E refers to the energy of the electronic state (see chapter 1). Starting from an initial equilibrium distribution $f_0(E)$ of the electrons at room temperature $T_0 = 295$ K, corresponding to the Fermi-Dirac distribution represented in figure 4.1a, we consider the modification of the electronic distribution consecutive to the absorption of a pump pulse, ruled by electron–electron and electron–phonon processes. The temporal evolution of $f(E,t)$ is given by the Boltzmann equation, which writes (assuming an isotropic parabolic conduction band) [106, 112]:

$$\frac{\mathrm{d}f(E,t)}{\mathrm{d}t} = \left.\frac{\mathrm{d}f(E,t)}{\mathrm{d}t}\right|_{exc} + \left.\frac{\mathrm{d}f(E,t)}{\mathrm{d}t}\right|_{e-e} + \left.\frac{\mathrm{d}f(E,t)}{\mathrm{d}t}\right|_{e-ph} . \tag{4.1}$$

The first term on the right side corresponds to the initial pulse excitation and the last two terms refer to the energy redistribution through electron–electron and electron–phonon interactions, respectively.

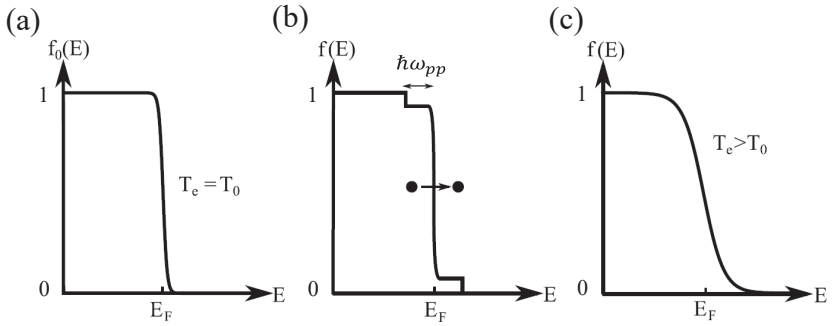

Figure 4.1 – Modification of the electron gas distribution following the absorption of a pump pulse. (a) Initial Fermi–Dirac distribution at temperature T_0. (b) Athermal distribution directly following pump excitation. (c) New Fermi–Dirac distribution at temperature $T_e > T_0$ obtained after thermalization of the electron gas by electron–electron scattering. E_F is the Fermi energy.

For a pump beam with a photon energy $\hbar\omega_{pp}$ below the onset of interband transitions ($\sim$ 2.4 eV in gold), the pulse is absorbed only through the generation of electron–hole pairs in the conduction band, which modifies the initial electronic distribution $f_0(E)$ resulting in the athermal distribution sketched in figure 4.1b, where a small fraction of the electrons below the Fermi energy ($E_F \approx 5.5$ eV) have been promoted to a state of higher energy by the absorption of a photon $\hbar\omega_{pp}$. Conversely, if the pump photon energy is higher than the interband threshold, it will also trigger interband transitions, promoting electrons from valence bands to the conduction band. Thus, the number of conduction electrons is no longer constant. However, these interband electron–hole pairs recombine within about 10 fs through Auger processes, thus quickly leading to a distribution similar to that obtained in the previous case (figure 4.1b). The excitation process is described by the first term in equation 4.1, which takes into account the temporal dependence of the pump pulse, whose duration is generally of the order of tens to hundreds of fs [106, 112]. Although the electronic distribution is strongly athermal at this stage, it is useful to quantify the excitation amplitude through an equivalent electronic excitation temperature $T_{exc} = T_0 + \Delta T_{exc}$, defined as the temperature of the thermalized electron gas with the same total energy as the athermal one after complete absorption of the pump pulse, corresponding to an additional enery density u_{abs}. It may thus be expressed from:

$$u_{abs} = \int_{T_0}^{T_{exc}} c_e(T_e)\,\mathrm{d}T_e \quad \Rightarrow \quad T_{exc} = \sqrt{T_0^2 + \frac{2u_{abs}}{a}}\,, \tag{4.2}$$

with a being defined from the expression of the volumetric electronic specific heat, $c_e = aT_e$ (equation 1.6 of chapter 1). In the context of our experiments, ΔT_{exc} lies in the 100–1000 K range.

From an athermal distribution, the energy states of the electrons are redistributed through electron–electron interactions, eventually leading to a new Fermi–Dirac distribution (figure 4.1c), with a typical ~ 500 fs time constant for gold in bulk materials and large nanoparticles [112]. This process is described by the second term in the Boltzmann equation (equation 4.1), consisting in a sum over all possible two-electron scattering processes satisfying energy and momentum conservation, where the interactions are described by a screened Coulomb potential [106, 112, 119].

Simultaneously with the former process, the electron excess energy is gradually transferred to the ionic lattice through electron–phonon scattering events, leading to the thermalization of the metal with a typical time constant $\tau_{e-L} \sim 1$ ps in gold [106] increasing for stronger excitation [120], and presenting a marked decrease for nanoparticles with sizes $\leqslant 10$ nm [5]. The last term of equation 4.1 denotes the corresponding electronic distribution changes, and is evaluated by integrating the electron–phonon coupling matrix element, assimilated to a deformation potential, over all available electronic and vibrational states satisfying energy and momentum conservation. At the end of this process, the electron gas and the lattice share the same temperature T_{eq}, typically increased of a few K compared to T_0. The excess energy is then evacuated by thermal transfer to the environment, which takes place over much longer timescales (> 100 ps), as discussed in detail in chapter 3.

In this work, the Boltzmann equation is solved using a numerical model based on the Euler method, which was initially developed in the FemtoNanoOptics group [112], yielding the temporal evolution of the electron distribution $f(E,t)$. As an example, figure 4.2 depicts the computed variation of the electronic distribution $\Delta f(E,t) = f(E,t) - f_0(E)$ in gold at several instants t following the absorption of a $\lambda_{pp} = 800$ nm pump pulse with a 50 fs FWHM, with an energy corresponding to a $\Delta T_{exc} = 100$ K equivalent electron temperature increase. Directly following the excitation, the electronic distribution is modified over a broad range of energies around the Fermi energy E_F, corresponding to the absorption of photons of energy $hc/\lambda_{pp} = 1.55$ eV (pink curve, $t = 0.1$ ps). The distribution change Δf rapidly narrows around the Fermi energy E_F (blue curve, $t = 0.5$ ps), resulting after 1–2 ps in a thermal distribution at a higher temperature T_e. Δf then progressively vanishes as the electron temperature decays by energy transfer to the lattice (green curve, $t = 3$ ps).

Starting from $\Delta f(E,t)$, the time-dependent temperature variations of the lattice and of the electron gas, $\Delta T_L(t)$ and $\Delta T_e(t)$, are also computed. Similarly to equation 4.2, $\Delta T_e(t)$ is computed as:

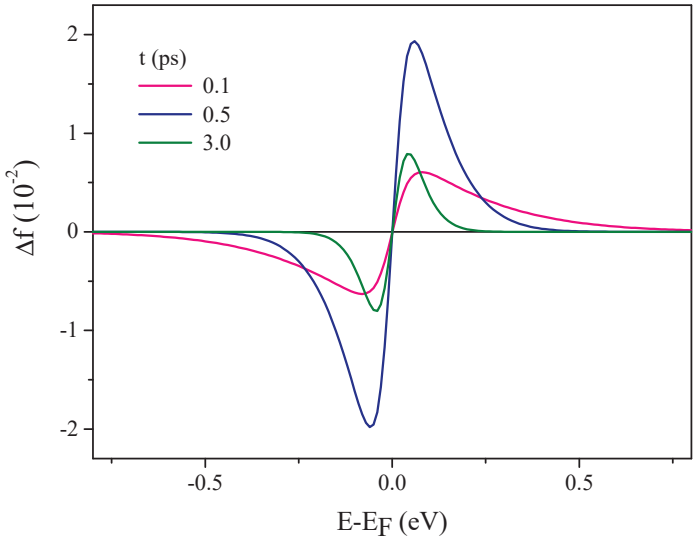

Figure 4.2 – Numerical computation of the modification of the electronic distribution in gold, $\Delta f(E,t)$, at several delays t after the absorption of a 50 fs (FWHM) pump pulse with an energy corresponding to a $\Delta T_{exc} = 100$ K equivalent excitation temperature.

$$\Delta T_e(t) = \sqrt{T_0^2 + \frac{2u_e(t)}{a}} - T_0 \ , \tag{4.3}$$

while $\Delta T_L(t)$ is calculated by dividing the lattice excess energy density, $\Delta u_L(t) = u_{abs} - u_e(t)$, by the lattice volumetric heat capacity c_L. Although those two quantities are computed at all times, the electronic temperature is not defined previous to the complete thermalization of the electrons. In this time range, $T_e(t)$ thus only represents an equivalent temperature, *i.e.* the temperature of the thermalized electron gas with the same total energy.

4.1.2 Time-dependent modification of the dielectric function

The transient changes of the optical properties of a metal after pump absorption result both from the modification of the electronic distribution $\Delta f(E,t)$ and from the increase $\Delta T_L(t)$ of the lattice temperature. We now describe these contributions in detail.

4.1.2.a Electronic contribution

Before the nano-object thermalization through electron–phonon interactions (while the excess energy injected by the pump pulse is still predominantly in the electron gas), the main changes of the dielectric function originate from the modification of the prob-

abilities of interband transitions to and from the conduction band (p band) caused by the evolution of the electron distribution $f(E,t)$ within this band. Evaluation of these probabilities allows to compute the modification of the interband component of the imaginary part of the dielectric function, $\Delta\varepsilon_2^{ib}(\omega,t)$, proportional to the total probability of a transition from an occupied state to an empty state by absorption of a photon of energy $\hbar\omega$. In this work, those probabilities are computed based on the Rosei model of Au band structure described in chapter 1 (paragraph 1.1.2.c) for the three mains transitions in gold ($d \rightarrow p$ and $p \rightarrow s$ around the L point of the first Brillouin zone, $d \rightarrow p$ around the L point). The calculation is performed numerically, based on the distribution changes $\Delta f(E,t)$ previously obtained from the resolution of the Boltzmann equation (equation 4.1).

After determination of $\Delta\varepsilon_2^{ib}(\omega,t)$, the real part $\Delta\varepsilon_1^{ib}(\omega,t)$ of $\Delta\varepsilon^{ib}$ is deduced using the Kramers–Kronig relation:

$$\Delta\varepsilon_1^{ib}(\omega,t) = \frac{2}{\pi}\ \text{p.v.}\int_0^{\infty}\frac{\omega'\Delta\varepsilon_2^{ib}(\omega',t)}{\omega'^2-\omega^2}\mathrm{d}\omega'\ , \tag{4.4}$$

where p.v. refers to the Cauchy principal value.

Modification of the electronic distribution additionally induces an increase of the electron-electron scattering rate γ_{e-e}, entering the overall scattering rate appearing in the Drude theory (equation 1.19). This change mostly affects the imaginary part of ε^D (equation 1.18), modifying it as:

$$\Delta\varepsilon_2^D = \frac{\omega_p^2}{\omega^3}\Delta\gamma_{e-e}\ . \tag{4.5}$$

The variation of the electron–electron scattering rate can be estimated using an approximate formula valid for a a thermal electron distribution with temperature T_e [28, 34, 121]:

$$\frac{\Delta\gamma_{e-e}}{\gamma_{e-e}} = \left(\frac{2\pi k_B}{\hbar\omega}\right)^2(T_e^2-T_0^2)\ , \tag{4.6}$$

with $\hbar\gamma_{e-e}\approx 15$ meV at room temperature in the visible range [122]—a value however affected by a large uncertainty, as measurement of the individual contribution of electron–electron scattering to the overall scattering rate $\gamma_0(\omega,T_e,T_L)$ (equation 1.19) is challenging. Combination of equations 4.5 and 4.6 shows that the modification $\Delta\varepsilon_2^D(\omega,\Delta T_e)$

scales as ω^{-5}, which implies in our case that this effect will be more visible in the red–infrared part of the investigated probe-wavelength window. In our model, this term was calculated by using the values of $T_e(t)$ obtained from the numerical simulations, which before the internal thermalization of the electron gas only represents an equivalent temperature. This corresponds to assuming that the modification of γ_{e-e} is equivalent for an athermal distribution and for a thermalized electron gas of same energy density. In the next section, comparison with experimental measurements on gold NDs will allow to determine *a posteriori* if the results obtained within this approximation are consistent with the experimental data.

4.1.2.b Lattice contribution

Lattice heating by energy transfer from the electron gas causes a modification of the dielectric function through different mechanisms, described in the following. This modification was calculated by Stoll *et al.* in a simple form, linear with the lattice temperature T_L [34]. The $\mathrm{d}\varepsilon_{1,2}/\mathrm{d}T_L$ derivatives resulting from this model are the ones used in chapter 3 (figure 3.16, dashed lines), where they were assimilated to $\mathrm{d}\varepsilon_{1,2}/\mathrm{d}T_p$, T_p representing the temperature of the thermalized nano-object. This is justified by the dominant contribution of the lattice to the optical changes in the case of thermalized nano-object, which will be quantified in paragraph 4.1.3.c.

The lattice temperature rise $\Delta T_L = T_L - T_0$ as compared to equilibrium leads to the dilation of the metal, which affects both interband and intraband parts of the dielectric function. The increase of the equilibrium interatomic distance causes a modification of the electronic band structure, mainly because of a reduction of the overlap between orbitals [123]. This modification results in the displacement of the onsets $\omega_{ib,l}$ of the different interband transitions contributing to ε^{ib} (see figure 1.5), whose effect on ε_2^{ib} is evaluated under the assumption of a rigid band shift ($\partial\varepsilon_{2,l}^{ib}/\partial\omega_{ib,l} = -\partial\varepsilon_{2,l}^{ib}/\partial\omega$) [34]:

$$\Delta\varepsilon_2^{ib}(\omega, \Delta T_L) = -\left(\sum_l \frac{\partial\varepsilon_{2,l}^{ib}}{\partial\omega}\frac{\partial\omega_{ib,l}}{\partial T_L}\right)\Delta T_L \ . \tag{4.7}$$

Values of the terms $\partial\omega_{ib,l}/\partial T_L$ are extracted from temperature-dependent ellipsometric measurements on bulk gold, while the $\partial\varepsilon_{2,l}^{ib}/\partial\omega$ derivatives are deduced from bulk measurements of gold dielectric function [121]. The same procedure is repeated in order to evaluate the modification of ε_1^{ib} with the lattice temperature, $\Delta\varepsilon_1^{ib}(\omega, \Delta T_L)$.

Heating of the lattice also induces a modification of the Drude part of the dielectric function $\varepsilon_{1,2}^D$. The imaginary part ε_2^D is impacted by the increase with ΔT_L of the electron-phonon scattering rate γ_{e-ph}, according to:

$$\Delta\varepsilon_2^D(\omega, \Delta T_L) = \frac{\omega_p^2}{\omega^3}\Delta\gamma_{e-ph}(\omega, \Delta T_L) \ . \tag{4.8}$$

To first order, the variation of γ_{e-ph} may be written as $\Delta\gamma_{e-ph} = (\partial\gamma_{e-ph}/\partial T_L)\Delta T_L$, with $\partial(\hbar\gamma_{e-ph})/\partial T_L \approx 0.125$ meV K^{-1} in gold in the visible range [124]. Conversely, modification of ε_1^D results mostly from the decrease of the plasma frequency $\omega_p \propto \sqrt{n_e}$ concomitant to that of the electron density n_e. This term may be written as:

$$\Delta\varepsilon_1^D(\omega, \Delta T_L) = -\frac{\omega_p^2}{\omega^2}\frac{\Delta n_e}{n_e} = \frac{\omega_p^2}{\omega^2} 3\alpha_L \Delta T_L \ , \tag{4.9}$$

with $\alpha_L \approx 1.42 \times 10^{-5}$ K^{-1} the linear dilation coefficient of gold.

4.1.2.c Induced extinction cross-section changes

Once determined the transient modification of the dielectric function $\Delta\varepsilon_{1,2}(\lambda_{pr}, t)$, the nano-object's extinction cross-section change $\Delta\sigma_{ext}(\lambda_{pr}, t)$ is obtained through equation 1.49. To reproduce the signals measured in time-resolved measurements, these extinction changes are then convoluted in the time-domain by the intensity profile of the probe pulse, assumed Gaussian with the same FWHM as the pump pulse.

In summary, our model of the transient modification of the dielectric function contains three terms. The first, denoted $\Delta f \rightarrow \Delta\varepsilon^{ib}$ in the following, is obtained by numerically solving the Boltzmann equation and calculating the induced modification of the interband absorption probabilities through Rosei's model. The second, $\Delta T_e \rightarrow \Delta\varepsilon_2^D$, considers the effect of the modification of the electron–electron scattering rate, and is calculated from the values of the equivalent electron temperature $T_e(t)$ derived from the resolution of the Boltzmann equation. Finally, the $\Delta T_L \rightarrow \Delta\varepsilon$ term regroups the contributions linked to lattice heating and is calculated from the numerically-obtained values of $T_L(t)$.

Similarly to the dielectric function, the transient extinction changes may then be separated into three terms:

$$\Delta\sigma_{ext} = \Delta\sigma_{ext}^{\Delta f \rightarrow \Delta\varepsilon^{ib}} + \Delta\sigma_{ext}^{\Delta T_e \rightarrow \Delta\varepsilon_2^D} + \Delta\sigma_{ext}^{\Delta T_L \rightarrow \Delta\varepsilon} \ , \tag{4.10}$$

each term being associated to the corresponding changes of the dielectric function.

4.1.3 Simplified approach for thermalized electron distributions

We now present a simplification of the model described in the previous section, valid only after the electron internal thermalization (*i.e.* when the lattice and electron gas can be characterized by well-defined temperatures T_e and T_L). In this approach, the evolutions of these temperatures are first determined using the well-known two-temperature model. We then propose a first-order development of the extinction cross-section in ΔT_e and ΔT_L, which will allow us to separate the contributions of electron and lattice temperature dynamics to the transient optical changes occurring in this time range.

4.1.3.a The two-temperature model

When it is possible to define an electronic temperature T_e, its time evolution and that of the lattice temperature T_L may be described by a simple model derived from the Boltzmann equation, the two-temperature model (TTM) [108, 111]. The TTM describes the coupled dynamics of the temperatures T_L and T_e of the lattice and the electron gas, whose interaction is characterized by the electron–phonon coupling constant g:

$$\begin{cases} c_e(T_e)\dfrac{\partial T_e}{\partial t} = -g(T_e - T_L) \\ \quad c_L\dfrac{\partial T_L}{\partial t} = g(T_e - T_L)\ . \end{cases} \tag{4.11}$$

Assuming an electronic heat capacity $c_e(T_e) = aT_e$, this system may be solved numerically, with parameters $a = 65\ \mathrm{J\,m^{-3}\,K^{-2}}$ and $g = 1.7 \times 10^{16}\ \mathrm{W\,m^{-3}\,K^{-1}}$ taken from bulk and nanoparticle measurements on gold, and valid for large nanoparticles [118, 125]. The final equilibrium temperature reached by the two systems (neglecting the coupling with the environment, which involves much longer timescales) writes:

$$T_{eq} = \sqrt{T_s^2 + T_{exc}^2 + 2T_sT_0} - T_s\ , \tag{4.12}$$

with $T_s = c_L/a$. T_{eq} may also be computed by dividing the density of absorbed energy u_{abs} by the specific heat of the metal at room temperature (assuming a not too high ΔT_{eq}), which may be identified to c_L, as the lattice specific heat is about 100 times larger than that of the electrons at room temperature. This method was used previously in chapter 3 to evaluate the experimental values of the ND heating $\Delta T_{eq} = T_{eq} - T_0$.

For weak electronic excitations ($\Delta T_{exc} \lesssim 100$ K), the temperature-dependence of c_e may be neglected. Resolution of system 4.11 in this case, with initial conditions $T_e(t=0) = T_{exc}$ and $T_L(t=0) = T_0$, yields exponential variations of $T_e(t)$ and $T_L(t)$, with char-

acteristic time $\tau_{e-L} = aT_0/g$ (the electron–lattice relaxation time at room temperature T_0):

$$\begin{cases} T_e(t) = T_{eq} + (T_{exc} - T_{eq})e^{-t/\tau_{e-L}} \\ T_L(t) = T_{eq} - (T_{eq} - T_0)e^{-t/\tau_{e-L}} \end{cases} . \tag{4.13}$$

In gold, a $\Delta T_{exc} = 100$ K excitation corresponds to a $\Delta T_{eq} < 1$ K final elevation temperature of the metal. Our experiments on gold nanodisks, with values of ΔT_{eq} of the order of 10 K, correspond to a stronger excitation. The decay of $T_e(t)$ is then not strictly exponential, due to the temperature-dependence of the electronic heat capacity $c_e(T_e)$.

4.1.3.b First-order approximation of the dielectric function changes

To facilitate the interpretation of the complex dynamics and spectral dependences of time-resolved signals, we write the transient change of the dielectric function, whose complete description was given in subsection 4.1.2, in the following simplified form:

$$\Delta\varepsilon_{1,2}(\lambda_{pr}, t) = \frac{\partial\varepsilon_{1,2}}{\partial T_e}(\lambda_{pr})\,\Delta T_e(t) + \frac{\partial\varepsilon_{1,2}}{\partial T_L}(\lambda_{pr})\,\Delta T_L(t) \ . \tag{4.14}$$

This expression separates two contributions related to heating of the electron gas and of the lattice, proportional to their respective temperature changes ΔT_e and ΔT_L. This writing presents the advantage of simply connecting the dynamical changes of the dielectric function to those of the electronic and lattice temperatures. However, it relies on several assumptions:

- thermalization of the quasi-free electron gas must be complete;
- ΔT_e must be low enough so that the $\Delta f \to \Delta\varepsilon^{ib}$ and $\Delta T_e \to \Delta\varepsilon_2^D$ contributions to $\Delta\varepsilon$ (constituting the first term on the right side of equation 4.14), can be considered linear in ΔT_e.

The last term in equation 4.14 corresponds to the $\Delta T_L \to \Delta\varepsilon$ contribution, and is unchanged as compared to its expression in the complete model (paragraph 4.1.2.b).

Electronic thermalization may be considered as complete a few τ_{e-e} (characteristic time of the electron–electron interactions) after the excitation of the metal by the pump pulse, τ_{e-e} being of the order of 500 fs in bulk gold [112]. Note that, when the electron gas is thermalized, its temperature T_e is already largely decreased compared to the equivalent excitation temperature T_{exc} (equation 4.2) due to energy transfer to the lattice. For

example, for a $\Delta T_{exc} = 455$ K excitation (consistent with the experiments, see next section), ΔT_e is close to 120 K after a 2 ps delay following pump absorption.

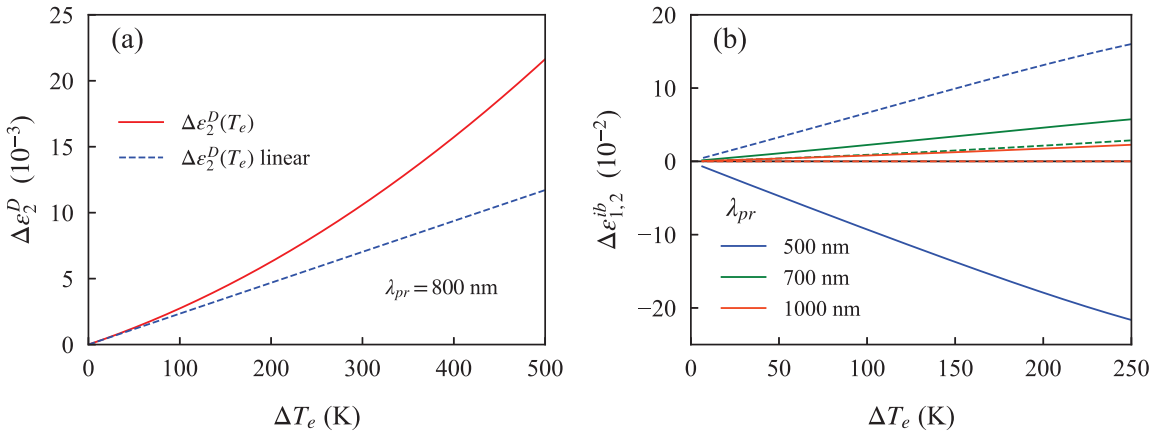

Figure 4.3 – T_e-dependence of the $\Delta T_e \to \Delta\varepsilon_2^D$ (a) and $\Delta f \to \Delta\varepsilon^{ib}$ (b) contributions in gold. (a) $\Delta\varepsilon_2^D(\Delta T_e)$ evaluated from equations 4.6 and 4.5 (red line) and 4.15 (blue dashed line). (b) $\Delta\varepsilon_1^{ib}(\Delta T_e)$ (solid lines) and $\Delta\varepsilon_2^{ib}(\Delta T_e)$ (dashed lines) obtained from a time-dependent calculation with $\Delta T_{exc} = 455$ K, plotted for several probe wavelengths as indicated in the legend.

The first-order development of the $\Delta T_e \to \Delta\varepsilon_2^D$ term (equations 4.6 and 4.5) yields:

$$\Delta\varepsilon_2^D \approx \frac{\omega_p^2}{\omega^3}\left(\frac{2\pi k_B}{\hbar\omega}\right)^2 2\gamma_{e-e}T_0\Delta T_e \ . \tag{4.15}$$

In the considered range of ΔT_e (0–150 K), linearization of the $\Delta T_e \to \Delta\varepsilon_2^D$ term is approximately valid, as shown by figure 4.3a, where the exact formula of $\Delta\varepsilon_2^D$ and its first-order development are plotted as a function of ΔT_e for a probe wavelength λ_{pr} =800 nm, using $\hbar\gamma_{e-e} = 15$ meV.

Concerning the $\Delta f \to \Delta\varepsilon^{ib}$ contribution, evaluation of the $\partial\varepsilon_{1,2}/\partial T_e$ derivatives was performed by dividing the time-dependent $\Delta\varepsilon_{1,2}^{ib}(t)$ values numerically computed for a very small $\Delta T_{exc} = 1$ K initial excitation, by the corresponding values of $\Delta T_e(t)$. The resulting signals are found to be nearly constant after a $\sim$ 2 ps delay, *i.e.* after the completion of electron thermalization. The same calculation was reproduced with $\Delta T_{exc} = 455$ K, yielding linear variations of $\Delta\varepsilon_{1,2}^{ib}$ with ΔT_e until at least 200 K, as illustrated by figure 4.3b. This validates our assumption of linearity of the $\Delta f \to \Delta\varepsilon^{ib}$ term with T_e in the temperature range of our experiments.

The individual $\Delta f \to \Delta\varepsilon^{ib}$ and $\Delta T_e \to \Delta\varepsilon^D$ contributions to the $\partial\varepsilon_{1,2}/\partial T_e$ derivatives, extracted *via* the methods described above, are presented in figure 4.4 as a function of the wavelength.

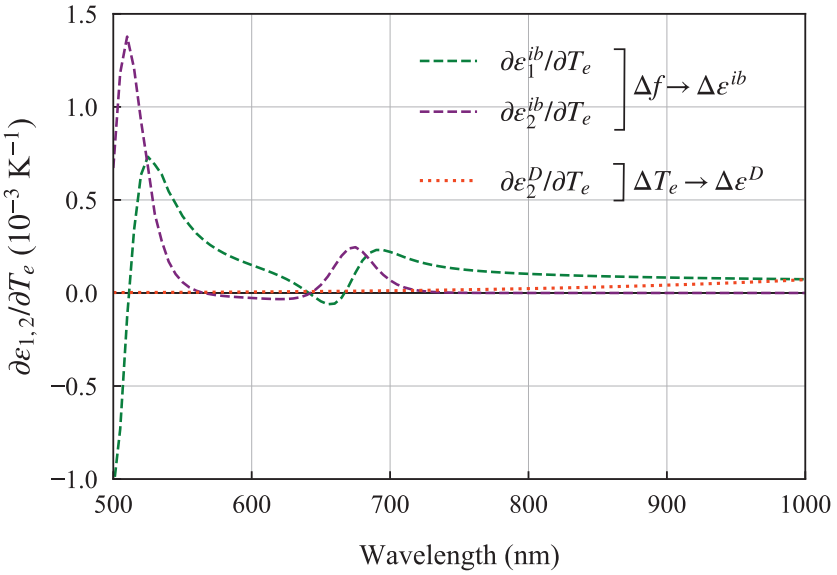

Figure 4.4 – Electronic $\partial\varepsilon_{1,2}/\partial T_e$ derivatives in gold deduced from the complete model described in section 4.1.2, where the $\Delta f \rightarrow \Delta\varepsilon^{ib}$ and $\Delta T_e \rightarrow \Delta\varepsilon_2^D$ contributions are separated.

In the case of nanoparticles, such as the gold NDs studied in this work, the extinction cross-section changes may be written in the following form, inspired by equation 3.8 of chapter 3 describing the thermal part of the extinction changes:

$$\Delta\sigma_{ext}(\lambda_{pr}, t) = A_e(\lambda_{pr})\,\Delta T_e(t) + A_L(\lambda_{pr})\,\Delta T_L(t)\ , \tag{4.16}$$

with

$$\begin{cases} A_e = \dfrac{\partial\sigma_{ext}}{\partial T_e} = \dfrac{\partial\sigma_{ext}}{\partial\varepsilon_1}\dfrac{\partial\varepsilon_1}{\partial T_e} + \dfrac{\partial\sigma_{ext}}{\partial\varepsilon_2}\dfrac{\partial\varepsilon_2}{\partial T_e} \\ A_L = \dfrac{\partial\sigma_{ext}}{\partial T_L} = \dfrac{\partial\sigma_{ext}}{\partial\varepsilon_1}\dfrac{\partial\varepsilon_1}{\partial T_L} + \dfrac{\partial\sigma_{ext}}{\partial\varepsilon_2}\dfrac{\partial\varepsilon_2}{\partial T_L}\ . \end{cases} \tag{4.17}$$

As discussed in chapter 3, following the ND internal thermalization, the observed decay of $\Delta\sigma_{ext}(t)$ reflects the dynamics of heat transfer from the ND to the environment, being proportional to the particle temperature difference to equilibrium $\Delta T_p(t)$ (equation 3.14). In contrast, before the ND internal thermalization, expression 4.16 shows that the transient extinction change is ruled by the temperature dynamics of both the electrons and of the ionic lattice (when these temperatures are well-defined), with wavelength-dependent weights $A_e(\lambda_{pr})$ and $A_L(\lambda_{pr})$. As the two temperatures $T_e(t)$ and $T_L(t)$ evolve towards the same value T_{eq}, equations 4.16 and 3.14 become simultaneously valid, implying that $A_e + A_L = A_p$. Because of the opposite temporal variations of $\Delta T_e(t)$ and $\Delta T_L(t)$, the

relative contributions of the terms $A_e\Delta T_e$ and $A_L\Delta T_L$ in equation 4.16 are expected to change with time, the former being more important at the beginning, when the electron temperature rise largely exceeds that of the lattice, and the latter becoming predominant as the temperatures of the electrons and of the lattice become close. Therefore, the spectral shape of $\Delta\sigma_{ext}(\lambda_{pr}, t)$ should approximately vary from one close to $A_e(\lambda_{pr})$ to one similar to $A_L(\lambda_{pr})$ during the internal thermalization process. This vision is however limited by the fact that the electronic temperature is only defined after ~ 2 ps in the case of gold, when the contribution of the lattice heating has already become non-negligeable compared to that of the electrons in the expression of $\Delta\sigma_{ext}$.

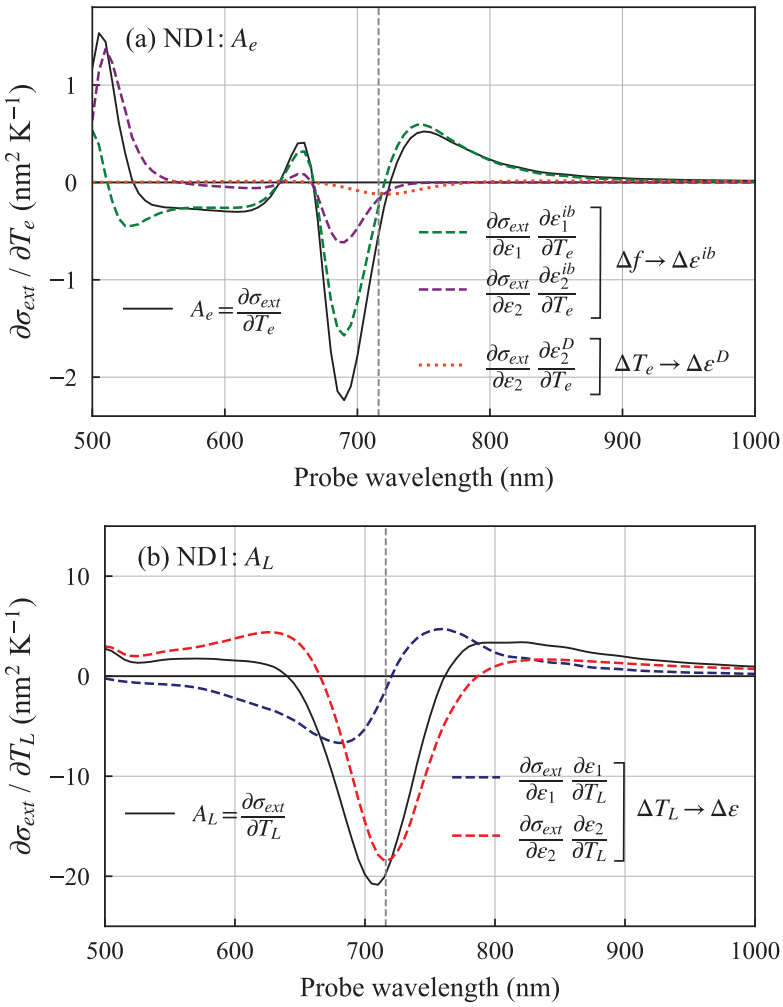

Figure 4.5 – $A_e = \partial\sigma_{ext}/\partial T_e$ **(a) and** $A_L = \partial\sigma_{ext}/\partial T_L$ **(b) spectra computed for gold nanodisk ND1 (plain lines).** The individual contributions of ε_1 and ε_2 modifications by the processes described in the main text are also shown (dashed lines). The LSPR position of ND1 is indicated by dashed vertical lines.

Figures 4.5 and 4.6 present the coefficients $A_e(\lambda_{pr})$ and $A_L(\lambda_{pr})$ obtained for ND1 and

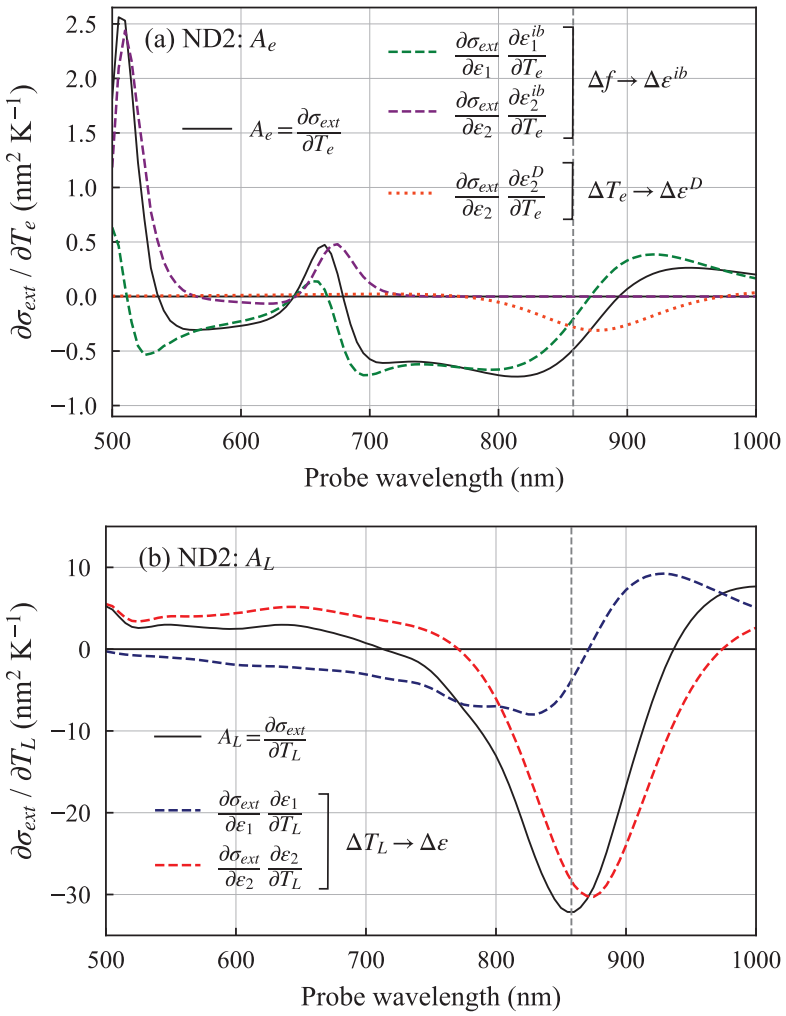

Figure 4.6 – $A_e = \partial\sigma_{ext}/\partial T_e$ **(a) and** $A_L = \partial\sigma_{ext}/\partial T_L$ **(b) spectra computed for gold nanodisk ND2 (plain lines).** The contributions of ε_1 and ε_2 modifications by the processes described in the main text are also shown (dashed lines). The LSPR position of ND2 is indicated by dashed vertical lines.

ND2, the two NDs studied in chapter 3, by multiplying the $\partial\varepsilon_{1,2}/\partial T_e$ and $\partial\varepsilon_{1,2}/\partial T_L$ values from our first-order model with the plasmonic derivatives $\partial\sigma_{ext}/\partial\varepsilon_{1,2}$ (equation 4.17). In these figures, the contributions linked to transient changes of ε_1 and ε_2 are separated, as well as those related to the Drude and interband parts (in A_e spectra). For both NDs, the shapes of the A_e and A_L spectra are dissimilar. Generally speaking, A_e being dominated by variations of ε_1, it presents a dispersive-like shape around the LSPR (associated to a LSPR shift). Conversely, A_L being dominated by changes of ε_2, it presents a large negative peak (associated to a LSPR broadening). However, more complex details can be observed from the quantitative model. For ND1, several sign changes of A_e are observed in the 500–650 nm range, which are absent for A_L. For the larger nanodisk ND2, the difference between the two spectra is even more striking: while a single broad

peak is observed in A_L, close to the LSPR central wavelength, A_e displays a more complex shape, with a plateau between 700 and 830 nm and several sign changes in the 500–700 nm range, similarly to ND1.

Additionally, figures 4.5 and 4.6 allow to evaluate the specific effect on the time-resolved signals of changes of the Drude contributions—related to the electron–electron scattering rate modification induced by changes of T_e—, $(\partial\sigma_{ext}/\partial\varepsilon_2)\,(\partial\varepsilon_2^D/\partial T_e)$ (orange dotted lines). While this contribution is very small for ND1, it is more substantial for ND2, whose LSPR is in the infrared range, because of the λ^5 dependence of this effect (equations 4.5 and 4.6).

4.1.3.c Comparison between the complete and simplified models

Figure 4.7 shows the (equivalent) electron and lattice temperatures changes $\Delta T_e(t)$ and $\Delta T_L(t)$ deduced from the numerical resolution of the Boltzmann equation (equation 4.1) for a $\Delta T_{exc} = 455$ K excitation temperature. These temperature changes are compared to the values predicted by the TTM, using as initial condition the temperatures given by the complete model at $t = 2$ ps, *i.e.* when the electron temperature becomes well-defined ($\Delta T_e \approx 120$ K and $\Delta T_L \approx 5$ K). A 820 fs (FWHM) pump pulse duration was assumed in the numerical model, close to the experimental value, whose estimation is discussed later in this chapter. The agreement between the two models is excellent in the considered time range.

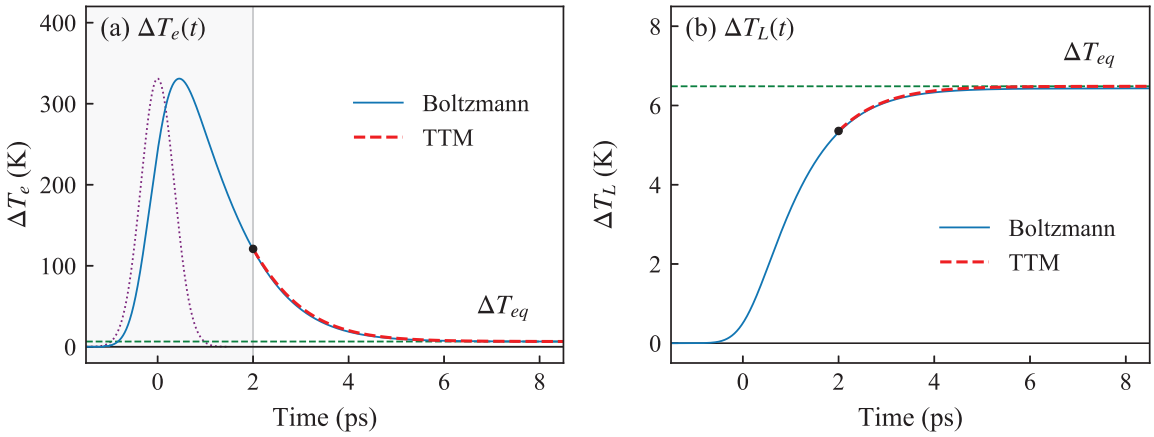

Figure 4.7 – $\Delta T_e(t)$ (a) and $\Delta T_L(t)$ (b) variations derived from the resolution of the Boltzmann equation or (for $t \geqslant 2$ *ps*) given by the TTM for a $T_0 = 295$ K initial temperature and a $\Delta T_{exc} = 455$ K excitation of gold. The purple dotted line in (a) represents the temporal profile of the excitation used (a Gaussian function with a 820 fs FWHM centered at $t = 0$), arbitrarily normalized. The grey area represents the temporal region where the electron gas is athermal. The dashed green lines indicate the final temperature increase $\Delta T_{eq} \sim 6.5$ K reached by both the electrons and the lattice.

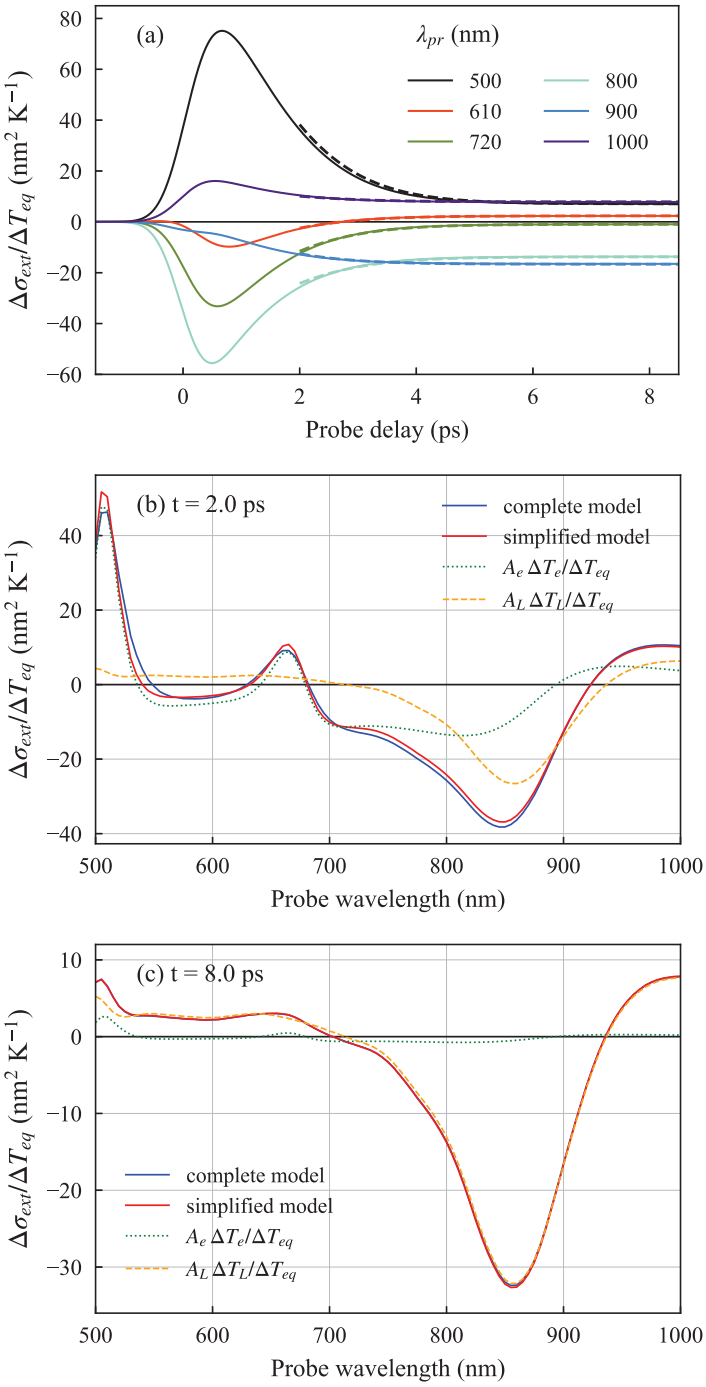

Figure 4.8 – Normalized extinction cross-section changes calculated for gold nanodisk ND2 from the complete and simplified models, plotted as a function of time for various λ_{pr} values (a) or of the probe wavelength at delays $t = 2$ ps (b) and $t = 8$ ps (c). The plain and dashed lines in (a) respectively correspond to the complete and simplified models, while the color code is indicated in the legend. In (b) and (c), the contributions of the electron and lattice temperature changes in the simplified model are also shown (green dotted and orange dashed lines, respectively).

Figure 4.8 presents the extinction cross-section changes calculated either from the complete model of from the simplified one (TTM + first-order development of $\Delta\varepsilon$), shown either in the time-domain (a) or as a function of the probe wavelength at probe delays of 2 ps (b) and 8 ps (c). In this figure, the extinction changes $\Delta\sigma_{ext}$ are divided by the final equilibrium temperature increase ΔT_{eq}—a choice of normalization identical to that made in chapter 3, that will be discussed in the following section. The calculations were performed with the same parameters as in figure 4.7 ($\Delta T_{exc} = 455$ K, 820 fs pump pulse FWHM), using the plasmonic derivatives of ND2 as an example. No convolution by the probe pulse was performed in the complete model (see paragraph 4.1.2.c), in order to facilitate the comparison with the simplified model. In figure 4.8a, the good agreement between the two models (plain and dashed lines) allows to further validate the hypotheses underlying the first-order development of ε in this time range, namely, that the electron thermalization is complete, and that the approximate linearity of the $\Delta f \rightarrow \Delta\varepsilon^{ib}$ and $\Delta T_e \rightarrow \Delta\varepsilon^{D}$ terms with ΔT_e is verified. The agreement between the two models is also visible in figures 4.8b–c (blue and red plain lines), the minor difference observed at $t = 2$ ps mostly reflecting the existence of a residual population of athermal electrons. The contributions of the electrons and of the lattice in the simple model are also shown (green dotted lines and orange dashed lines, respectively). While their spectral shapes (which are those of $A_e(\lambda_{pr})$ and $A_L(\lambda_{pr})$) are independent of time, their relative amplitudes vary from being approximately equivalent at $t = 2$ ps (when $\Delta T_e \approx 25\Delta T_L$, see figure 4.7) to a final distribution where the lattice contribution is largely predominant at $t = 8$ ps (when $\Delta T_e = \Delta T_L = \Delta T_{eq}$).

Note that, during the subsequent cooling of the ND, the particle remains internally thermalized, with $\Delta T_e(t) = \Delta T_L(t) = \Delta T_p(t)$. Therefore, the $[A_e(\lambda_{pr})\Delta T_e(t)]/[A_L(\lambda_{pr})\Delta T_L(t)]$ ratio remains identical to its value at $t = 8$ ps. Figure 4.8c thus allows to appreciate the small error made in the analysis of the amplitude A_p of the thermal component of the extinction change, when we assimilated the $\mathrm{d}\varepsilon_{1,2}/\mathrm{d}T_p$ derivatives to their $\partial\varepsilon_{1,2}/\partial T_L$ counterparts, by neglecting the electronic contribution (*i.e.* by assuming $A_p = A_e + A_L \approx A_L$).

4.1.4 Summary

The two models described in this section are complementary and serve different purposes. The complete model (subsections 4.1.1 and 4.1.2) is intended to quantitatively describe the experimental results that will be presented in the next section over the whole investigated time range, from the beginning of the excitation to the complete internal thermalization of the metal, taking into account the pump and probe pulse durations. Conversely, the simplified model, valid only after the electron internal thermalization (~ 2 ps in the experimental conditions), does not primarily aim at reproducing the experimental data, but rather at providing a simple interpretation of the time-resolved

signals. Derived from the complete model, its interest lies in the possibility to write the transient extinction changes in the form of equation 4.16, reducing the description of the complex time and probe wavelength dependences of $\Delta\sigma_{ext}(\lambda_{pr}, t)$ to those of the spectral dependences of amplitudes $A_e(\lambda_{pr})$ and $A_L(\lambda_{pr})$ (figures 4.5 and 4.6) and of the time dependences of temperatures $\Delta T_e(t)$ and $\Delta T_L(t)$ (figure 4.7). Within the validity range of this model, the A_e and A_L spectra provide the sensitivity of time-resolved measurements to temperature variations of the electron gas and of the ionic lattice, respectively. Because their spectral shapes are different, it should in particular be possible to find probe wavelengths that selectively cancel one of the two amplitudes. This model will therefore be a useful guide in the analysis of experimental signals, which is the object of the next section.

4.2 Experimental work

4.2.1 Samples and time-resolved measurements

Measurements of the transient optical response occuring at <10 ps pump–probe delays were performed on the same gold NDs (ND1 and ND2) that were used in the study of the probe-wavelength dependence of the amplitudes of thermal signals presented in chapter 3. The two series of measurements were in fact executed conjointly in order to perform only once the alignment of pump and probe beams and the determination of all parameters (pump power, pump and probe beam sections) allowing quantitative analysis of the signals. For each investigated probe wavelength, short- and long-timescale signals were acquired one after the other, the large transmission change due to the electronic excitation by the pump pulse being used to optimize the 3-dimensional positioning of the ND in the beams.

As compared to the long-timescale measurements presented in chapter 3, the time step was reduced from 4 ps down to 30 fs (corresponding to a 9 µm displacement of the translation stage), while the lock-in amplifier time constant was maintained at 100 ms. To verify that the detailed dynamics was correctly captured in the measured signals, several control measurements were performed using lower values for these two parameters, leading to a better temporal resolution but increasing the measurement time. Signals measured in these different ways all led to the same dynamics, confirming the validity of our choice.

To avoid the irreversible modification of the properties of the NDs discussed in chapter 3, low pump fluences ($< 1\ \mathrm{J\,m^{-2}}$) were used and signal averaging was performed on a limited number of traces (< 10) to limit the exposure time.

4.2.2 Determination of ND initial heating

While keeping the temperature increase constant was not crucial in the former study of the thermal amplitude A_p because of the proportionality of the signals to pump fluence after a 10–20 ps delay (provided no irreversible modification of the signals occured during the measurement), it plays a greater role in the present study of time-resolved signals previous to thermalization. Indeed, the kinetics of electron–lattice energy exchanges depends on the amount of energy injected by the pump pulse. This is illustrated by figure 4.9 presenting measurements of the transient response of ND1 at $\lambda_{pr} = 700$ nm for different pump fluences, yielding equivalent temperature increases ΔT_{eq} in the 2–20 K range. While the initial rises of the signals share the same dynamics and display approximate proportionality to the pump fluence, the signal decay becomes slower as the excitation power increases. As noted in paragraph 4.1.3.a, this is a consequence of the $c_e \propto T_e$ dependence of the electronic specific heat. In order to safely compare different experimental signals, one must therefore make sure that the energy injected by the pump pulse shows weak variations between the measurements.

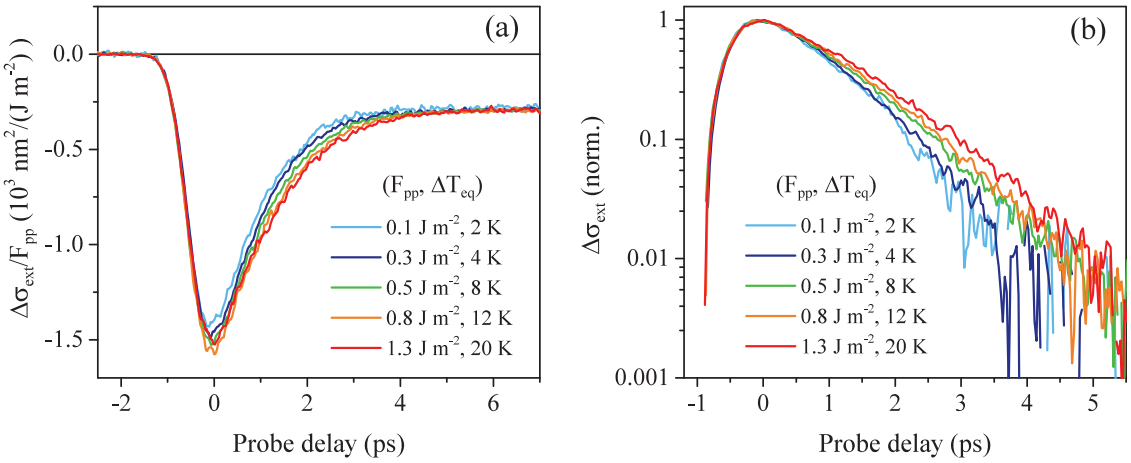

Figure 4.9 – Effect of pump fluence on the dynamics of the short-timescale extinction changes, measured on gold nanodisk ND1 at $\lambda_{pr} = 700$ nm and $\lambda_{pp} = 410$ nm. (a) Transient extinction cross-section changes divided by the pump fluence F_{pp}. Values of F_{pp} are given in the legend, as well as the corresponding equilibrium ND temperature increases ΔT_{eq}. (b) Same signals, normalized after subtraction of the offset corresponding to long delays (in semi-log scale).

During time-resolved measurements, successively performed with many probe wavelength values, an attempt was made to control the pump power so that the ND initial heating ΔT_{eq}, calculated using equation 3.12, remained relatively constant. This goal was however complicated by the fact that some of the parameters involved in the determination of ΔT_{eq}, such as the pump spot area S_{pp} or the ND absorption cross section at pump

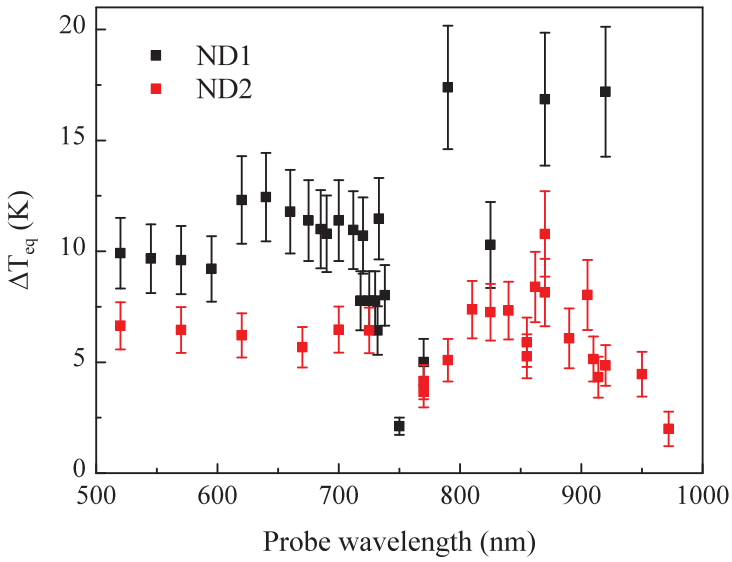

Figure 4.10 – ND heating ΔT_{eq} after the nano-object internal thermalization in the measurements performed on gold nanodisks ND1 and ND2. Calculation of the error bars was performed as described in paragraph 3.3.1.b.

wavelength $\sigma_{abs}(\lambda_{pp})$, vary with experimental conditions. Values of ΔT_{eq} obtained after complete analysis of all signals measured on ND1 and ND2 (short- and long-timescale) are reported in figure 4.10. Their average values and standard deviations are (10±3) K and (6±2) K, respectively. A weak dispersion of ΔT_{eq} was achieved for signals with a probe beam delivered by the OPO (λ_{pr} in the 500–740 nm range), for which the pump wavelength was fixed at $\lambda_{pp} = 410$ nm. For $\lambda_{pr} > 750$ nm (output of the Ti:Sapphire laser used as probe beam), the pump wavelength varies as $\lambda_{pp} = \lambda_{pr}/2$ as it is produced by frequency doubling of the probe. This wavelength change, necessarily associated to modification of the beam alignment and divergence, leads to unavoidable variations of its transmission through the objective and its size in the sample plane. Additionally, the distance between the waists of the two beams is important when probing in the IR (with a pump in the blue), as the objective does not fully compensate for chromatic aberrations in this range. Finally, the maximal incident power achieved for λ_{pp} between 375–390 nm (λ_{pr} = 750–780 nm) was reduced because of the poor transmission of the optical components in the UV. Pump power was also too low for measurements with λ_{pr} close to 1000 nm, *i.e.* near the end of the operating range of the Ti:Sapphire laser.

Signals were normalized to take into account the differences in amplitude due to variations of the pump fluences and wavelengths. The time-resolved $\Delta Tr/Tr$ signals, once converted into extinction cross-section changes $\Delta\sigma_{ext}$, were divided by their respective values of ΔT_{eq}. This choice of normalization is the same as the one made in chapter 3 in the context of the analysis of the amplitudes of the thermal components of time-

resolved signals. Therefore, the experimental transient spectra, with such normalization, are expected to identify with the A_p spectra (neglecting the presence of oscillations) immediately following the internal thermalization of the ND.

This normalization procedure is relevant only if ΔT_{eq} is weak or weakly dispersed within the measurements. Indeed, the proportionality between time-resolved signals and the total density of absorbed energy u_{abs} (or alternatively, the equivalent temperature increase $\Delta T_{eq} = u_{abs}/c_{Au}$) is verified only in the low-excitation regime. Experiments, however, go beyond this regime, as is shown in figure 4.9 by the change of dynamics observed between measurements with fluences corresponding to $\Delta T_{eq} = 2$, 4 and 8 K. Therefore, in the analyses of experimental time-resolved signals performed in the following of this chapter, one should keep in mind that differences in the signal dynamics may be partly attributed to the dispersion of ΔT_{eq} values shown in figure 4.10.

4.2.3 Measurement results

Examples of experimental time-resolved signals recorded on ND1 and ND2 are shown in figure 4.11. As with the long-timescale signals discussed in chapter 3 (figure 3.14), large variations of the maximal values and signs of the transient extinction changes are observed as a function of the probe wavelength. However, the signals measured at short timescales also display very different dynamics depending on the probe wavelength. This is more clearly evidenced by figure 4.12, where the signals have been normalized by their maxima in absolute value, $\Delta\sigma_{ext}|_{max}$. Almost all signals show a fast rise around delay $t = 0$ ps, followed after $t = 0.8$–1.5 ps by a decay leading to a constant value in the $t = 5$–8 ps range. However, the values of the normalized signals at $t = 8$ ps, corresponding to the ratio $\Delta\sigma_{ext}(t = 8\,\text{ps})/\Delta\sigma_{ext}|_{max}$, undergo large variations with the probe wavelength, being in some cases close to 1 (*e.g.* at $\lambda_{pr} = 855$ nm for ND2), close to 0 (at $\lambda_{pr} = 700$ nm for ND2) or slightly negative (at $\lambda_{pr} = 735$ nm for ND1 and $\lambda_{pr} = 905$ nm for ND2). Additionally, the signal measured with $\lambda_{pr} = 890$ nm on ND2 presents no initial peak, but instead features a slow rise between $t = 0$ and ~ 5 ps, followed by a plateau.

In figure 4.13, the experimental extinction cross-section changes of ND1 and ND2, divided by the ND equilibrium heating ΔT_{eq}, are shown as a function of the probe wavelength at selected pump-probe delays. Several differences may be noted between the two NDs. For ND1 (figure 4.13a), the shape of the transient spectrum undergoes little modification in the considered time range, while its amplitude first increases between $t = 0$ ps and $t = 0.7$ ps, then decreases until ~ 6 ps, and remains constant in the next few ps (not shown). This spectrum shows at all times a marked negative peak near 700 nm (slightly blue-shifted as compared to the position of the LSPR, indicated by the dashed line), as well as sign changes on both sides of this peak (at ~ 620 and ~ 730 nm). For ND2

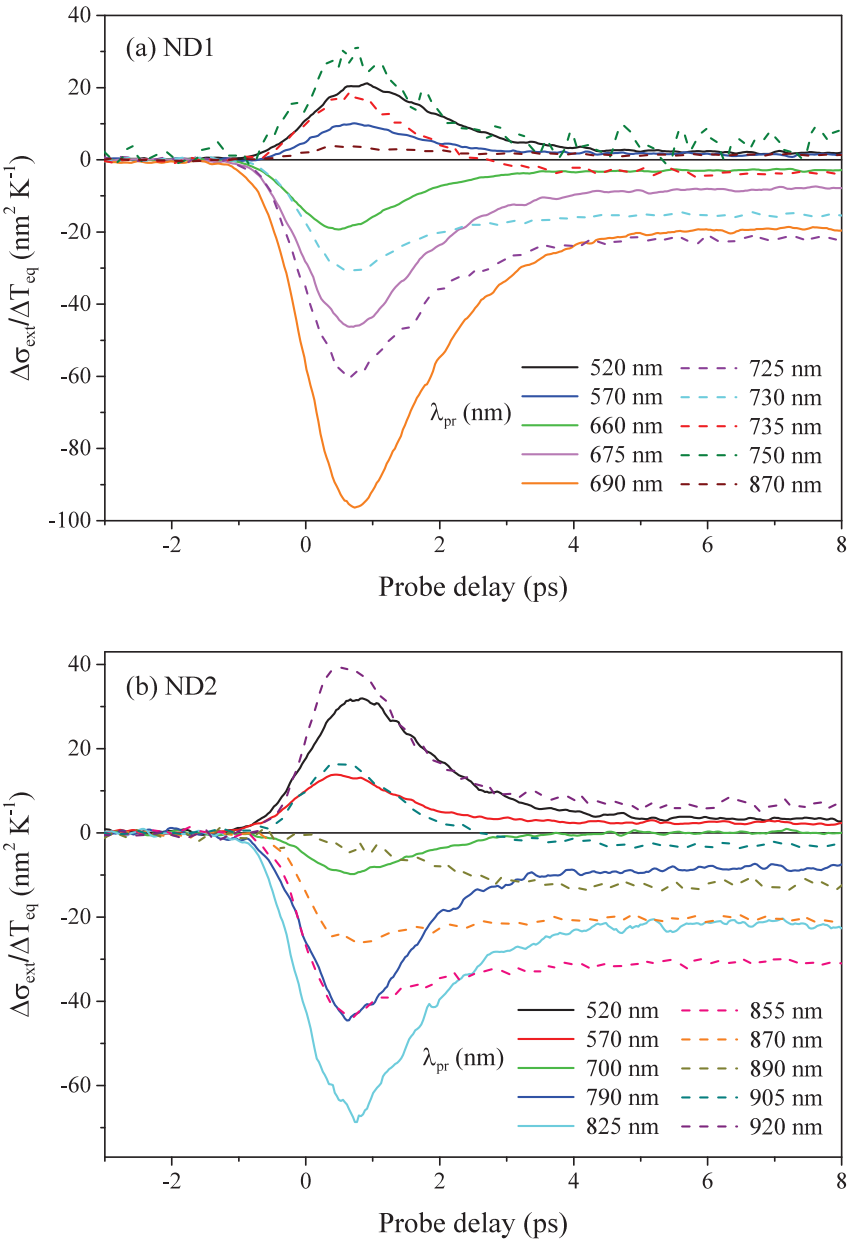

Figure 4.11 – Short-timescale time-resolved signals measured on gold nanodisks ND1 (a) and ND2 (b) at several probe wavelengths, as indicated in the legend. The extinction spectra of these NDs may be found in figure 3.9. The LSPR positions are ∼715 nm and ∼860 nm for ND1 and ND2, respectively.

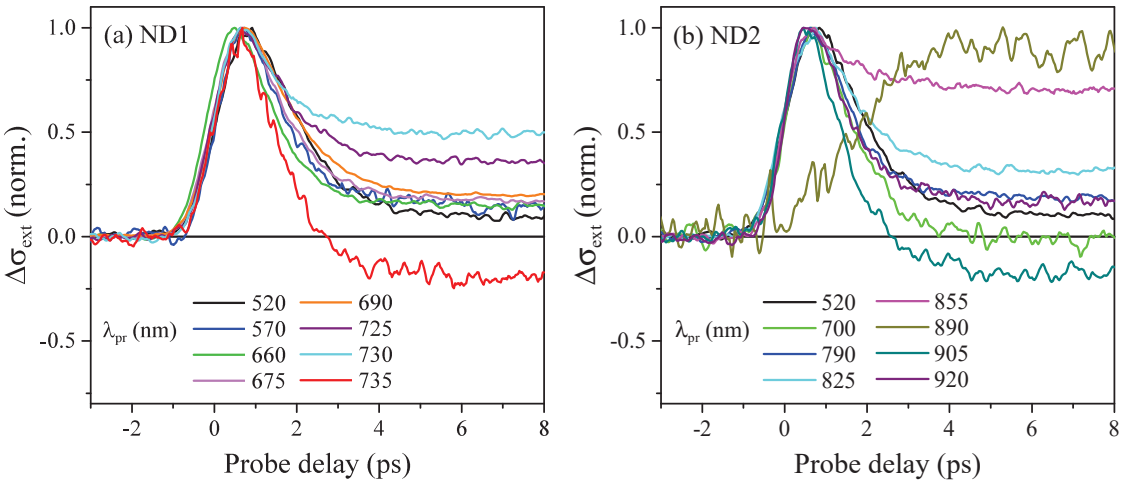

Figure 4.12 – Short-timescale time-resolved signals measured on gold nanodisks ND1 (a) and ND2 (b) at several probe wavelengths (indicated in the legend), normalized to their maximal value. The color code used is the same as in figure 4.11.

(figure 4.13b), similar variations of the signal amplitude with the pump–probe delay are observed for most wavelengths, but the spectral shape undergoes more important changes in time, with a red-shift of its minimum for longer delays. In the first ∼2 ps, the spectrum displays a negative peak near 830 nm and a positive one near 920 nm, thus showing a similarity to the $\partial\sigma_{ext}/\partial\varepsilon_1$ plasmonic derivative (figure 3.9d). After 3 ps, the spectrum is more similar to the $\partial\sigma_{ext}/\partial\varepsilon_2$ component, featuring a large negative peak near the LSPR central position (indicated by the dashed line). The positions of the sign changes also vary, from ∼ 680 nm and ∼ 890 nm at $t = 0$ ps to ∼ 700 nm and ∼ 920 nm at $t = 8$ ps. Another difference between the spectral responses of the two NDs lies in the ratio between the maximal amplitudes reached by the negative peaks at the end of the initial signal rise (at ∼0.5 ps) and in the final plateau (at ∼8 ps), this ratio being approximately 4 for ND1 and only 2 for ND2.

As we will see in the next section, the probe-wavelength dependence of the amplitudes and temporal shapes of the signals can be partly understood at the light of the simple model developed in section 4.1.3 as resulting from a modification of the different weights of the contributions related to the temperature changes of the electrons and of the lattice in equation 4.16. However, this approach, valid only after the establishment of a well-defined electronic temperature, does not account for the differences observed in the dynamics for pump–probe delays < 2 ps, such as the variations in the temporal position of the maximum. Such effects can only be accounted for by a model describing the precise evolution of the electron distribution $\Delta f(t)$ and its consequences on the dielectric function changes $\Delta\varepsilon(\lambda_{pr}, t)$. Therefore, the complete model given in subsections 4.1.1 and 4.1.2 will be used for a quantitative comparison with the experimental signals in the next section. Note that in figures 4.11 and 4.12 the temporal origin of the signals

(defined as the instant at which the pump and probe pulses present a maximal overlap) was determined by comparison with the complete model, as our measurement method does not allow a precise determination of this information.

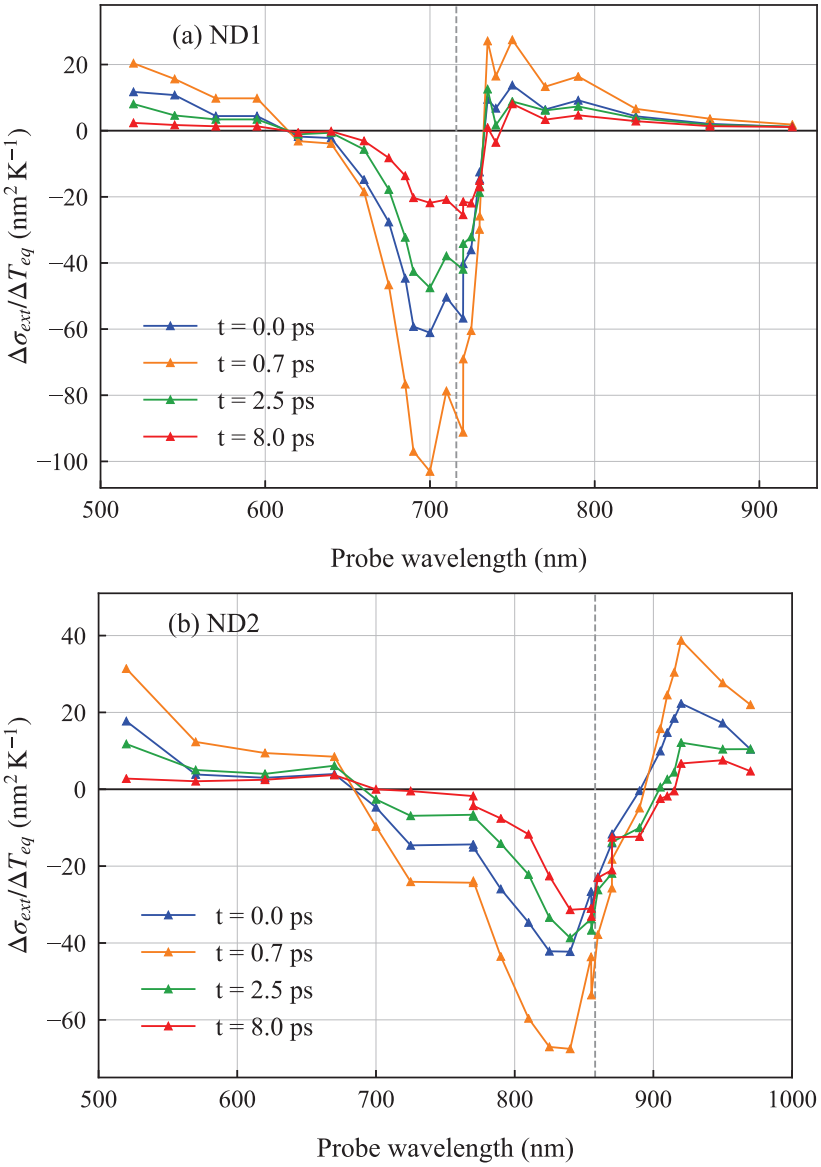

Figure 4.13 – Transient extinction spectra of gold nanodisks ND1 (a) and ND2 (b) measured at selected probe delays, as indicated in the legend. The vertical dashed lines indicate the LSPR central wavelength.

4.3 Comparison of experimental signals to models and interpretation

4.3.1 Adjustment of the dynamical parameters

In order to try to model the experimental results using the complete description made in section 4.1, based on the computation of the electron and lattice dynamics and of the transient extinction changes that they induce, one first needs to determine the values of the unknown parameters entering the model. Practically, this is achieved by successively varying these parameters in order to optimize the agreement between the experimental curves and our model.

Two parameters in the calculations need to be adjusted: the FWHM of the temporal profiles of the pump and probe pulses, assumed equal, and the electron-lattice relaxation time at room temperature, τ_{e-L}, which is known to be of the order of 1 ps in gold [5, 106, 118, 126] but may slightly vary from one sample to the other (*e.g.* depending on the density of crystalline defects [127])[1]. Although these parameters mostly affect the dynamics of the signal rise and decay, respectively, their estimation from a single pump-probe signal is not straightforward in the general case. Indeed, the experimental rise times show a dependence on the probe wavelength, and are expected to coincide with the pump-probe cross-correlation only in specific conditions, discussed below. Likewise, the decay times are not constant in the experimental signals, both because of the already noted differences in the equilibrium heatings ΔT_{eq} (figure 4.10), and because of the intrinsic probe-wavelength dependence of the decay dynamics, which will be clarified in this chapter.

Although their description is not simple, these dependences of the signal dynamics on the probe wavelength are fully included in the complete model. Therefore, an approach based on systematic fitting of the rises and decays of both the experimental and calculated signals was developed. The adjustment of the simulation parameters (the FWHM of the pump and probe pulses and the electron–lattice relaxation time) is then performed by attempting to reach the same values of rise and decay times when comparing the measured and simulated curves. This procedure was deemed superior to direct signal-to-signal comparison, as the latter method is unable to provide a global criterion for parameter adjustment because of the variable quality of the agreement between experimental and computed signals in the set of investigated wavelengths.

[1] See discussion p. 137

4.3.1.a Fit of the signal rise and pump/probe pulse durations

To determine the duration of the pump and probe pulses (assumed equal), the initial rises of the experimental signals are fitted by an *ad-hoc* function, defined below, and compared to fits by the same function of simulated signals calculated with an arbitrary pulse duration. This operation is repeated with a different value of this parameter until a good agreement is found between the fits of experimental and calculated signals.

When the probe photon energy is small enough compared to the interband transition threshold (around 2.4 eV in gold [34]), the rise of the measured signals follows the temporal evolution of the energy injection into the electron gas, $\Delta u_e(t)$ (at times shorter than the time constant τ_{e-L} of electron–lattice coupling) [107]:

$$\Delta\sigma_{ext}(t) \propto \Delta u_e(t) \propto \int_{-\infty}^{t} \mathrm{d}t' \; I_{pp}(t') \;, \tag{4.18}$$

with $I_{pp}(t)$ the pump pulse temporal intensity profile. The pump-probe signal displays the same dynamics convoluted by the probe pulse profile $I_{pr}(t)$:

$$\begin{aligned}
\frac{\Delta Tr}{Tr}(t) &\propto \int_{-\infty}^{+\infty} \mathrm{d}t' \; I_{pr}(t')\Delta u_e(t-t') && (4.19)\\
&\propto \int_{-\infty}^{+\infty} \mathrm{d}t' \; I_{pr}(t') \int_{-\infty}^{t-t'} \mathrm{d}t'' \; I_{pp}(t'') && (4.20)\\
&\propto \int_{-\infty}^{t} \mathrm{d}t'' \; \int_{-\infty}^{+\infty} \mathrm{d}t' \; I_{pr}(t')I_{pp}(t''+t') && (4.21)\\
&\propto \int_{-\infty}^{t} \mathrm{d}t'' \; (I_{pr} \star I_{pp})(t'') \;, && (4.22)
\end{aligned}$$

where $\star$ denotes the cross-correlation product. For pump and probe pulses with Gaussian temporal shapes of the form:

$$I(t) \propto e^{-4\ln(2)\frac{t^2}{\tau^2}} \;, \tag{4.23}$$

with τ the pulse FWHM, the cross-correlation of I_{pp} and I_{pr} is also a Gaussian function, with a FWHM equal to $\tau_{cc} = (\tau_{pp}^2 + \tau_{pr}^2)^{1/2}$. Integration of this quantity from $-\infty$ to t yields:

$$\int_{-\infty}^{t} \mathrm{d}t' \; e^{-4\ln(2)\frac{t'^2}{\tau_{cc}^2}} = \frac{1}{2}\left[1 + \mathrm{erf}\left(\frac{2\sqrt{\ln 2}\; t}{\tau_{cc}}\right)\right] , \tag{4.24}$$

where we used the error function erf, defined as $\mathrm{erf}(t) = \frac{2}{\sqrt{\pi}} \int_{-\infty}^{+\infty} \mathrm{d}t \; e^{-t^2}$.

The temporal shape defined by equation 4.24 was used to fit the rises of all experimental and calculated signals by replacing the FWHM of the pump–probe cross-correlation τ_{cc} by an empirical rise time τ_r, which was left as a free parameter. The fit was performed between delay −2 ps and the end of the rise (at the maximum of the signal).

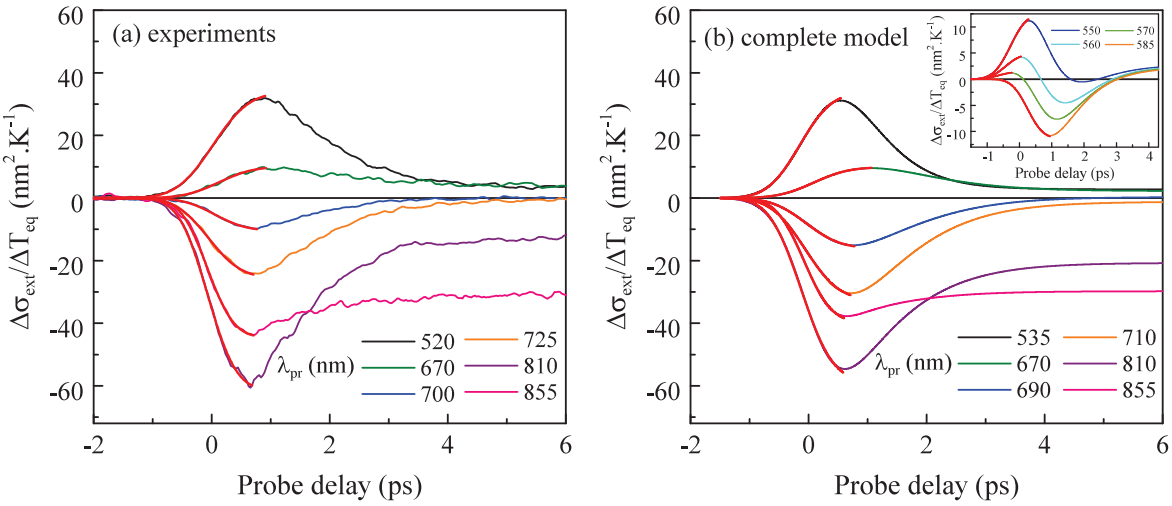

Figure 4.14 – Fitting of the signal rise of experimental (a) and calculated (b) transient signals of gold nanodisk ND2 by the function defined in equation 4.24.

Examples of experimental and calculated signals for ND2 fitted with this function are given in figure 4.14. The fit was good for almost all experimental signals of both NDs (as shown in figure 4.14a for several signals measured on ND2). Minor issues arose in the fitting process of calculated signals in specific spectral regions, as illustrated in the inset of figure 4.14b. In these zones, the model predicts the existence of signals with complex temporal shapes, featuring two peaks of opposite signs in the first few ps. The fitting function of equation 4.24 is not appropriate for such signals, therefore leading to important deviations of the fitting parameter τ_r from the value of the pump–probe cross-correlation τ_{cc}. Such signal shapes were however not observed experimentally, corresponding to signals with low amplitudes (inset of figure 4.14b), close to sign changes of the initial peak.

The values of τ_r obtained by fitting the experimental and calculated signals for ND1 and ND2 are reported in figure 4.15. The calculations were performed with excitation

equivalent temperatures ΔT_{exc} = 570 K and 455 K for ND1 and ND2, corresponding to the average measured temperature elevations ΔT_{eq} = 9 K and 6.5 K. The pump and probe pulse FWHM were assumed equal and fixed at 820 fs (corresponding to τ_{cc} = 1160 fs), chosen by trial-and-error in attempting to match the overall trends of the τ_r parameters from the experiments and the model for the two NDs. Tests allowed to verify that the rise times in the simulations were independent of the excitation energy and of the electron-lattice time τ_{e-L}. The grey boxes in figure 4.15 correspond to the previously discussed signals featuring a sign change in the first 1–2 ps (see inset of figure 4.14b), for which the fitting approach is not meaningful.

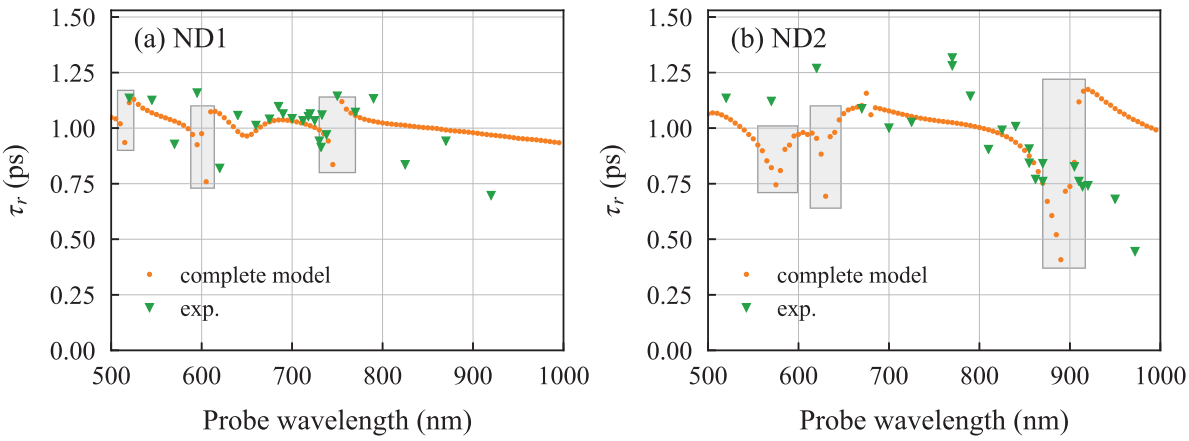

Figure 4.15 – Rise times τ_r for gold nanodisks ND1 (a) and ND2 (b) deduced from the fitting of experimental (green triangles) and computed (orange dots) transient signals. 820 fs pump and probe pulse durations were used in the calculation, leading to an optimal general agreement between the values of τ_r extracted from the experiments and from the calculations. The grey regions correspond to spectral ranges where the fitting function (equation 4.24) is unable to correctly reproduce the computed signals, as described in the main text.

An important decrease of τ_r is observed in the experimental data as the probe moves towards the infrared, especially visible for ND2. It is possible that the pump and probe pulse durations presented real variations with wavelength during the measurements, while they were assumed constant in the simulations. A wavelength dependence of the pump and/or probe pulse durations could indeed account for the constant decrease of τ_r seen in ND2 (and with less clarity in ND1) for λ_{pr} between 780 and 980 nm (also corresponding to variable $\lambda_{pp} = \lambda_{pr}/2$).

The value of the pump and probe pulse FWHM durations provided by the latter analysis, 820 fs, is much larger than the ones of the femtosecond sources, the Ti:Sapphire laser nominally delivering 150 fs pulses. The BBO crystals (used for second-harmonic generation in the OPO and to generate the pump beam), which are known to extend the pulse durations, as well as the high number of optical components encountered along the laser

paths (in particular, the microscope objective), account for such temporal elongation of the pulses. In future experiments, prism compression of the pulses should be used if necessary.

4.3.1.b Signal decay and electron–lattice relaxation time

The electron–lattice relaxation time τ_{e-L} describes the time needed for the energy injected in the electrons to be transferred to the lattice in the low excitation regime, *i.e.* when the temperature difference $\Delta T_e = T_e - T_0$ is low enough so that the temperature dependence of the electronic specific heat can be neglected. In this case, resolution of the TTM yields an exponential decay of $\Delta T_e(t)$ and of $\Delta u_e(t) = c_e \Delta T_e(t)$, the electron excess energy, with time constant τ_{e-L} (see paragraph 4.1.3.a). Therefore, to directly extract the value of τ_{e-L} from a single time-resolved measurement using its decay kinetics, two conditions must be met:

- The excitation must be weak enough so that the decay of $\Delta u_e(t)$ is exponential;
- The extinction cross-section changes must reflect the dynamics of $\Delta u_e(t)$, which requires a probe wavelength far from the interband region and from any resonance in the extinction spectrum (see paragraph 4.3.1.a). Moreover, there must be no contribution of the lattice heating to the transient extinction changes (which corresponds to $|A_L| \ll |A_e|$, within the hypotheses of our simple model of subsection 4.1.3).

The first of these conditions is not met in our experiments, since, as discussed in subsection 4.2.2, excitation is in general too high. This explains why the decays of most signals measured on ND1 and ND2 cannot be fitted by a monoexponential function. Therefore, accessing the value of τ_{e-L} required in the calculation demands a different approach. Similarly to what was done in the last paragraph to determine the pump and probe pulse duration, the decays of all experimental and calculated signals were fitted by an *ad hoc* function, and the comparison of the fitting results allowed to adjust τ_{e-L} by trial-and-error.

The fitting function used is a monoexponential decay of the type $Ae^{-t/\tau_d} + y_0$, with time constant τ_d (referred to as *decay time*), amplitude A, and offset y_0. Fitting is performed from the instant where the signal is the average between the extremal value preceding the decay and the value reached at the end of the internal thermalization, near 8 ps (the latter value defining y_0). This definition allows fitting only the end of the decay, for which the agreement with an exponential is generally correct. Indeed, this part corresponds to lower values of the (equivalent) electronic temperature T_e as compared to its maximal value, reducing the effect of the $c_e(T_e)$ temperature dependance which is at the origin of non-exponential decays. Examples of experimental and calculated signals

fitted by this function are shown in figure 4.16. The inset of figure 4.16b illustrates a fitting issue occuring for specific signals (here, with $\lambda_{pr} = 640\ nm$) which remain quasi-constant after the absorption of the pump pulse. These signals are inaccurately fitted by the exponential decay, which often leads to divergent time constant τ_d. These signals, which occur around an exchange of the relative importance of the electron and lattice contributions, will be discussed in more detail in the next paragraph.

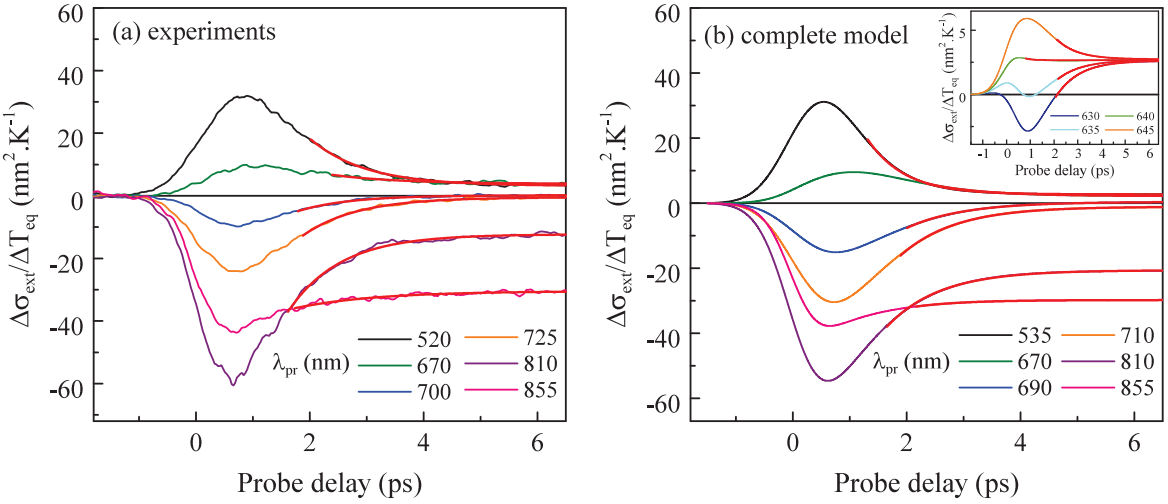

Figure 4.16 – Fitting of the signal decay of experimental (a) and calculated (b) transient signals of gold nanodisk ND2 by an exponential with offset.

The values of parameter τ_d extracted from the fits of all experimental and simulated signals for ND1 and ND2 are shown in figure 4.17. The calculations were performed with the same parameters as in the previous paragraph ($\Delta T_{exc} = 570$ K and 455 K for ND1 and ND2, respectively, and 820 fs pump and probe pulse FWHMs), and with τ_{e-L} fixed at 800 fs after best adjustment.

In the simulations, the average values of τ_d are 970 fs for ND1 (calculation with $\Delta T_{exc} =$ 570 K) and 920 fs for ND2 ($\Delta T_{exc} = 455$ K). These two values are larger than the τ_{e-L} introduced in the model (800 fs), which is a signature of the high-excitation regime, as discussed above. τ_d is almost independent of the probe wavelength, except in restricted spectral regions (grey zones) corresponding to events similar to that depicted in the inset of figure 4.16b, where the exponential fit is no longer appropriate. The fact that the decay times remain approximately constant with the probe wavelength, while the amplitudes A_e and A_L of the contributions of the electron and lattice temperature changes undergo important relative variations, results from the fact that the dynamics of the decrease of $\Delta T_e(t)$ and of the increase of $\Delta T_L(t)$ are very similar in this time range. Therefore, any linear combination of these two quantities leads to a signal with also the same dynamics[2].

[2]Except in the specific cases where the two contributions perfectly compensate, resulting in a quasi-

The fitting results of the experimental data are more dispersed, which may be partly attributed to variations of the excitation energy (see figure 4.10) as well as to the variable quality of the fits. For instance, the fits are imprecise for ND2 between 840 and 870 nm because of the high relative contribution of lattice heating in this range (figure 4.6), leading to a decay of very small amplitude (see for instance the 855 nm signal in figure 4.16a, pink curve). Because of the limited signal-to-noise ratio, the fitting of these signals is imperfect, contrary to that of the calculated signals in the same spectral region. Aside from these special cases, the overall agreement between the parameters deduced from the model and from the experiments is very good for the two NDs.

The value of τ_{e-L} deduced from this analysis, 800 fs, is consistent with the 700–1100 fs values reported in the literature, measured using various time-resolved spectroscopy techniques on Au films [106, 126] or Au nanoparticles [5, 118]. The diverse states of cristallinity of the samples may be partly responsible for the observed dispersion of the electron–phonon relaxation times, as suggested by studies on gold [128] or aluminum [127] nanoparticles.

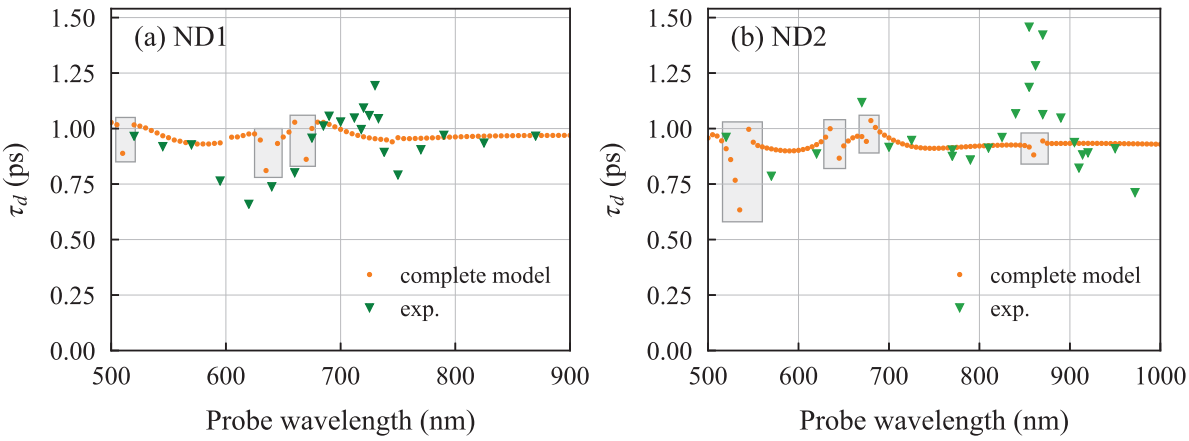

Figure 4.17 – Decay times τ_d for gold nanodisks ND1 (a) and ND2 (b) deduced from the fitting of experimental (green triangles) and computed (orange dots) transient signals. τ_{e-L} = 800 fs was used for the computed signals. The grey regions correspond to spectral ranges where the fitting function used is unable to correctly reproduce the computed signals, as discussed in the main text.

constant signal, as discussed above (see inset of figure 4.16b).

4.3.2 Comparison between calculated and experimental signals

4.3.2.a Analysis of the temporal dynamics

Now that the values of parameters τ_{cc} and τ_{e-L} entering the model have been determined, a detailed and quantitative comparison between the experimental and calculated signals can be performed[3]. This comparison is first used to determine the temporal origin of the experimental signals, obtained by shifting the temporal axis of the measurement to obtain a good agreement between the signal rises. A normalization is sometimes necessary for this operation so as to perfectly match the amplitudes of both signals. Additionally, direct comparison of an experimental signal to the simulated one at the same wavelength often being not optimal, comparison to signals computed using slightly different probe wavelengths (within < 15 nm) was sometimes performed, in order to correct differences in the amplitudes that may complicate the comparison of the dynamics. This approach is justified by the small modifications of the extinction spectra of NDs sometimes observed between the beginning and the end of time-resolved measurements (see paragraph 3.2.2.b).

In figures 4.18 and 4.19, examples of experimental time-resolved signals and the corresponding calculations at the same wavelength (or a close one) are shown for ND1 and ND2. The agreement between the calculated and experimental signals is generally good (regarding both their absolute amplitudes and their kinetics), especially when considering that this model is free of any fitting parameters, aside from constants τ_{cc} and τ_{e-L}. The three contributions to the extinction changes defined in the complete model (subsection 4.1.2) are also shown, clarifying the physical origins of the observed transient variations.

Several signals with peculiar temporal profiles are shown in figures 4.18 and 4.19. Their qualitative interpretation can be performed by using the simplified model developed in section 4.1.3, valid after the internal thermalization of the electrons. Figures 4.5 and 4.6, in particular, provide a simple way to evaluate the effects of temperature changes of the electron gas and of the lattice through amplitudes $A_e(\lambda_{pr})$ and $A_L(\lambda_{pr})$. Three specific cases may be distinguished.

- First, signals decreasing to (nearly) zero at the end of the ND internal thermalization, such as the ones shown in figures 4.18b,e and 4.19a,f, are explained by the vanishing of amplitudes A_L of ND1 at $\lambda_{pr} \approx 640$ and 760 nm (figure 4.5b) and of ND2 at $\lambda_{pr} \approx 710$ and 930 nm (figure 4.6b). In these cases, the dynamics of time-resolved signals directly reflect the heating and cooling of the electrons.

[3] Note that such quantitative comparison is made possible by the single-particle character of our time-resolved measurements.

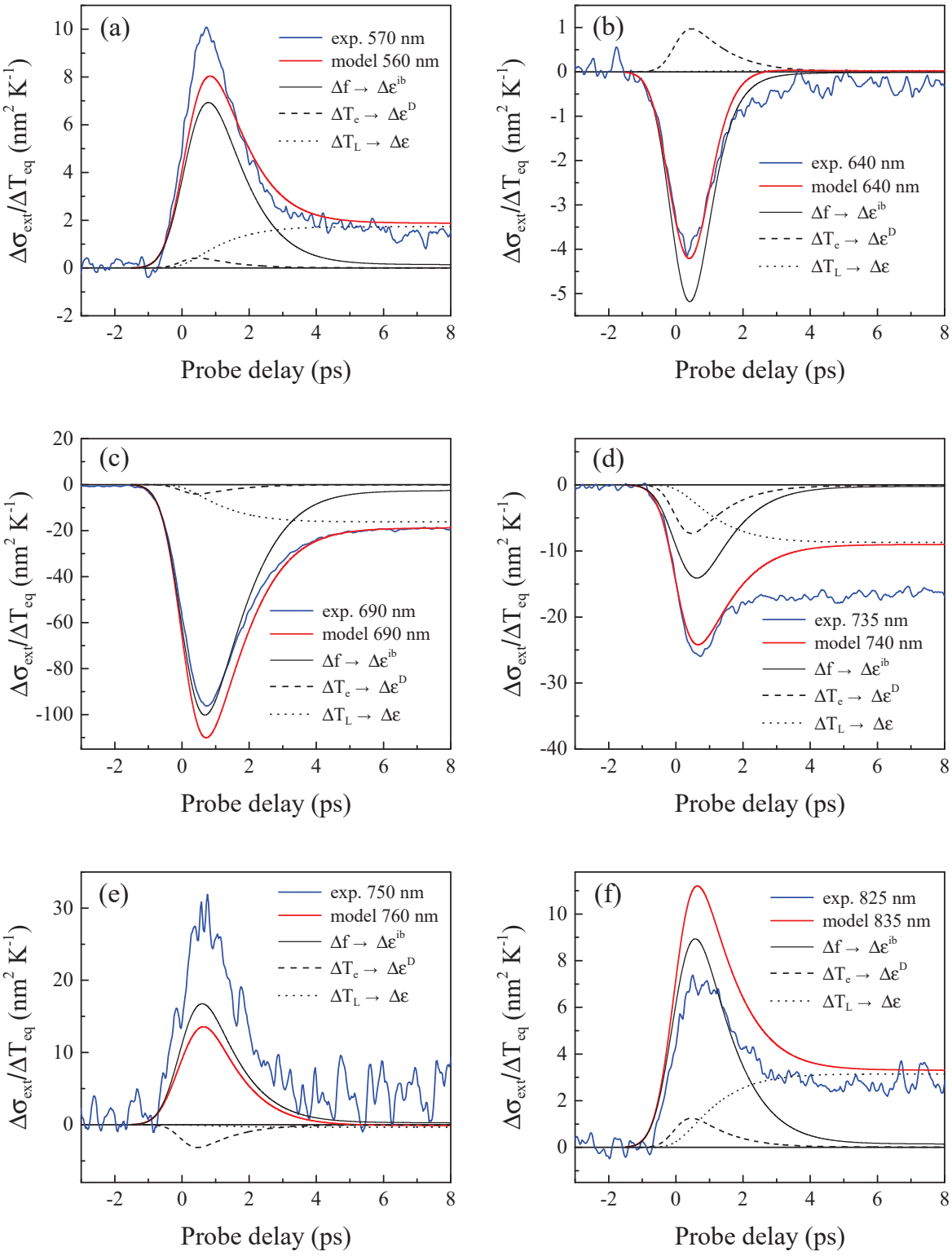

Figure 4.18 – Examples of time-resolved signals measured on gold nanodisk ND1 and calculation from the complete model. Probe wavelengths are indicated in the legend. The different contributions appearing in the model are also shown.

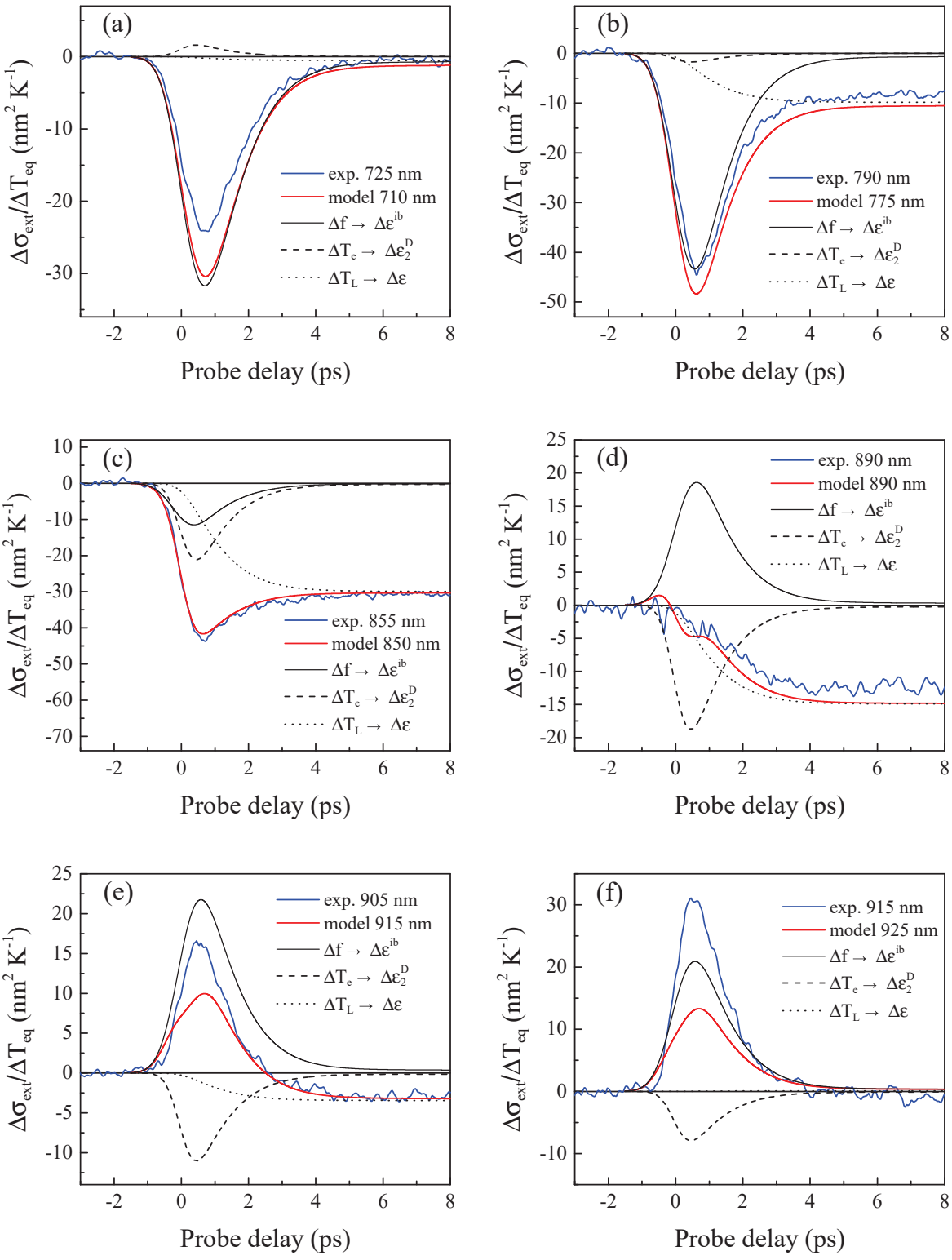

Figure 4.19 – Same as figure 4.18 for gold nanodisk ND2.

This analysis is confirmed by the complete model, which predicts very small lattice contributions at these wavelengths (figures 4.18b,e and 4.19a,f).

- Symetrically, cancellations of amplitude A_e should correspond to time-resolved signals mostly ruled by the lattice heating dynamics following electronic thermalization. This is indeed verified in the signal measured at $\lambda_{pr} = 890$ nm on ND2 (figure 4.19d), where a slow increase is observed (in absolute value) instead of the rapid rise followed by a decay seen in the other experimental signals. In figure 4.6a (solid black line), a cancellation of A_e is effectively predicted at $\lambda_{pr} = 890$ nm, resulting in this case from the compensation of the terms related to the interband and Drude components of the dielectric function (green and red dashed lines). In figure 4.19d, the complete model shows that this compensation also occurs prior to electron thermalization (*i.e.* < 2 ps, outside the range of the simplified model), in spite of the fact that the $\Delta f \rightarrow \Delta\varepsilon^{ib}$ and $\Delta T_e \rightarrow \Delta\varepsilon_2^D$ components present slightly different dynamics.

- Finally, another particular signal shape arises when the transient extinction change remains constant after the end of the ND excitation and of electron thermalization. Experimental time-resolved signals close to this case correspond to the measurement made on ND1 with $\lambda_{pr} = 735$ nm (figure 4.18d) or that performed with $\lambda_{pr} = 855$ nm on ND2 (figure 4.18c), which display nearly constant signals for delays $\gtrsim 2$ ps. According to the simplified model (equation 4.16) and to the temporal dynamics of $\Delta T_e(t)$ and $\Delta T_L(t)$ in the low excitation regime (equation 4.13), the sum $A_e(\lambda_{pr})\Delta T_e(t) + A_L(\lambda_{pr})\Delta T_L(t)$ is predicted to be constant when A_e and A_L fulfill the condition $A_e/A_L = c_e/c_L$. Indeed, in this case, $A_e\Delta T_e(t)/[A_L\Delta T_L(t)] = \Delta u_e(t)/\Delta u_L(t)$, with Δu_e and Δu_L the increases of electron and lattice energy densities as compared to equilibrium. Because of energy conservation (expressed here as $u_{abs} = \Delta u_e(t) + \Delta u_L(t)$), the condition on A_e and A_L implies the conservation of $\Delta\sigma_{ext}(t)$, as it is in this case proportional to the total energy density of the ND.

Other signals presenting less specific shapes are shown in figures 4.18a,c,f and 4.19b. They are representative of the majority of the time-resolved measurements performed on ND1 and ND2, for which both the $\Delta f \rightarrow \Delta\varepsilon^{ib}$ and the $\Delta T_L \rightarrow \Delta\varepsilon$ contributions are required to account for the observed kinetics. While the latter term is sometimes neglected in analyses of short-timescale time-resolved signals, leading to the quasi-vanishing of calculated signals at the end of internal thermalization [13], its inclusion proves crucial in the present case, where thermal effects are important. The $\Delta T_e \rightarrow \Delta\varepsilon_2^D$ term yields a more minor contribution in most calculated signals, except for some probe wavelengths in the infrared in the case of ND2, where this component becomes equivalent to the other two (see for instance figures 4.19c–e).

4.3.2.b Time-dependent spectral response

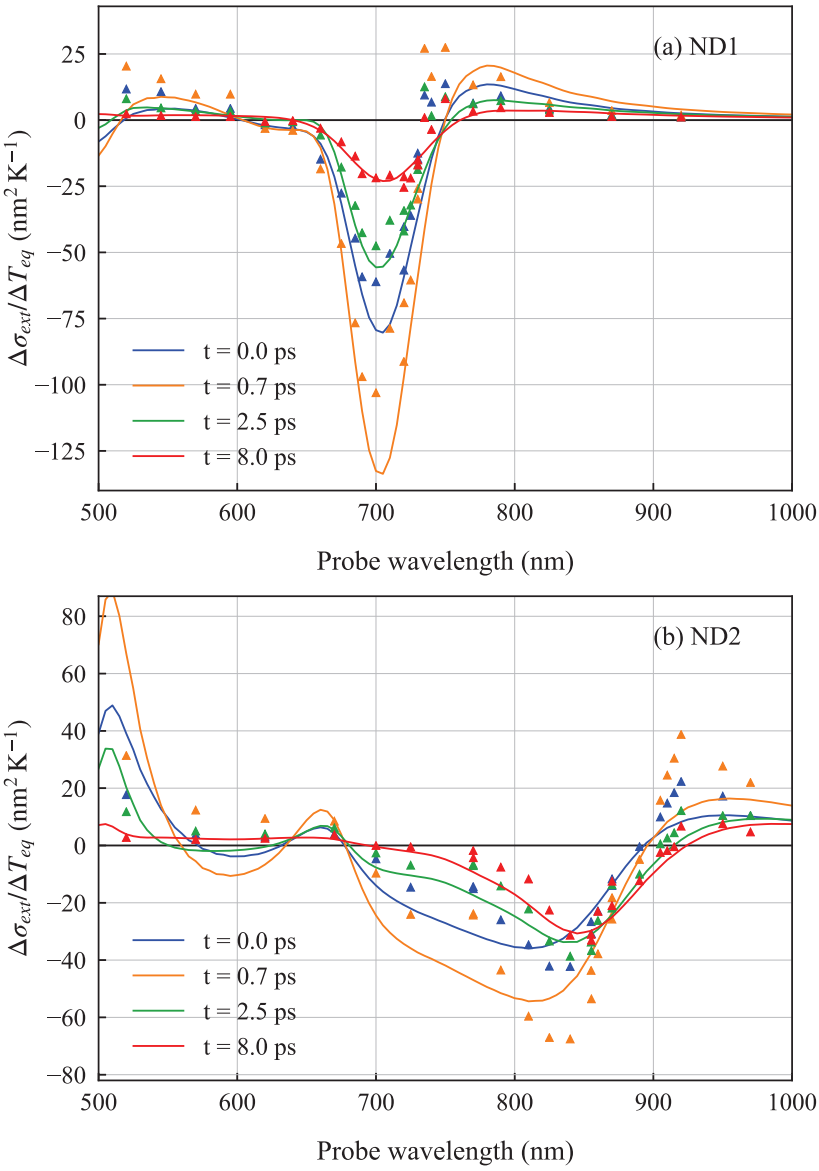

Figure 4.20 – Transient spectra of the experimental and calculated normalized extinction changes $\Delta\sigma_{ext}/\Delta T_{eq}$ of gold nanodisks ND1 (a) and ND2 (b) at several probe delays t. The experimental data and the simulation results are shown as triangles and plain lines, respectively, while the color code is indicated in the legend.

Complementary to the time-domain comparison made in the last paragraph between the measured and calculated transient extinction changes, we now perform the same comparison in the spectral domain. Figure 4.20 presents the experimental and calculated normalized transient extinction spectra of ND1 and ND2, plotted as a function of the probe wavelength at selected pump-probe delays. To elucidate the physical origins of the observed spectral shapes, the same data are reproduced in figures 4.21 and 4.22, together

with the different components of the complete model ($\Delta f \rightarrow \Delta\varepsilon^{ib}$, $\Delta T_e \rightarrow \Delta\varepsilon_2^D$, and $\Delta T_L \rightarrow \Delta\varepsilon$). Here too, good quantitative agreement is generally observed between the model and the measurements, although a few differences are observed.

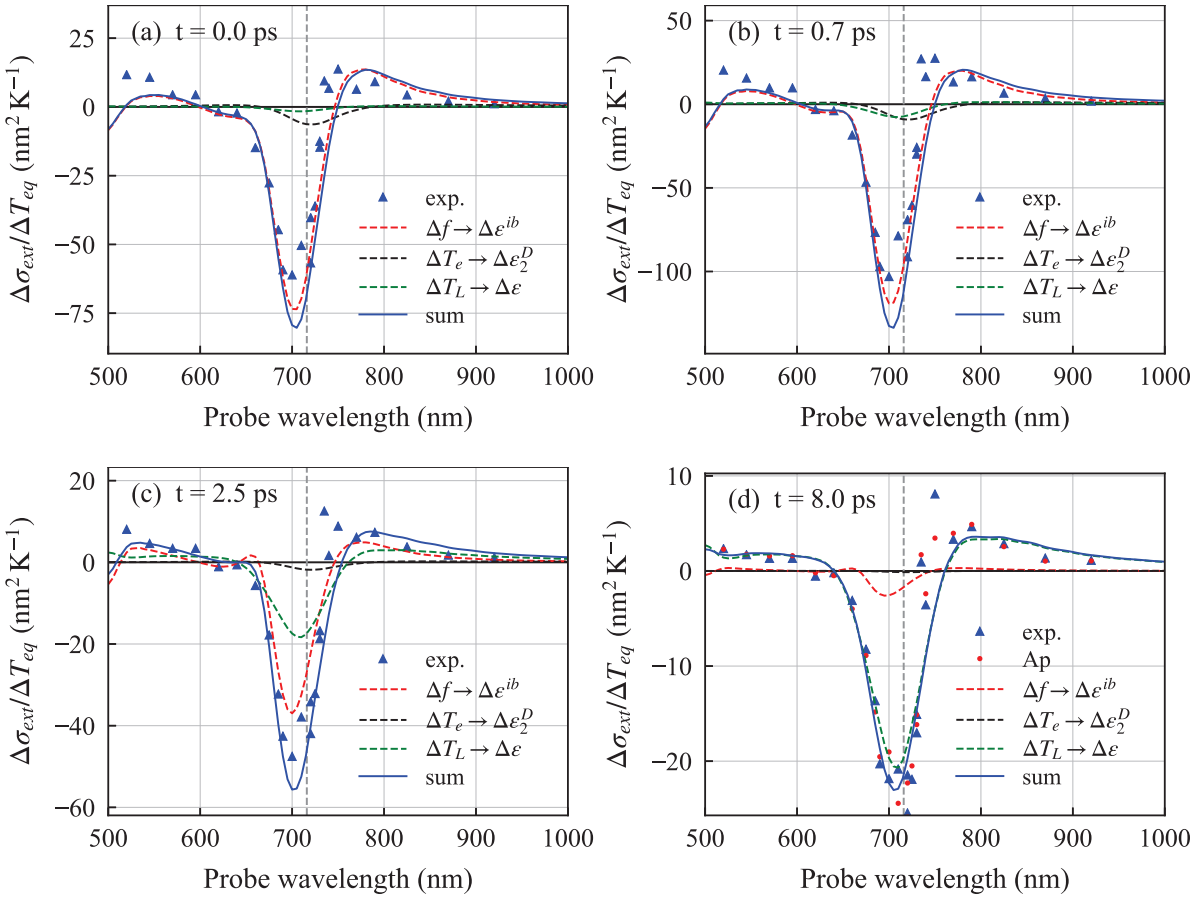

Figure 4.21 – Experimental and calculated spectra of the transient extinction changes of gold nanodisk ND1 at several probe delays t. The different contributions included in the complete model (blue line) are shown as dashed lines of different colors, as indicated in the legend. The grey dashed line indicates the LSPR position.

For ND1, the quantitative agreement between the model and the data is very good at all pump-probe delays (figures 4.20a and 4.21). The model predicts a negative peak near 700 nm, close to the LSPR position (vertical dashed line in figure 4.21), whose spectral shape remains similar in time (aside from a slight broadening), while its amplitude increases until 0.5–1 ps and decreases thereafter, stabilizing near 5–6 ps (which corresponds to the temporal variations shown in figure 4.18c). The position and width of this peak are in nearly perfect correspondence with the experimental data at all pump–probe delays. The main observed difference lies in the amplitude of this peak, which is about 15% larger in the calculations in the first $\sim$ 2 ps (when the contribution of the $\Delta f \rightarrow \Delta\varepsilon^{ib}$ effect is dominant), while the agreement becomes much better at 6 ps (when only the

$\Delta T_L \rightarrow \Delta\varepsilon$ component remains). A small discrepancy is also found in the position of the sign change near 750 nm, which is red-shifted by $\sim$ 10 nm in the calculations as compared to the measurements. Although minor, this difference—probably caused by a small error in the experimental determination of the ND extinction spectrum, or a small modification of this spectrum during the course of the experiments—is a cause for important discrepancies between the amplitudes of calculated and measured signals for probe wavelengths in the 700–750 nm range, justifying our choice to compare signals with different but close values of λ_{pr} in some cases in the previous paragraph.

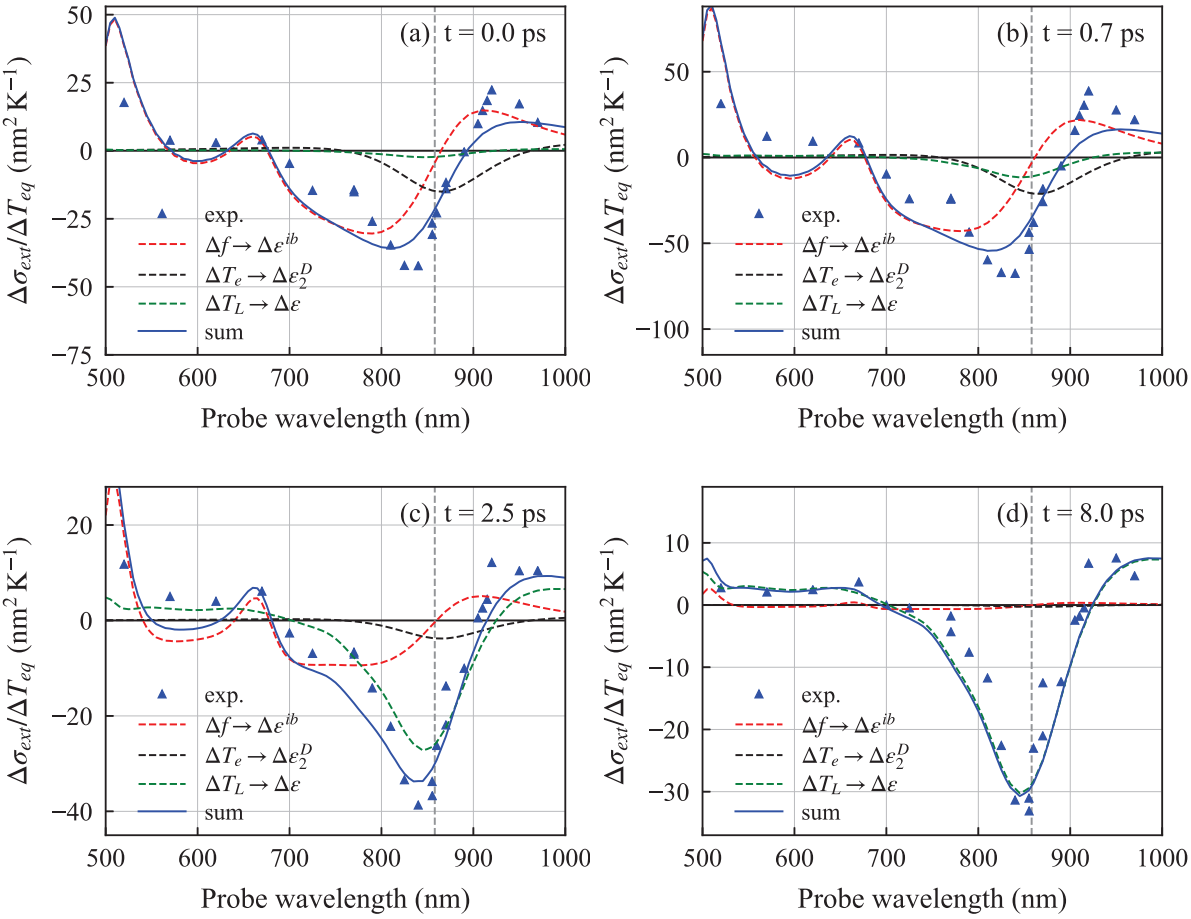

Figure 4.22 – Experimental and calculated spectra of the transient extinction changes of gold nanodisk ND2 at several probe delays t. The different contributions included in the complete model (blue line) are shown as dashed lines of different colors, as indicated in the legend. The grey dashed line indicates the LSPR position.

In the case of ND2, the overall agreement between the computed and experimental transient spectra remains good, but some discrepancies are observed at times $t <$ 2–3 ps, while the agreement becomes very good after this delay. In the range of the LSPR (700–1000 nm), the model correctly explains the general shape of the experimental

spectra between $t = 0$ ps and $t = 2$ ps, including negative and positive peaks at $\lambda_{pr} =$ 830 and 920 nm, respectively. While the correct positions for the sign changes are predicted by the model (at $\lambda_{pr} = 680$ and 900 nm), the amplitudes of the minimum and maximum are lower in the calculated signals as compared to the experimental data. In the interband spectral zone, some structures are visible at delays $t < 3$ ps in the calculated spectra (near 520 and 660 nm), mainly resulting from the high sensitivity of ε^{ib} to changes in the electronic distribution around the different interband transitions thresholds (see section 1.1.2.c), as is for instance illustrated by figure 4.4 showing the $\partial\varepsilon^{ib}_{1,2}/\partial T_e$ derivatives (in the particular case of a thermal electron distribution). For ND1, the effects of these dielectric function changes are difficult to separate from those of the plasmonic derivatives, the LSPR being in the same spectral range. Conversely, the LSPR of ND2 is well-separated from the interband transition region (which extends until ∼710 nm), making these effects clearly visible in the simulated transient spectra. In these spectra, these structures are visible in the first 2-3 ps and consist in two sign changes (at ∼560 and 630 nm) and a high peak near 500 nm. In the experimental spectra, an increase is effectively seen for $\lambda_{pr} = 520$ nm (though smaller than in the calculations), however the two sign changes are not observed, the signals remaining positive at all times from 500 to 670 nm.

At $t = 8$ ps, an excellent quantitative agreement is found for both NDs at all probe wavelengths between the model and the mesurements. These spectra correspond almost exactly to those of A_p (describing the nano-object optical sensitivity to temperature changes), studied in chapter 3 (figure 3.15), where a good agreement between the experimental and modeled spectra had already been noted. Minor differences however exist between the figures of the two chapters. First, the model of the present chapter, describing shorter timescales, includes the residual contribution of the electrons to the dielectric function changes, which is not included in the tables of $\partial\varepsilon_{1,2}/\partial T_p$ used in chapter 3. This effect, more important for ND1 than for ND2 (figures 4.21d and 4.22d), remains weak in both cases at $t = 8$ ps, accounting for less than 10% of the transient extinction changes. Second, the method used in chapter 3 to determine the values of A_p, based on the complete fitting of long-timescale time-resolved signals, took into account the potential contribution of ND vibrations in the signal by subtracting it. This effect has not been corrected in the measurements presented in this chapter, which may induce a small difference between these data and the simulations.

Figures 4.21 and 4.22 also allow to separate the effects of the different contributions of our model on the transient spectra of the two NDs. At delay 0 ps, the extinction changes entirely originate from the effect of the electrons (mostly through the $\Delta f \rightarrow \Delta\varepsilon^{ib}$ component), whereas the contribution of the lattice becomes dominant at 8 ps, after the internal thermalization of the ND ($\Delta T_L \rightarrow \Delta\varepsilon$ component). For ND1, the shape of the transient spectra undegoes little modification in time, due to the fact that the spectral

responses induced by these two effects are similar. This is not true for ND2, where the spectral shapes of the $\Delta f \rightarrow \Delta\varepsilon^{ib}$ and $\Delta T_L \rightarrow \Delta\varepsilon$ contributions are very dissimilar. For delays $t > 2$ ps, the variations of the transient spectra can be understood at the light of our simple model. In this time range, the spectral shapes of these components become independent of time and identical to those of the A_e and A_L terms showed in figures 4.5 and 4.6 (which display similar spectra for ND1 and largely different ones for ND2), while the evolution of their amplitudes is ruled by the dynamics of the electron and lattice temperature changes.

Finally, the effect of the $\Delta T_e \rightarrow \Delta\varepsilon_2^D$ component is diversely important for the two NDs. While it is found to be negligible at all times in the case of ND1 (figure 4.21), its consideration appears necessary to reproduce the measurements made on ND2 (figure 4.22). As we saw in the theoretical section of this chapter, changes of ε_2^D caused by the T_e-related augmentation of the γ_{e-e} scattering rate have a λ_{pr}^5 dependence. However, for these modifications to be reflected in the extinction cross-section changes, the $\partial\sigma_{ext}/\partial\varepsilon_2$ partial derivative also needs to be large enough relative to the $\partial\sigma_{ext}/\partial\varepsilon_1$ derivative. Combination of these two effects results in a negative bump in the transient extinction spectra of ND2, with an allure similar to its $\partial\sigma_{ext}/\partial\varepsilon_2$ spectrum, though slightly shifted towards the infrared. The amplitude of this effect is comparable to that of the $\Delta f \rightarrow \Delta\varepsilon^{ib}$ term and roughly results in a 20-30 nm red-shift of the predicted sign change. Although our description of the changes of γ_{e-e}, strictly valid only for a well-defined electronic temperature T_e, was used out of its validity domain (by introducing an equivalent electronic temperature defined at all times), including this term in the model largely improves the agreement with the experimental data from the moment of excitation to $t \approx 2$ ps.

4.4 Summary and conclusion

In this chapter, we reported the results of a study of the ultrafast phenomena following the photo-excitation of a single gold nano-object, leading to its internal thermalization through electron–electron and electron–phonon energy exchanges. The transient optical response induced by these processes was measured for two gold NDs of different sizes using time-resolved spectroscopy with many different probe wavelengths. These signals were compared to the results of a complete model taking into account the effects of the transient changes of both the electronic distribution and the lattice temperature on the dielectric function. This comparison yielded a good quantitative agreement, demonstrating the quantitative character of single-object time-resolved spectroscopy, as well as the predictive nature of our model. A simplified version of this model was also developed, aimed at highlighting the respective roles of the temperature evolutions of the electrons and of the ionic lattice in the transient optical changes. The large variations observed in the amplitudes and temporal shapes of the experimental time-resolved signals

were accounted for by the different sensitivities of the extinction changes to the effects of electron and lattice heating, whose relative importance is strongly dependent on the probe wavelength.

The detailed analyses presented in chapters 3 and 4 thus demonstrate that the transient extinction changes following the impulsive excitation of a single metal nanoparticle and resulting from ultrafast internal (electron–electron and electron–phonon scattering) and external (nano-object thermal loss) energy exchanges can be quantitatively predicted by thermo-optical models without free parameters other than the durations of the light pulses used and the characteristic times of the above processes.

This demonstrates that in single particle experiments the amplitudes of time-resolved signals can be used to estimate the absolute electron and lattice temperatures. This approach could represent a useful alternative to the method presented in chapter 3—based on the estimation of the energy injected by the pump pulse—, which requires precise knowledge of the pump pulse fluence and a numerical estimation of the absorption cross-section of the investigated nanoparticle.

Conclusion

In this work, the ultrafast relaxation dynamics of individual gold nano-objects have been investigated by means of optical time-resolved spectroscopy. The relaxation mechanisms occurring in a gold nanodisk after impulsive excitation were quantitatively studied on the different timescales involved. Measurements in a ∼10 ps time window, presented in chapter 4, allowed investigating the dynamics of the electron gas excitation and of its subsequent relaxation via electron–electron and electron–lattice energy exchanges, leading to the internal thermalization of the nano-object. In chapter 3, measurements on a nanosecond timescale allowed us to probe the dynamics of the nanodisk cooling by heat transfer to its supporting sapphire substrate. To quantitatively investigate these dynamics and the transient optical response that they induce, single-particle time-resolved spectroscopy was combined to a linear optical spectroscopy technique (spatial modulation spectroscopy) allowing to perform quantitative measurements of the extinction spectra of individual nanodisks, and permitting the characterization of their dimensions in combination with optical finite-element calculations. This analysis enabled in particular the calculation of the energy injected in the nano-objects by the pump pulses and thus to determine the absolute initial temperature increases of the nanodisks.

The ensemble of results achieved during this thesis can be grouped into two main axes, each presenting an important novelty as compared to previous investigations of the ultrafast dynamics of metal nanoparticles. The first axis, described in chapter 3, addressed the dynamics of thermal transfer from a heated gold nanodisk to its sapphire substrate. In this context, time-resolved measurements were performed on a large number of individual nanodisks of various thicknesses (18 or 40 nm) and diameters (60–200 nm). In the suitable measurement conditions—implying low pump fluences—, the dynamics of these signals were quasi-exponential and were shown to be proportional to the nanodisks' temperature difference to equilibrium. Such dynamics are characteristic of an interface-limited heat transfer, as was confirmed by the results of thermal FEM simulations. A near proportionality dependence of the cooling time constant with the nanodisk thickness was observed in the experiments, while much weaker variations were seen with the nanodisk diameter, in correct agreement with the simulations. Comparison between the experiments and the simulations allowed to extract average values for the gold–sapphire thermal boundary conductance (or Kapitza conductance), in agreement with the values reported in the literature. The single-particle character of our experiments also enabled us to investigate the interparticle dispersion of this quantity, which was found small for the samples used. While several previous studies on nano-objects (such as nickel nanolines) reported deviations from the Fourier law of heat conduction, attributed to quasi-ballistic phonon transport in the substrate near the nanostructures, we showed that

our experiments are unaffected by such possible effects. Indeed, due the poor thermal conductance of the gold-sapphire interface, as well as to the efficient heat propagation in the substrate permitted by the geometry of the nanosystem, our measurements are weakly sensitive to the modalities of thermal transport in the substrate. Finally, we reported irreversible modifications of the nanodisk cooling dynamics, occuring for excessive pump pulses fluences. Despite multiple tests and a model attempting to describe the observed changes, the origin of this effect was not elucidated.

In the future, reproduction of these experiments on chemically-synthesized gold nanodisks, differing from lithographed ones by their higher crystallinity, but also by the presence of surfactant molecules at their surface, would be very interesting. Another possible study, taking full advantage of the single-particle character of our thermal time-resolved measurements, would be the investigation of the propagation of heat between two close nanoparticles with different LSPR energies (resulting for instance from differences in their composition or shape), which could be selectively heated and probed using suitable pump and probe wavelengths. These themes will be addressed in the framework of the ULTRASINGLE project funded by the ANR, starting in early 2021 (the project involving a collaboration with chemists from ICMCB in Bordeaux and CEA Saclay).

In the longer term, the combination of time-resolved spectroscopy with a diamond anvil cell, allowing to study the transient properties of single nano-objects at high pressure, is also considered in the FemtoNanoOptics group. In such experiments, the pressure would allow to finely modulate the physical properties of the nano-objects, their environment, and their interface. Applied to nanodisks, this could for example enable a better understanding of interfacial heat transfer.

The second axis and main novel result of this thesis, covered in both chapters 3 and 4, concerned the amplitudes of the nano-object transient extinction changes in response to the individual effects of the different relaxation mechanisms mentioned above (electron and lattice dynamics, nano-object vibration and cooling). These amplitudes, which are wavelength-dependent, quantify the sensitivity of time-resolved measurements to these phenomena. Though they are all strongly enhanced in the spectral range of the nano-object LSPR, their spectra differ for each relaxation process. In this thesis, these amplitudes were experimentally determined as a function of the wavelength of the probe beam through systematic time-resolved measurements performed on two nanodisks of different dimensions (about 18 nm thickness and 100 or 150 nm diameter). In chapter 3, signals measured on a 3 ns time window presented identical decay dynamics for all probe wavelengths, and were shown to reflect the temperature evolution of the nanodisks. The initial amplitudes of these signals (divided by the initial temperature increases of the nanodisks), noted $A_p(\lambda_{pr})$, thus reflect the sensitivity of time-resolved detection to the temperature changes of the nano-object. For the two considered NDs, $A_p(\lambda_{pr})$ showcased a strong enhancement around the LSPR. An optothermal finite-element model permitted

the calculation of these spectra, in excellent quantitative agreement with the experiments. These results provide an experimental confirmation for a previously-published theoretical study based on a similar opto-thermal model [14]. In chapter 4, we focused on the electron and lattice dynamics preceding the nano-object internal thermalization. Measurements performed at different probe wavelengths were compared to the result of a complete model based on the calculation of the time-dependent modification of the electronic distribution (obtained through the numerical resolution of the Boltzmann equation), and also accounting for the effects of the lattice heating and of the modification of the electron–electron scattering rate. The quantitative agreement between this model and our experimental results was very good, given that only two parameters (the duration of the pump and probe pulses and the electron–lattice relaxation time) were left free for this comparison. Contrary to the long-timescale measurements, the observed dynamics were highly dependent on the probe wavelength. To achieve a better understanding of these complex dynamics, a simplified version of the former model was proposed, approximately valid after the end of the electron internal thermalization ($\sim$2 ps). In this model, the transient signals dynamics are explained as reflecting a combination of the opposite transient temperature changes of the electrons and of the lattice, with probe wavelength-dependent weights (respectively noted $A_e(\lambda_{pr})$ and $A_L(\lambda_{pr})$). Thus, these amplitudes correspond to the sensitivity of time-resolved measurements to the electron and lattice temperature changes. Particular experimental signals, reflecting only the electron or lattice dynamics, were succesfully identified and interpreted using this model. Finally, the transient spectra of the two nanodisks were interpreted at the light of our complete model, where the contributions of the different physical effects were separated. In the preparation of a time-resolved experiment, this model may prove very useful, as it allows selecting the probe wavelength maximizing the desired effect (or cancelling others). In the future, it could for instance be used for accurate measurements of the electron–phonon relaxation time, whose dependence on the sample crystallinity is not well-known.

To complement our analysis of the optical sensivities to transient changes of the temperatures of the electrons, of the ionic lattice, and of the thermalized nano-object, a complete study of the optical detection of the nano-object vibrations remains to be carried out, in the wake of the preliminary results presented at the end of chapter 3. Modeling of these effects is however expected to be more complex than the analysis of the cooling kinetics performed in chapter 3, as the transient modifications of the dielectric functions may no longer be assumed homogeneous in the nano-object and in the substrate.

Bibliography

[1] U. Kreibig and M. Vollmer, *Optical Properties of Metal Clusters*, Springer Series in Materials Science 25, Berlin: Springer, 2010, 532 pp. (cit. on p. 1).

[2] N. S. Abadeer and C. J. Murphy, "Recent Progress in Cancer Thermal Therapy Using Gold Nanoparticles", *The Journal of Physical Chemistry C* **120** (2016), 4691–4716 (cit. on p. 1)

[3] Pilot, Signorini, Durante, Orian, Bhamidipati, and Fabris, "A Review on Surface-Enhanced Raman Scattering", *Biosensors* **9** (2019), 57 (cit. on p. 1)

[4] S. Nie, "Probing Single Molecules and Single Nanoparticles by Surface-Enhanced Raman Scattering", *Science* **275** (1997), 1102–1106 (cit. on p. 1)

[5] A. Arbouet, C. Voisin, D. Christofilos, P. Langot, N. D. Fatti, F. Vallée, et al., "Electron-Phonon Scattering in Metal Clusters", *Physical Review Letters* **90** (2003), 177401 (cit. on pp. 1, 107, 110, 131, 137)

[6] C. Voisin, D. Christofilos, P. A. Loukakos, N. Del Fatti, F. Vallée, J. Lermé, M. Gaudry, E. Cottancin, M. Pellarin, and M. Broyer, "Ultrafast electron-electron scattering and energy exchanges in noble-metal nanoparticles", *Physical Review B* **69** (2004), 195416 (cit. on p. 1)

[7] A. Crut, P. Maioli, N. Del Fatti, and F. Vallée, "Acoustic vibrations of metal nano-objects: Time-domain investigations", *Physics Reports* **549** (2015), 1–43 (cit. on pp. 1, 54)

[8] L. Qiu, N. Zhu, Y. Feng, E. E. Michaelides, G. Żyła, D. Jing, X. Zhang, P. M. Norris, C. N. Markides, and O. Mahian, "A review of recent advances in thermo-physical properties at the nanoscale: From solid state to colloids", *Physics Reports* **843** (2020), 1–81 (cit. on p. 1)

[9] D. G. Cahill, W. K. Ford, K. E. Goodson, G. D. Mahan, A. Majumdar, H. J. Maris, R. Merlin, and S. R. Phillpot, "Nanoscale Thermal Transport", *Journal of Applied Physics* **93** (2003), 793–818 (cit. on pp. 1, 53)

[10] D. G. Cahill, P. V. Braun, G. Chen, D. R. Clarke, S. Fan, K. E. Goodson, et al., "Nanoscale thermal transport. II. 2003–2012", *Applied Physics Reviews* **1** (2014), 011305 (cit. on pp. 1, 53)

[11] J. Gomis-Bresco, S. Dommers, V. V. Temnov, U. Woggon, M. Laemmlin, D. Bimberg, E. Malic, M. Richter, E. Schöll, and A. Knorr, "Impact of Coulomb Scattering on the Ultrafast Gain Recovery in InGaAs Quantum Dots", *Physical Review Letters* **101** (2008) (cit. on p. 1)

[12] F. Medeghini, A. Crut, M. Gandolfi, F. Rossella, P. Maioli, F. Vallée, F. Banfi, and N. Del Fatti, "Controlling the Quality Factor of a Single Acoustic Nanoresonator by Tuning its Morphology", *Nano Letters* **18** (2018), 5159–5166 (cit. on pp. 2, 54, 62, 73, 95, 97)

[13] H. Baida, D. Mongin, D. Christofilos, G. Bachelier, A. Crut, P. Maioli, N. Del Fatti, and F. Vallée, "Ultrafast Nonlinear Optical Response of a Single Gold Nanorod Near Its Surface Plasmon Resonance", *Physical Review Letters* **107** (2011) (cit. on pp. 2, 3, 15, 48, 49, 54, 107, 141)

[14] M. Gandolfi, A. Crut, F. Medeghini, T. Stoll, P. Maioli, F. Vallée, F. Banfi, and N. Del Fatti, "Ultrafast Thermo-Optical Dynamics of Plasmonic Nanoparticles", *The Journal of Physical Chemistry C* **122** (2018), 8655–8666 (cit. on pp. 3, 54, 55, 60, 61, 80, 101, 151)

[15] O. M. Wilson, X. Hu, D. G. Cahill, and P. V. Braun, "Colloidal metal particles as probes of nanoscale thermal transport in fluids", *Physical Review B* **66** (2002) (cit. on pp. 3, 53, 90)

[16] M. Hu and G. V. Hartland, "Heat Dissipation for Au Particles in Aqueous Solution: Relaxation Time versus Size", *The Journal of Physical Chemistry B* **106** (2002), Publisher: American Chemical Society, 7029–7033 (cit. on pp. 3, 53)

[17] T. Stoll, P. Maioli, A. Crut, S. Rodal-Cedeira, I. Pastoriza-Santos, F. Vallée, and N. Del Fatti, "Time-Resolved Investigations of the Cooling Dynamics of Metal Nanoparticles: Impact of Environment", *The Journal of Physical Chemistry C* **119** (2015), 12757–12764 (cit. on pp. 3, 53–55, 58, 60, 61, 80)

[18] J. Park and D. G. Cahill, "Plasmonic Sensing of Heat Transport at Solid–Liquid Interfaces", *The Journal of Physical Chemistry C* **120** (2016), 2814–2821 (cit. on pp. 3, 53)

[19] F. Banfi, V. Juvé, D. Nardi, S. Dal Conte, C. Giannetti, G. Ferrini, N. Del Fatti, and F. Vallée, "Temperature dependence of the thermal boundary resistivity of glass-embedded metal nanoparticles", *Applied Physics Letters* **100** (2012), 011902 (cit. on pp. 3, 53)

[20] M. Zavelani-Rossi, D. Polli, S. Kochtcheev, A.-L. Baudrion, J. Béal, V. Kumar, et al., "Transient Optical Response of a Single Gold Nanoantenna: The Role of Plasmon Detuning", *ACS Photonics* **2** (2015), 521–529 (cit. on pp. 3, 107)

[21] T. Li and W. A. Schroeder, "Nonparametric Modeling of Face-Centered Cubic Metal Photocathodes", *arXiv:1704.05371 [physics]* (2017) (cit. on p. 7)

[22] N. Ashcroft and N. Mermin, *Solid State Physics*, HRW International Editions, 1976 (cit. on pp. 8–10, 12, 15).

[23] T.-S. Choy, *3D (VRML) Fermi Surface Database*, URL: http://www.phys.ufl.edu/fermisurface/index.html (cit. on p. 9).

[24] P. B. Johnson and R. W. Christy, "Optical Constants of the Noble Metals", *Physical Review B* **6** (1972), 4370–4379 (cit. on pp. 12, 14, 18, 23, 25, 27)

[25] N. Del Fatti, "Dynamique électronique femtoseconde dans les systèmes métalliques massifs et confinés", PhD thesis, Ecole Polytechnique, 1999 (cit. on p. 15).

[26] Chin-Yi Tsai, Chin-Yao Tsai, Chih-Hsiung Chen, Tien-Li Sung, Tsu-Yin Wu, and Fang-Ping Shih, "Theoretical model for intravalley and intervalley free-carrier absorption in semiconductor lasers: beyond the classical Drude model", *IEEE Journal of Quantum Electronics* **34** (1998), 552–559 (cit. on p. 15)

[27] T. Stoll, "Ultrafast electronic, acoustic and thermal properties of metal nanoparticles and clusters", PhD thesis, Université Claude Bernard-Lyon I, 2014, URL: https://tel.archives-ouvertes.fr/tel-01128276/ (cit. on pp. 15, 61).

[28] R. N. Gurzhi, "Mutual electron correlations in metal optics", *Soviet Journal of Experimental and Theoretical Physics* (1959) (cit. on pp. 15, 112)

[29] N. Goubet, I. Tempra, J. Yang, G. Soavi, D. Polli, G. Cerullo, and M. P. Pileni, "Size and nanocrystallinity controlled gold nanocrystals: synthesis, electronic and mechanical properties", *Nanoscale* **7** (2015), Publisher: The Royal Society of Chemistry, 3237–3246 (cit. on pp. 15, 68)

[30] F. Medeghini, R. Rouxel, A. Crut, P. Maioli, F. Rossella, F. Banfi, F. Vallée, and N. Del Fatti, "Signatures of Small Morphological Anisotropies in the Plasmonic and Vibrational Responses of Individual Nano-objects", *The Journal of Physical Chemistry Letters* (2019), 5372–5380 (cit. on pp. 15, 62, 64–66, 68)

[31] A. Kawabata and R. Kubo, "Electronic Properties of Fine Metallic Particles. II. Plasma Resonance Absorption", *Journal of the Physical Society of Japan* **21** (1966), Publisher: The Physical Society of Japan, 1765–1772 (cit. on p. 15)

[32] V. Juvé, M. F. Cardinal, A. Lombardi, A. Crut, P. Maioli, J. Pérez-Juste, L. M. Liz-Marzán, N. Del Fatti, and F. Vallée, "Size-Dependent Surface Plasmon Resonance Broadening in Nonspherical Nanoparticles: Single Gold Nanorods", *Nano Letters* **13** (2013), 2234–2240 (cit. on pp. 15, 27)

[33] M. Guerrisi, R. Rosei, and P. Winsemius, "Splitting of the interband absorption edge in Au", *Physical Review B* **12** (1975), 557–563 (cit. on p. 16)

[34] T. Stoll, P. Maioli, A. Crut, N. Del Fatti, and F. Vallée, "Advances in femto-nano-optics: ultrafast nonlinearity of metal nanoparticles", *The European Physical Journal B* **87** (2014) (cit. on pp. 17, 22, 29, 80, 82–84, 88, 112, 113, 132)

[35] T. Rangel, D. Kecik, P. E. Trevisanutto, G.-M. Rignanese, H. Van Swygenhoven, and V. Olevano, "Band structure of gold from many-body perturbation theory", *Physical Review B* **86** (2012), 125125 (cit. on p. 18)

[36] A. Crut, P. Maioli, N. Del Fatti, and F. Vallée, "Optical absorption and scattering spectroscopies of single nano-objects", *Chemical Society Reviews* **43** (2014), 0.5, 3921 (cit. on pp. 19, 25, 27, 32, 54)

[37] R. Gans, "Über die Form ultramikroskopischer Goldteilchen", *Annalen der Physik* **342** (1912), 881–900 (cit. on p. 22)

[38] C. F. Bohren and D. R. Huffman, *Absorption and Scattering of Light by Small Particles*, Wiley-VCH Verlag GmbH, 1983, pp. 82–129 (cit. on pp. 22, 26).

[39] F. Medeghini, "Optics and acoustics with a single nano-object: environment effects", PhD thesis, 2018, p. 173 (cit. on pp. 24, 44, 97).

[40] K. L. Kelly, E. Coronado, L. L. Zhao, and G. C. Schatz, "The Optical Properties of Metal Nanoparticles: The Influence of Size, Shape, and Dielectric Environment", *The Journal of Physical Chemistry B* **107** (2003), 668–677 (cit. on pp. 25, 26)

[41] N. I. Grigorchuk, "Radiative damping of surface plasmon resonance in spheroidal metallic nanoparticle embedded in a dielectric medium", *Journal of the Optical Society of America B* **29** (2012), Publisher: Optical Society of America, 3404–3411 (cit. on p. 25)

[42] G. Mie, "Beiträge zur Optik trüber Medien, speziell kolloidaler Metallösungen", *Annalen der Physik* **330** (1908), 377–445 (cit. on p. 26)

[43] P. Latimer, "Light scattering by ellipsoids", *Journal of Colloid and Interface Science* **53** (1975), 102–109 (cit. on p. 26)

[44] N. V. Voshchinnikov and V. G. Farafonov, "Optical properties of spheroidal particles", *Astrophysics and Space Science* **204** (1993), 19–86 (cit. on p. 26)

[45] V. Myroshnychenko, J. Rodríguez-Fernández, I. Pastoriza-Santos, A. M. Funston, C. Novo, P. Mulvaney, L. M. Liz-Marzán, and F. J. G. d. Abajo, "Modelling the optical response of gold nanoparticles", *Chemical Society Reviews* **37** (2008), Publisher: The Royal Society of Chemistry, 1792–1805 (cit. on p. 26)

[46] H. Baida, P. Billaud, S. Marhaba, D. Christofilos, E. Cottancin, A. Crut, et al., "Quantitative Determination of the Size Dependence of Surface Plasmon Resonance Damping in Single AgSiO $_2$ Nanoparticles", *Nano Letters* **9** (2009), 3463–3469 (cit. on p. 27)

[47] A. Arbouet, D. Christofilos, N. Del Fatti, F. Vallée, J. R. Huntzinger, L. Arnaud, P. Billaud, and M. Broyer, "Direct Measurement of the Single-Metal-Cluster Optical Absorption", *Physical Review Letters* **93** (2004) (cit. on p. 32)

[48] W. E. Moerner and L. Kador, "Optical detection and spectroscopy of single molecules in a solid", *Physical Review Letters* **62** (1989), 2535–2538 (cit. on p. 33)

[49] C. R. Carey, T. LeBel, D. Crisostomo, J. Giblin, M. Kuno, and G. V. Hartland, "Imaging and Absolute Extinction Cross-Section Measurements of Nanorods and Nanowires through Polarization Modulation Microscopy", *The Journal of Physical Chemistry C* **114** (2010), 16029–16036 (cit. on p. 33)

[50] O. L. Muskens, N. Del Fatti, and F. Vallée, "Femtosecond Response of a Single Metal Nanoparticle", *Nano Letters* **6** (2006), 0, 552–556 (cit. on pp. 33, 48, 107)

[51] M. Husnik, S. Linden, R. Diehl, J. Niegemann, K. Busch, and M. Wegener, "Quantitative Experimental Determination of Scattering and Absorption Cross-Section Spectra of Individual Optical Metallic Nanoantennas", *Physical Review Letters* **109** (2012), 233902 (cit. on p. 33)

[52] M. Born and E. Wolf, *Principles of Optics*, Pergamon Press, New York, 1965 (cit. on p. 36).

[53] R. A. Askey and A. B. Daalhuis, "Generalized hypergeometric functions and Meijer G-function", in: *NIST Handbook of Mathematical Functions*, Cambridge University Press, 2010, URL: `https://dlmf.nist.gov/16` (cit. on pp. 41, 44).

[54] A. Jayaraman, "Ultrahigh pressures", *Review of Scientific Instruments* **57** (1986), Publisher: American Institute of Physics, 1013–1031 (cit. on p. 43)

[55] L. Dubrovinsky, N. Dubrovinskaia, V. B. Prakapenka, and A. M. Abakumov, "Implementation of micro-ball nanodiamond anvils for high-pressure studies above 6 Mbar", *Nature Communications* **3** (2012) (cit. on p. 43)

[56] F. Medeghini, M. Hettich, R. Rouxel, S. D. Silva Santos, S. Hermelin, E. Pertreux, et al., "High-Pressure Effect on the Optical Extinction of a Single Gold Nanoparticle", *ACS Nano* **12** (2018), 10310–10316 (cit. on p. 44)

[57] E. Pop, S. Sinha, and K. Goodson, "Heat Generation and Transport in Nanometer-Scale Transistors", *Proceedings of the IEEE* **94** (2006), 1587–1601 (cit. on p. 53)

[58] G. J. Snyder and E. S. Toberer, "Complex thermoelectric materials", *Nature Materials* **7** (2008), 105–114 (cit. on p. 53)

[59] E. T. Swartz and R. O. Pohl, "Thermal boundary resistance", *Reviews of Modern Physics* **61** (1989), 605–668 (cit. on pp. 53, 56, 57)

[60] R. J. Stoner and H. J. Maris, "Kapitza conductance and heat flow between solids at temperatures from 50 to 300 K", *Physical Review B* **48** (1993), 16373–16387 (cit. on pp. 53, 57, 59, 91)

[61] V. Juvé, M. Scardamaglia, P. Maioli, A. Crut, S. Merabia, L. Joly, N. Del Fatti, and F. Vallée, "Cooling dynamics and thermal interface resistance of glass-embedded metal nanoparticles", *Physical Review B* **80** (2009) (cit. on pp. 53, 90)

[62] C. Giannetti, B. Revaz, F. Banfi, M. Montagnese, G. Ferrini, F. Cilento, et al., "Thermomechanical behavior of surface acoustic waves in ordered arrays of nanodisks studied by near-infrared pump-probe diffraction experiments", *Physical Review B* **76** (2007) (cit. on p. 53)

[63] C. Giannetti, F. Banfi, D. Nardi, G. Ferrini, and F. Parmigiani, "Ultrafast Laser Pulses to Detect and Generate Fast Thermomechanical Transients in Matter", *IEEE Photonics Journal* **1** (2009), 21–32 (cit. on pp. 53, 91)

[64] G. Chen, "Nonlocal and Nonequilibrium Heat Conduction in the Vicinity of Nanoparticles", *Journal of Heat Transfer* **118** (1996), 539–545 (cit. on p. 53)

[65] M. E. Siemens, Q. Li, R. Yang, K. A. Nelson, E. H. Anderson, M. M. Murnane, and H. C. Kapteyn, "Quasi-ballistic thermal transport from nanoscale interfaces observed using ultrafast coherent soft X-ray beams", *Nature Materials* **9** (2010), 26–30 (cit. on pp. 53, 54, 58, 95)

[66] M. Gandolfi, G. Benetti, C. Glorieux, C. Giannetti, and F. Banfi, "Accessing temperature waves: A dispersion relation perspective", *International Journal of Heat and Mass Transfer* **143** (2019), 118553 (cit. on p. 53)

[67] M. Simoncelli, N. Marzari, and A. Cepellotti, "Generalization of Fourier's Law into Viscous Heat Equations", *Physical Review X* **10** (2020) (cit. on p. 53)

[68] A. J. Schmidt, R. Cheaito, and M. Chiesa, "A frequency-domain thermoreflectance method for the characterization of thermal properties", *Review of Scientific Instruments* **80** (2009), 094901 (cit. on p. 53)

[69] K. T. Regner, D. P. Sellan, Z. Su, C. H. Amon, A. J. McGaughey, and J. A. Malen, "Broadband phonon mean free path contributions to thermal conductivity measured using frequency domain thermoreflectance", *Nature Communications* **4** (2013) (cit. on p. 53)

[70] R. B. Wilson and D. G. Cahill, "Anisotropic failure of Fourier theory in time-domain thermoreflectance experiments", *Nature Communications* **5** (2014) (cit. on pp. 53, 58)

[71] A. J. Minnich, J. A. Johnson, A. J. Schmidt, K. Esfarjani, M. S. Dresselhaus, K. A. Nelson, and G. Chen, "Thermal Conductivity Spectroscopy Technique to Measure Phonon Mean Free Paths", *Physical Review Letters* **107** (2011), 095901 (cit. on p. 53)

[72] J. A. Johnson, A. A. Maznev, J. Cuffe, J. K. Eliason, A. J. Minnich, T. Kehoe, C. M. S. Torres, G. Chen, and K. A. Nelson, "Direct Measurement of Room-Temperature Nondiffusive Thermal Transport Over Micron Distances in a Silicon Membrane", *Physical Review Letters* **110** (2013) (cit. on p. 53)

[73] A. Plech, V. Kotaidis, S. Grésillon, C. Dahmen, and G. von Plessen, "Laser-induced heating and melting of gold nanoparticles studied by time-resolved x-ray scattering", *Physical Review B* **70** (2004), Publisher: American Physical Society, 195423 (cit. on pp. 53, 77)

[74] S. Link and M. A. El-Sayed, "Spectroscopic determination of the melting energy of a gold nanorod", *The Journal of Chemical Physics* **114** (2001), 2362–2368 (cit. on p. 53)

[75] M. Kitz, S. Preisser, A. Wetterwald, M. Jaeger, G. N. Thalmann, and M. Frenz, "Vapor bubble generation around gold nano-particles and its application to damaging of cells", *Biomedical Optics Express* **2** (2011), 291 (cit. on p. 53)

[76] M. Ferrera, G. Della Valle, M. Sygletou, M. Magnozzi, D. Catone, P. O'Keeffe, et al., "Thermometric Calibration of the Ultrafast Relaxation Dynamics in Plasmonic Au Nanoparticles", *ACS Photonics* (2020) (cit. on p. 54)

[77] K. M. Hoogeboom-Pot, J. N. Hernandez-Charpak, X. Gu, T. D. Frazer, E. H. Anderson, W. Chao, et al., "A new regime of nanoscale thermal transport: Collective diffusion increases dissipation efficiency", *Proceedings of the National Academy of Sciences* **112** (2015), 4846–4851 (cit. on pp. 54, 58, 95)

[78] T. D. Frazer, J. L. Knobloch, K. M. Hoogeboom-Pot, D. Nardi, W. Chao, R. W. Falcone, M. M. Murnane, H. C. Kapteyn, and J. N. Hernandez-Charpak, "Engineering Nanoscale Thermal Transport: Size- and Spacing-Dependent Cooling of Nanostructures", *Physical Review Applied* **11** (2019), 024042 (cit. on pp. 54, 58, 95)

[79] Y. Hu, L. Zeng, A. J. Minnich, M. S. Dresselhaus, and G. Chen, "Spectral mapping of thermal conductivity through nanoscale ballistic transport", *Nature Nanotechnology* **10** (2015), 701–706 (cit. on p. 54)

[80] H. Zhang, C. Hua, D. Ding, and A. J. Minnich, "Length Dependent Thermal Conductivity Measurements Yield Phonon Mean Free Path Spectra in Nanostructures", *Scientific Reports* **5** (2015) (cit. on p. 54)

[81] M. Hu, C. Novo, A. Funston, H. Wang, H. Staleva, S. Zou, P. Mulvaney, Y. Xia, and G. V. Hartland, "Dark-field microscopy studies of single metal nanoparticles: understanding the factors that influence the linewidth of the localized surface plasmon resonance", *Journal of Materials Chemistry* **18** (2008), 1949 (cit. on p. 54)

[82] P. V. Ruijgrok, P. Zijlstra, A. L. Tchebotareva, and M. Orrit, "Damping of Acoustic Vibrations of Single Gold Nanoparticles Optically Trapped in Water", *Nano Letters* **12** (2012), 1063–1069 (cit. on p. 54)

[83] H. Staleva and G. V. Hartland, "Vibrational Dynamics of Silver Nanocubes and Nanowires Studied by Single-Particle Transient Absorption Spectroscopy", *Advanced Functional Materials* **18** (2008), 3809–3817 (cit. on p. 54)

[84] P. L. Kapitza, *J. Phys. (USSR)* **4** (1941) (cit. on p. 56)

[85] I. M. Khalatnikov, *Zh. Eksp. Teor. Fiz. (USSR)* **22** (1952) (cit. on p. 57)

[86] R. M. Mazo, "Theoretical studies on low temperature phenomena", PhD thesis, Yale University, 1955 (cit. on p. 57).

[87] E. T. Swartz, "Solid-solid thermal boundary resistance", PhD thesis, Cornell University, 1987 (cit. on p. 57).

[88] R. J. Stevens, A. N. Smith, and P. M. Norris, "Measurement of Thermal Boundary Conductance of a Series of Metal-Dielectric Interfaces by the Transient Thermoreflectance Technique", *Journal of Heat Transfer* **127** (2005), 315–322 (cit. on p. 57)

[89] D. A. Young and H. J. Maris, "Lattice-dynamical calculation of the Kapitza resistance between fcc lattices", *Physical Review B* **40** (1989), 3685–3693 (cit. on p. 57)

[90] Y. Xu, H. Wang, Y. Tanaka, M. Shimono, and M. Yamazaki, "Measurement of Interfacial Thermal Resistance by Periodic Heating and a Thermo-Reflectance Technique", *Materials Transactions* **48** (2007), 148–150 (cit. on pp. 59, 91)

[91] J. P. Freedman, X. Yu, R. F. Davis, A. J. Gellman, and J. A. Malen, "Thermal interface conductance across metal alloy–dielectric interfaces", *Physical Review B* **93** (2016) (cit. on pp. 59, 91)

[92] M. Blank and L. Weber, "Influence of the thickness of a nanometric copper interlayer on Au/dielectric thermal boundary conductance", *Journal of Applied Physics* **124** (2018), 105304 (cit. on pp. 59, 91)

[93] M. Blank and L. Weber, "Towards a coherent database of thermal boundary conductance at metal/dielectric interfaces", *Journal of Applied Physics* **125** (2019), 095302 (cit. on pp. 59, 91, 94, 95)

[94] W. W. Hu, K. Sarveswaran, M. Lieberman, and G. H. Bernstein, "Sub-10 nm electron beam lithography using cold development of poly(methylmethacrylate)", *Journal of Vacuum Science & Technology B: Microelectronics and Nanometer Structures Processing, Measurement, and Phenomena* **22** (2004), Publisher: American Institute of Physics, 1711–1716 (cit. on p. 64)

[95] U. Okoroanyanwu, *Chemistry and Lithography*, SPIE Press, 2011 (cit. on p. 64).

[96] M. E. Thomas, S. K. Andersson, R. M. Sova, and R. I. Joseph, "Frequency and temperature dependence of the refractive index of sapphire", *Infrared Physics & Technology* **39** (1998), 235–249 (cit. on pp. 80, 85)

[97] R. B. Wilson, B. A. Apgar, L. W. Martin, and D. G. Cahill, "Thermoreflectance of metal transducers for optical pump-probe studies of thermal properties", *Optics Express* **20** (2012), 28829 (cit. on pp. 80, 82–84)

[98] Y.-J. Chen, M.-C. Lee, and C.-M. Wang, "Dielectric function dependence on temperature for Au and Ag", *Japanese Journal of Applied Physics* **53** (2014), 08MG02 (cit. on p. 83)

[99] P.-T. Shen, Y. Sivan, C.-W. Lin, H.-L. Liu, C.-W. Chang, and S.-W. Chu, "Temperature- and roughness-dependent permittivity of annealed/unannealed gold films", *Optics Express* **24** (2016), 19254 (cit. on p. 83)

[100] H. Reddy, U. Guler, A. V. Kildishev, A. Boltasseva, and V. M. Shalaev, "Temperature-dependent optical properties of gold thin films", *Optical Materials Express* **6** (2016), 2776 (cit. on p. 83)

[101] S. Zhang, Y. Pei, and L. Liu, "Dielectric function of polycrystalline gold films: Effects of grain boundary and temperature", *Journal of Applied Physics* **124** (2018), 165301 (cit. on p. 83)

[102] M. Magnozzi, M. Ferrera, L. Mattera, M. Canepa, and F. Bisio, "Plasmonics of Au nanoparticles in a hot thermodynamic bath", *Nanoscale* **11** (2019), 1140–1146 (cit. on p. 83)

[103] F. Banfi, F. Pressacco, B. Revaz, C. Giannetti, D. Nardi, G. Ferrini, and F. Parmigiani, "*Ab initio* thermodynamics calculation of all-optical time-resolved calorimetry of nanosize systems: Evidence of nanosecond decoupling of electron and phonon temperatures", *Physical Review B* **81** (2010) (cit. on pp. 91, 92)

[104] R. Rouxel, M. Diego, F. Medeghini, P. Maioli, F. Rossella, F. Vallée, F. Banfi, A. Crut, and N. Del Fatti, "Ultrafast Thermo-Optical Dynamics of a Single Metal Nano-Object", *The Journal of Physical Chemistry C* **124** (2020), 15625–15633 (cit. on p. 100)

[105] A. Ahmed, M. Pelton, and J. R. Guest, "Understanding How Acoustic Vibrations Modulate the Optical Response of Plasmonic Metal Nanoparticles", *ACS Nano* **11** (2017), 9360–9369 (cit. on p. 103)

[106] C.-K. Sun, F. Vallée, L. H. Acioli, E. P. Ippen, and J. G. Fujimoto, "Femtosecond-tunable measurement of electron thermalization in gold", *Physical Review B* **50** (1994), 15337–15348 (cit. on pp. 107–110, 131, 137)

[107] N. Del Fatti, R. Bouffanais, F. Vallée, and C. Flytzanis, "Nonequilibrium Electron Interactions in Metal Films", *Physical Review Letters* **81** (1998), Publisher: American Physical Society, 922–925 (cit. on pp. 107, 132)

[108] P. B. Allen, "Theory of thermal relaxation of electrons in metals", *Physical Review Letters* **59** (1987), 1460–1463 (cit. on pp. 107, 115)

[109] R. W. Schoenlein, W. Z. Lin, J. G. Fujimoto, and G. L. Eesley, "Femtosecond studies of nonequilibrium electronic processes in metals", *Physical Review Letters* **58** (1987), 1680–1683 (cit. on p. 107)

[110] H. E. Elsayed-Ali, T. B. Norris, M. A. Pessot, and G. A. Mourou, "Time-resolved observation of electron-phonon relaxation in copper", *Physical Review Letters* **58** (1987), 1212–1215 (cit. on p. 107)

[111] S. D. Brorson, A. Kazeroonian, J. S. Moodera, D. W. Face, T. K. Cheng, E. P. Ippen, M. S. Dresselhaus, and G. Dresselhaus, "Femtosecond room-temperature measurement of the electron-phonon coupling constant γ in metallic superconductors", *Physical Review Letters* **64** (1990), 2172–2175 (cit. on pp. 107, 115)

[112] N. Del Fatti, C. Voisin, M. Achermann, S. Tzortzakis, D. Christofilos, and F. Vallée, "Nonequilibrium electron dynamics in noble metals", *Physical Review B* **61** (2000), 16956–16966 (cit. on pp. 107–110, 116)

[113] J. .-Y. Bigot, J. .-Y. Merle, O. Cregut, and A. Daunois, "Electron Dynamics in Copper Metallic Nanoparticles Probed with Femtosecond Optical Pulses", *Physical Review Letters* **75** (1995), 4702–4705 (cit. on p. 107)

[114] M. Nisoli, S. Stagira, S. De Silvestri, A. Stella, P. Tognini, P. Cheyssac, and R. Kofman, "Ultrafast Electronic Dynamics in Solid and Liquid Gallium Nanoparticles", *Physical Review Letters* **78** (1997), 3575–3578 (cit. on p. 107)

[115] J. H. Hodak, I. Martini, and G. V. Hartland, "Spectroscopy and Dynamics of Nanometer-Sized Noble Metal Particles", *The Journal of Physical Chemistry B* **102** (1998), 6958–6967 (cit. on p. 107)

[116] C. Voisin, N. Del Fatti, D. Christofilos, and F. Vallée, "Ultrafast Electron Dynamics and Optical Nonlinearities in Metal Nanoparticles", *The Journal of Physical Chemistry B* **105** (2001), 2264–2280 (cit. on p. 107)

[117] C. Voisin, D. Christofilos, N. Del Fatti, F. Vallée, B. Prével, E. Cottancin, J. Lermé, M. Pellarin, and M. Broyer, "Size-Dependent Electron-Electron Interactions in Metal Nanoparticles", *Physical Review Letters* **85** (2000), 2200–2203 (cit. on p. 107)

[118] N. Del Fatti, A. Arbouet, and F. Vallée, "Femtosecond optical investigation of electron–lattice interactions in an ensemble and a single metal nanoparticle", *Applied Physics B* **84** (2006), 175–181 (cit. on pp. 107, 115, 131, 137)

[119] P. Nozières and D. Pines, *Theory of Quantum Liquids*, W.A. Benjamin, 1966 (cit. on p. 110).

[120] J. H. Hodak, A. Henglein, and G. V. Hartland, "Photophysics of Nanometer Sized Metal Particles: Electron–Phonon Coupling and Coherent Excitation of Breathing Vibrational Modes", *The Journal of Physical Chemistry B* **104** (2000), 9954–9965 (cit. on p. 110)

[121] F. Vallée and N. Del Fatti, *Challenges and advances in computational chemistry and physics*, Springer, 2013 (cit. on pp. 112, 113).

[122] J. B. Smith and H. Ehrenreich, "Frequency dependence of the optical relaxation time in metals", *Physical Review B* **25** (1982), 923–930 (cit. on p. 112)

[123] N. E. Christensen and B. O. Seraphin, "Relativistic Band Calculation and the Optical Properties of Gold", *Physical Review B* **4** (1971), 3321–3344 (cit. on p. 113)

[124] G. R. Parkins, W. E. Lawrence, and R. W. Christy, "Intraband optical conductivity $\sigma(\omega, T)$ of Cu, Ag, and Au: Contribution from electron-electron scattering", *Physical Review B* **23** (1981), 6408–6416 (cit. on p. 114)

[125] J. H. Weaver and H. P. R. Frederikse, *CRC Handbook of Chemistry and Physics*, CRC Press, 1977 (cit. on p. 115).

[126] J. Hohlfeld, S.-S. Wellershoff, J. Güdde, U. Conrad, V. Jähnke, and E. Matthias, "Electron and lattice dynamics following optical excitation of metals", *Chemical Physics* **251** (2000), 237–258 (cit. on pp. 131, 137)

[127] M.-N. Su, C. J. Ciccarino, S. Kumar, P. D. Dongare, S. A. Hosseini Jebeli, D. Renard, et al., "Ultrafast Electron Dynamics in Single Aluminum Nanostructures", *Nano Letters* **19** (2019), 3091–3097 (cit. on pp. 131, 137)

[128] W. Huang, W. Qian, M. A. El-Sayed, Y. Ding, and Z. L. Wang, "Effect of the Lattice Crystallinity on the Electron–Phonon Relaxation Rates in Gold Nanoparticles", *The Journal of Physical Chemistry C* **111** (2007), 10751–10757 (cit. on p. 137)

Résumé en langue française

Dans cette thèse, la spectroscopie optique résolue en temps (pompe-sonde) a été utilisée pour étudier les dynamiques de thermalisation interne et de refroidissement de nanoparticules métalliques individuelles. Tout au long de ces travaux, l'accent a été mis sur une analyse quantitative de la réponse optique transitoire des nano-objets observée au long de ces processus ultra-rapides. En particulier, la dépendance en longueur d'onde des changements optiques transitoires est explorée expérimentalement et théoriquement, ce qui permet de caractériser la sensibilité des mesures résolues en temps aux différents processus physiques affectant la réponse optique.

Ce travail est organisé en quatre chapitres. Dans le premier, les propriétés physiques des métaux nobles massifs et à l'échelle nanométrique sont décrites d'un point de vue théorique. Les propriétés électroniques et thermiques des métaux massifs sont d'abord passées en revue, ainsi que leur réponse optique. L'effet du confinement diélectrique est ensuite expliqué dans les cas d'une sphère ou d'un ellipsoïde petits par rapport à la longueur d'onde de la lumière (approximation dipolaire), et généralisé au cas de nano-objets plus grands. Une approche numérique basée sur la méthode des éléments finis, permettant de calculer la réponse optique de nano-objets de toute forme, taille et environnement, est également présentée. Enfin, les mécanismes de relaxation ultra-rapides déclenchés par l'excitation impulsionnelle d'une nanoparticule métallique sont brièvement présentés.

Le chapitre 2 décrit les techniques expérimentales utilisées au cours de ce travail, dont la configuration a été optimisée pour permettre des mesures hautement quantitatives. Nous présentons tout d'abord la technique de spectroscopie par modulation spatiale (SMS), qui permet de détecter un nano-objet unique isolé et de mesurer sa section efficace d'extinction en fonction de la longueur d'onde et de la polarisation de la lumière. Le principe de la spectroscopie optique résolue en temps (adaptée pour la mesure de nano-objets individuels) est ensuite présenté dans une deuxième partie.

Le troisième chapitre présente une étude expérimentale et théorique du refroidissement de nanodisques d'or individuels lithographiés sur un substrat de saphir après un échauffement rapide. L'objectif de cette étude est double. Le premier aspect de ce travail est consacré à l'étude de la sensibilité du signal pompe–sonde (qui correspond à la modification de la section efficace d'extinction) aux changements de température du nanodisque, qui dépend de la longueur d'onde. Des mesures pompe-sonde systématiques, effectuées sur deux nanodisques de dimensions différentes (environ 18 nm d'épaisseur et 100 ou 150 nm de diamètre), ont permis de déterminer expérimentalement cette sensibilité en fonction de la longueur d'onde du faisceau de sonde. Pour les deux nanodisques considérés, ce paramètre a montré une forte exaltation autour de la longueur d'onde de la résonance plasmon de surface. Ces spectres ont également été calculés au moyen

d'un modèle opto-thermique à éléments finis, en excellent accord quantitatif avec les expériences.

Le deuxième aspect de ce chapitre a trait à la dynamique de refroidissement des nanodisques d'or par transfert thermique vers leur substrat de saphir. Dans cette optique, des mesures résolues en temps ont été effectuées sur un grand nombre de nanodisques individuels d'épaisseurs (18 ou 40 nm) et de diamètres (60–200 nm) variables. L'utilisation de fluences de pompe modérées limitant le chauffage du réseau à des valeurs de < 15 K était essentielle pour éviter une modification permanente des signaux mesurés pendant les expériences. Dans ces conditions, la dynamique de ces signaux—reflétant directement l'évolution de la température des nanodisques—a été trouvée quasi-exponentielle. Une telle dynamique, confirmée par une simulation thermique par éléments finis, est caractéristique d'un transfert de chaleur limité par l'interface. Les expériences montrent que le temps caractéristique de refroidissement augmente quasi-proportionnellement avec l'épaisseur du nanodisque, tandis que les variations en fonction du diamètre sont beaucoup plus faibles, tendances confirmées par les calculs numériques. La comparaison entre les mesures et les simulations a permis d'extraire des valeurs moyennes de la conductance thermique de l'interface or–saphir (conductance de Kapitza), qui sont en accord avec les valeurs rapportées dans la littérature. Nos expériences sur particules individuelles nous ont également permis d'étudier la dispersion de cette quantité d'un nano-objet à l'autre, qui s'est avérée faible pour les échantillons utilisés. Alors que plusieurs études antérieures sur des nano-objets (tels que des nanolignes de nickel) ont fait état d'écarts par rapport à la loi de Fourier de la conduction thermique, attribués à un transport quasi-balistique des phonons dans le substrat à proximité des nanostructures, nous avons montré que, pour le nanosystème étudié, nos expériences sont insensibles à ces effets éventuels. En effet, en raison de la faible conductance thermique de l'interface or–saphir, ainsi que de la géométrie particulière du nanosystème permettant la propagation efficace de la chaleur dans le substrat, nos mesures sont peu sensibles aux modalités du transport thermique dans le saphir. Pour conclure ce chapitre, nous avons cherché à comprendre l'origine de modifications irréversibles de la dynamique de refroidissement des nanodisques fréquemment observées pour des fluences excessives des impulsions de pompe. Malgré plusieurs tests expérimentaux et un modèle permettant de décrire les changements observés, l'origine de cet effet n'a pas été entièrement élucidée.

Le quatrième et dernier chapitre se concentre sur les phénomènes ultra-rapides se produisant immédiatement après la photo-excitation du nano-objet, et conduisant à sa thermalisation interne par des échanges d'énergie électron–électron et électron–phonon. En particulier, la sensibilité de l'extinction optique des nanodisques à ces phénomènes est étudiée expérimentalement en fonction de la longueur d'onde de la sonde sur deux nanodisques de tailles différentes. Les mesures effectuées à de nombreuses longueurs d'onde de sonde sont comparées au résultat d'un modèle complet basé sur le calcul de l'évolution

de la distribution électronique (obtenue grâce à la résolution numérique de l'équation de Boltzmann), et prenant également compte les effets de l'échauffement du réseau ionique et de la modification du taux de collisions électron–électron. L'accord quantitatif entre ce modèle et nos résultats expérimentaux est très bon, étant donné que seuls deux paramètres (la durée des impulsions de pompe et de sonde et le temps de relaxation électrons–réseau) ont été laissés libres pour cette comparaison. Contrairement aux mesures à plus longue échelle présentées dans le chapitre 3, la dynamique observée dépend fortement de la longueur d'onde de la sonde. Afin de mieux comprendre ces dynamiques complexes, une version simplifiée du modèle susmentionné a été proposée, approximativement valable après la fin de la thermalisation interne des électrons ($\sim$2 ps). Dans ce modèle, la dynamique des signaux transitoires est expliquée comme reflétant une combinaison des variations de température des électrons et du réseau, avec des poids dépendant de la longueur d'onde de la sonde (respectivement notés $A_e(\lambda_{pr})$ et $A_L(\lambda_{pr})$). Ainsi, ces amplitudes correspondent à la sensibilité des mesures résolues en temps aux changements de température des électrons et du réseau. Des signaux expérimentaux particuliers, reflétant uniquement la dynamique des électrons ou du réseau, ont été identifiés et interprétés avec succès à l'aide de ce modèle. Enfin, les spectres transitoires des deux nanodisques ont été décrits à la lumière du modèle complet, où les contributions des différents effets physiques ont pu être séparées. Dans la préparation d'une expérience de spectroscopie résolue en temps, ce modèle peut s'avérer très utile, car il permet de sélectionner la longueur d'onde de sonde maximisant l'effet souhaité, ou en annulant d'autres.

En conclusion de ce manuscrit, les principaux résultats de cette thèse sont rassemblés selon deux axes. Le premier concerne l'étude de la dynamique de refroidissement. Ce projet représente la première étude thermique réalisée en spectroscopie résolue en temps sur des nano-objets individuels. Dans cette thèse, cette particularité a permis d'évaluer la dispersion d'une particule à l'autre de la quantité mesurée (conductance de Kapitza), ainsi que d'obtenir des signaux hautement quantitatifs, permettant une analyse plus fine des phénomènes en jeu. À l'avenir, ces expériences pourront être étendues à des nano-objets de différentes compositions et géométries, ce qui ouvre ainsi la voie à l'étude directe des différents régimes de transport thermique à l'échelle nanométrique sur des particules individuelles. Le second axe, développé à la fois dans les chapitres 3 et 4, a pour objet la sensibilité des mesures pompe-sonde aux différents processus physiques ayant lieu suite à l'excitation du nano-objet. Ces sensibilités, dont la connaissance est utile à la planification d'une expérience pompe-sonde, ont pu être prédites quantitativement par des modèles thermo-optiques sans paramètres libres autres que les durées des impulsions lumineuses utilisées et les temps caractéristiques des différents processus physiques. L'accord remarquable entre ces modèles et les mesures réalisées aux différentes échelles de temps confirme l'aspect quantitatif de la technique de pompe-sonde sur nano-objets individuels, impliquant notamment que les élévations de températures absolues

peuvent être déduites à partir des signaux optiques. Dans un futur proche, les modèles développés dans ce travail pourraient par exemple être exploités pour une caractérisation plus fine des échanges d'énergie entre électrons et réseau, ce qui permettrait notamment de préciser leur dépendance vis-à-vis de la cristallinité du métal.

Ultrafast thermo-optical dynamics of single plasmonic nanoparticles

Abstract:

The ultrafast dynamics of individual gold nanodisks supported on a sapphire substrate occurring at femtosecond to nanosecond timescales have been investigated using the combination of single-particle spatial modulation and time-resolved optical spectroscopies. Nanodisks are excited out of equilibrium by the absorption of an optical pump pulse, and their relaxation is optically probed by measuring the transmission of a second probe pulse. In the first part of this work, the dynamics of heat transfer from the nano-object to the substrate have been systematically measured for nanodisks of various dimensions. Quasi-exponential cooling kinetics were found, with a time constant mainly depending on the disk thickness and weakly on its diameter. Comparison of experimental signals with the results of finite-element calculations indicates that the cooling dynamics are primarily limited by the Kapitza thermal boundary resistance at the nanodisk-substrate interface, whose value could be extracted. Additionally, the sensitivity of pump-probe measurements to transient temperature changes in the nano-object was experimentally determined as a function of the probe wavelength, its values and spectral variations presenting a good quantitative agreement with the results of a thermo-optical finite-element model. The second part of this thesis focuses on the ultrafast phenomena immediately following the nano-object photo-excitation, leading to its internal thermalization through electron-electron and electron-phonon energy exchanges. In particular, the sensitivity of the optical extinction of individual nanodisks to these phenomena has been experimentally investigated as a function of the probe wavelength. These measurements were compared with the results of a complete numerical model based notably on the resolution of the Boltzmann equation and also taking into account the effect of lattice heating, yielding a good quantitative agreement. A simplified version of this model also allowed to highlight the respective roles of the temperature evolutions of the electrons and of the ionic lattice, greatly clarifying the temporal and spectral dependences of the measured time-resolved signals.

Keywords:

Pump-probe spectroscopy, Spatial modulation spectroscopy, Single metal nanoparticles, Thermoplasmonics, Nanothermics, Thermal boundary conductance, Finite element method, Electron-phonon coupling

Dynamique thermo-optique ultrarapide de nanoparticules plasmoniques individuelles

Résumé :

Les changements de propriétés dynamiques de nanodisques d'or individuels supportés sur un substrat de saphir ont été étudiés sur des échelles de temps allant de la femtoseconde à la nanoseconde par la combinaison des techniques de spectroscopie par modulation spatiale et de spectroscopie optique résolue en temps. Les nanodisques sont mis hors-équilibre par l'absorption d'une impulsion optique de pompe, et leur relaxation est sondée optiquement par la mesure de la transmission d'une seconde impulsion. Dans la première partie de ce travail, la dynamique du transfert de chaleur du nano-objet au substrat a été mesurée de manière systématique pour des nanodisques de différentes dimensions. Les refroidissements observés sont quasi-exponentiels, avec une constante de temps dépendant principalement de l'épaisseur du disque, et faiblement de son diamètre. La comparaison des signaux expérimentaux avec les résultats de calculs par éléments finis indique que la dynamique de refroidissement est principalement limitée par la résistance thermique de Kapitza à l'interface nanodisque-substrat, dont la valeur a pu être extraite. En outre, la sensibilité des mesures pompe-sonde aux changements de température du nano-objet a été déterminée expérimentalement en fonction de la longueur d'onde de la sonde, ses valeurs et variations spectrales présentant un bon accord quantitatif avec les résultats d'un modèle thermo-optique par éléments finis. La deuxième partie de cette thèse se concentre sur les phénomènes ultra-rapides consécutifs à la photo-excitation d'un nano-objet, qui conduisent à sa thermalisation interne par des échanges d'énergie électron-électron et électron-phonon. En particulier, la sensibilité à ces phénomènes de l'extinction optique de nanodisques individuels a été étudiée expérimentalement en fonction de la longueur d'onde de la sonde. Ces mesures ont été comparées aux résultats d'un modèle numérique complet basé notamment sur la résolution de l'équation de Boltzmann et prenant également en compte l'effet du chauffage du réseau ionique, conduisant à un bon accord quantitatif. Une version simplifiée de ce modèle a également permis de mettre en évidence les rôles respectifs de l'évolution des températures des électrons et du réseau, clarifiant ainsi grandement les dépendances temporelle et spectrale des signaux résolus en temps.

Mots-clefs :
Spectroscopie pompe-sonde, spectroscopie par modulation spatiale, Nanoparticules métalliques individuelles, Thermoplasmonique, Nanothermique, Conductance thermique d'interface, Méthode des éléments finis, Couplage électron-phonon